NUCLEAR SCIENCE and ENGINEERING

THE JOURNAL OF THE AMERICAN NUCLEAR SOCIETY

VOLUME 13, NUMBER 4, AUGUST 1962

CONTENTS

Indexed in "Engineering Index" and Abstracted in "Nuclear Science Abstracts"

Published monthly at Mt. Royal and Guilford Aves., Baltimore, Md., for Academic Press Inc.
111 Fifth Avenue, New York 3, N. Y.
During 1962, Volumes 12, 13, and 14 will be published. Price of each volume: $21.00.
Subscription orders should be sent to the publishers.
Notice of change of address must be received two months prior to the date of issue. Include both old and new addresses.
For Member Subscriptions: Notice should be sent to the Secretary of the American Nuclear Society,
John Crerar Library, 86 East Randolph Street, Chicago 1, Illinois.
For Non-member Subscriptions: Notice should be sent to the publishers.
Second-class mail postage paid at Baltimore, Md.

NUCLEAR SCIENCE AND ENGINEERING: **13**, 301-305 (1962)

Reflector Moderated Reactors*

C. B. MILLS

University of California, Los Alamos Scientific Laboratory, Los Alamos, New Mexico

Received October 2, 1961; revised February 23, 1962

The complete spatial separation of moderator and uranium fuel bearing regions are shown by experiment to result in critical reactors with low critical mass and relatively uniform fissioning density. Studies of several of these experiments to establish the accuracy of a numerical method of calculation (SNG) for this class of problems show good correspondence between theory and experiment. This method is then used for a useful survey of critical mass and U^{235} atomic density as a function of geometry for the best moderators, D_2O and Be.

I. INTRODUCTION

The spatial separation of neutron moderation from absorption processes in nuclear reactors is made possible by the neutron diffusion properties of several materials. If excellent moderators such as deuterium, beryllium, or graphite fill a region of a reactor exclusively, they serve as a trap, holding the neutrons with a small change in position until, by simple elastic scattering processes, their mean energy has been reduced to thermal values. Since the thermal absorption cross sections of these moderators are small, many of the neutrons will eventually diffuse back into the region containing the fissionable material to support a chain reaction. Others may travel in other directions and escape from the reactor. Beryllium and deuterium are particularly good materials in these respects; beryllium, because of its large inelastic scattering of neutrons (almost as good a moderator for very fast neutrons as hydrogen), and deuterium because it has both good moderation properties and an almost zero thermal absorption cross section. Both materials retain the fast neutrons within distances of the order of 10 cm from the neutron source. Graphite serves the same functions but not as well.

The separation of fissioning from moderating regions makes it possible to surround a U^{235}-containing fissioning volume by a moderating reflector. This arrangement may be shown to be a critical system. A reflector so used may serve both as a moderator and an attenuator of the neutron and gamma radiation of the fissioning process. This duality is important for portable reactors where shield weight must be minimized. Also, where the fissioning-density distribution must be flat, the exponential spatial distribution of fission-producing absorptions, as the neutrons stream into the U^{235}-bearing region from the reflector, can be made more nearly constant by causing thermal neutrons to stream into both sides of an annulus. This is effected by the use of a central spherical (or cylindrical) moderating region, in the position where U^{235} is least important for a peripheral thermal neutron source such as the reflector. However, if the critical U^{235} atomic density is small, the exponential decrease by absorption will be small, and the central moderator need not be used. Both high and low U^{235} atomic density systems are discussed below, the first being appropriate to minimum size, maximum power density reactors (U^{235} in a liquid for heat transfer reasons) and the second to maximum temperature gaseous fuel region reactors.

The reflector moderated reactor was first conceived by Karl Cohen and associates (*1*) for use in nuclear-powered aircraft and was independently conceived, proved possible, and developed at ORNL for the same purpose. The gaseous core reactor was first discussed by Bell (*2*). For this reason the concept is called the Bell cavity.

The reflector-moderator reactor concept was noted in the early stages of the development of the multigroup diffusion approximation method (*3*) of solution of the neutron transport equation and was among the first examples of the generality and power of multigroup numerical machine methods of solving the difficult energy- and space-dependent neutron con-

* Work performed under the auspices of the U. S. Atomic Energy Commission.

TABLE 1

BE REFLECTOR MODERATED EXPERIMENTS AT ORNL

	Radii (cm)				Material atomic densities ($\times 10^{-24}$/cc)			
	Island	Fuel	Be reflector	C reflector	Be (island)[a]	U^{235}	Be refl	C
CA-10	15.2	22.3	51.6	70.3	0.1434	0.000613	0.1135	0.0735
CA-11[b]	11.43	22.8	52.6	68.6	0.1434	0.000295	0.1135	0.0774
CA-14[b, c]	11.43	22.8	52.6	68.6	0.1434	0.00061	0.1135	0.0774

[a] The Be island was actually almost cylindrical so that the effective density was large.
[b] CA-11 and -14 had a Zr, Na, F, C mixture with the U^{235}, to simulate a fused fluoride.
[c] CA-14 had 0.3 cm of SS-316 simulating shells to contain the fluoride.

servation equations. In the computing scheme used, many monoenergetic (but connected) groups of neutrons were required to diffuse and slow down in a manner consistent with neutron age measurements (which fixed the complex fast $0.1 < E < 10$ Mev neutron scattering processes) and to be absorbed at low energy with an approximately (1/velocity) dependence.

Although crude, the early work was adequate for the predictive aspects of the first experimental program on the reflector moderated reactor concept. The more exact SNG method (*4*), which computes neutron flux angle-dependent effects, was used for analysis of later, more "computable" experimental studies as well as for analyses of reflector moderated or cavity reactors of current interest. The SNG method also uses relatively accurate neutron cross section studies (*5*) based on differential measurements (*6*), and careful integral studies by Hansen and Roach (*7*) instead of the integral age studies necessary in the earlier context. Since both the earlier and more recent theoretical methods have been presented in some detail elsewhere (*3*, *4*, *8*, *9*), they will not be discussed here. Instead, the experiments will be briefly described and discussed as a foundation for the present parametric studies. The analyses were all done by Mills.

II. EXPERIMENTS

A. BE REFLECTED REACTORS, ORNL

This set of experiments, performed by D. V. P. Williams in 1953 and recently released, used 10 mil U^{235} foils (93.4% U^{235} in U) and beryllium blocks in a supporting aluminum lattice. The foils were separated by canned sodium, and the lattice had a very roughly spherical geometry. Summary values for equivalent spherical reactors, based on the lattice geometries, are shown in Table I.

The conversion to spherical systems consistent with the method of analysis was of course approximate. Within a considerable uncertainty, an integral comparison of theory and experiment is shown in Table II.

TABLE II

INTEGRAL COMPARISON OF COMPUTED AND EXPERIMENTAL VALUES

Reactor	Critical mass U^{235} (kg)		Fissioning density	
	Computed	Experimental	Computed	Experimental
CA-10	10	15	1.3 /0.82	1.25/0.85
CA-11	7.3	7.7	2.06/0.59	2.0 /0.61
CA-14	16.5	19.3	2.0 /0.61	2.2 /0.56

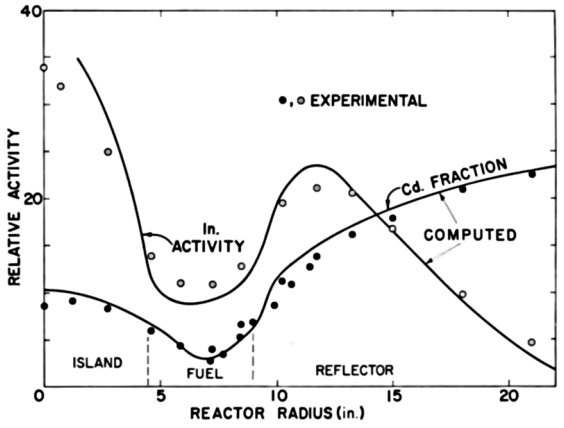

FIG. 1. Integral flux measurement using indium and cadmium foils radially in Critical Assembly 11.

The close correspondence of computed to experimental criticality encouraged foil activation measurements to explore the neutron flux spectrum. Figure 1 shows a comparison of computed to experimental indium foil activity (relative) and the cadmium fraction (absolute) which is essentially the ratio of epithermal to total indium foil activity. Figure 2 compares computed with experimental fissioning density in the fuel-filled annulus. Many other details were studied, but the relative coarseness of the detailed experimental structure along with still existing limi-

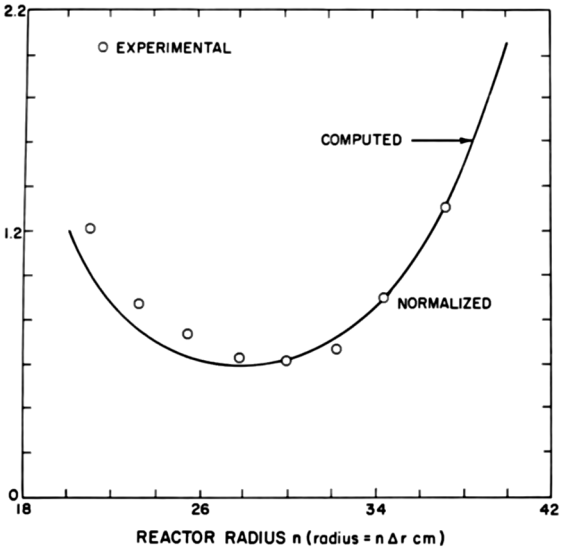

FIG. 2. Fissioning density radially in Critical Assembly 11.

TABLE III

BE REFLECTED CAVITY REACTORS
(BERYLLIUM AVERAGE DENSITY 1.77 gm/cc)

Geometry	Critical mass (kg U^{235})	Annular region radii (cm)	k_{eff}
U^{235} foil on cavity surface	11.0	28.4/63.9	1.01
Homogeneous cavity	7.64	28.4/63.9	1.02
U^{235} in central region	8.62	25.4/28.4/63.9	0.98
Homogeneous cavity	10.0	22.5/58.1	1.03

Note: The cavity reactor experiments were not geometrically simple.

tations in practicable computing techniques reduces interest in a cross-comparison of experimental and computed details.

B. D_2O Reflected Reactor, LASL

This experiment, performed by C. C. Byers and D. Wood, used D_2O in a symmetric right circular cylinder 80 in. in length and diameter, with a 40 in. length and diameter central cylindrical void. Aluminum shells of $\frac{3}{16}$ in. total thickness around a central void supported a surface layer of U^{235} foil (93.4%) and contained the D_2O reflector moderator. The critical mass of U^{235} was 6.0 kg of U^{235}. The D_2O was approximately 99.23% pure, i.e., 0.77% by weight H_2O.

The computed k_{eff} for the complete assembly, with neutron cross sections validated by a study of homogeneous D_2O reactors (*10*), was 1.01.

C. Be Reflected Reactors, LASL

This experiment, by C. C. Byers and G. Jarvis, used Be in an annular cylinder with several arrangements of U^{235}, first as foil on the surface of a cavity and second as a dispersed material in graphite, in the cavity. Table III describes the reactors as equal cavity volume spheres.

III. PARAMETRIC STUDIES OF GAS-FILLED REFLECTOR MODERATED REACTORS

The purpose of this section is to establish the minimum critical mass and concentration of U^{235} in a wide variety of cavity (or reflector moderated) reactors. These are of current interest because of the essentially unlimited temperatures possible with the fissioning process in the gaseous state. The parameters are geometry (spheres and cylinders) and radii, with some attention given to neutron absorption by structural materials.

The relative value of D_2O, Be, and C as reflectors of a U^{235} gas-filled cavity is shown in Fig. 3. Note that Be and D_2O are equivalent for thicknesses less than 50 cm, and that the use of D_2O in a thick layer is consistent with the lowest critical concentration of U^{235}. The dependence of critical core (cavity) radius

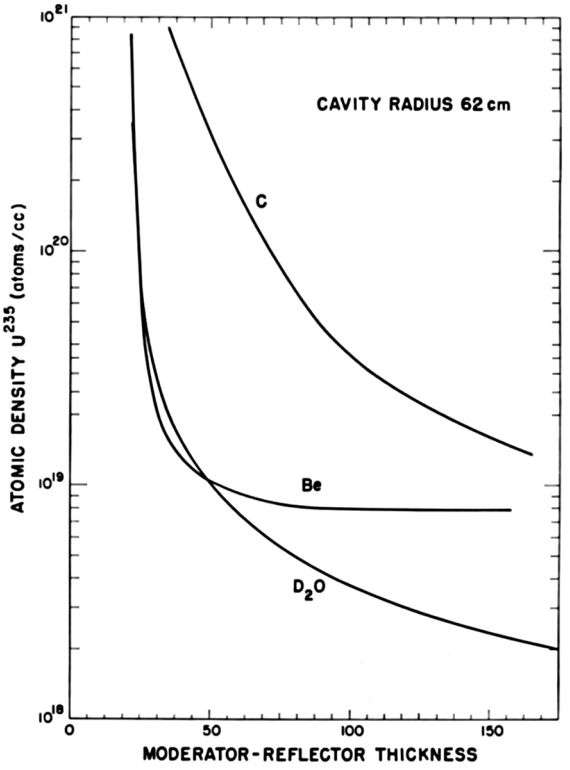

FIG. 3. Critical concentration of U^{235} gas as a function of D_2O, Be, and C reflector thickness.

on the reflector is shown in Fig. 4. Note the minimum in the critical mass of U^{235} gas with a Be reflector.

The limits of criticality of U^{235} gas are explored in Figs. 5–7, which show critical mass and atomic density of U^{235} for large spherical and cylindrical cavities reflected by D_2O. Note the small value of increased D_2O thickness and the relatively large effect of a structural layer at the cavity wall.

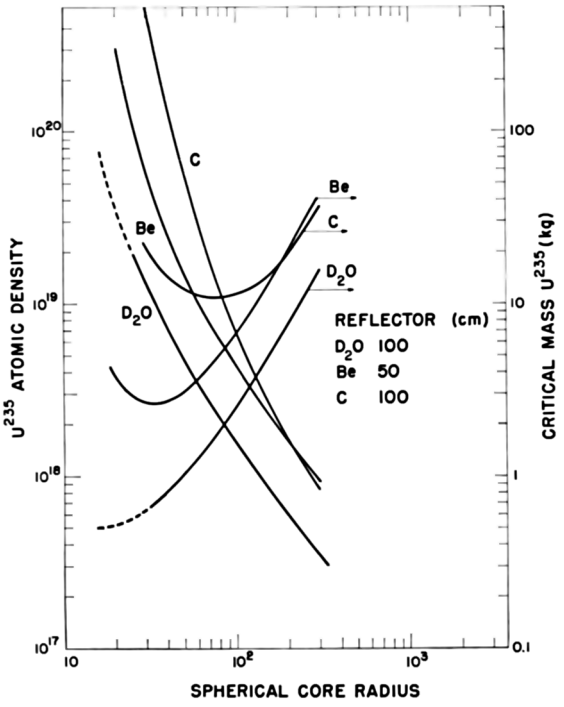

FIG. 4. Critical concentration of U^{235} gas as a function of D_2O, Be, and C reflected core radius.

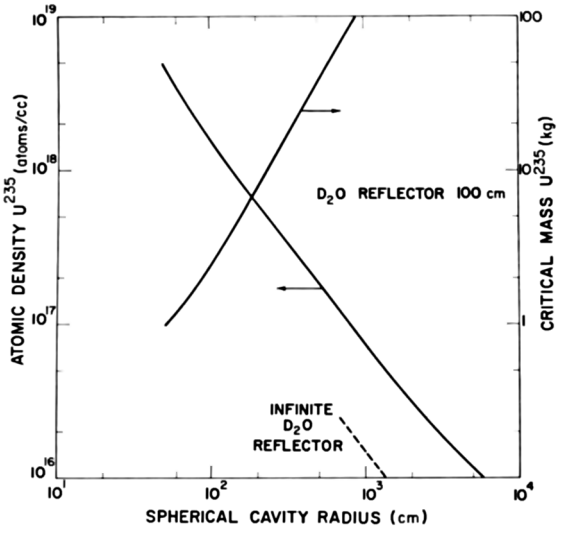

FIG. 5. Critical concentration and mass of U^{235} gas vs. spherical core radius for a cavity reflected by 100 cm D_2O.

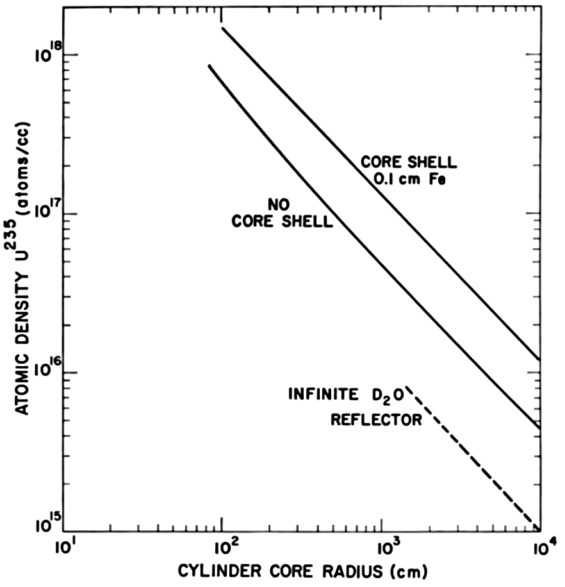

FIG. 6. Critical concentration of U^{235} gas vs. cylinder core radius for a cavity reflected by 100 cm D_2O.

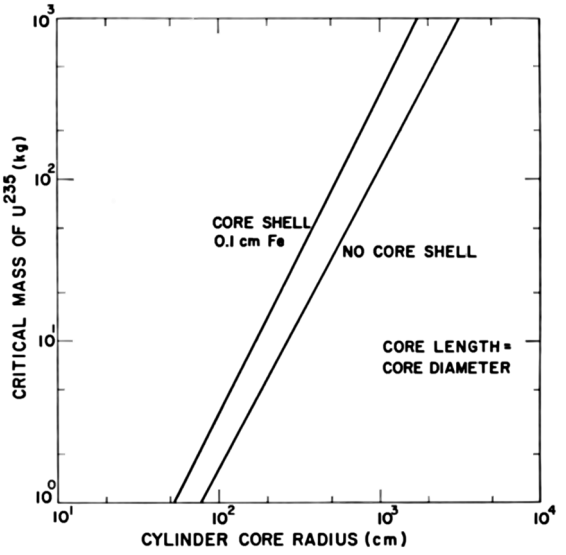

FIG. 7. Critical U^{235} mass vs. cylinder core radius for a cavity reflected by 100 cm D_2O.

An interesting extrapolation of the cavity reactor concept is shown in Fig. 8, for a cylinder reflected by 100 cm (0.1 cm Fe lining the cavity wall) D_2O but with the U^{235} restrained to smaller radii (the S_4–S_{16} approximations (*4*) were required for these curves) than the radius of the core (dotted line). Figure 9 shows the critical mass dependence for this set for cylinder length equals diameter. Neither critical mass nor atomic density of U^{235} is a strong function of gas radius until the area reduction is very large.

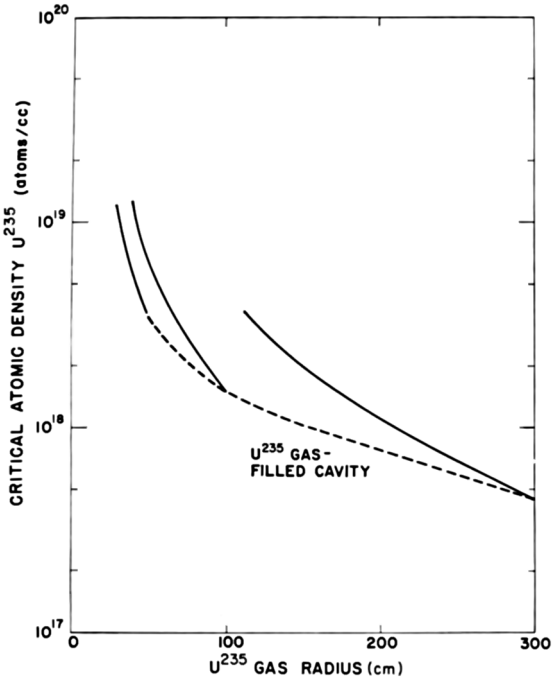

FIG. 8. Critical concentration of U^{235} gas vs. axial cylindrical column of radius for a cavity of constant radius reflected by 100 cm D_2O.

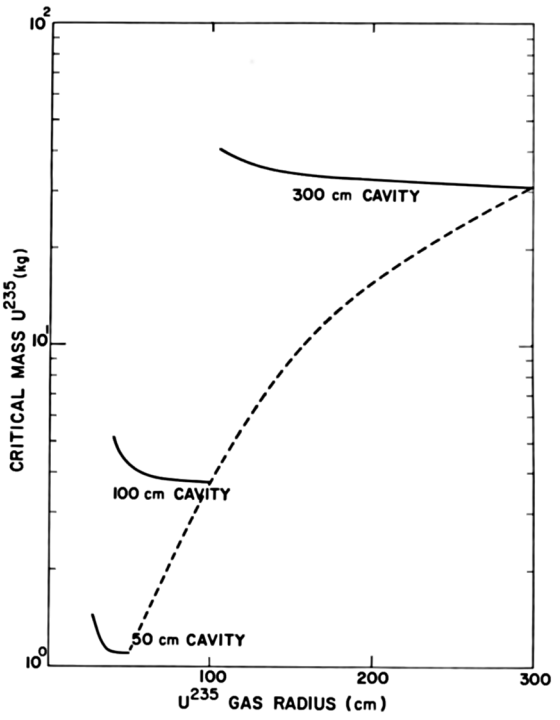

FIG. 9. Critical U^{235} mass vs. axial cylindrical column radius for a cavity of constant radius reflected by 100 cm D_2O.

A. CHARACTERISTICS OF THE BELL CAVITY

The analyses made in the course of experimental studies and parametric surveys permit the formation of several qualitative statements:

1. The system is sensitive to U^{235} content, with a $\Delta k/(\Delta U/U) \simeq 0.3$.

2. The system is not sensitive to core diameter changes with a constant amount of U^{235}. The relation of U^{235} concentration to core radius is approximately $N(U^{235}) = K/R(\text{core})$.

3. The system is very sensitive to neutron absorption, either in the core shell or D_2O reflector. This fact reduces the value of the cavity as a container for a thick surface layer of "dust" containing a fissionable isotope. As examples, a 10 cm layer of metal with U^{235} in a 50 cm radius spherical cavity results in critical mass vs. metal of 6 kg for Zr, 100 kg for Mo, and 600 kg for Ta.

4. Critical mass increases approximately as cavity radius squared.

5. Minimum volume and weight systems for very high total reactor power are possible with fluid-fueled reflector moderated reactors, with lower critical mass (a factor of ½) and more constant power density resulting from a central moderating volume.

ACKNOWLEDGMENTS

This study was suggested by R. W. Bussard. Earlier work in reflector-moderated reactor systems was supported by R. C. Bryant and A. P. Fraas of ORNL. Other studies of this reactor type have been made by G. Safonov and by R. C. Ragsdale and R. E. Hyland.

REFERENCES

1. KARL COHEN, HKF-109, 1950 (Secret Report by H. K. Ferguson Co., New York, N.Y.).
2. G. I. BELL, Calculation of the critical mass of UF_6 as a gaseous core, with reflectors of D_2O, Be, and C. Los Alamos Scientific Laboratory Report LA-1874 (1955).
3. C. B. MILLS, The general methods of reactor analysis used by the ANP physics group. ORNL-1493 (November 1953).
4. B. G. CARLSON, Solution of the transport equations by S_n approximations. Los Alamos Scientific Laboratory Report LA-1891 (1955).
5. C. B. MILLS, Neutron cross sections for fast and intermediate reactors. Los Alamos Scientific Laboratory Report LAMS-2255 (1959).
6. D. J. HUGHES AND R. B. SCHWARTZ, Neutron cross sections. BNL-325 (1958).
7. G. E. HANSEN AND W. H. ROACH, Six and sixteen group cross sections for fast and intermediate critical assemblies. Los Alamos Scientific Laboratory Report LA-2543 (1961).
8. C. B. MILLS, Reactor computing practices. Los Alamos Scientific Laboratory Report LA-2240 (1958).
9. M. V. MEGHREBLIAN AND D. K. HOLMES, "Reactor Analysis." McGraw-Hill, New York, 1960.
10. R. N. OLCOTT, Homogeneous heavy water moderated critical assemblies, Part 1, Experimental. *Nuclear Sci. and Eng.* **1**, 327–341 (1956).

NUCLEAR SCIENCE AND ENGINEERING: **13**, 306–324 (1962)

Thermal Neutron Spectra in Graphite*

D. E. PARKS, J. R. BEYSTER, AND N. F. WIKNER

John Jay Hopkins Laboratory for Pure and Applied Science, General Atomic Division of General Dynamics Corporation, San Diego, California

Received October 13, 1961

A pulsed, high-current, electron linear accelerator is used to excite thermal-neutron spectra in a graphite assembly. The steady-state energy spectra of neutrons are measured at several temperatures by pulsed-beam time-of-flight techniques. We compare the measured spectra with theoretical predictions which use free- and bound-carbon scattering kernels.

The scattering kernel for carbon bound in graphite is obtained through a realistic treatment of the neutron–phonon interactions. With this kernel, theoretical calculations of spectra agree extremely well with the experimental results. Predictions derived from a scattering law in which the carbon atoms are treated as free differ markedly from the measured spectra, even up to a temperature of 810°K. Additional calculations show that the effects of chemical binding are significant in problems of reactor design physics.

INTRODUCTION

In recent months, the problem of the thermalization of neutrons in graphite has been the subject of considerable experimental and theoretical activity. Experimental techniques for measuring low-energy neutron spectra have been developed at many laboratories (*1–5*). These methods have been utilized extensively in the study of spectra in hydrogen-moderated assemblies, but, until recently, to a considerably less extent in the study of moderation by heavy atoms bound in crystals. Although measurements of neutron spectra have been made in weakly absorbing graphite thermal columns (*3*), the neutrons are so nearly in equilibrium with the moderator that the effects of binding of the carbon atoms are not observable. For the effects of chemical binding to be significant, the thermal neutrons must be excited in an assembly sufficiently poisoned to produce appreciable departures from the Maxwellian spectrum. The proper understanding of these departures from equilibrium is a problem of considerable theoretical complexity.

The work of Schofield and Hassitt was one of the first attempts to calculate neutron spectra in graphite in a realistic way (*6*). Although their method for treating the neutron–phonon interaction in graphite leads to appreciable correction to the spectra because of the effects of chemical binding, it suffers from deficiencies which result in a considerable underestimate of the magnitude of these corrections.

The present paper deals with the measurement and theory of neutron spectra in poisoned graphite systems at several temperatures. We begin with a description of experimental procedures. This is followed by a discussion of the method of treating the neutron–phonon interactions. The remainder of the paper consists of a presentation of the experimental results, their comparison with theory, and a consideration of the importance of chemical-binding effects in graphite for problems of reactor design physics.

Since the method for calculating the neutron–phonon interaction is the subject of another paper (*7*), here we only outline the essential features of the method. Our theoretical treatment begins with a discussion of the lattice vibrations in graphite and their interaction with slow neutrons. As a consequence of the symmetry of the lattice and the particular kind of anisotropy exhibited by its vibrations, it is possible, in the incoherent approximation, to replace the extremely complicated exact expression for the microscopic energy-transfer cross section, $\sigma(E_0 \rightarrow E, \theta)$, by one that is relatively

* The work reported herein was performed in part under Contract AT(04-3)-314, in part under Contract AT(04-3)-167, Project Agreement No. 2, both with the U. S. Atomic Energy Commission, and in part with General Atomic private research funds.

simple and tractable for numerical evaluation on a high-speed computer. To accomplish the numerical evaluation of $\sigma(E_0 \rightarrow E, \theta)$, we make use of the phonon and short-collision-time expansions. A proper combination of the two expansions ameliorates the inherently slow convergence of the phonon expansion for the case of collisions which involve large neutron momentum transfers. Although the code for computing the scattering kernel has been applied only for the case of inelastic scattering by graphite, it is also capable of evaluating the scattering kernel associated with other moderating materials.

DESCRIPTION OF EXPERIMENT

Experimental Design

Until recently, measurements of neutron spectra in graphite lattices have been performed by standard slow-chopper techniques rather than by pulsed-beam methods (*2*, *3*). However, with the availability of sharp time and energy resolution and with the high neutron intensities produced by electron linear accelerators, accurate, pulsed spectrum measurements in some graphite systems are now feasible. Ordinarily, only neutron spectra in highly poisoned graphite systems are amenable to study by pulsed techniques, since a short neutron lifetime is necessary to prevent excessive widening of the neutron burst. A moderately high neutron absorption is also desirable to emphasize the effects of chemical binding on the measured spectrum.

Ideally, in this class of experiment the absorbing material should be homogeneously distributed in the solid graphite. In practice, we approach this ideal condition by using thin, borated, stainless steel sheets spaced less than a transport mean free path (2.5 cm) apart. A reasonable compromise between high absorption on the one hand and low self-absorption and flux depression on the other is attained by using 5-mil sheets of Type 304 stainless steel containing 1 wt. % boron and by spacing them 0.525 in. apart. This yields a volume-averaged absorption cross section of about 0.4 barns per carbon atom at a neutron energy of 0.025 ev. The spectral hardness parameter for this condition is $\Sigma_a(0.025 \text{ ev})/\xi\Sigma_s = 0.53$.

Having fixed the absorbing properties of the matrix, we next determine that a cube measuring 24½ in. on a side provides a reasonable geometry. At first, it appears that a very large graphite system would be more desirable for minimizing the effect of neutron leakage on the spectrum. However, since a point fast-neutron source is used to excite the assembly, the localized leakage at the point of measurement depends mainly on its distance from the source and on the effective age to thermal energies, rather than on the proximity of boundaries. Thus, the spectrum and neutron lifetime in the assembly used for the present experiments are not very different from those in a larger assembly. Furthermore, the use of a small assembly considerably simplifies the handling and heating procedures.

The general layout of the experimental assembly, together with the simple heating arrangement, is shown in Fig. 1. Figure 2 is a photograph of the assembly with the graphite half unstacked, taken after high-temperature operation. The entire assembly is contained in a 31-in., cubical, aluminum box. The strip heaters are mounted on ¼-in.-thick copper plates that press firmly against the poisoned graphite stack on all six sides. Boral plates behind the heaters establish the boundaries of the assembly. Fiberfrax thermal insulation separates the aluminum box from the boral sheets. Strip heaters serviced by up to 100 kva of electrical power are used to heat the assembly from room temperature to 810°K. Temperature profiles taken during this process and during the actual spectrum measurements indicate a spatial temperature variation of approximately ±5°K throughout the assembly.

The fast-neutron source is produced by bombarding tungsten alloy (Fansteel 77) with the 20-Mev electron beam from the General Atomic linear accelerator. The resulting bremsstrahlung produces an intense, pulsed neutron source owing to (γ, n) reactions in the tungsten. Thermal neutrons are extracted from a re-entrant hole terminating at the center of the assembly (see Fig. 1). The central location for a re-entrant hole in the assembly minimizes the influence on the neutron spectrum of even harmonics in the spatial flux distribution. Backgrounds are measured by replacing the graphite at the base of the re-entrant hole with boron carbide. The residual counting rate results from neutrons going into the detectors from locations in the assembly other than the point of measurement.

In addition to spectral measurements, two auxiliary studies were conducted to specify the properties of the poisoned graphite system. First, axial and transverse flux distributions of the indium-resonance neutron flux were mapped. These are to be used in establishing the leakage corrections to the neutron spectrum. Second, neutron-lifetime, or die-away, experiments were performed to determine the thermal-neutron lifetime at the point of measurement in the graphite stack.

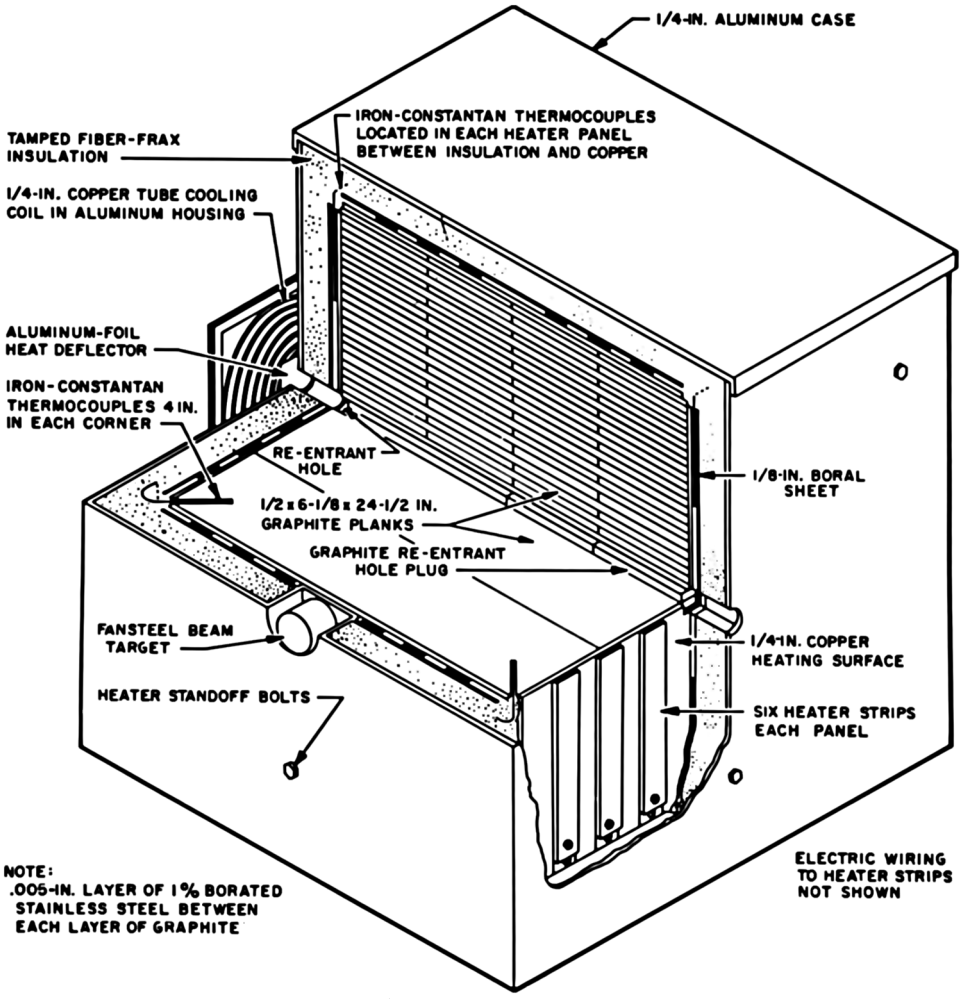

FIG. 1. General layout of graphite assembly and associated heating and insulating equipment

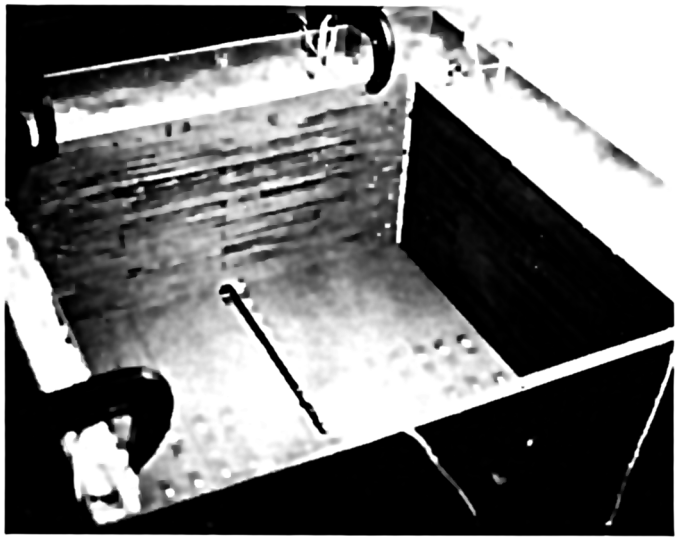

FIG. 2. View of the graphite assembly after heating operation (one half of the graphite has been removed).

Experimental Analysis

The measurements of neutron spectra excited in the shielded neutron-cave area shown in Fig. 3 were made using a 16-meter flight station on a 50-meter flight path. The experimental techniques, utilizing the calibrated BF_3 neutron-detection system, had already been developed (*1*). Experimental data were corrected for neutron background, the energy-dependent transmission of the flight path, the energy-dependent sensitivity of the BF_3 detector bank, and the mean emission time of the neutrons from the assembly. A considerable improvement has been made in the method for determining the mean time, $T(E)$, spent in the assembly by a neutron that escapes with an energy E. The mean emission time for each energy is now calculated in the diffusion approximation by procedures outlined below, and then is subtracted from the measured time between the accelerator pulse and the detection of the event.

To calculate $T(E)$, we identify it with the first time moment of the flux spectrum, $\phi(E, t)$, resulting from a monoenergetic fast burst at $t = 0$:

$$T(E) = \frac{\int_0^\infty t\phi(E, t)\, dt}{\int_0^\infty \phi(E, t)\, dt} = \frac{\phi_1(E)}{\phi_0(E)}. \qquad (1)$$

The time-dependent diffusion of neutrons following a fast monoenergetic burst at $t = 0$, and spatially distributed in a fundamental mode with a buckling

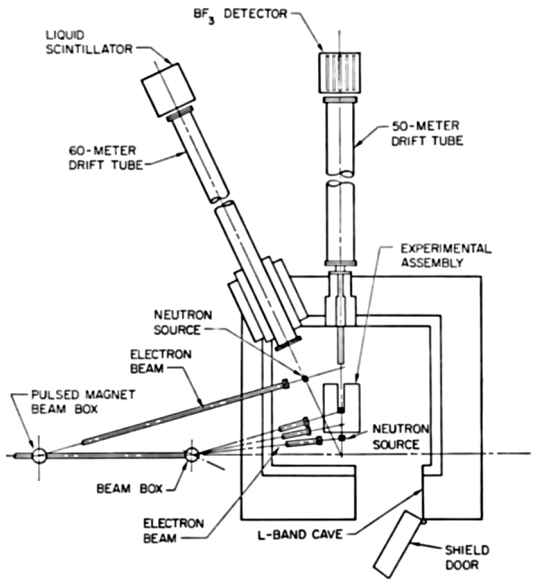

FIG. 3. Plan view of target area showing experimental assembly, drift tube, and detector locations.

B^2, satisfies

$$-\frac{1}{v(E)}\frac{d\phi(E, t)}{dt} = [\Sigma_a(E) + \Sigma_s(E) + D(E)B^2]\phi(E, t) - \int_0^\infty \Sigma(E' \to E)\phi(E', t)\, dE' - \delta_0(E - E_0)\delta_0(t), \qquad (2)$$

where Σ_a, Σ_s, and $\Sigma(E' \to E)$ are the absorption, scattering, and energy-transfer cross sections, respectively, $D(E)$ is the diffusion coefficient, and the delta functions represent the fast source at $t = 0$.

The quantity $\phi_0(E)$ satisfies the equation of balance for the steady-state spectrum of neutrons induced by a spatially flat, fast source:

$$[\Sigma_a(E) + \Sigma_s(E) + DB^2]\phi_0(E) - \int_0^\infty \Sigma(E' \to E)\phi_0(E')\, dE' = \delta(E - E_0). \qquad (3a)$$

We obtain an equation for $\phi_1(E)$ by multiplying Eq. (2) by t and integrating over all times. Thus,

$$[\Sigma_a(E) + \Sigma_s(E) + DB^2]\phi_1(E) - \int_0^\infty \Sigma(E' \to E)\phi_1(E')\, dE' = \frac{\phi_0(E)}{v(E)}. \qquad (3b)$$

For a given scattering kernel, we can solve Eq. (3a), and then Eq. (3b), by first using the extensively developed methods of slowing-down theory to compute the rate at which neutrons slow down into the energy range below 1 ev and then by employing well-known numerical methods (*2*) to find $\phi_0(E)$ and $\phi_1(E)$ for E less than 1 ev.

By methods of Fourier analysis, the mean emission time may also be computed for the case of a spatially dependent source (*8*). However, the generalization is not made here, since for our case the corrections to the result obtained by considering only the fundamental mode are negligible.

Figure 4 shows the curve for the calculated mean emission time that is used for correcting the experimental data (the value of 240 μsec for $T(E)$ at low energies is nearly equal to the rough estimate of 275 μsec obtained by adding the thermal die-away time to the time required to slow down to 0.1 ev). For all energies below a few electron volts, the mean emission time is small compared with the flight time and can be estimated with considerable confidence.[1]

[1] Actually, the mean emission time is temperature dependent; however, since this correction is small we have neglected its temperature dependence.

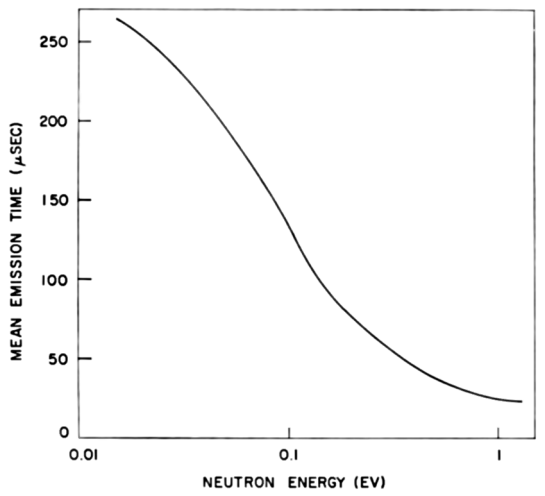

FIG. 4. Mean emission time of neutrons from 24½-in. graphite assembly as a function of neutron energy.

LATTICE VIBRATIONS OF GRAPHITE AND THEIR INTERACTION WITH SLOW NEUTRONS

A realistic description of the scattering of slow neutrons by crystals requires the solution of two different problems: (1) we must understand those aspects of atomic motions which are significant for the scattering problem; and (2) it is necessary to develop good approximate procedures for calculating the scattering kernel. We consider first the vibrations of carbon atoms in the graphite lattice.

ATOMIC MOTIONS

The atoms of graphite crystallize in sheets, forming a highly anisotropic structure. Within a sheet, the atoms form an array of contiguous regular hexagons, each of which is similar to the benzene ring (the carbon-carbon spacing between nearest neighbors in a sheet is $a = 1.42$ A—somewhat greater than the corresponding value of 1.39 A in benzene). The arrangement of atoms in a typical ideal sheet (basal plane) is indicated by the points in Fig. 5.

The atomic arrangement in an adjacent plane is obtained by displacing every crystal site in the basal plane outlined in Fig. 5 though a distance a in the $+x$ direction and a distance $c/2 = 3.35$ A in the $\pm z$ direction, which is perpendicular to the plane of the paper. In the next-nearest planes, a distance c from the plane of the paper, the x-y coordinates of the crystal sites are the same as in Fig. 5.

The structure of graphite suggests that the valence bond between carbon atoms acts almost completely within the separate basal planes, so that the forces which hold the sheets together are very weak compared with intraplanar forces. This idea is common to the many theoretical treatments of the lattice vibrations in graphite (*9–11*). The theory which is most applicable to the present work is that of Yoshimori and Kitano (*9*). Their theory is based on the assumption of four types of forces between the atoms. Two of these are valence forces and are associated with changes in bond length and bond angle. They act wholly within the basal planes. The third is a noncentral force and is determined by the displacement perpendicular to the basal plane of each atom relative to the average perpendicular displacement of its three nearest neighbors from the same basal plane. The fourth force acts in a direction that is perpendicular to the basal planes, and is related to the z-component of the relative displacements of atoms which are on adjacent planes and are nearest neighbors in the z-direction. This is the only coupling that is assumed to exist between different planes. The ratio, ϵ, of the force constant associated with this force to that associated with the third force is of the order of 10^{-2} (*9*).

There are forces other than those described above. In addition to the interaction between atoms which are nearest neighbors in the z-direction, there are interactions between atoms and their distant neighbors in adjacent and more distant planes. These interactions give rise to additional compressional, as well as shearing, forces between different planes. However, Komatsu (*10*) has shown that the shearing forces become significant only for extremely low frequencies of lattice vibration, $\hbar\omega/k \cong 10°$K, whereas we are primarily interested in much higher frequencies. Yoshimori and Kitano further point out that it is a good approximation to absorb the additional compressional forces into a single force of the fourth kind discussed above.

Let us now examine some of the particular aspects of the problem of the normal modes of vibration of the atoms in graphite. From the previous assumptions regarding the interatomic forces, we see that the component of an atomic vibration which is parallel to the basal planes is uncorrelated with the motion of atoms in different planes and with the

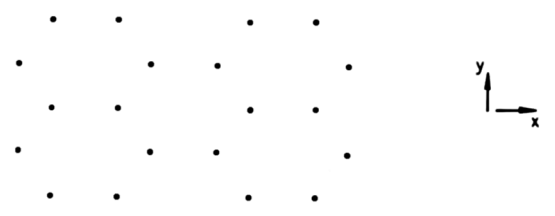

FIG. 5. Typical layer of a graphite lattice

z-component of vibration of atoms in the same plane. Consequently, the polarization vectors of the normal vibrations are either parallel or perpendicular to the basal planes. Furthermore, since the parallel vibrations of atoms in a given plane are correlated only with the parallel vibrations of atoms in the same plane, the polarization vectors and frequencies associated with these vibrations depend only on $\mathbf{q}_\parallel$, the component parallel to the basal planes of the wave vector $\mathbf{q}$. Thus, in the approximation considered, the planar vibrations in graphite are completely equivalent to the planar vibrations of a two-dimensional crystal.

The one-dimensional vibration of an atom perpendicular to a basal plane is correlated with the perpendicular vibrations of atoms in the same and in neighboring planes. Consequently, the frequencies and polarization of these vibrations depend on all three components of the propagation vector $\mathbf{q}$. If we were to neglect the forces which couple adjacent planes ($\epsilon = 0$), the normal-mode frequencies and polarizations would depend only on $\mathbf{q}_\parallel$ and we would be concerned with the transverse vibrations of a two-dimensional crystal. The effect of the interplanar coupling is important, however, at frequencies for which $\hbar\omega/k \cong 300°\text{K}$ and, therefore. is significant for the interaction between lattice vibrations and thermal neutrons.

Neutron-Scattering Law

By considering the symmetry properties of a crystal, we can deduce symmetry properties of quantities defined in the reciprocal lattice space. Such relations have been obtained for the frequencies and polarization vectors of phonons with a propagation vector $\mathbf{q}$, and the results have been applied to the formal study of the interaction of slow neutrons with the lattice vibrations in graphite (*12*). If the coupling forces between the principal planes of the graphite crystal are weak compared with the other interatomic forces, and if interference effects are neglected, then we have shown that a knowledge of the frequency-distribution function associated with vibrations parallel and perpendicular to the principal planes is sufficient to describe the interaction of neutrons with the lattice.

Although there are no theoretical predictions which allow one to assess the accuracy of the incoherent approximation for calculating energy-angle distributions, it is reasonable to expect that this approximation is a good one for inelastic scattering from polycrystalline samples. For the inelastic-scattering cross sections of aluminum and magnesium, the calculations of Marshall and Stuart (*13*) show that the use of the incoherent approximation leads to an error of less than 6%, even for neutron wavelengths as large as 9 A. At the moment, we cannot say anything more quantitative about this problem. We only conclude that it is quite unlikely that interference effects significantly influence thermal-neutron spectra.

Using the Fermi pseudopotential approximation (*14*) and neglecting interference effects, the expression obtained for the differential energy-transfer cross section for polycrystalline graphite (*15*) is ($\hbar$ = Boltzmann's constant = 1)

$$\frac{d\sigma}{d\mathbf{k}} = (8\pi^2 k_0)^{-1}\sigma_b \int_{-\infty}^{\infty} dt e^{i[(k^2-k_0^2)/2]t}\,\chi(\kappa, t)\,, \quad (4)$$

where

$$\chi(\kappa, t) = \int_0^1 \exp\left\{\frac{\kappa^2}{2M}[\gamma(l, t) - \gamma(l, 0)]\right\} dl\,. \quad (5)$$

Here, $\mathbf{k}_0$ and $\mathbf{k}$ are the initial and final neutron momenta, respectively, $\kappa = |\,\mathbf{k} - \mathbf{k}_0\,|$, σ_b is the bound-atom scattering cross section for carbon, and M is the ratio of the mass of the carbon nucleus to that of the neutron. The quantity $\gamma(l, t)$ is defined by

$$\gamma(l, t) = \int_0^\infty \frac{\rho(\omega, l)}{\omega}\left[\coth\frac{\omega}{2T}\cos\omega t + i\sin\omega t\right] d\omega\,,$$

where T is the temperature,

$$\rho(\omega, l) = l^2\rho_\perp(\omega) + (1 - l^2)\rho_\parallel(\omega),$$

$\rho_\perp$ and $\rho_\parallel$ are the frequency spectra associated with vibrations perpendicular and parallel, respectively, to the basal planes of the crystal, and l is the cosine of the angle between the normal to the basal planes and $\boldsymbol{\kappa} = \mathbf{k} - \mathbf{k}_0$. The integration over l in Eq. (5) represents an average over orientations of randomly oriented single crystals in a polycrystalline sample. We note that if $\rho(\omega, l)$ is independent of l, Eq. (5) reduces to the form that is appropriate for discussing the noninterference part of the scattering by an isotropic crystal. The numerical procedures for computing $d\sigma/d\mathbf{k}$, which we discuss below, are developed in such a way as to apply to the case of scattering by an isotropic crystal, as well as that of scattering by a crystal having an anisotropy of the type exhibited by graphite.

The case of graphite is of particular interest because of its frequent use in reactors and its tight binding. The highest frequencies for lattice vibrations parallel and perpendicular to the basal planes are $\omega_{\parallel\max} \cong 2600°\text{K}$ and $\omega_{\perp\max} \cong 1600°\text{K}$, respec-

tively. One therefore expects a strong reduction in the rate of thermalization of neutrons in graphite, particularly at low temperatures.

The problem now is to find a suitable frequency spectrum. In this connection, we emphasize that the calculation is not at all simplified by assuming a simple vibration spectrum. The essential complication lies in the dependence of $d\sigma/d\mathbf{k}$ on $\rho(\omega, l)$, and not in the dependence of $\rho(\omega, l)$ on ω. Therefore, as realistic a phonon spectrum as possible should be used in the calculation of $d\sigma/d\mathbf{k}$. For detailed calculations of $d\sigma/d\mathbf{k}$ for graphite, we have used the vibration spectrum calculated by Yoshimori and Kitano (*9*).

Having obtained a knowledge of the phonon spectrum, there remains the problem of developing good approximate methods for carrying out the integral over t in Eq. (4). Following this, the scattering kernel is easily obtained from

$$\sigma(E_0 \rightarrow E) = \int_\Omega \frac{d\sigma}{d\mathbf{k}}\, k d\Omega \,.$$

For neutron energies that are a few times larger than the high-frequency cutoff of the crystal vibration spectrum, the short-collision-time approximation (*16*) is a good one. For a tightly bound moderator such as graphite, the short-collision-time approximation is not a satisfactory procedure for neutron energies of $\leqq 0.5$ ev. Then it becomes desirable to make an expansion in the number of phonons exchanged in a collision. For a Debye crystal and for aluminum, Sjölander (*17*) has shown that the central limit theorem of probability theory can be used to approximate the n-fold convolution integral which determines the n-phonon cross section. This works quite well, even for n as low as two. Since the first few phonons can be calculated exactly with very little difficulty, the Sjölander approximation provides a simply defined procedure for completely calculating the kernel for a Debye crystal.

For crystalline materials which are used as moderators, the distributions of frequencies include optical branches and, in general, are considerably more complicated than the Debye distribution. For these more complicated frequency spectra, the Sjölander approximation does not work well, and better approximate procedures are needed, particularly for large momentum transfers.

To obtain a useful approximate procedure, we first express $\rho(\omega, l)$ as the sum of a function $\rho_1(\omega, l)$, which vanishes for $\omega \geqq \omega_c$, and a function $\rho_2(\omega, l)$, which is proportional to ω^2 for $\omega \leqq \omega_c$. Thus,

$$\rho(\omega, l) = \rho_1(\omega, l) + \rho_2(\omega, l) \,,$$

where

$$\rho_1(\omega, l) = 0 \qquad \omega \geqq \omega_c \,,$$

$$\rho_2(\omega, l) = \rho(\omega_c, l) \left(\frac{\omega}{\omega_c}\right)^2 \qquad \omega \leqq \omega_c \,.$$

A suitable choice for the value of ω_c depends on the crystal under consideration, but, in principle, ω_c may range from zero to the maximum frequency of vibration. Next, to evaluate $d\sigma/d\mathbf{k}$ for the case of large momentum transfers, we use the short-collision-time approximation for the low-frequency modes with the distribution $\rho_1(\omega, l)$, while using the phonon expansion for frequencies distributed with the density $\rho_2(\omega, l)$. This is a well-defined procedure, since the scattering law for harmonic motion is a convolution of contributions from various normal modes.

For graphite, it is convenient to choose $\omega_c = 486°\text{K}$ and to use the short-collision-time approximation for the low-frequency modes for values of $\kappa^2/2 \gtrsim 0.763\ [300/T(°\text{K})]$ ev. The resulting expansion converges considerably more rapidly than the straightforward phonon expansion.

In the calculation of the scattering kernel for graphite, for values of $\kappa^2/2 \lesssim 0.763\ [300/T(°\text{K})]$ ev, a significant difficulty arises because of the highly anisotropic nature of the lattice. Owing to the similarity of the lattice vibrations to those of a two-dimensional crystal, both $\rho_\parallel(\omega)$ and $\rho_\perp(\omega)$ are proportional to ω for low frequencies extending down to $\omega \cong 15°\text{K}$. This contrasts with a Debye crystal, where $\rho(\omega)$ is proportional to ω^2 for all frequencies up to the Debye frequency, θ.

To understand the problems involved, it is sufficient to consider $\rho(\omega, l)$ for a single value of l. An expansion in the number of phonons exchanged in a single collision is obtained by extracting the Debye-Waller factor $\exp[-(\kappa^2/2M)\gamma(l, 0)]$ from $\chi(\kappa, t)$ in Eq. (4) and expanding the rest of the exponential function in powers of its argument. In order to evaluate the Fourier transform of $[(\kappa^2/2M)\gamma(l, t)]^n$, we may follow Sjölander and use the Edgeworth series of probability theory to obtain an expansion of the n-phonon term as a Gaussian with Hermite polynomial corrections, the expansion being an asymptotic series in powers of $n^{-1/2}$. For a Debye crystal, this expansion works quite well. In the case where $\rho(\omega, l)$ is proportional to ω, however, the

integral defining $\gamma(l, t)$ is divergent at $\omega = 0$, so that the phonon expansion does not exist. Even if we account for the ω^2 dependence of ρ for $\omega \lesssim$ 15°K, the number of low-frequency phonons emitted is very large, and the expansion converges slowly. Furthermore, the Sjölander expansion does not work well, even for $n = 4$.

These difficulties are eliminated by treating frequencies below some frequency ω_0 in the static approximation and by making the phonon expansion only for the case of excitation by the neutron of high-frequency phonons. Physically, this amounts to neglecting the contribution of modes with frequency $\omega < \omega_0$ to the motion of the carbon atoms during their time of interaction with the neutron. This is a good approximation for all energy transfers except those less than approximately ω_0. If ω_0 is much less than the temperatures normally encountered in reactors, the energy transfers less than approximately ω_0 do not significantly influence the thermal spectrum. For $T \geqq 300$°K, we have used $\omega_0 = 55$°K in detailed calculations of $d\sigma/d\mathbf{k}$.

The shape of $\rho(\omega, l)$ is still such that one must modify Sjölander's method for computing the multiphonon terms. This modification again consists in representing $\rho(\omega, l)$ by a sum of two nonidentical distributions, $\rho_1(\omega, l)$ and $\rho_2(\omega, l)$, and noting that the convolution integrals which determine the multiphonon terms may be expanded into a sum of $n + 1$ terms. It is easy to choose the two nonidentical distributions so that each term in the sum may be accurately approximated by means of the Edgeworth series. Numerical comparisons with the results of exact calculations show that this approximate procedure works very well, even for $n = 2$ (*6*).

The mathematical schemes discussed above have been incorporated into an IBM-7090 program for computing scattering kernels associated with crystalline moderators (*18*). The machine computes $\sigma(E_0 \rightarrow E)$ by numerical integration of the differential energy-transfer scattering cross section. Both the total and differential scattering kernel are listed in the machine output. The time for computing a 70×70, 422°K, graphite-scattering matrix in the energy range extending from 0 to 0.75 ev is about 1 hr. In the case of an isotropic crystal for which no average over crystal orientations is required, the computing time is reduced by about a factor of four. In general, the computing time is nearly proportional to the temperature, to the largest energy, and to the square of the number of energies at which the kernel is computed.

COMPARISON BETWEEN THEORY AND EXPERIMENT

In order to compare theoretical calculations with measured low-energy neutron spectra, it is important to take account of geometrical perturbations. Source localization, small heterogeneities, and the re-entrant hole introduce such perburbations.

Experiments performed in water systems have shown that perturbations induced by square re-entrant tubes varying in size from ½ to 2 in. are negligible. The same conclusion is expected to apply here, since the experiments utilized a 1-in.-square re-entrant hole.

The absorptions occur almost entirely in $t =$ 0.005-in.-thick stainless steel foils which are separated by 0.525 in. of graphite. After theoretical homogenization of the absorber over the entire volume of the cube, we apply a self-shielding factor at each energy equal to the single-velocity escape probability $P_0(\Sigma_a(E)t)$, calculated by Case, Placzek, and de Hoffman (*19*) for the case of a foil immersed in an isotropic neutron bath. The self-shielding factors determined in this manner are very nearly unity for all neutron energies of importance for the neutron spectrum. At 0.09 ev, where the 300°K flux per unit energy is a maximum, $P_0 = 0.943$. At 0.025 ev, $P_0 = 0.914$. Thus, the self-shielding corrections are quite small although they cannot be made with extreme confidence for multi-velocity problems.

Corrections for the localization of the fast source can be made with considerable confidence if the spatial distribution of the thermal source is known. This is determined by an age-theory fit to the experimentally determined activation of cadmium-covered indium foils. The method that we apply for calulating the spectrum in terms of the assembly composition and thermal-source distribution is easily executed and gives definite predictions.

The problem is formulated in energy-dependent diffusion theory. The approximation employed for its solution is based on the smallness of the thermal migration area, L^2, as compared with τ, the migration area in slowing down from the initial source energies to thermal. Under these conditions, the thermal flux tends to follow the thermal source, and the thermal spectrum is approximately independent of position. The method of approximation results in a solution expressed as a series in powers of L^2/τ, the corrections to the first approximation beginning with terms of the order of L^4/τ^2.

We consider the region of neutron energy from zero to the indium resonance energy $E_0 = 1.44$ ev.

The important assumption required is that the source of thermal neutrons slowing down past indium resonance have a spatial distribution independent of the energy with which the neutrons first enter the thermal-energy region, $0 < E \leqq E_0$. (This is a very good assumption for graphite and other heavy moderators.) We can then write our fundamental equation for the flux per unit energy, $\phi(E, r)$, at point r as (*20*)

$$-D\nabla^2\phi(E, \mathbf{r}) + C\phi(E, \mathbf{r}) = f(E)Q(\mathbf{r}), \tag{6}$$

where

$$f(E) = \frac{(E - \alpha E_0)}{E} \qquad \text{for } E \geqq \alpha E_0,$$

$$= 0 \qquad \text{for } E < \alpha E_0,$$

$$\alpha = \left(\frac{M-1}{M+1}\right)^2,$$

and the collision operator, C, is defined by

$$C\phi(E, r) = \Sigma_t(E)\phi(E, \mathbf{r}) - \int_0^{E_0} \Sigma(E' \to E)\phi(E', \mathbf{r})dE'. \tag{7}$$

Here,

$$\Sigma_t(E) = \Sigma_a(E) + \Sigma_s(E),$$

where $\Sigma_a(E)$ and $\Sigma_s(E)$ are the macroscopic absorption and scattering cross sections for neutrons with the energy E. The diffusion coefficient is denoted by D. The quantity $f(E)$ is the energy distribution of neutrons slowing down from above E_0 to below E_0 by collisions with free moderating nuclei at rest, and $Q(\mathbf{r})$ is the spatial distribution of indium-resonance flux as determined from the activations of cadmium-covered indium foils.

We begin by assuming a solution of the form

$$\phi(E, \mathbf{r}) = \phi_0(E)Q(\mathbf{r}) + R(E, \mathbf{r}) \tag{8}$$

and choose $\phi_0(E)$ to satisfy

$$DB_0^2\phi_0(E) + C\phi_0(E) = f(E), \tag{9}$$

where

$$B^2(\mathbf{r}) = -\frac{\nabla^2 Q(\mathbf{r})}{Q(\mathbf{r})} = B_0^2 + \delta B^2(\mathbf{r}) \tag{10}$$

and B_0^2 is the value of $B^2(\mathbf{r})$ at the point of observation, $\mathbf{r} = \mathbf{r}_0$. Thus, $R(E, \mathbf{r})$ satisfies

$$-D\nabla^2 R + CR = \bar{\Sigma}\phi_0\bar{Q}, \tag{11}$$

where

$$\bar{Q} = -\frac{D}{\bar{\Sigma}}\delta B^2(\mathbf{r})Q(\mathbf{r}). \tag{12}$$

Here, $\bar{\Sigma}$ is arbitrary, but we will provide a convenient definition for it later. We note that Eq. (11) is similar to Eq. (6) in that the source term in both equations is separable in energy and position. The essential difference is that the source term is now well thermalized compared with the slowing-down source.

The purpose of our subsequent procedure is to show that $R(E, \mathbf{r})$ is calculable and small. To find R, we expand it in the series

$$R(E, \mathbf{r}) = \bar{Q}R_0(E) + L^2\nabla^2\bar{Q}R_1(E) + \cdots + L^{2n}\nabla^{2n}\bar{Q}R_n(E) + \cdots, \tag{13}$$

where $L^2 = D/\bar{\Sigma}$. If we choose $R_n(E)$ to satisfy

$$CR_0(E) = \bar{\Sigma}\phi_0(E),$$
$$CR_n(E) = \bar{\Sigma}R_{n-1}(E), \tag{14}$$

then the series in Eq. (13) is a formal solution of Eq. (11). We further note that the sequence of Eq. (14) defines an iterative procedure for computing the eigenfunction associated with the lowest eigenvalue of the operator C. If $\bar{\Sigma}$ is this eigenvalue, then L^2 is the thermal diffusion length in the medium under investigation. Thus, since

$$\frac{\bar{Q}}{Q} = O\left(\frac{L^2}{\tau}\right) \quad \text{and} \quad \frac{\nabla^{2n}\bar{Q}}{Q} = O\left(\frac{L^2}{\tau^{n+1}}\right),$$

the right-hand side of Eq. (13) is a series whose terms decrease in order of magnitude like the sequence of positive powers of L^2/τ. If $L^2 \ll \tau$, the correction term, R, is small and at the point of observation is of the order of L^4/τ^2 compared with $\phi_0(E)Q(\mathbf{r}_0)$.

In general, the convergence of the series in Eq. (13) will be rapid. It may happen, however, that the correction term, R, is small, but that the series in Eq. (13) converges slowly. Then it is convenient to sum the series approximately. To show that this is possible, we note that for n greater than or equal to some integer, N, it is a good approximation to write

$$R_n = R_{n-1}. \tag{15}$$

Thus,

$$R(E, \mathbf{r}) \cong \bar{Q}R_0 + L^2\nabla^2\bar{Q}R_1 + \cdots + L^{2N-4}\nabla^{2N-4}\bar{Q}R_{N-2} + R_{N-1}L^{2N-2}\nabla^{2N-2}[\bar{Q} + L^2\nabla^2\bar{Q} + \cdots].$$

The quantity in square brackets,

$$F = \bar{Q} + L^2\nabla^2\bar{Q} + \cdots,$$

satisfies the inhomogeneous equation governing the diffusion of thermal neutrons,

$$-L^2\nabla^2F + F = \bar{Q}. \tag{16}$$

Equation (16), together with the condition that F vanish at the extrapolated boundary of the system, determines F completely. Over the range of energies for which R_n has an appreciable magnitude, and for the practical cases considered in this paper, the approximation, Eq. (15), is a very good one for N as low as two or three.

The foregoing procedure has been applied to the analysis of the spectrum measurements in graphite systems performed at the General Atomic electron linear accelerator facility. For this purpose, we required the thermal-source shape $Q(\mathbf{r})$, which was induced by a fast source located at a face center of a cube with a width of 2 ft. The source $Q(\mathbf{r})$ determined from measurements of the activation of cadmium-covered indium foils is plotted in Figs. 6, 7, and 8. The indium-resonance flux traverses were made along the three perpendicular lines connecting the face centers of the cube. Along two of the lines, the indium-resonance flux follows a cosine law. Along the third line, which passes through the source, the indium-resonance flux is adequately represented by the expression

$$Axe^{-(x^2/4\tau)}.$$

Here, A is a normalizing constant, x is the distance from the source along the considered axis, and $\tau = 236$ cm^2 is the age from source energies to indium resonance. This is just the expression that follows from the solution of the age equation for the case

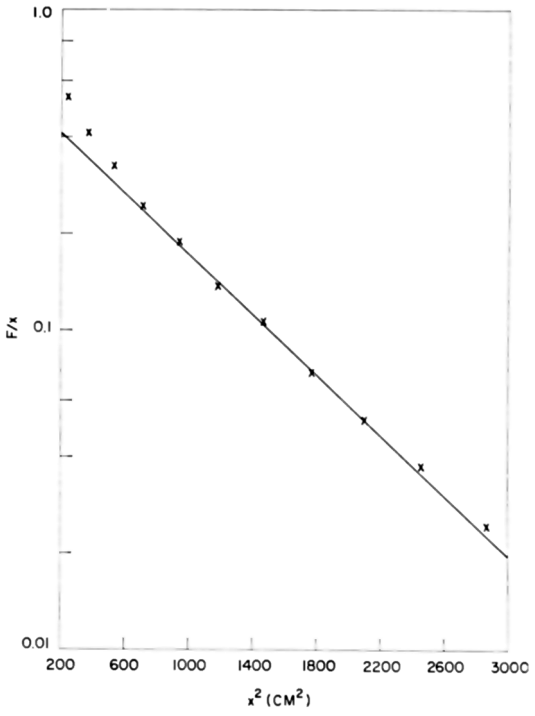

FIG. 6. F/x versus x^2

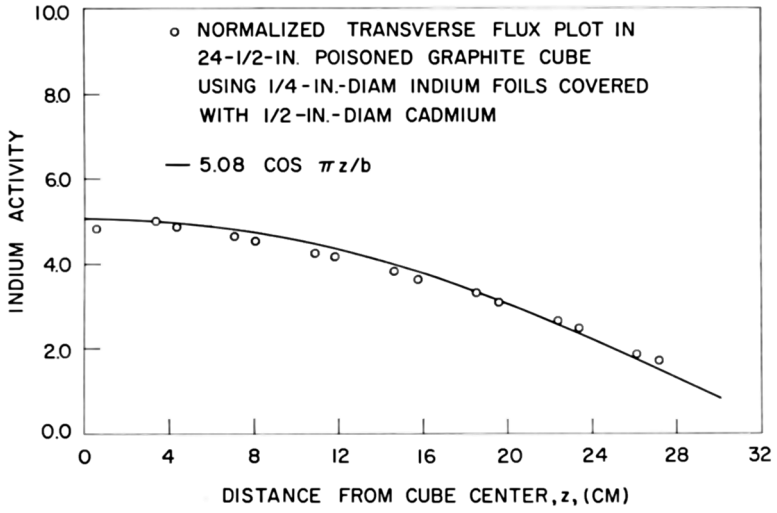

FIG. 7. Normalized indium-resonance activity versus position (perpendicular)

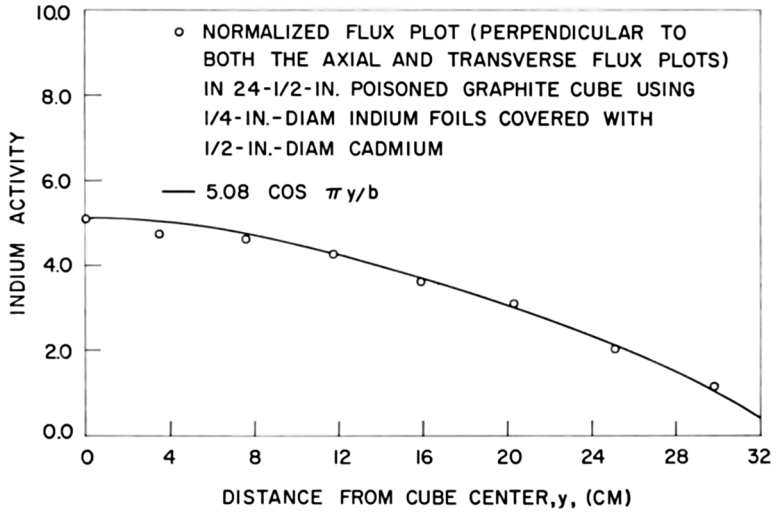

FIG. 8. Normalized indium-resonance activity versus position (transverse)

of a plane isotropic source at the boundary $x = 0$ of a semi-infinite medium. The deviation between the age-theory and the measured results for small values of x is due to the indium activation produced by neutrons with energies above 1.44 ev and to the fact that the experiment employs a point source rather than a plane source. The deviation for large values of x is due primarily to the increased ratio of thermal to fast flux.

To determine the effects of fast-source localization on the neutron spectrum, we first use the fact of the cosine dependence of the flux in two of the three directions to reduce Eq. (6) to an equation in one dimension. This procedure results in an effective total cross section equal to

$$\Sigma_a + \Sigma_s + 2D\left(\frac{\pi}{b}\right)^2,$$

where

$$b = a + 1.42\,\lambda_{tr}$$

and

$$\lambda_{tr} = \frac{1}{\Sigma_0(1-\mu)}.$$

Here, $\Sigma_0 = 0.373$ cm^{-1} is the free-atom macroscopic scattering cross section and $\mu = \frac{1}{18}$.

Thus, we must solve

$$-D\frac{\partial^2\phi(E,x)}{\partial x^2} + C\phi(E,x) = f(E)Q(x), \quad (17)$$

with

$$C\phi(E,x) = \left[\left(\Sigma_t(E) + 2D\left(\frac{\pi}{b}\right)^2\right)\right]\phi(E,x) - \int_0^{E_0}\Sigma(E'\to E)\phi(E',x)dE'$$

and

$$Q(x) = xe^{-(x^2/4\tau)}$$

The first approximation is $\phi_0(E)Q(x)$, where $\phi_0(E)$ is determined by

$$DB_0^2\phi_0(E) + C\phi_0(E) = f(E)$$

and

$$B_0^2 = -\frac{\nabla^2 Q(x_0)}{Q(x_0)}.$$

In the present case, the correction $R(E, x)$ is expressed as

$$R(E,x) = R_0(E)\bar{Q}(x) + R_1(E)L^2\nabla^2F(x), \quad (18)$$

where $\bar{Q}(x) = -(D/\bar{\Sigma})\delta B^2(x)Q(x)$ and F satisfies

$$-L^2\nabla^2F + F = \bar{Q}. \quad (19)$$

Introducing the Green function, $G(x\,|\,x')$, associated with Eq. (19), we may write

$$F(x) = \int_0^a G(x|x')\bar{Q}(x')\,dx'.$$

In the computations, we approximated the actual Green function by the one appropriate to an infinite medium as follows:

$$G(x\,|\,x') = \frac{e^{-(|x-x'|/L)}}{2L}.$$

This approximation is justified because the perpendicular distance from any cube face to the point of observation is large compared with L.

The correction $R(E, x)$ calculated by the pre-

ceding procedure is negligible above about 0.3 ev; it is negative and equal to about 7% of $\phi_0(E)Q(r_0)$ at 0.08 ev. Because of the hardening of the spectrum by absorption effects, the magnitude of the correction term, R, is not very sensitive to temperature variations between 300° and 800°K.

Experimental and theoretical results for neutron spectra are compared in Figs. 9 through 13 for temperatures ranging from 323° to 810°K. Statistical experimental errors are shown at the lower neutron energies. At energies above 0.03 ev, the statistical counting error is very small. At higher energies, there may exist a small (6%) systematic error in the relative energy sensitivity of the BF_3 detector system. This possibility is due to the extreme difficulty in calibrating the BF_3 detector system over three decades of energy.

Theoretical spectra were computed using the model for bound-carbon described earlier and a free-gas model. All calculations included the diffusion and self-shielding corrections. The spectra obtained from the bound-carbon model agree extremely well with the experimental results. In contrast, predictions based on the free-gas model are considerably different from the measured spectra, especially at 323°K. Even at 810°K, the free-gas result differs significantly from the experimental one.

We conclude that the theory of slow-neutron interactions in graphite which we have presented

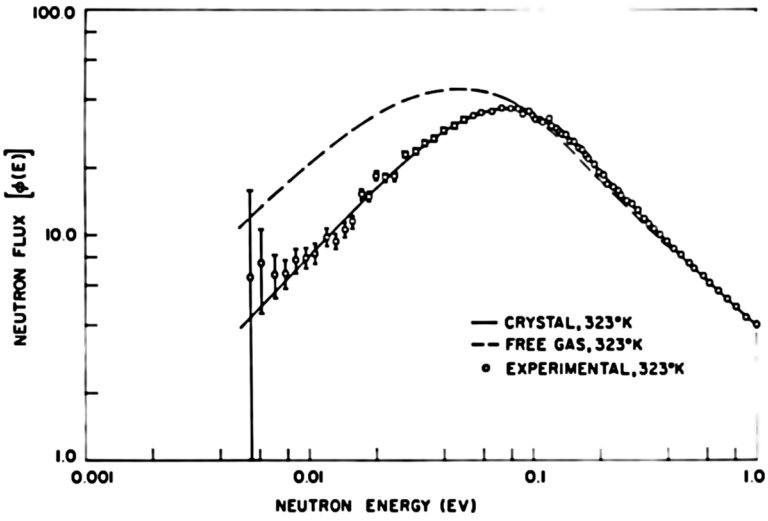

FIG. 9. Neutron flux versus neutron energy at 323°K

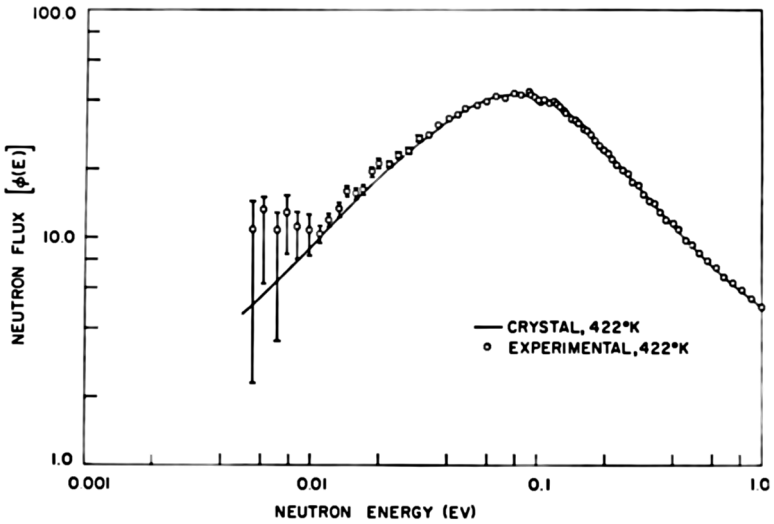

FIG. 10. Neutron flux versus neutron energy at 422°K

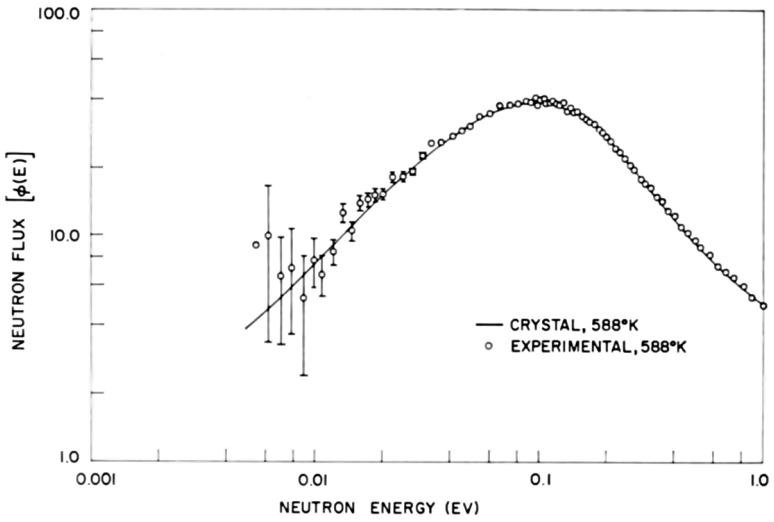

FIG. 11. Neutron flux versus neutron energy at 588°K

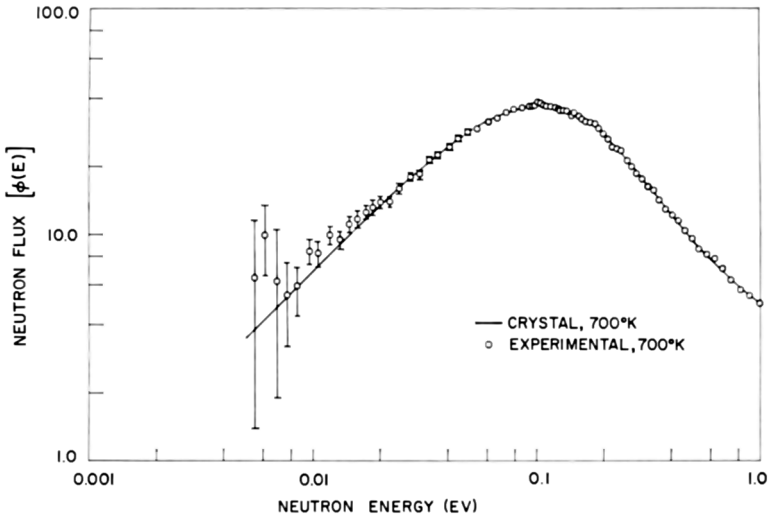

FIG. 12. Neutron flux versus neutron energy at 700°K

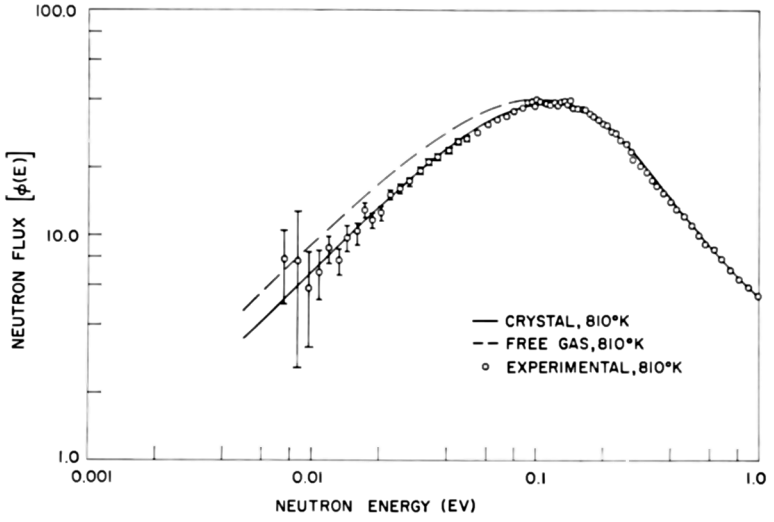

FIG. 13. Neutron flux versus neutron energy at 810°K

is quite adequate for the purposes of reactor physics, and that the chemical binding of the carbon atoms significantly influences the neutron spectrum for the poison concentration and temperatures which we have considered.

EFFECTS OF CHEMICAL BINDING ON THE NEUTRONICS OF GRAPHITE-MODERATED REACTORS

We have demonstrated that our theory accounts for the considerable influence that chemical-binding effects may have on the thermal-neutron spectrum. Now we apply the theory to determine the extent to which the chemical binding of the carbon atoms affects the spectrum for different rates of absorption at a few fixed temperatures. From the calculated spectra, we then determine the sensitivity of some important reactor parameters to the effects of chemical binding.

For this purpose, we calculate spectra, average fission and absorption cross sections, the Pu^{239} to U^{235} fission ratio, effective multiplication constants, and temperature coefficients of reactivity for bare, homogeneous, critical graphite–U^{235} cubes

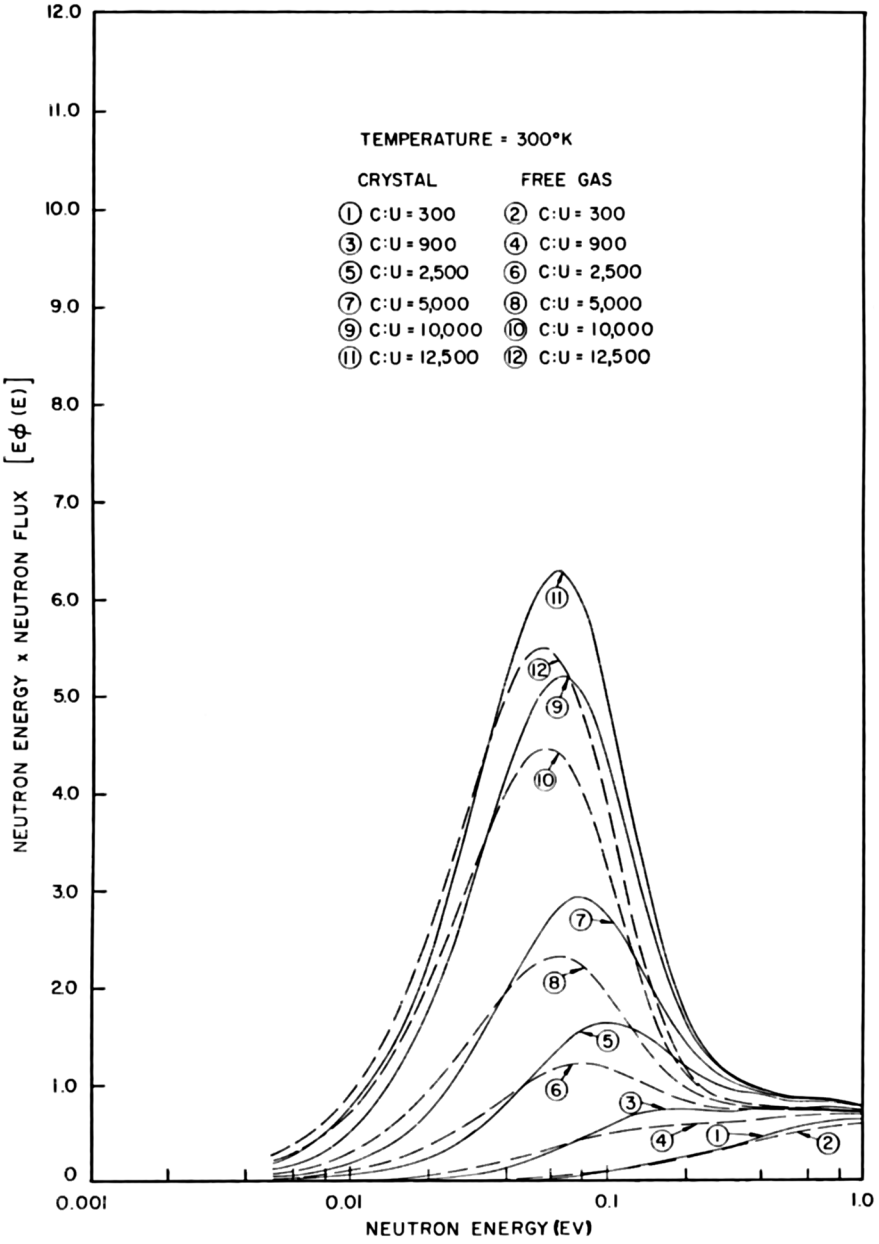

FIG. 14. Neutron energy times neutron flux versus neutron energy at 300°K for C:U^{235} atom ratios of 300; 900; 2500; 5000; 10,000; and 12,500.

In all cases, thermalization by both free and bound carbon is considered. We neglect the Doppler broadening of the U^{235} resonances and the temperature dependence of the graphite density. Thus, we are only concerned with changes produced by the variation of spectra with temperature. In subsequent calculations, all thermal-group constants are obtained by averaging from zero energy to the thermal cutoff at 2 ev. We choose the relatively high thermal cutoff of 2 ev so that the one thermal group used in our analysis will include all significant thermalization effects (*21*).

Figures 14 and 15 show calculated thermal spectra for several C:U^{235} atom ratios and for moderator temperatures of 300° and 1200°K, respectively. These figures represent the flux per unit lethargy, $E\phi(E)$, for the case of thermalization by free carbon as well as that of thermalization by bound carbon. The effects of chemical binding are apparent for all U^{235} loadings for which there is a significant

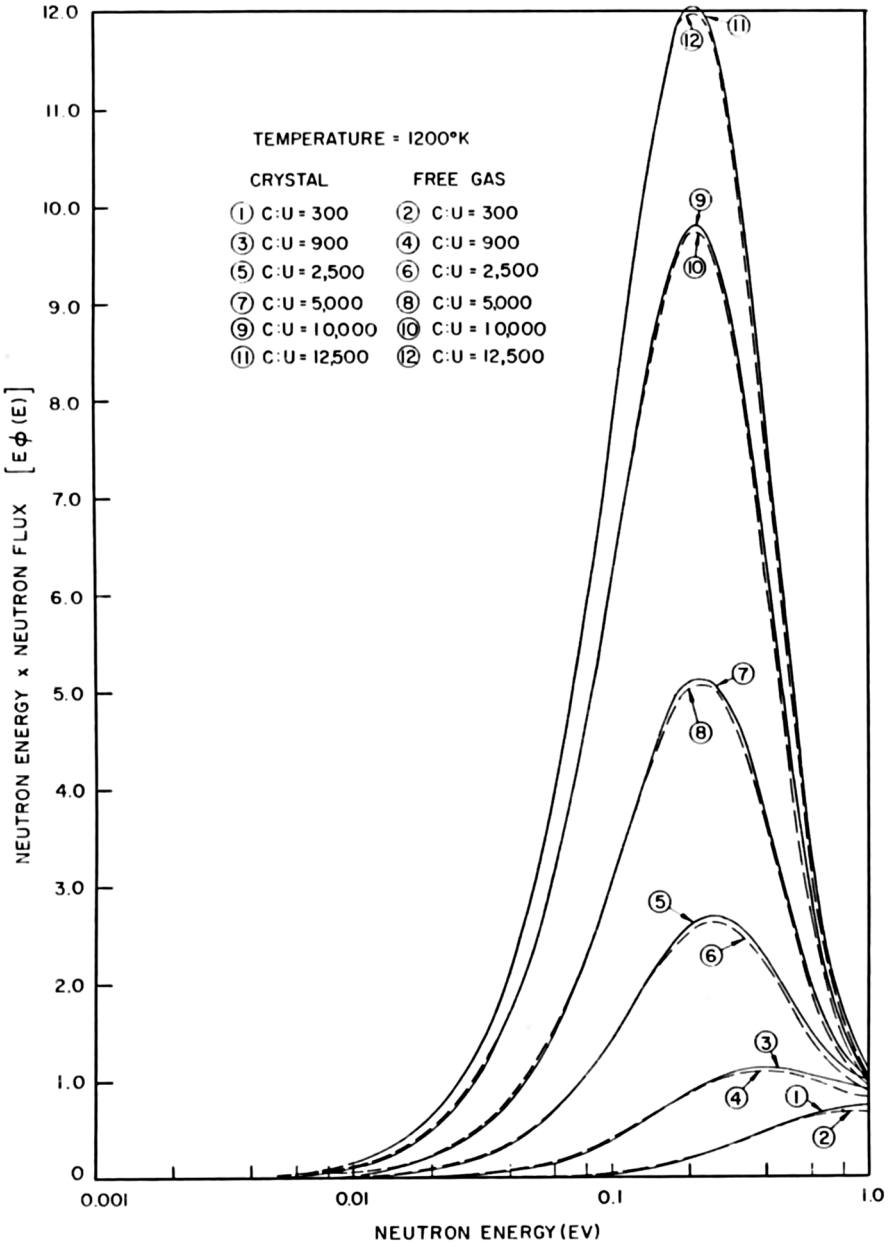

FIG. 15. Neutron energy times neutron flux versus neutron energy at 1200°K for C:U^{235} atom ratios of 300; 900; 2500; 5000; 10,000; and 12,500.

number of thermal neutrons. For $C:U^{235}$ atom ratios of less than a thousand, the number of thermal neutrons is small, and the spectral effects of binding are less pronounced than for more thermal systems. (For zero absorption, the calculated free-gas and crystal spectra are identical, since the neutrons are in a Maxwellian distribution at the temperature of the graphite.) Finally, Fig. 15 shows that the effects of chemical binding on the thermal spectra are small for a moderator temperature of 1200°K.

We have also computed spectra for the case where the neutron–phonon interaction in graphite is calculated by the method of Schofield and Hassitt (*5*). In Fig. 16, this spectrum is compared with those obtained by using the free-gas and bound-carbon models. If significant amounts of Pu^{239} are present, appreciable perturbations of the thermal spectrum result because of the strong resonance at 0.3 ev. This is demonstrated for a $C:Pu^{239}$ atom ratio of 5000 in Fig. 17 for the three models of the neutron–phonon interaction. In all cases, the Schofield kernel yields a thermal spectrum which is harder than that obtained by using a free-gas kernel; however, the change in the spectrum owing to binding is underestimated by about 50%.

Frequently, nuclear analysts are interested in the

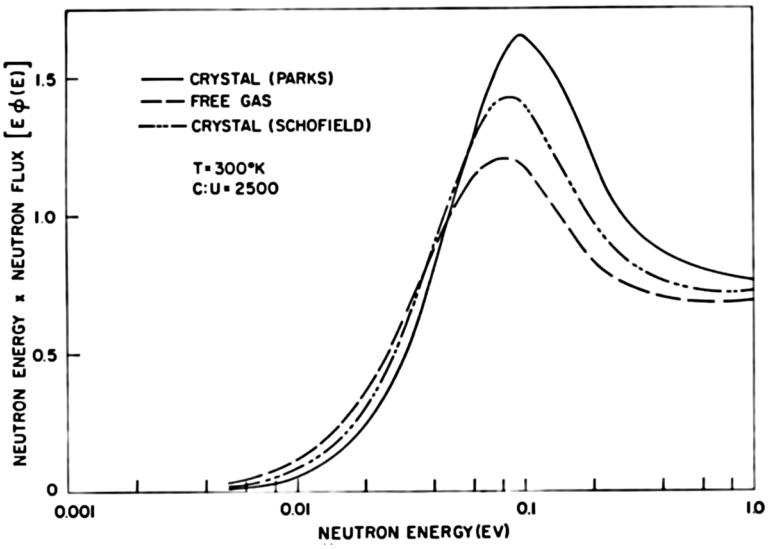

FIG. 16. Thermal neutron spectra at 300°K for a $C:U^{235}$ atom ratio of 2500 for three representations of the chemical binding of graphite.

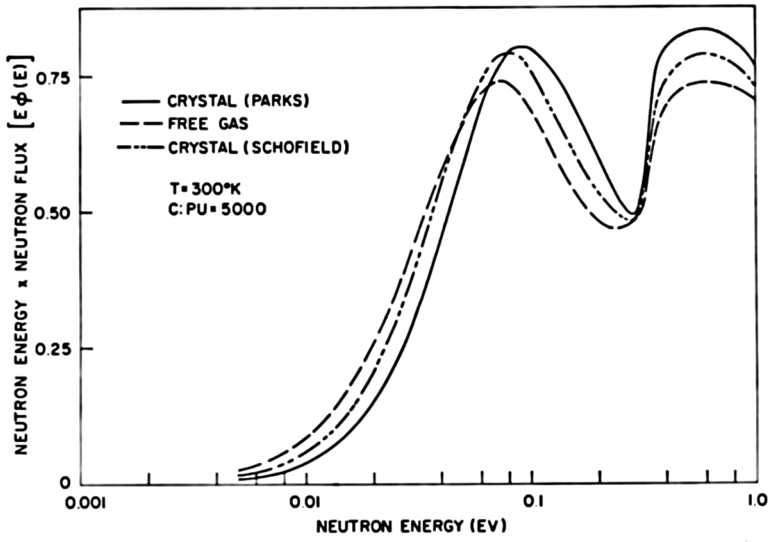

FIG. 17. Thermal neutron spectra at 300°K for a $C:Pu^{239}$ atom ratio of 5000 for three representations of the chemical binding of graphite.

differences in spectrum-averaged cross sections obtained with different scattering kernels. Hence, we have recorded average values of the absorption and fission cross sections for U^{235} and Pu^{239} and the absorption cross section for boron (see Table I). Nuclear data were taken from GA-2113 (*22*) and are consistent with 2200 meters/sec quantities given in the supplement to the second edition of BNL-325 (*23*).

The values recorded in Table I are indicative of the significant hardening of the spectrum owing to absorption and chemical-binding effects. For a very thermal system, i.e., a $C:U^{235}$ atom ratio of 12,500, the spectrum-averaged boron cross section has roughly two-thirds of its 2200 meters/sec value of 755 barns. By averaging the boron cross section over a Maxwellian at the temperature of the moderator, one obtains a value of 669 barns. If the thermal distribution is a Maxwellian at an effective neutron temperature, determined by $T_n = T(1 + \Delta)$ where $\Delta = [4\Sigma_a(kT)/\xi\Sigma_s]$, then the average absorption cross section of boron is 591 barns. This is almost 100 barns larger than the cross section obtained using the spectrum in bound carbon.

As an index of spectral hardening, the ratio of the fission rates in trace quantities of Pu^{239} and U^{235} has been used. Values of

$$\int_0^{0.5\,ev} \sigma_f^{239}\phi(E)\,dE \Big/ \int_0^{0.5\,ev} \sigma_f^{235}\phi(E)\,dE,$$

i.e., the Pu^{239} to U^{235} fission ratio for sub-cadmium neutrons, are recorded in Table II for spectra determined from the free-gas, Schofield, and bound-carbon models. As expected, the values obtained from the bound-carbon scattering kernel are larger than those obtained from either the Schofield or the free-gas scattering kernels. The maximum difference between the bound-carbon and the free-gas results is only 9.6% for a $C:U^{235}$ atom ratio of 2500 at 300°K. It is apparent that this fission ratio is not a very definitive measure of the effects of crystalline binding on the spectrum. When comparing calculated and measured values of these fission

TABLE I

SPECTRUM-AVERAGED ABSORPTION AND FISSION CROSS SECTIONS FOR BORON, U^{235}, AND Pu^{238} FOR THE CRYSTAL AND FREE-GAS THERMAL SPECTRA FOR VARIOUS $C:U^{235}$ ATOM RATIOS (IN BARNS)

$C:U^{235}$ Atom ratio	Crystal (300°K)					Free gas (300°K)				
	$\bar{\sigma}_a$*			$\bar{\sigma}_f$*		$\bar{\sigma}_a$*			$\bar{\sigma}_f$*	
	B	U^{235}	Pu^{239}	U^{235}	Pu^{239}	B	U^{235}	Pu^{239}	U^{235}	Pu^{239}
300	164.32	108.36	651.78	89.051	400.03	171.14	114.98	673.52	94.762	414.01
900	236.47	177.70	914.98	148.35	566.65	254.91	195.19	889.12	163.51	555.69
2500	334.13	268.78	956.69	226.86	609.92	368.97	303.20	937.77	256.45	607.00
5000	408.42	338.92	946.57	287.33	619.33	450.48	380.79	942.47	323.22	626.59
10,000	477.95	405.35	937.27	344.52	628.58	518.34	445.59	941.71	378.98	640.31
12,500	497.69	424.32	935.55	360.84	631.78	535.82	462.30	941.11	393.35	643.62

TABLE II

VALUES OF THE SUB-CADMIUM Pu^{238} TO U^{235} FISSION RATIO AT 300°, 600°, 900°, AND 1200°K AND VARIOUS $C:U^{235}$ ATOM RATIOS FOR SPECTRA OBTAINED WITH THE FREE-GAS, SCHOFIELD, AND CRYSTAL SCATTERING KERNELS

C:U Atom ratio	Free gas				Schofield				Crystal			
	300°K	600°K	900°K	1200°K	300°K	600°K	900°K	1200°K	300°K	600°K	900°K	1200°K
300	5.907	6.179	6.384	6.523	6.062	6.274	6.497	6.523	6.294	6.398	6.526	6.625
900	3.731	4.322	4.941	5.422	3.932	4.452	5.044	5.422	4.257	4.650	5.148	5.559
2500	2.434	3.107	3.987	4.719	2.563	3.195	4.052	4.719	2.779	3.339	4.132	4.808
5000	1.962	2.648	3.630	4.462	2.045	2.706	3.669	4.462	2.187	2.801	3.721	4.516
10,000	1.698	2.392	3.432	4.320	1.750	2.426	3.453	4.320	1.836	2.483	3.484	4.351
12,500	1.643	2.339	3.390	4.290	1.686	2.366	3.408	4.290	1.759	2.414	3.434	4.316

ratios, one should note that there is a reported 4% uncertainty in the low-energy cross sections of Pu^{239} (*24*).

In order to determine the effects of chemical binding on the effective multiplication constant and the temperature coefficient of reactivity, a series of one-dimensional criticality calculations has been performed in slab geometry for the six $C:U^{235}$ atom ratios given in Table II. The appropriate spectrum-averaged thermal cross sections for U^{235} are given in Table I. The cross sections were averaged over spectra appropriate for thermalization by both bound and unbound carbon. In Table III, the percentage difference

$$100\,[(k_{\text{crystal}} - k_{\text{gas}})/k_{\text{gas}}]$$

between effective multiplication constants are recorded for the two models of interest for moderator temperatures of 300° and 1200°K.

As expected, the values of k_{eff} computed with thermal parameters determined from the crystal model are lower than those obtained with free-gas parameters. For systems with a reasonable number of thermal neutrons, binding effects reduce k_{eff} by from 1% to 2%. The variation of the percentage difference in k_{eff} with $C:U^{235}$ atom ratio is reasonable. For very heavy loadings, there are very few thermal neutrons, so that details of the thermalization process are not important. In the limit of zero absorption, the calculated thermal spectra are identical, and the difference in eigenvalues is zero. Consequently, a peak in the percentage difference should exist. For the cases considered here, this maximum difference is nearly 2.5% and occurs for a $C:U^{235}$ atom ratio of 10,000. This difference decreases as the temperature is increased above room temperature, being less than 0.5% at 1200°K.

TABLE III

PERCENTAGE DIFFERENCE IN CALCULATED EFFECTIVE MULTIPLICATION CONSTANTS USING THE CRYSTAL AND FREE-GAS SCATTERING KERNELS FOR SEVERAL $C:U^{235}$ ATOM RATIOS

$C:U^{235}$ Atom ratio	Percentage difference in k_{eff}	
	300°K	1200°K
300	−0.162	−0.159
900	−0.787	−0.296
2500	−1.70	−0.426
5000	−2.19	−0.405
10,000	−2.45	−0.344
12,500	−2.42	−0.315

TABLE IV

VALUES OF $(1/k)(\partial k/\partial T)$/°C OBTAINED USING THE CRYSTAL AND FREE-GAS SCATTERING KERNELS AT THERMAL ENERGIES FOR SEVERAL $C:U^{235}$ ATOM RATIOS

$C:U^{235}$ Atom ratio	$-(1/k)(\partial k/\partial T)$/°C		Difference (%)
	Crystal	Free gas	
300	6.07×10^{-7}	2.42×10^{-6}	74.9
900	1.07×10^{-5}	2.14×10^{-5}	50.2
2500	4.91×10^{-5}	7.65×10^{-5}	35.8
5000	1.07×10^{-4}	1.49×10^{-4}	28.2
10,000	2.04×10^{-4}	2.52×10^{-4}	19.0
12,500	2.41×10^{-4}	2.88×10^{-4}	16.3

In addition to their general interest, the results of these calculations are significant for a proper analysis of several graphite–U^{235} assemblies (*25*). Past calculations (*25*, *26*) of these assemblies have employed thermal-average cross sections obtained by assuming free-gas thermalization or by using simple phenomenological prescriptions.

The results of Table III indicate that the close agreement between measured and calculated eigenvalues for these assemblies is probably fortuitous. A systematic review of these calculations is now in progress (*27*).

Values of the temperature coefficient, $(1/k)(\partial k/\partial T)$, are recorded in Table IV for both the free-gas and crystal treatments of the thermal group. The tabulations were obtained by taking the difference between calculated eigenvalues at 600° and 300°K and dividing by the product of k_{eff} at 300°K and the temperature difference.

For the bare cubes of graphite and U^{235} which we have considered, the changes in thermal leakage account for most of the negative temperature coefficient. The calculated temperature coefficients are considerably smaller for the crystal model than for the free-gas model. The variation of $(1/k)(\partial k/\partial T)$ with atom ratio shows that lower values of $(1/k)(\partial k/\partial T)$ result for harder spectra.

We have demonstrated that the effects of chemical binding have a significant influence on the reactivity and its temperature coefficient in homogeneous graphite–U^{235} systems, particularly at room temperature. Thus, a free-gas kernel is not adequate to describe the thermal spectrum at room temperature for any practical range of absorptions. However, above 1200°K, the effects of binding become negligible, so that for temperatures appropriate to the operating conditions of proposed graphite power systems, a free-gas model gives an adequate description of the thermalization process.

CONCLUSION

Experiments in poisoned graphite at several temperatures show that the effects of crystalline binding on the thermal spectrum are considerable for temperatures of less than 800°K. The theory which we presented accounts for the effects of chemical binding in a realistic way and gives good agreement with the measured spectra. It has also been demonstrated that the effects of chemical binding must be considered for a complete understanding of room-temperature graphite reactors and for the practical problems of extrapolating the results of room-temperature critical assemblies to proposed operating conditions.

ACKNOWLEDGMENT

The authors wish to acknowledge several stimulating discussions with Dr. M. S. Nelkin and Dr. Alf Sjölander. We are grateful to Dr. R. B. Walton, J. L. Wood, G. Houghton, and D. Houston for their assistance in the experimental program. Thanks are also due to Joan Bell for programming the mathematical expressions of the scattering kernel for computation on the IBM-7090 and to Beverly Suneson, now Mrs. Carl Crafton, and Barbara Bingham for the hand computations which they performed in order to check the results of the program.

The continued support of Dr. H. B. Stewart, Dr. L. W. Nordheim, and Dr. R. B. Duffield was essential for the successful completion of this work.

REFERENCES

1. J. R. Beyster, J. L. Wood, W. M. Lopez, and R. B. Walton, *Nuclear Sci. and Eng.* **9,** 168 (1961).
2. M. J. Poole, M. S. Nelkin, and R. S. Stone, *Progr. in Nuclear Energy* (Ser. 1) **2,** 91 (1959).
3. R. S. Stone and R. Slovacek, *Trans. Am. Nuclear Soc.*, Washington, D. C., November, 1956.
4. V. I. Mostovoi, V. S. Dikarev, M. B. Egiasarov, and Yu.S. Saltzkov, *Proc. Second Intern. Conf. Peaceful Uses Atomic Energy, Geneva, 1958* **16,** 256.
5. R. Ramanna, N. Sarma, C. S. Somanathan, K. Usha, and G. Venkatarawar, *Proc. Second Intern. Conf. Peaceful Uses Atomic Energy, Geneva, 1958* **16,** 260.
6. P. Schofield and A. Hassitt, *Proc. Second Intern. Conf. Peaceful Uses Atomic Energy, Geneva, 1958* **16,** 217.
7. D. E. Parks, The calculation of thermal neutron scattering kernels in graphite. General Atomic, Report GA-2438 (to be issued).
8. D. E. Parks, Mean time of emission of neutrons from pulsed non-multiplying assemblies. General Atomic, Report GA-2189 (May 10, 1961).
9. A. Yoshimori and Y. Kitano, *J. Phys. Soc. Japan* **11,** 352 (1956).
10. K. Komatsu, *J. Phys. Soc. Japan* **10,** 346 (1955).
11. J. Krumhansl and H. Brooks, *J. Chem. Phys.* **21,** 1663 (1953).
12. D. E. Parks, Relation of crystal symmetry in graphite to lattice vibrations and their interaction with slow neutrons. General Atomic, Report GA-2125 (March 15, 1961).
13. W. Marshall and R. Stuart, University of California, Lawrence Radiation Laboratory, Report UCRL-PTN-149 (1959).
14. E. Fermi, *Ricerca sci.* **7,** 13 (1936).
15. R. J. Glauber, *Phys. Rev.* **98,** 1692 (1955).
16. M. S. Nelkin and D. E. Parks, *Phys. Rev.* **119,** 1060 (1960).
17. Sjölander, *Arkiv Fysik* **14,** 315 (1958).
18. Joan Bell, SUMMIT: An IBM-7090 program for the computation of crystalline scattering kernels. General Atomic, Report GA-2497 (to be issued).
19. K. M. Case, F. de Hoffmann, and G. Placzek, "Introduction to the Theory of Neutron Diffusion," Vol. I, Sec. 10.2. Los Alamos (1953).
20. M. S. Nelkin, and D. E. Parks, Spatially dependent neutron spectrum. General Atomic, Report GAMD-805 (unpublished).
21. D. E. Parks, *Nuclear Sci. and Eng.* **9,** 430 (1961).
22. N. F. Wikner and S. Jaye, Energy-dependent and spectrum-averaged thermal cross sections for the heavy elements and fission products for various temperatures and C:U^{235} atom ratios. General Atomic, Report GA-2113 (June 16, 1961).
23. D. J. Hughes and R. B. Schwartz, Brookhaven National Laboratory, Report BNL-325 (2d ed.), U. S. Government Printing Office, Washington, D. C. (1958).
24. B. R. Leonard, Jr., Survey of the status of low energy cross sections of fissile nuclides. Hanford Works, Report HW-69342 (April 21, 1961).
25. H. L. Reynolds, *Proc. Second Intern. Conf. Peaceful Uses Atomic Energy, Geneva, 1958* **12,** 632.
26. C. B. Mills, Neutron cross sections for fast and intermediate nuclear reactors. Los Alamos Scientific Laboratory, Report LAMS-2255 (1958).
27. G. D. Joanou and N. F. Wikner, private communication.

NUCLEAR SCIENCE AND ENGINEERING: **13**, 325-337 (1962)

Transient Thermal Behavior of Experimental UO_2 Fuel Elements in the Sodium Reactor Experiment (SRE)*

J. T. REAM† AND R. P. VARNES

Atomics International, A Division of North American Aviation, Inc., Canoga Park, California

Received November 17, 1961; Revised May 1, 1962

It was planned to test full scale UO_2 test elements in the SRE core. Before doing this, an analysis of the transient behavior of the system in part and the whole was carried out. This analysis concerns the problem of determining transient thermal gradients in the Sodium Reactor Experiment core due to the inability of the after-scram braked flow of the sodium to properly cool the UO_2 fuel test elements.

The analysis showed that the UO_2 fuel elements could not be irradiated at the desired core position for maximum power density without exceeding the allowable transient thermal gradient limit. It was necessary to shift them to a position of 25% lower power. An experimental scram of the SRE verified these results for the 19-rod cluster type element. It was possible to concentrate the investigation on the region of the core containing the UO_2 test elements using the assumption that the steady-state relationship between core pressure drop and reactor flow was valid during flow coastdown. Distributed spatial parameter effects were approximated by a "lumped"-parameter model and were incorporated in sets of coupled finite difference equations which were then solved by use of a general purpose dc analogue computer. The transient flow in the test elements were computed from the SRE quasi-steady-state pressure drop as a function of time. The higher sodium outlet temperature in the UO_2 test element channels results in an elevation head greater than the elevation head in an SRE channel. This nonlinear buoyant force could not be neglected because it significantly increases the transient flow in the UO_2 fuel element and stabilizes the channel outlet temperature.

NOMENCLATURE

A = heat transfer surface area, ft²
C = specific heat, Btu/lb-°F
k = thermal conductivity, Btu/lb-ft-°F
L = active fuel length, ft
g = gravitational constant = 32.2 ft/sec²
H = core height, ft
P = pressure in core, psi
ΔP = core pressure drop, psi
Q = average heat generation rate in fuel node, Btu/hr-ft³
r = radius of elemental volume, ft
R = outer radius of rod, ft
R_1 = inner radius of tubular UO_2 element, ft
R_2 = outer radius of tubular UO_2 element, ft
T = temperature, °F
$\bar{T}$ = average temperature, °F
ΔT = temperature rise, °F
U = heat transfer coefficient, Btu/hr-ft²-°F
v = velocity, ft/sec
V = volume of fuel node, ft³
W = mass flow rate, lb/hr
z = dimension in axial direction along fuel element, ft
β = inverse of volumetric expansion coefficient, lb/ft³-°F
ρ = density, lb/ft³
$\bar{\rho}$ = average density
δ = reflector savings, ft
θ = time, hr
τ = time constant, sec
τ_{DS} = delay time of scram after loss of flow, sec

Subscripts

a = denotes inner rod and channel of tubular element

* Presented at the 1960 Spring Meeting of the American Nuclear Society, Chicago, Illinois, June 1960.

† Present Address: John Jay Hopkins Laboratory for Pure and Applied Science, General Atomic Division of General Dynamics Corporation, San Diego, California.

b = denotes outer tube and channel of tubular element
c = denotes coolant
f = denotes fuel
j = denotes nodal position
1 = denotes inner surface of tubular element
2 = denotes outer surface of tubular element
0 = initial condition
l = lower plenum
u = upper plenum
in = denotes coolant channel inlet

I. INTRODUCTION

It was planned to irradiate UO_2 fuel in the form of full-size fuel elements in the Sodium Reactor Experiment (SRE). However, it was first necessary to determine that their presence was not detrimental to the reactor during both steady-state and transient operation. In sodium cooled reactors, the transient thermal shock effects are of principal concern. The zirconium cans of the SRE, which contain the graphite moderator logs and which are adjacent to the coolant channels, are the most susceptible to these effects. The analytical studies described in this paper were performed before testing to predict local thermal gradients in the UO_2 fuel element test channels during loss of forced convection flow and subsequent scram of the SRE. The resulting analogue computations are correlated with experimental results obtained during reactor operation. Natural flow coastdown and braked flow conditions are compared.

The analysis utilized two fuel element designs: a circular cluster of 19 UO_2 fuel rods, and a tubular fuel element consisting of an outer hollow ring of UO_2 concentric with a solid UO_2 rod in the center. The parameters studied were channel power or average fuel temperature, irradiation or burnup effects, scram delay time after loss of flow, flow coastdown characteristics, and decay heat fraction. The effect of neglecting nonlinear parameters in the analogue analysis is discussed.

II. DISCUSSION OF PROBLEM

One experimental phase of the fuel development program included plans to irradiate UO_2 fuel elements in the high-flux regions of the SRE. These analytical investigations were required to determine that the presence of the elements would not cause thermal damage to the SRE core during operation. Since the standard fuel element of the SRE core contains uranium metal fuel, and the test elements contain UO_2 fuel, a potential problem arose from the fact that two types of fuels are in the same core but their energy storage capacity and thermal time constants are different. A compatible flow decay for transient heat transfer can be obtained for either fuel but not necessarily for both fuels in the same core.

Reactor Characteristics

The SRE design power level is about 20 Mw with a flow rate of 483,000 lb/hr and a core ΔT of 460°F. The SRE first core loading consisted of 43 fuel elements, resulting in an average power of 465 kw per element and 530 kw in the maximum power element. The sodium temperatures were 500°F inlet and 960°F outlet. The graphite moderator blocks are contained in zirconium sheet-metal cans to separate them from the sodium coolant.

The hydraulic characteristics of the SRE primary coolant system that are important for this analysis are those that pertain to the transient flow decay, or coastdown after a scram due to loss of pumping power (loss of flow). The thermal convection, or buoyancy force, of the sodium along the channel is relatively large compared to the low channel friction pressure drop. If the flow is allowed to coast down freely after a reactor scram, the inertia and convective forces act to delay reduction of the flow rate. This is illustrated by curve A in Fig. 1. The resulting natural transient coolant flow rate is too high for the low heat storage and the short thermal time constant of the uranium metal fuel, and the reactor outlet temperature tends to drop rapidly after a few seconds. To protect the core against thermal shock, an electromagnetic eddy-current brake is used to automatically control the coolant flow and prevent rapid decrease of reactor outlet temperature (*1*, *2*).

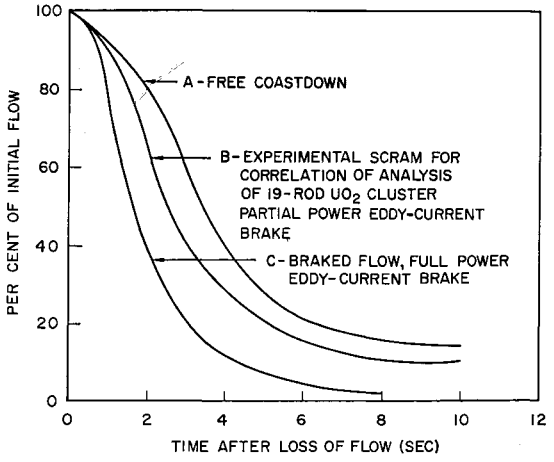

Fig. 1. SRE primary coolant loop flow decay after loss of pumping power.

Curve C of Fig. 1 shows that this brake very effectively retards the transient flow rate.

In summary, the problem was that the UO_2 test fuel elements might tend to overheat the sodium coolant locally. This could be serious because the zirconium moderator can between a UO_2 test channel and SRE channels could be subjected to a radial thermal gradient. From tests conducted on the zirconium can, it was concluded that this radial thermal gradient should be limited to 200°F. Thus, the limit for transient sodium outlet temperature in a UO_2 test channel is 1160°F when the SRE is operating at its design power of 20 Mw.

Fuel Element Characteristics

The standard SRE first core fuel elements were 7-rod clusters, 6 ft long, contained in 60-ft long Type 304 stainless steel jackets. Each contained NaK-bonded unalloyed uranium metal fuel slugs. A cross-sectional view is shown in Fig. 2. The cross sections of the UO_2 fuel elements are also shown schematically in Fig. 2.

The stored heat and the fuel and coolant time constants for both the test and the SRE fuel elements are compared in Table I. The values given in Table I are calculated for elements located in a 6th ring position of the SRE and a reactor power level of 20 Mw. The thermal parameters are different for the irradiated condition of the UO_2 fuel because of the effect of irradiation in lowering the apparent thermal conductance of UO_2 fuel. The time constants are defined as follows:

$$\text{Heat stored} = \rho_f C_f(\bar{T}_f - \bar{T}_c)$$

$$\text{Fuel time constant, } \tau_f = \frac{\rho_f V_f C_f}{UA}$$

$$\text{Coolant time constant, } \tau_c = \frac{\rho_c V_c C_c}{UA + 2WC_c}$$

$$\text{Coolant transport delay time, } \tau_{ct} = \frac{L}{v_c}$$

To discuss the problem in the light of these characteristics and obtain a qualitative comparison of the transient behavior of the test and SRE elements, it is useful to study these time constants, which are an indication of the response of the fuel element temperatures during a transient. The UO_2 test element has a longer fuel time constant and a longer coolant time constant, indicating that the test channel outlet temperature could exceed the standard SRE outlet temperatures during flow tran-

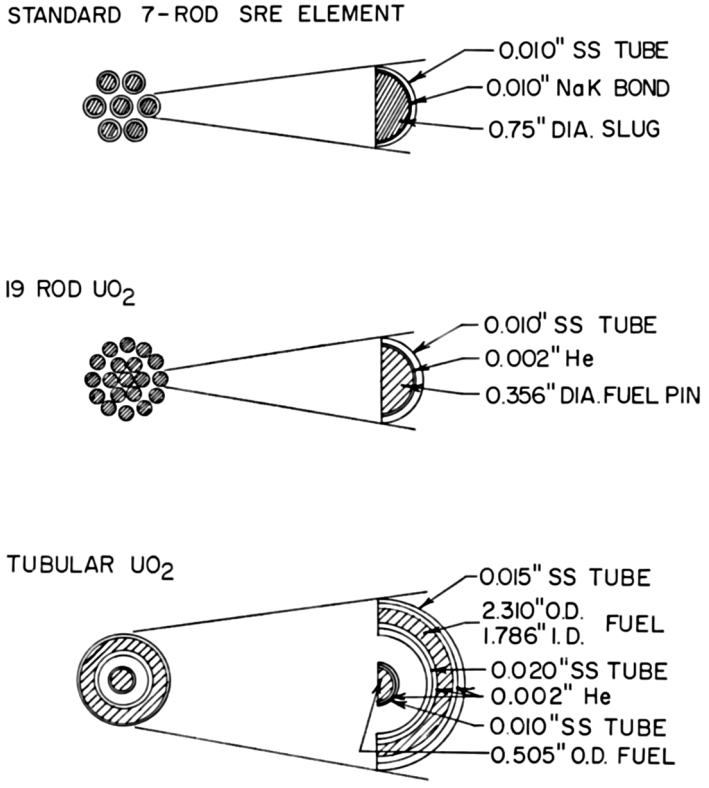

Fig. 2. Cross-section views of SRE standard uranium metal and experimental UO_2 fuel elements.

TABLE I
THERMAL PARAMETERS

Parameter	UO_2 fuel elements		SRE element
	Tubular	19-Rod	7-Rod
Fuel element power level (kw)[a]	302	336	465
Average fuel temperatures (°F)[a]			
Unirradiated	1470	1310	1150
Irradiated	2230	1520	1150
Average heat stored in fuel (BTU/ft³)[a]			
Unirradiated	35,800	28,000	4020
Irradiated	73,000	38,400	4020
Velocity (ft/sec)[a]	0.6[b] 1.9[c]	1.5	3.0
Flow coastdown time (sec)[d]	8	8	8
Coastdown time to 50% (sec)[d]	1.6	1.6	1.6
Fuel time constant (sec)			
Unirradiated	7[e] 9.5[f]	6.5	0.52
Irradiated	13[e] 21[f]	8.9	0.52
Coolant time constant (sec)[a]	0.836	0.334	0.157
Coolant transport delay (sec)[a]	10	4	2

[a] Located in the 6th ring of the SRE.
[b] Inner channel.
[c] Outer channel.
[d] Time for SRE reactor primary flow decay with maximum braking from eddy-current brake and complete loss of pump pressure.
[e] Center fuel rod.
[f] Outer fuel tube.

sients. Also, the coolant transport delay times are longer for the UO_2 test element channels than for a standard SRE channel, which indicates an over-all slower time response of the coolant outlet temperature to transients in power and coolant flow. Considering the combination of higher stored heat and longer time constants of the UO_2 test channels, it was most probable that they would not be completely thermally compatible in the same core with the SRE metal fuel elements during transient cooling.

On the positive side, however, is a factor that acts to reduce the coolant transport delay time of the UO_2 channels during the flow coastdown. This is the buoyancy pressure force which increases, due to increasing channel coolant temperature rise (decreasing density), relative to the channel friction pressure loss as flow decreases (*3*). If this nonlinear buoyant force is neglected, a highly conservative estimate of the higher transient coolant temperature of the UO_2 channels is obtained. However, a determination of the hazard associated with the test would be misleading if it is based on a limited analysis. It is necessary to evaluate all of the complex nonlinear parameters involved during the transient with an active-element analogue computer to determine the true transient thermal performance of a UO_2 fuel test element at a given location in the SRE.

III. ANALYSIS

System Characteristics and Assumptions

The objective of the analysis was to determine the transient thermal behavior of the coolant temperature of the UO_2 test channels during a loss of SRE pumping power, compared to the behavior of the standard SRE channels. Since the transient behavior of the SRE core and system was known to a certain extent and it was reasonable to assume that the localized thermal behavior of a test channel does not appreciably affect the SRE system, it was not necessary to simulate the whole core or primary coolant system. Thus, the problem reduced to determining the response of a cell in the system to the over-all system thermal behavior.

The determination of a reliable SRE system behavior required establishing a transient flow function using the assumption that quasi-steady-state performance was valid. Shown in Fig. 3 is a plot of the SRE reactor core friction pressure loss as a function of percent of initial flow. Combining this pressure-drop flow function with the appropriate coolant coastdown curve of Fig. 1 resulted in the curves of reactor core pressure drop as a function of time, shown in Fig. 4, for use as input data to the analogue computer.

The effects of rod motion and of fuel, coolant, and moderator temperature on neutron kinetics were neglected in the model simulation. The power generation transient simulation was by direct reduction of the heat source to a decay-heat percentage value at the end of the simulated scram time. The scram delay times were the average rod insertion times for operational scram data of the SRE.

Some of the other assumptions are related to physical properties and fundamentals and were incorporated because of a desire to be slightly conservative, or because preliminary analysis showed that neglecting them would have small effect on the results. The thermal conductivity of the UO_2 fuel was assumed to be constant in the final analysis. In a preliminary analysis, it was made inversely proportional to the fuel temperature. A comparison between the two analyses showed that this refinement was not warranted. The effect of axial heat conduction in the fuel and coolant was neglected.

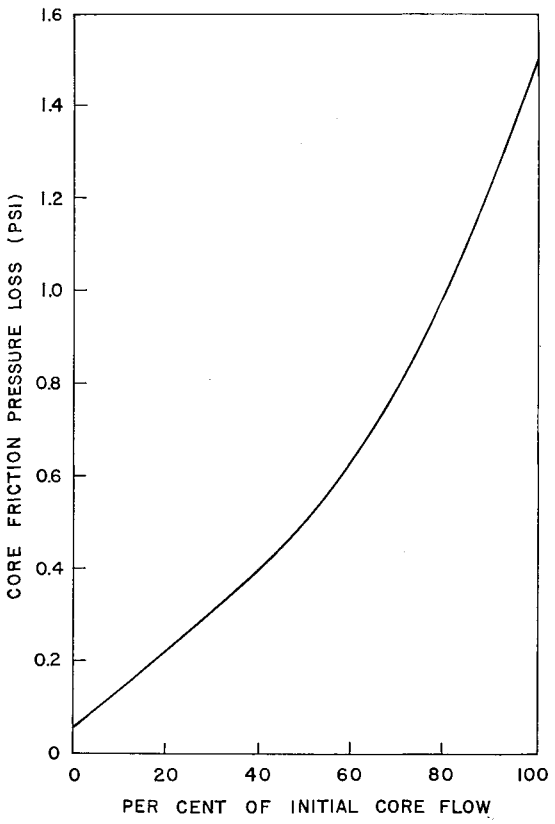

FIG. 3. SRE core pressure drop as a function of percent of initial core flow.

Also, channeled slug flow along the surface of the fuel cladding was used, i.e., transverse or redistributed flow inside the element was neglected. An investigation indicated that the decay heat source would be around 3 % of the steady-state power. This source strength is assumed "constant" for 20 to 30 sec after loss of flow. Heat transfer between the fuel process tube and the graphite moderator coolant channels was neglected; i.e., the boundaries of the unit cell model were assumed to be insulated.

It was assumed that all physical properties of the fuel element remained constant during the transient. The only physical property of the coolant which was varied during the transient was the density. The thermal resistance of the sodium film, or inverse of the film heat-transfer coefficient was assumed to be constant during the coolant flow transient; it is a very small part of the over-all thermal resistance and is not a strong function of velocity.

MODELS FOR ANALOGUE STUDIES

The model for a 19-rod cluster element consisted of an average fuel element rod and its associated coolant. The model for the tubular element was a prototype of the entire element, as shown in Fig. 2.

The average rod in the 19-rod cluster was chosen for the simulation because the parameter of interest was the transient temperature rise of the bulk coolant outlet temperature, which is a direct function of the total stored energy in the channel fuel cluster. Also, the boundary conditions of the model restricted the coolant flow to a definite channel around the average rod. The results of axial coolant temperature distribution, thus, are representative of an element with perfect thermal mixing between all fuel rods. With sodium, this is fairly representative because of its high thermal diffusivity. The simulation of an entire tubular element was necessary because it was desirable to know the time-temperature history of the inner and outer fuel cladding. The models were divided into axial and radial nodes to accommodate spatial thermal dependence between the adjacent regions of fuel and coolant. The radial regions of each model node consisted of cylindrical elemental volumes of fuel, helium gap, stainless steel clad, and sodium coolant. The required size of the lumped elemental volumes, or number of node points, depends on the relation between spatial and time changes, the regions and parameters which are of importance, and the accuracy required. In this model, the axial lumping was of greater importance because of the axial variation of fission heat generation in the fuel and the extreme transient imposed on the heat sink, or coolant flow rate. The nuclear heat generation rate decays rapidly but the long fuel time constant maintains the stored heat source at a high level during the major portion of the flow transient time. That is, with 8 axial fuel nodes, a lumped radial node has sufficient frequency response to give accurate peak transient coolant temperatures

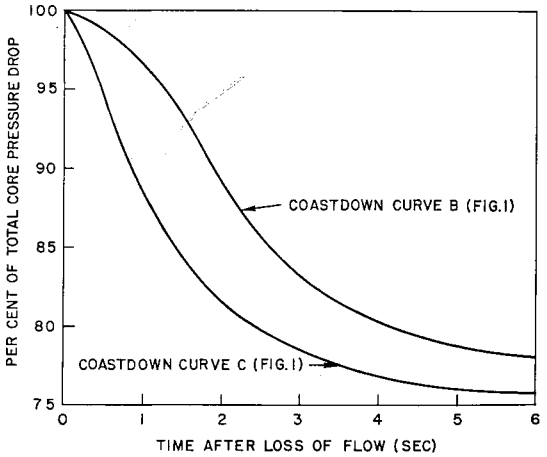

FIG. 4. SRE percent of total core pressure drop as a function of time for flow coastdown curves B and C of Fig. 1.

inasmuch as the heat sink decays so much faster than the heat source. The relaxation time for the problem is affected, but not until the stored heat in the fuel is very low.

For purposes of this transient study, the radial boundary of a model is spatially located where the radial flow of heat between the moderator and coolant regions is zero, i.e., assumed to be an insulated boundary. This is only an assumption, but it proved to be only slightly conservative. The axial boundaries of the model were located at the extremities of the active fuel length.

Equations for Analogue

The equations which define the dependent variables within the model are functions of space and time. An exact solution describing the nonlinear response of the model was considered impractical. The equations can be written in partial linear form for lumped parameter models if the spatial variation of heat source and sink are small compared to time changes. The heat source, heat transfer, and coolant flow equations used for the analogue are derived in the following section; the parameters are defined under nomenclature. The model description and assumptions have been discussed previously.

Heat-Source Equation

The total power of the element was assumed to have a chopped cosine power distribution from which an average source strength, Q, is calculated for each appropriate analogue model node. In the case of the 19-rod cluster, the total power of the element is divided by 19 when obtaining Q. For the tubular element, the total power was proportioned between the center fuel rod and the cylindrical fuel ring. According to the nuclear calculations, the proportion was 8 % generated in the center rod and 92 % generated in the cylinder.

Heat-Transfer Equations

19-Rod Cluster. If the fuel rod is divided into axial nodes using average heat generation rates per section, assuming no axial heat conduction, and the radial distribution of heat generation rate is uniform, the following fundamental fuel and coolant heat transfer equations are derived for any axial node. Due to the small rod diameter, the assumption of a uniform radial distribution of heat generation rate is valid. Since the fuel rod is long and thin, the axial conduction will be relatively small. An energy balance on an axial node of the fuel rod yields

$$\rho_f C_f V_f \frac{d\bar{T}_f}{d\theta} = QV_f - U_f' A_f(\bar{T}_f - T_c). \quad (1)$$

where U_f' is the effective heat-transfer coefficient between the average temperature of the fuel and the coolant temperature obtained from the steady-state heat-transfer relationship between the average volume of the fuel and the coolerant.

$$U_f' = \frac{4U_f k}{4k + R_f U_f}. \quad (2)$$

The partial differential equation describing the fluid temperatures is

$$\rho_c C_c V_c \left[\frac{\partial T_c}{\partial \theta} + v_c \frac{\partial T_c}{\partial Z}\right] = U_f' A_f[\bar{T}_f(Z) - T_c(Z)]. \quad (3)$$

Using the subscript j to denote the nodal points, Eq. (3) is written in difference form to eliminate the partial derivative of T_c with respect to Z; also noting that $W = v_c \rho_c V_c/\Delta Z$.

$$\rho_c C_c V_c \frac{dT_{cj}}{d\theta} + WC_c[T_{c(j+1/2)} - T_{c(j-1/2)}] = U_f' A_f(\bar{T}_{fj} - T_{cj}). \quad (4)$$

Using the method of central differences on Eq. (4) and writing Eq. (1) for the jth node results in the following set of equations for the thermal simulation of the 19-rod UO_2 fuel element:

For the fuel nodes

$$\rho_f C_f V_f \frac{d\bar{T}_{fj}}{d\theta} = Q_j V_f - U_f' A_{fj}(\bar{T}_{fj} - T_{cj}), \quad (5)$$

for all nodes, and for the coolant nodes

$$\rho_c C_c V_c \frac{dT_{cj}}{d\theta} = \frac{WC_c}{2}(2T_{cin} - T_{c(j+1)} - T_{cj}) + U_{fj}' A_f(T_{fj} - T_{cj}), \quad (6)$$

for node number 1, and

$$\rho_c C_c V_c \frac{dT_{cj}}{d\theta} = \frac{WC_c}{2}(T_{c(j-1)} - T_{c(j+1)}) + U_{fj}' A_f(\bar{T}_{fj} - T_{cj}), \quad (7)$$

for nodes number 2 through 7, and

$$\rho_c C_c V_c \frac{dT_{cj}}{d\theta} = WC_c(T_{c(j-1)} - T_{cj}) + U_{fj}' A_{fj}(\bar{T}_{fj} - T_{cj}), \quad (8)$$

for node number 8.

The scram during a loss of flow was simulated by instantaneously changing the heat generation rate from the initial power level to the decay heat value at the end of the rod scram delay time.

Tubular UO_2 *Fuel Element.* The center rod portion of the tubular fuel element was simulated in the same manner as the average rod of the 19-rod UO_2 fuel element; thus Eqs. (1) through (8) apply for the center rod. The derivation for the effective heat-transfer coefficients between the average fuel temperature of the hollow fuel cylinder and the coolant on both surfaces of the cylinder is somewhat more tedious than for the solid center fuel rod. Imposing the boundary conditions that $T = T_1$ when $r = R_1$ and $T = T_2$ when $r = R_2$ and integrating a general energy equation over r, a general solution was obtained. Then rearranging to eliminate the surface temperature, a complete solution for the average temperature of the fuel as a function of the dimensions, physical properties, heat-transfer coefficients, heat-generation rate, and coolant temperature is derived. Complete details of the solution are available in ref. *5*. The desired form of the solution is a steady-state energy balance on any axial hollow cylindrical section. This energy balance results in

$$\rho_f C_f V_{fbj} \frac{d\bar{T}_{fbj}}{d\theta} = Q_{bj} V_{fb} - U'_{b1} A_{b1}(\bar{T}_{fbj} - T_{caj}) - U'_{b2} A_{b2}(\bar{T}_{fbj} - T_{cbj}), \quad (9)$$

where the prime denotes an effective heat-transfer coefficient between the average temperature of the fuel and the coolant. The method of solution followed was to assume T_{caj} was equal to T_{cbj} in the steady state. The algebra involved to obtain expressions for U'_{b1} and U'_{b2} is then straightforward, although quite tedious (*5*). The assumption that inner and outer coolant temperatures are equal in steady state is based on the thermal design conditions at full power. However, it is noted that this assumption is only valid for a tubular fuel element at its design point. This is because of the nonlinear heat transfer effects on heat distribution between the inner and outer channels, at different conditions of temperature, thermal expansion, fission gas accumulation, etc.

The differential equation used for the coolant on the outside of the tubular fuel cylinder is essentially the same as Eq. (4). The differential equation used for the coolant between the solid fuel cylinder and the hollow fuel cylinder is merely an extension of Eq. (4) to include the energy supplied by the tubular fuel cylinder, as follows:

$$\rho_c C_c V_{ca} \frac{dT_{caj}}{d\theta} + W_a C_a[T_{ca(j+1/2)} - T_{ca(j-1/2)}] = U_a' A_a(\bar{T}_{faj} - T_{caj}) + U'_{b1} A_{b1}(\bar{T}_{fbj} - T_{caj}). \quad (10)$$

Writing Eqs. (10) and (4) for the various coolant nodes using the method of central differences, and using equations of the form of (9) and (1) for the fuel results in the following set of equations for the thermal simulation of the tubular UO_2 fuel element:

For all nodes

$$\rho_f C_f V_{faj} \frac{dT_{faj}}{d\theta} = Q_{aj} V_{fa} - U_a' A_a(\bar{T}_{faj} - T_{caj}), \quad (11)$$

$$\rho_f C_f V_{fbj} \frac{d\bar{T}_{fbj}}{d\theta} = Q_{bj} V_{fb} - U'_{b1} A_{b1}(\bar{T}_{fbj} - T_{caj}) - U'_{b2} A_{b2}(\bar{T}_{fbj} - T_{cbj}), \quad (12)$$

For node 1

$$\rho_c C_c V_{caj} \frac{dT_{caj}}{d\theta} = \frac{W_a C_c}{2}(2T_{cain} - T_{ca(j+1)} - T_{caj}) + U_a' A_a(\bar{T}_{faj} - T_{caj}) + U'_{b1} A_{b1}(\bar{T}_{fbj} - T_{caj}), \quad (13)$$

$$\rho_c C_c V_{cb} \frac{dT_{cbj}}{d\theta} = \frac{W_b C_c}{2}(2T_{cbin} - T_{cb(j+1)} - T_{cbj}) + U'_{b2} A_{b2}(\bar{T}_{fbj} - T_{cbj}). \quad (14)$$

For nodes 2 through 7

$$\rho_c C_c V_{caj} \frac{dT_{caj}}{2} = \frac{W_a C_c}{2}[T_{(acj-1)} - T_{ca(j+1)}] + U_a' A_a(T_{faj} - T_{caj}) + U'_{b1} A_{b1}(\bar{T}_{fbj} - T_{caj}), \quad (15)$$

and

$$\rho_c C_c V_{caj} \frac{dT_{cbj}}{d\theta} = \frac{W_b C_c}{2}[T_{cb(j-1)} - T_{cb(j+1)}] + U'_{b2} A_{b2}(\bar{T}_{fbj} - T_{cbj}). \quad (16)$$

for node 8

$$\rho_c C_c V_{ca8} \frac{dT_{cb8}}{d\theta} = W_a C_c(T_{ca7} - T_{ca8}) + U_a' A_a(\bar{T}_{fa8} - T_{fa8}) + U'_{b1} A_b(\bar{T}_{fb8} - T_{ca8}), \quad (17)$$

and

$$\rho_c C_c V_{cb8} \frac{dT_{cb8}}{d\theta} = W_b C_c(T_{cb7(j-1)} - T_{cb8}) + U'_{b2} A_b(\bar{T}_{fb8} - T_{cb8}). \quad (18)$$

Again, the scram was simulated by instantaneously

changing the heat generation rate from the initial power level to the decay heat value or zero.

Coolant Flow Equations

The energy balance flow in a channel is given by the following:

$$\frac{v_u^2 - v_l^2}{2g_c} + \int_{P_l}^{P_u} \frac{1}{\rho}\, dP + \int_0^H dZ + \frac{1}{g_c}\int_0^H \left[\frac{\partial v}{\partial \theta} + \frac{fv^2}{2D_e}\right] dZ + \frac{cv^2}{2g_c} = 0 \tag{19}$$

and $P_u - P_l \equiv \Delta P(\theta)$, the total core pressure drop as a function of time θ.

The definitions of the parameters are given under nomenclature. The equation is written between the lower plenum designated by P_l and the upper plenum designated by P_u ; the differences between velocities v_l and v_u are negligible.

The constant c includes all contraction and expansion losses in addition to the orifice loss. The density ρ is assumed to be the average channel coolant density as a function of average coolant temperature. The solution obtained is for the average channel velocity if v is a function of θ only. This makes the expression under the integral an exact differential, and thus it can be integrated. The following equation relating flow and pressure drop as a function of space and time results:

$$H\frac{dv}{d\theta} + \left(\frac{fH}{2D_e} + \frac{c}{2}\right)v^2 = g_c\frac{\Delta P}{\bar{\rho}c} - g_c H; \tag{20}$$

then let $K = (fH/2D_e) + \frac{1}{2}c$ be defined as the combined head loss coefficient for all channel and orifice friction losses.

Equation (20) is arranged in terms of dimensionless ratios as follows:

$$\frac{v_0}{v_0}\frac{dv}{d\theta} = g_c\frac{\Delta P}{\bar{\rho}H}\frac{\Delta P_0}{\Delta P_0} - Kv^2\left(\frac{v_0}{v_0}\right)^2 - g_c, \tag{21}$$

or

$$\frac{1}{v_0}\frac{dv}{d\theta} = g_c\frac{\Delta P_0}{\bar{\rho}Hv_0}\left(\frac{\Delta P}{\Delta P_0}\right) - Kv_0\left(\frac{v}{v_0}\right)^2 - \frac{g}{v_0} \tag{22}$$

The average density $\bar{\rho}$ is given by

$$\bar{\rho} = \rho_{in}(1 - \tfrac{1}{2}\beta\Delta Tc). \tag{23}$$

Equations (22) and (23) are the basic equations describing the flow in the channel receiving heat from the fuel. For application to the tubular element, two analogue circuit simulations of Eqs. (22) and (23) were necessary to describe the inner and outer coolant channels. The ratio $\Delta P/\Delta P_0$ was a quasi-steady-state function of time obtained from experimental flow tests of the SRE core. The value of K was calculated from the same experimental tests using the average channel density.

The average density is used for the solution of Eq. (19) because the calculated output is the average channel velocity, or flow rate. The net buoyant driving force which increases the average flow rate is a function of the difference in average coolant densities between the UO_2 test channels and an average SRE channel. That is, there is a flow redistribution between the parallel channels proportional to a thermal buoyancy pressure force which is given by the following equation (*3*).

$$\Delta P_B = \int_0^H \bar{\rho}_{UO_2}\, dz - \int_0^H \bar{\rho}_{SRE}\, dz \tag{24}$$

where

ΔP_B = buoyancy pressure force, psi
$\bar{\rho}_{UO_2}$ = average density in a UO_2 test channel
$\bar{\rho}_{SRE}$ = average density in a SRE channel.

The average density $\bar{\rho}_{UO_2}$ is calculated from a computer circuit simulation of Eq. (23) for input to Eq. (22). The transient flow rate, W, at any time is computed from the flow coastdown v/v_0 (the output of Eq. (22)) and put into the thermal Eqs. (6), (7), (8), etc., for the coolant nodes. Since the ratio v/v_0 of the UO_2 test element will vary in an inverse manner with the average coolant density, the resulting transient flow rate, W, will vary in the same inverse manner.

IV. DISCUSSION OF RESULTS

Preliminary Analogue Investigation

The first 19-rod cluster model simulated included a division of the fuel rod in both the radial and axial direction into twenty-four volumes, i.e., 3 radial nodal points and 8 axial nodes. The fuel conductivity at each fuel node was varied inversely with the fuel temperature. The element power level used was 450 kw, which corresponded to a position in the 4th ring of the SRE. The SRE flow decay was simulated by an input function generator using the experimental transient curve C given in Fig. 1. The nonlinear density change effect on flow during the transient was not included. The resulting channel temperature rise was well over 500°F above the normal SRE channel temperature rise, or over 300°F above the established limit of a 200°F rise. These results showed that the steady-state fuel temperature, or stored heat level, would have to be reduced by irradiating the fuel in a lower-power location of the SRE. Thus, the test location was changed to the SRE's 6th ring,

where the element power was reduced by 25% to 336 kw.

The first analogue investigations did not include the nonlinear transient buoyant pressure force. It was known intuitively that this buoyant force effect could be appreciable at very large temperature differences and low flows, but the order of magnitude of the effect was not known. During the transient in the SRE, the rising sodium temperature results in increasing elevation head or buoyancy pressure force opposite in sign to friction pressure forces, which decrease with channel flow rate. The ratio of these two opposite forces is a measure of their relative effect on the local mass flow rate; when this ratio is greater than 20, the buoyancy force very effectively increases the local channel mass flow rate in a parallel channel flow system (*3*). This ratio for the UO_2 test elements reaches approximately 20 between

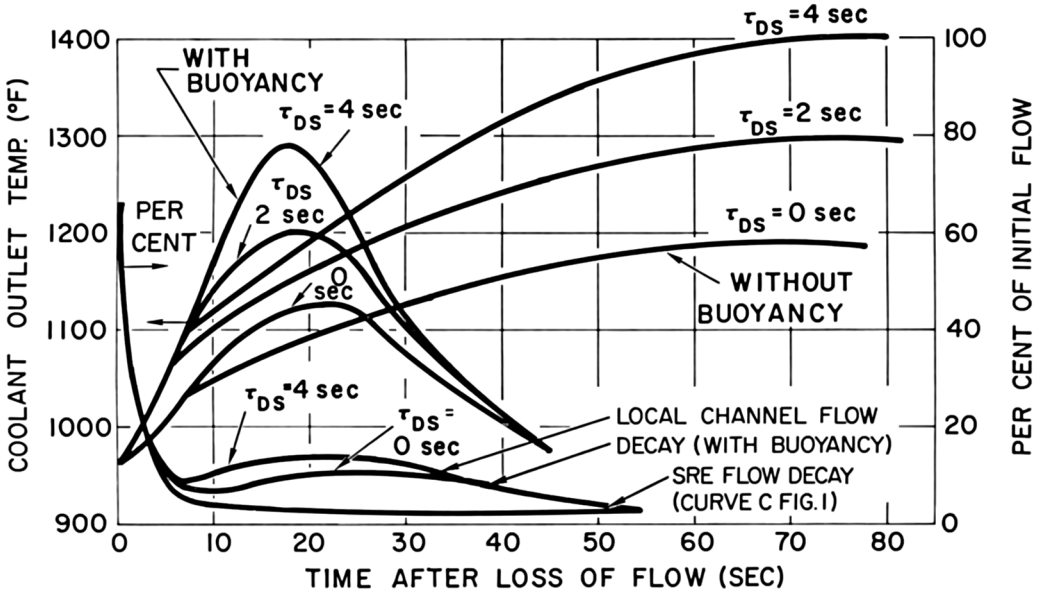

FIG. 5. Coolant outlet temperature and flow of 19-rod UO_2 cluster test element after scram of the SRE with UO_2 fuel rradiated to 15,000 Mw-days/ton, showing the effects of scram delay time and local buoyancy.

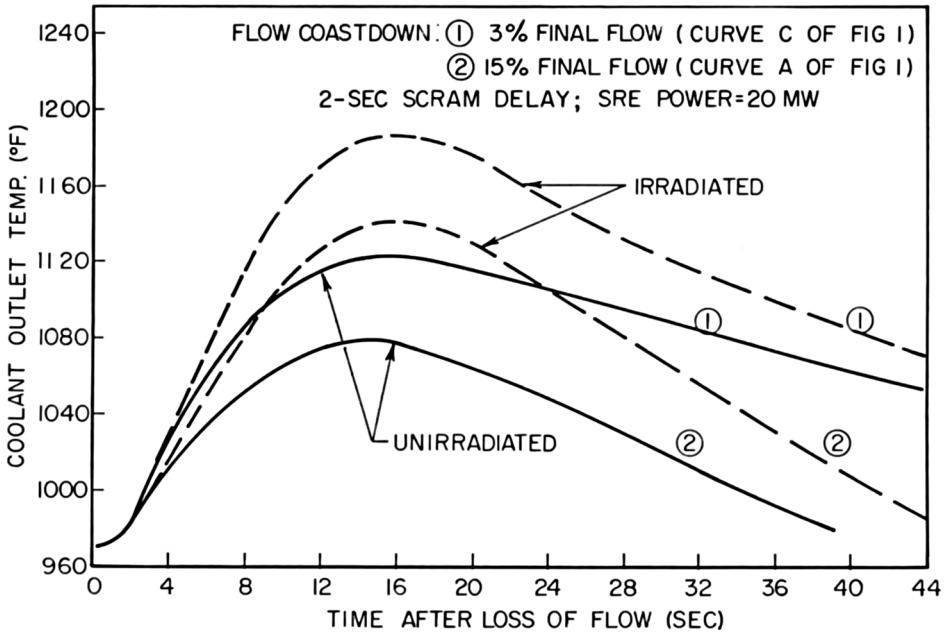

FIG. 6. Coolant outlet temperature of 19-rod UO_2 cluster test element after scram of the SRE, showing the effects of flow coastdown and fuel irradiation.

3 and 4 sec after loss of flow in the SRE. Obviously, the analogue model could not accurately predict coolant temperature rise unless a nonlinear function was included for the density change effects; the buoyancy force was therefore included in the subsequent analogue models.

The first analysis had also shown that the frequency response of the fuel was so low that dividing the fuel into radial nodes was unnecessary; therefore, a single node was used subsequently to represent the fuel rod in the radial direction.

Subsequent Analogue Investigations

To change to the single radial node model the cladding was lumped with the slug of sodium coolant for each node. Thus, the transfer function for heat was from the average fuel temperature to the average coolant temperature at each jth axial node. Also,

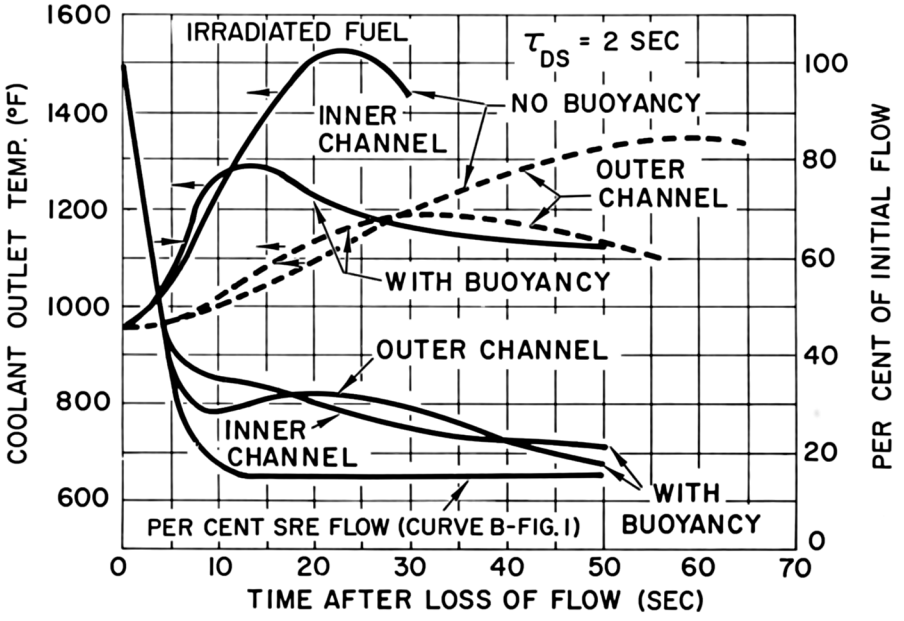

FIG. 7. Coolant outlet temperature and flows of tubular UO_2 test element after scram of the SRE with UO_2 fuel irradiated to 15,000 Mw-days/ton, showing effects of local buoyancy.

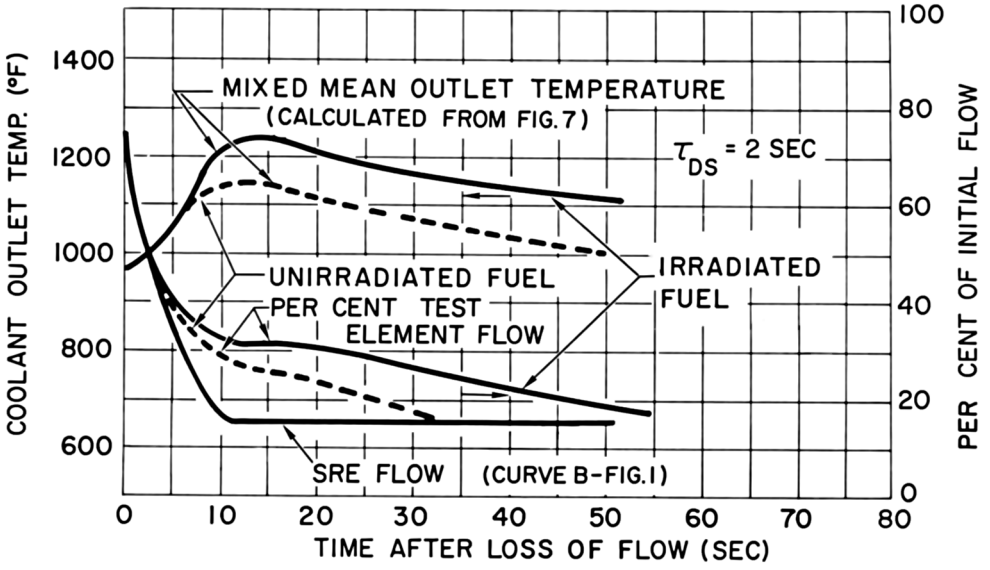

FIG. 8. Mixed mean coolant outlet temperatures and flow of tubular UO_2 test element after scram of the SRE showing effects of fuel irradiation to 15,000 Mw-days/ton.

the fuel thermal conductivity was kept constant at its initial average value.

In the final analyses, the parameters studied were channel power (corresponding to specified reactor power levels), fuel conductivity (irradiation effects), fuel temperature, and the effect of buoyancy. The effect of decay heat, scram delay time, and thermal resistance of the helium bond were also observed.

The results of the analogue analyses for the 19-rod cluster are shown in Figs. 5 and 6. The results for the nonbuoyancy case are shown in Fig. 5 for comparison only and do not represent a realistic case. Also shown in Fig. 5 is the effect of the scram delay time, τ_{DS}, on the coolant temperatures. In Fig. 6, the effects of the coolant coastdown and irradiation are shown for given reactor scram conditions. The

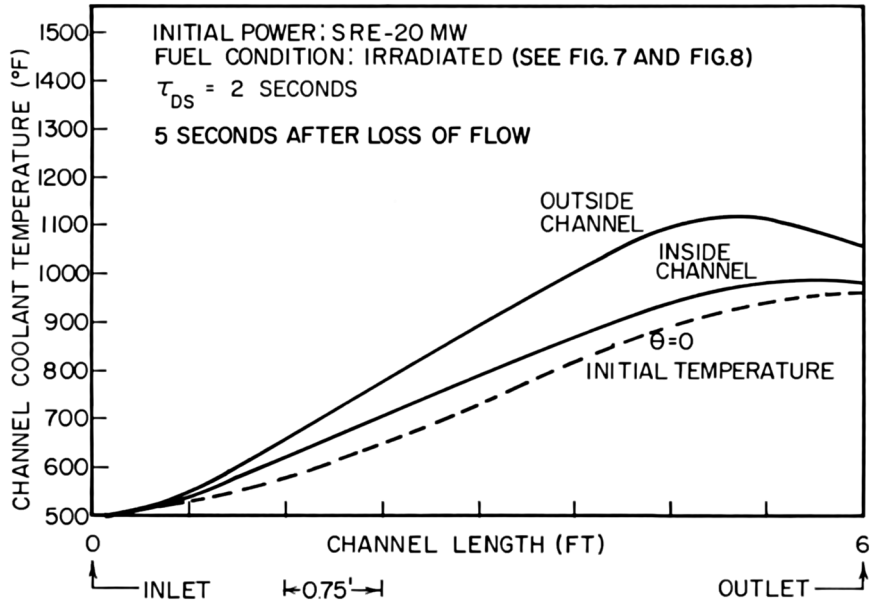

FIG. 9. Coolant axial temperature distributions for inner and outer channels of tubular UO_2 fuel test element at 5 sec after loss of flow.

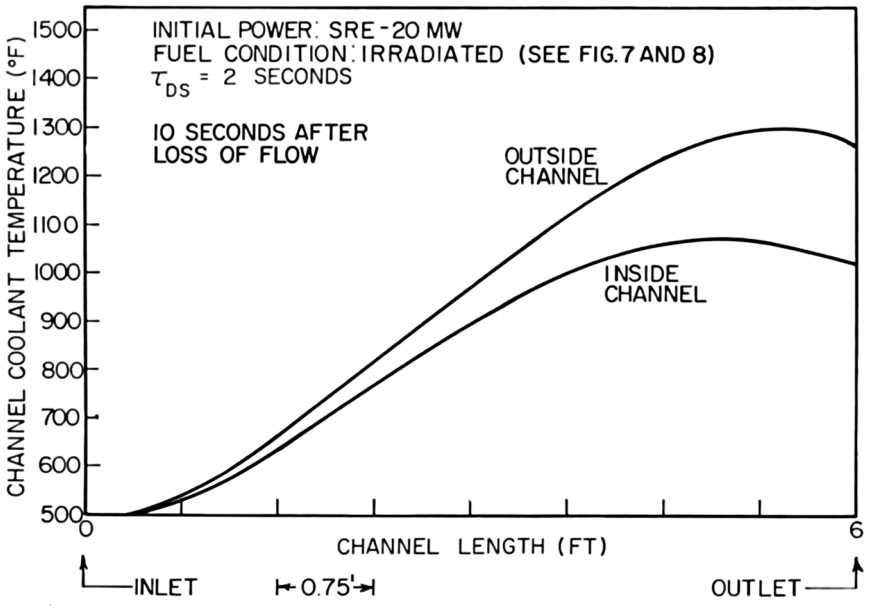

FIG. 10. Coolant axial temperature distributions for inner and outer channels of tubular UO_2 fuel test element at 10 sec after loss of flow.

irradiation effect is for a burnup of about 15,000 Mw-days/ton and is primarily due to the effect of a lower fuel thermal conductivity causing a higher initial fuel temperature, or stored heat level.

The analytical results for the tubular element are shown in Figs. 7, 8, 9, and 10. The inner and outer channel outlet coolant temperatures and flow rates shown in Fig. 7 include the case without buoyancy to show the effect of buoyancy on the analysis. Figure 8 is a plot of the mixed-mean coolant temperature at the channel outlet for the entire tubular element, for unirradiated UO_2 fuel, and for UO_2 fuel irradiated for 15,000 Mw-days/ton. Figures 9 and 10 show the difference in coolant temperature distributions between the two cladding surfaces of the cylindrical fuel portion.

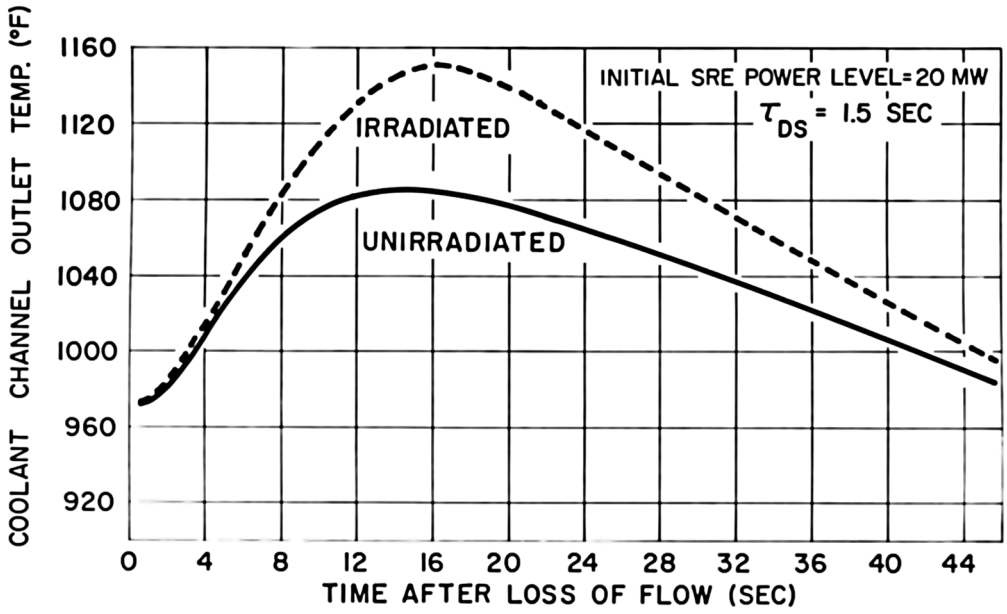

FIG. 11. Predicted transient coolant outlet temperature of 19-rod UO_2 cluster element after loss of flow in SRE using experimental coastdown curve B of Fig. 1 and scram delay time of 1.5 sec and showing effects of irradiation of UO_2 to 15,000 Mw-days/ton.

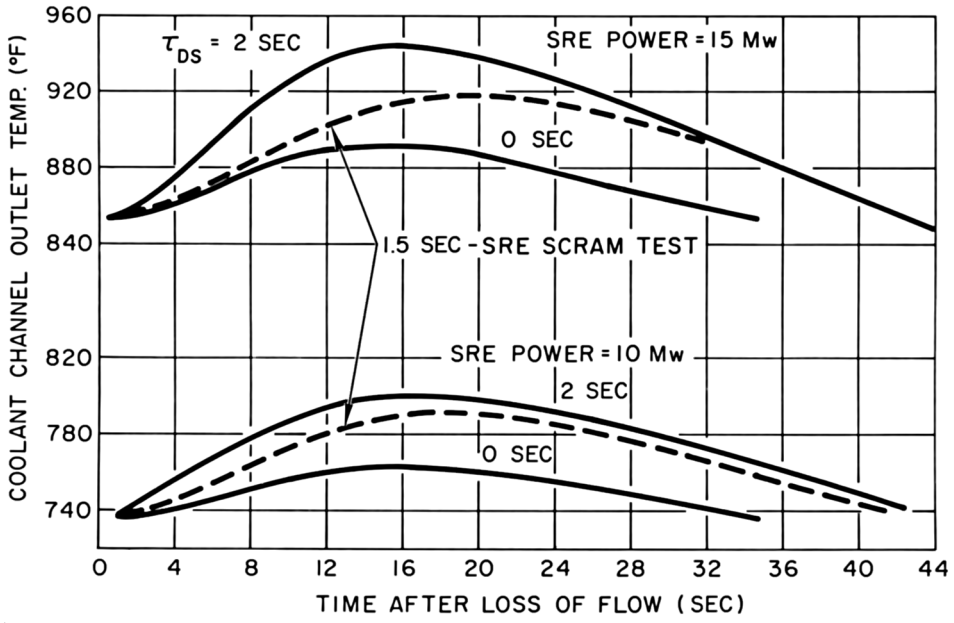

FIG. 12. Correlation of predicted coolant outlet temperatures from analogue studies with experimental data (curve B, Fig. 1) after loss of flow and scram of the SRE for unirradiated 19-rod cluster UO_2 test element.

Figure 11 gives the predicted transient coolant temperature data for the 19-rod cluster after loss of pump power and scram from full power level of the SRE (20 Mw) for both unirradiated UO_2 fuel and UO_2 fuel irradiated to about 15,000 Mw-days/ton.

Correlation with Experiment

The 19-rod UO_2 fuel element was tested in the SRE to check the results of this analysis. These tests included a loss of flow from a reactor power level of 10 Mw and a loss of flow from a reactor power level of 15 Mw. The transient temperature rise of the outlet coolant temperature was measured and recorded during these tests. The experiment was conducted with unirradiated fuel, and the experimentally simulated loss of pump power and braked flow coastdown was as shown in curve B in Fig. 1. A final analysis was conducted simulating the actual operating conditions of the SRE and the unirradiated condition of the UO_2 test elements. The correlation of the experimental and analytical results is shown in Fig. 12.

V. CONCLUSIONS

The only estimate of accuracy of the analysis that can be made will come from a comparison of the experimental with the analytical results. It is estimated from Fig. 12 that the analytical methods predicted the maximum coolant temperature rise for the 19-rod cluster element within 10%. The variation of the thermal conductivity of UO_2 is probably the prime source of error. The decrease in conductivity with increasing temperatures near the center of the rod would, in fact, effectively increase the relaxation time of a solid cylindrical fuel rod. With a shorter relaxation time, the stored energy appears to be released prematurely to the coolant in the analysis. The temperature rise in the coolant and the associated buoyant effects due to this delayed energy release account for the fact that the predicted channel flow rate is slightly higher than the apparent experimental channel flow rate. It was not felt profitable to account for this difference in thermal conductivity in the model for a transient analysis because of the scatter in the experimental data for the thermal conductivity of UO_2.

The results of this analysis show that the most important parameters for predicting transient thermal performance of UO_2 fuel elements cooled by sodium are the initial fuel temperature, or heat source level, and the decay of the heat sink. In addition, it is important to include the coolant density variation in the analytical method to predict transient coolant temperatures.

It was mentioned in Section II of this paper that the criterion for establishing the feasibility of testing the UO_2 fuel elements in any core location of the SRE was that the transient coolant channel outlet temperature could not rise to more than 1160°F when the SRE is operated at 20 Mw. Thus, it was concluded that it was safe to test the 19-rod cluster UO_2 fuel element in the 6th ring location even after long irradiation time based on the results shown in Fig. 11. However, it was concluded that the tubular UO_2 fuel could not be safely tested in the 6th ring after long irradiation and would only be marginally safe if tested in an unirradiated condition. This conclusion was based on the results shown in Figs. 7 and 8.

An additional problem that might arise with the tubular element would be the strain between the inner and outer fuel cladding due to differential thermal expansions. The temperature differences shown in Figs. 9 and 10 cause an axial and radial thermal stress between the two fuel cylinders for about 10 sec. The combined stress due to the temperature difference shown in Figs. 9 and 10 is not large (estimated to be under 30,000 psi), but it does indicate that a hazard might exist if some of the assumptions made are too nonconservative.

REFERENCES

1. W. S. DeBear, Preliminary investigation for control of SRE convection flow problem. NAA TDR 2116 (1957).
2. R. S. Baker, Eddy current brake for throttling natural convection flow. NAA TDR 131 (August 13, 1957).
3. C. F. Bonilla, "Nuclear Engineering," pp. 287–325. McGraw-Hill, New York, 1957.
4. P. Spiegler, Decay heat generation in UO_2 fuel clusters. NAA TDR 3907 (1959).
5. J. T. Ream and R. P. Varnes, NAA Memo 5989 (December 27, 1960).

NUCLEAR SCIENCE AND ENGINEERING: **13**, 338–344 (1962)

The Effect of Modal Interaction in the Xenon Instability Problem

GEZA L. GYOREY

Department of Nuclear Engineering, The University of Michigan, Ann Arbor, Michigan

Received December 27, 1962

This paper deals with the space and time dependent reactor stability problem of neutron flux shape variations due to xenon-135. The effect of modal interaction on stability is investigated for a simple reactor model when the characteristic functions of the wave equation are used in a modal expansion. It is shown that modal interaction may contribute to or detract from stability depending on the circumstances, and that in the case of a very large reactor, stability can be seriously overestimated if modal interaction is neglected.

NOMENCLATURE

$a_i(t)$	the time dependent part of the ith term in the expansion of $\delta\phi(\mathbf{r}, t)$
$b_i(t)$	same as above in the expansion of $\delta X(\mathbf{r}, t)$
$c_i(t)$	same as above in the expansion of $\delta I(\mathbf{r}, t)$
p	the resonance escape probability
q	the slowing down kernel
$\mathbf{r}$	space variable
t	time variable
x	space variable
C_n	the criticality factor of the nth mode of the neutron flux distribution in the reactor
D	the thermal diffusion constant
F_{ij}	the modal coupling coefficient associated with the steady state neutron flux distribution
H	the thickness of the slab reactor
$I(\mathbf{r}, t)$	the concentration of iodine-135
$I_0(\mathbf{r})$	the steady state iodine-135 distribution
$I_n(t)$	the reduced amplitude of the nth mode in the expansion of $\delta I(\mathbf{r}, t)$
$\delta I(\mathbf{r}, t)$	the deviation of the iodine-135 distribution from the steady state
L	the thermal diffusion length
M	the migration length
$N_n(t)$	the reduced amplitude of the nth mode in the expansion of $\delta\phi(\mathbf{r}, t)$
P_{ij}	the modal coupling coefficient associated with the steady state poison distribution
$Q(K_n)$	the fast leakage escape probability associated with the nth mode
S_n	the reduced subcriticality of the nth mode of the neutron flux distribution
T	the dimensionless time variable
$X(\mathbf{r}, t)$	the concentration of xenon-135
$X_0(\mathbf{r})$	the steady state xenon-135 distribution
$X_n(t)$	the reduced amplitude of the nth mode in the expansion of $\delta X(\mathbf{r}, t)$
$\delta X(\mathbf{r}, t)$	the deviation of the xenon-135 distribution from the steady state
γ_X	the fission yield of xenon-135
γ_I	the fission yield of iodine-135
γ	$\gamma_X + \gamma_I$
δ_{ij}	Kronecker's delta
ϵ	the fast fission factor
λ_X	the decay constant of xenon-135
λ_I	the decay constant of iodine-135
λ	$\lambda_X + \lambda_I$
ν	the average number of neutrons produced upon fission
σ_X	the microscopic thermal neutron absorption cross section of xenon-135
τ	the neutron generation time in an infinite medium
$\phi(\mathbf{r}, t)$	the thermal neutron flux
$\phi_0(\mathbf{r})$	the steady state thermal neutron flux distribution
$\phi_0(\max)$	the maximum value of $\phi_0(\mathbf{r})$
$\delta\phi(\mathbf{r}, t)$	the deviation of the thermal neutron flux distribution from the steady state
$\psi_n(\mathbf{r})$	the nth characteristic function of the wave equation

$\psi_n(\max)$ the maximum value of $\psi_n(\mathbf{r})$
Γ_n the maximum effect of the poison on the criticality factor of the nth mode
K_n the nth characteristic value of the wave equation
Σ_a the thermal absorption cross section in the clean core
Σ_f the thermal fission cross section
Φ the reduced maximum steady state thermal neutron flux

INTRODUCTION

In the treatment of the space and time dependent reactor stability problem of neutron flux shape variations due to xenon-135, the method of harmonics is often used. Through this method, the finite set of partial differential equations describing the problem is replaced by an infinite set of ordinary differential equations which describe the time behavior of the various modes or harmonics of distribution. There is a finite subset of equations associated with each mode. It was pointed out by Kaplan (*1*) that particular sets of harmonics can be found such that each subset of these equations is independent of the other subsets, that is, such that the time behavior of each mode of distribution can be described independently of the behavior of the other modes. Often, however, it is desirable to choose a set of harmonics, such as the characteristic functions of the wave equation, which are simple, well known, and not dependent on the power level. Such a choice is made in several papers which treat the xenon instability problem (*2–4*). The use of such a set of harmonics will in general result in an interdependence of the subsets of ordinary differential equations mentioned above, such that the time behavior of each mode is influenced by the behavior of the other modes. It is convenient to attempt to predict the stability of the shape of the neutron flux distribution by examining the stability of each mode by itself, that is, when modal interaction is neglected. The results of such an attempt may not be very meaningful however, if it is possible than an unstable system is produced when several modes, each of which is by itself stable, interact. This work deals with the effect of modal interaction on stability. The characteristic functions of the wave equation are used in the modal expansion. The reactor model used is described in a subsequent section.

In this work, some of the terminology and notations of Weinberg and Wigner (*5*) are used. The term "criticality factor" and the symbol C are used in place of the more usual term "effective multiplication factor" and the symbol k_{eff}. In the modal expansion the first term will be called the *first* harmonic or fundamental mode; this in general should be distinguished from the steady state neutron flux distribution.

THE REACTOR MODEL

The reactor model used in this work is a bare, thermal reactor with stationary fuel; it is homogeneous except for the xenon poison. It is assumed that variation in the xenon-135 density is the only process through which a change in neutron flux level affects the properties of the core medium, that is, xenon poisoning is the only feedback effect. It is assumed that the xenon affects only the thermal absorption cross section. Linear theory is used: the treatment is restricted to small deviations from the steady state.

The attention is focused on the stability of the *shape* of the neutron flux distribution, and therefore it is assumed that the fundamental mode of the flux distribution is held constant by a suitable control system which has negligible effect on the higher modes.

All numerical computations and results are given for a slab reactor with effective boundaries at $x = 0$ and $x = H$, and in which no variations are allowed in the y and z directions in any of the variables.

Subject to the enumerated assumptions, the reactor system can be described to a good approximation by the following equations:

$$0 \approx \Sigma_a \tau \frac{\partial}{\partial t}\phi(\mathbf{r}, t) \approx D\nabla^2\phi(\mathbf{r}, t) - \Sigma_a\phi(\mathbf{r}, t) - \sigma_X X(\mathbf{r}, t)\phi(\mathbf{r}, t) + \nu\epsilon p\Sigma_f \int_{\text{all space}} \phi(\mathbf{r}', t)q(|\mathbf{r} - \mathbf{r}'|)d^3\mathbf{r}' \tag{1}$$

$$\frac{\partial}{\partial t}X(\mathbf{r}, t) = \lambda_I I(\mathbf{r}, t) + \gamma_X \epsilon\Sigma_f\phi(\mathbf{r}, t) - \lambda_X X(\mathbf{r}, t) - \sigma_x X(\mathbf{r}, t)\phi(\mathbf{r}, t) \tag{2}$$

$$\frac{\partial}{\partial t}I(\mathbf{r}, t) = \gamma_I \epsilon\Sigma_f\phi(\mathbf{r}, t) - \lambda_I I(\mathbf{r}, t) \tag{3}$$

with the boundary conditions that the variables are zero at the effective boundaries.

The approximation that (1) is zero is reasonable for the higher modes of distribution, provided that the reactor dimensions are not more than a few hundred times the migration length.

THE MODAL EXPANSION

It is convenient to separate the variables into steady state and time dependent parts:

$$\phi(\mathbf{r}, t) = \phi_0(\mathbf{r}) + \delta\phi(\mathbf{r}, t) \tag{4}$$

$$X(\mathbf{r}, t) = X_0(\mathbf{r}) + \delta X(\mathbf{r}, t) \tag{5}$$

$$I(\mathbf{r}, t) = I_0(\mathbf{r}) + \delta I(\mathbf{r}, t) \tag{6}$$

Substituting these into the equations of motion, subtracting the steady state equations from the resulting ones, and then neglecting the terms involving the product $\delta\phi\delta X$, one obtains a set of equations describing the behavior of small deviations from the steady state. The time variables are now expanded in the following manner:

$$\delta\phi(\mathbf{r}, t) = \sum_{i=1}^{\infty} a_i(t)\psi_i(\mathbf{r}) \tag{7}$$

$$\delta X(\mathbf{r}, t) = \sum_{i=1}^{\infty} b_i(t)\psi_i(\mathbf{r}) \tag{8}$$

$$\delta I(\mathbf{r}, t) = \sum_{i=1}^{\infty} c_i(t)\psi_i(\mathbf{r}) \tag{9}$$

where

$$\nabla^2\psi_i(\mathbf{r}) + K_i^2\psi_i(\mathbf{r}) = 0 \tag{10}$$

$$\int_{\text{reactor volume}} \psi_i(\mathbf{r})\psi_j(\mathbf{r})\, d^3\mathbf{r} = \delta_{ij} \tag{11}$$

and the ψ's satisfy the same boundary conditions as the variables. Multiplying the resulting equations by ψ_n and integrating them over the reactor volume, one obtains the desired infinite set of ordinary differential equations. These equations are cast into a convenient dimensionless form by defining the following quantities.

$$N_n(t) \equiv \frac{\psi_n\,(\max)}{\phi_0\,(\max)}\, a_n(t), \tag{12}$$

$$X_n(t) \equiv \frac{\lambda_X \psi_n\,(\max)}{\gamma\epsilon\Sigma_f\,\phi_0\,(\max)}\, b_n(t), \tag{13}$$

$$I_n(t) \equiv \frac{\lambda_I \psi_n\,(\max)}{\gamma_I\,\epsilon\Sigma_f\,\phi_0\,(\max)}\, c_n(t), \tag{14}$$

the reduced amplitudes of the nth modes of the neutron flux, xenon, and iodine concentration deviations from steady state;

$$\Phi \equiv \frac{\sigma_X}{\lambda_X}\,\phi_0\,(\max), \tag{15}$$

the reduced maximum steady state flux,

$$F_{ij} \equiv \frac{\sigma_X}{\lambda_X}\int_{\text{reactor volume}} \phi_0(\mathbf{r})\psi_i(\mathbf{r})\psi_j(\mathbf{r})\, d^3\mathbf{r}, \tag{16}$$

$$P_{ij} \equiv \frac{\sigma_X}{\gamma\epsilon\Sigma_f}\int_{\text{reactor volume}} X_0(\mathbf{r})\psi_i(\mathbf{r})\psi_j(\mathbf{r})\, d^3\mathbf{r}, \tag{17}$$

the modal coupling coefficients associated with the steady state flux and poison distribution respectively;

$$\Gamma_n \equiv \frac{\gamma\epsilon\Sigma_f}{\Sigma_a(1 + L^2K_n^2)}; \tag{18}$$

the maximum effect of the steady state poison on the criticality factor of the nth mode (so that $\Gamma_n P_{nn}$ is the actual effect on it);

$$C_n \equiv \frac{\nu\epsilon p\Sigma_f\, Q(K_n)}{\Sigma_a(1 + L^2K_n^2)} - \Gamma_n P_{nn}, \tag{19}$$

the criticality factor of the nth mode;

$$S_n \equiv \frac{1 - C_n}{\Gamma_n}, \tag{20}$$

the reduced subcriticality of the nth mode, and finally

$$T \equiv \lambda_X t, \tag{21}$$

the dimensionless time variable.

In terms of the newly defined quantities, the equations of motion can be written in the following form.

$$0 \approx S_n N_n + F_{nn} X_n + \sum_{i\neq n} [P_{in} N_i + F_{in} X_i], \tag{22}$$

$$\frac{dX_n}{dT} = \frac{\gamma_I}{\gamma} I_n + \left(\frac{\gamma_X}{\gamma} - P_{nn}\right) N_n - (1 + F_{nn})X_n - \sum_{i\neq n} [P_{in}N_i + F_{in} X_i], \tag{23}$$

$$\frac{dI_n}{dT} = \frac{\lambda_I}{\lambda_X}(N_n - I_n), \quad n = 1, 2, 3, \cdots, \infty. \tag{24}$$

The influence of the ith mode on the nth one is represented by the expression within the brackets in Eqs. (22) and (23).

THE MODAL COUPLING COEFFICIENTS

The values of the modal coupling coefficients F_{ij} and P_{ij}, as indicated in (16) and (17), are influenced by the shapes of the steady state flux and poison distributions, the latter distribution being uniquely determined by the former. The shape of the flux distribution depends on the maximum flux level as well as on the reactor size. In the poisoned reactor the flux distribution is flatter than the fundamental mode of the expansion used here, but for the combinations of reactor sizes and flux levels considered in this work, it is not much flatter. For

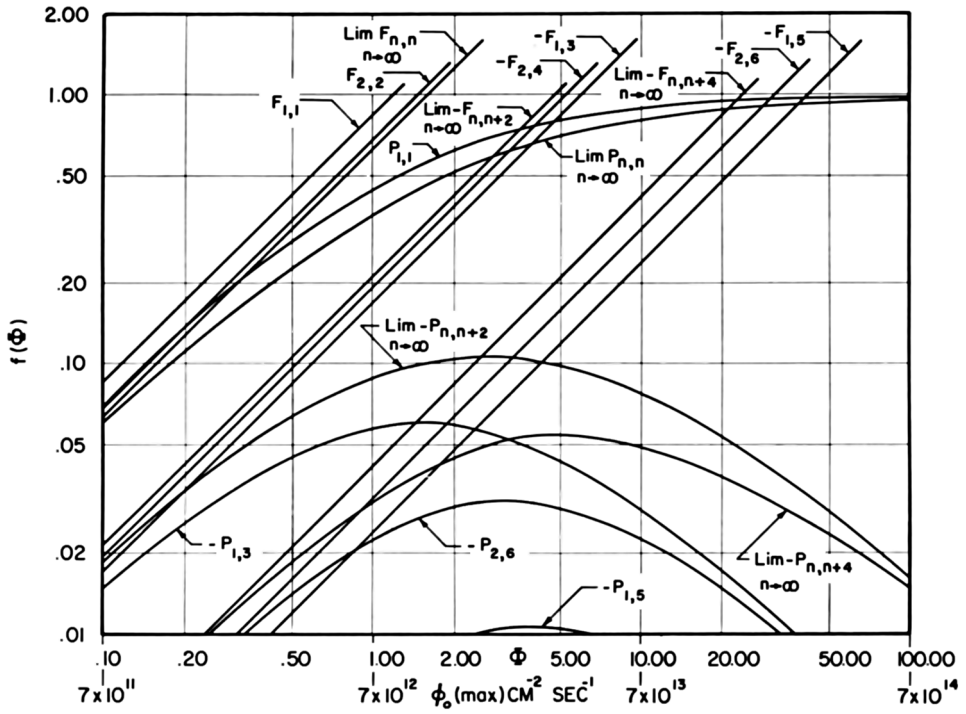

FIG. 1. The behavior of the modal coupling coefficients F_{ij} and P_{ij} as functions of Φ

numerical computation of the coupling coefficients, therefore, the shape of the steady state flux distribution is approximated by the fundamental mode ψ_1. A flattening in ϕ_0, and therefore also in X_0, increases the values of F_{ij} and P_{ij} for $i = j$ (which might be called the self-coupling coefficients), and decreases the values of the coefficients for $i \neq j$, because the ψ's are orthogonal functions. The approximation mentioned above, therefore, results in a slight apparent strengthening of modal interaction. The values of some of the coupling coefficients are shown in Fig.1 as functions of the flux level. When the nonlinearities are neglected, as is done here, there is no interaction between an even and an odd harmonic. The absolute magnitudes of the coefficients fall off quite rapidly as $|i-j|$ increases, and therefore one may expect the strongest interaction to appear between the ith and jth modes when $j = i \pm 2$.

ANALYTICAL INVESTIGATION

An approximate stability criterion can be derived for the higher modes when modal interaction is neglected. Under this condition, the system represented by Eqs. (22), (23), and (24) is stable if

$$S_n > \frac{F_{nn}\,(P_{nn} - \gamma_X/\gamma)}{\lambda/\lambda_X + F_{nn}}, \quad n = 2, 3, \cdots, \infty. \tag{25}$$

This criterion predicts marginal stability for the nth mode when S_n equals the right hand side of (25); this value will be referred to as the critical value of S_n as predicted by the approximate stability criterion. This critical value is shown as a function of flux level in Fig. 2.

It is desirable to have a rough indication of what this criterion means in terms of reactor size rather than in terms of subcriticality. For $n \neq 1$, but not very large, and for the range of reactor sizes of interest here, one may write (6) as a rough approximation

$$S_n \approx \frac{M^2}{\Gamma_n}\,(K_n^2 - K_1^2). \tag{26}$$

For a slab reactor with $\Gamma_n = 0.03$:

$$S_n \approx \frac{\pi^2}{0.03}\,(n^2 - 1)\left(\frac{M}{H}\right)^2. \tag{27}$$

Table I shows this approximate correspondence between reactor size and S_n. It should be noted here that the exact relationship between S_n and reactor size involves terms which are dependent on the power level.

The analytical investigation carried out was directed at answering the following question: if the nth mode is predicted to be marginally stable by the approximate stability criterion given above, then will the combined system of the nth and mth modes be stable or unstable? In order to attempt to

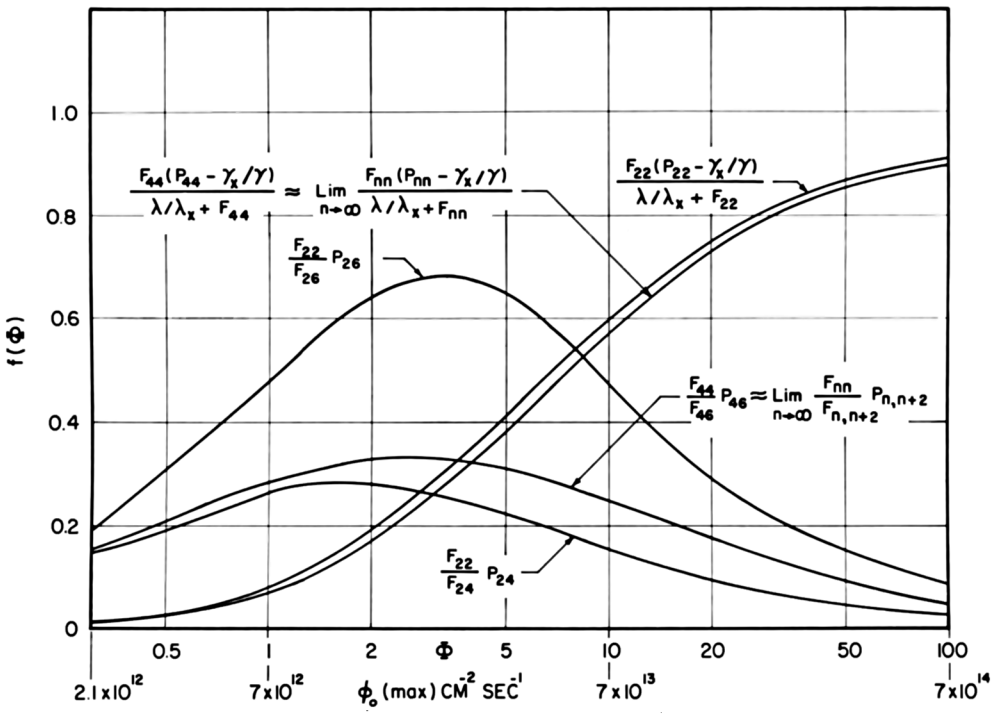

FIG. 2. The behavior of the functions $F_{nn}(P_{nn} - \gamma_x/\gamma)/(\lambda/\lambda_x + F_{nn})$ and $F_{nn}P_{nm}/F_{nm}$

TABLE I

APPROXIMATE CORRESPONDENCE BETWEEN H/M AND S_n

H/M:	31	35	41	50	70	99	140
S_2 :	1	0.8	0.6	0.4	0.2	0.1	0.05
S_4 :	5	4	3	2	1	0.5	0.25

answer this question, the equations of motion (22), (23), and (24) of the nth and mth modes were combined under the assumption that $F_{ij} = P_{ij} = 0$ except when $i = n$ or $i = m$ and $j = n$ or $j = m$. The resulting fourth order differential equation, which is too long to exhibit here, was subjected to a rather tedious examination in the light of the Hurwitz-Routh stablity criterion (7) under the condition that the nth mode is predicted to be marginally stable by the approximate criterion (25). For the reactor model used here, this examination yielded the following results. For $S_n < F_{nn}P_{nm}/F_{nm}$ the combined system is unstable, irrespectively of the stability of the mth mode. The behavior of the right hand side of this inequality as a function of flux level is shown in Fig. 2. For $S_n > F_{nn}P_{nm}/F_{nm}$ the combined system is stable if the mth mode is by itself sufficiently stable, otherwise it is unstable. Except for a very small region where $S_n \approx F_{nn}P_{nm}/F_{nm}$, in order that the mth mode be by itself "sufficiently stable" in this sense, the requirement

$$S_m > \frac{F_{mm}(P_{mm} - \gamma_X/\gamma)}{\lambda/\lambda_X + F_{mm}} \tag{28}$$

is necessary, but not sufficient. In other words, the value of S_m must be larger by some amount than that necessary for marginal stability as predicted by the approximate criterion (28). A necessary and sufficient condition simple enough to be useful was not found for this "sufficient stability" of the mth mode. The numerical computations discussed in the next section, however, indicate that the value of S_m does not have to be significantly greater than that required by condition (28).

For very large values of S_m, the equation of motion of the combined system becomes independent of S_m and the effect of modal interaction approaches a nonzero limit. This fact is quite significant. According to Eq. (22), an infinitely large S_m means that N_m, the mth mode of the flux distribution, is not allowed to vary. Nevertheless, it was found that interaction with the mth mode has a nonzero effect on the stability of the nth mode. The reason for this is that although the mth mode of the flux distribution is not allowed to vary, the mth mode of the xenon distribution will be forced into oscillation by variations in the nth mode of the flux dis-

tribution. In other words, even if the oscillations in the flux distribution are purely in a single mode, the oscillations in the xenon distribution will involve all the other modes. This result agrees with those reported by Pearce (*8*). This means that even if the magnitude of the fundamental mode of the flux distribution is held constant by some control system, in examining the stability of the third mode, interaction between it and the fundamental must be taken into account.

NUMERICAL RESULTS

Since the least stable higher mode is the second harmonic, the numerical calculations were centered on it. An exploration, by means of analog computer simulation, of the behavior of the system consisting of the second, fourth, and sixth harmonics coupled together indicated that the effect of the sixth harmonic on the second is negligible unless the reactor size is in excess of a few hundred migration lengths. Such large reactor sizes are not considered here because they are beyond the range of validity of the approximations used. Therefore, in further numerical computations, which were done on a digital computer, the system consisting of only the second and fourth modes was considered. Table II shows the values of the constants which were used in the calculations.

TABLE II

THE VALUES OF THE CONSTANTS USED IN THE NUMERICAL CALCULATIONS

σ_X	$= 3 \times 10^{-18}$ cm^2
λ_X	$= 2.1 \times 10^{-5}$ sec^{-1}
λ_I	$= 2.9 \times 10^{-5}$ sec^{-1}
γ_X	$= 0.003$
γ_I	$= 0.061$

For a given reactor composition the power level and the reactor size uniquely determine the values of S_2 and S_4, or alternately, the reactor power level and the value of S_2 determine the value of S_4. In the computations, however, the value of S_4 was varied in the full range $S_2 \leqq S_4 \leqq \infty$ (effectively). Although this led to some computations which may not be physically realizable, the results are quite interesting and do contribute to the understanding of the problem.

In the previous section, it was stated that in the region where $S_2 > F_{2,2}P_{2,4}/F_{2,4}$, interaction with the fourth mode will enhance stability provided the value of S_4 is sufficiently large. Figure 3 shows the results of the search for values of S_4 in this region such that the critical value of S_2 as predicted by the approximate stability criterion (25) is also the critical value for the combined system of the second and fourth modes. The plot shows ΔS_4:

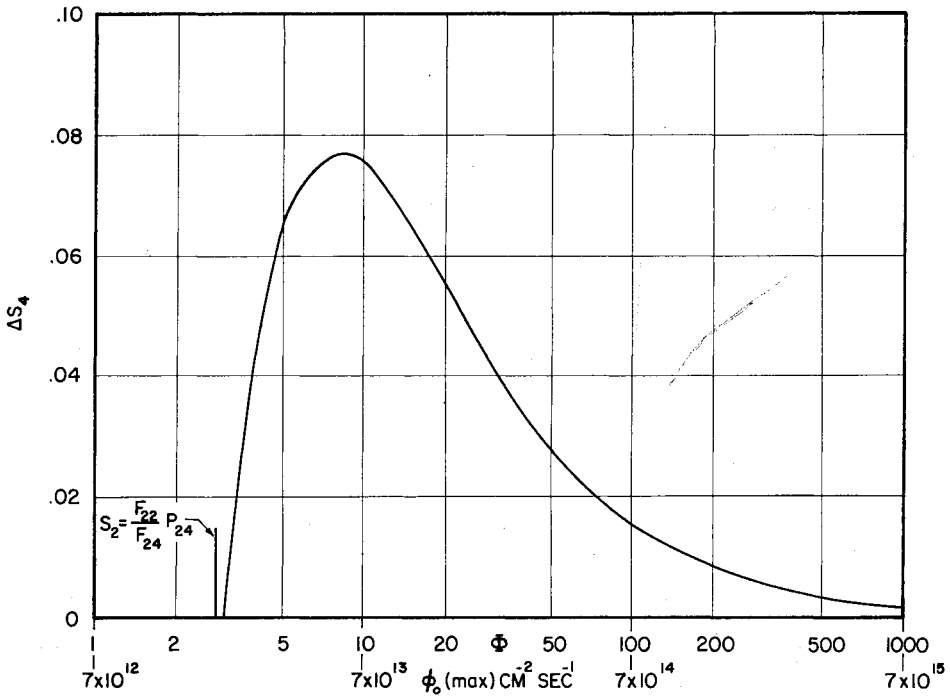

FIG. 3. The values of ΔS_4 for the condition $\Delta S_2 = 0$ in the region $S_2 > F_{2,2}P_{2,4}/F_{2,4}$

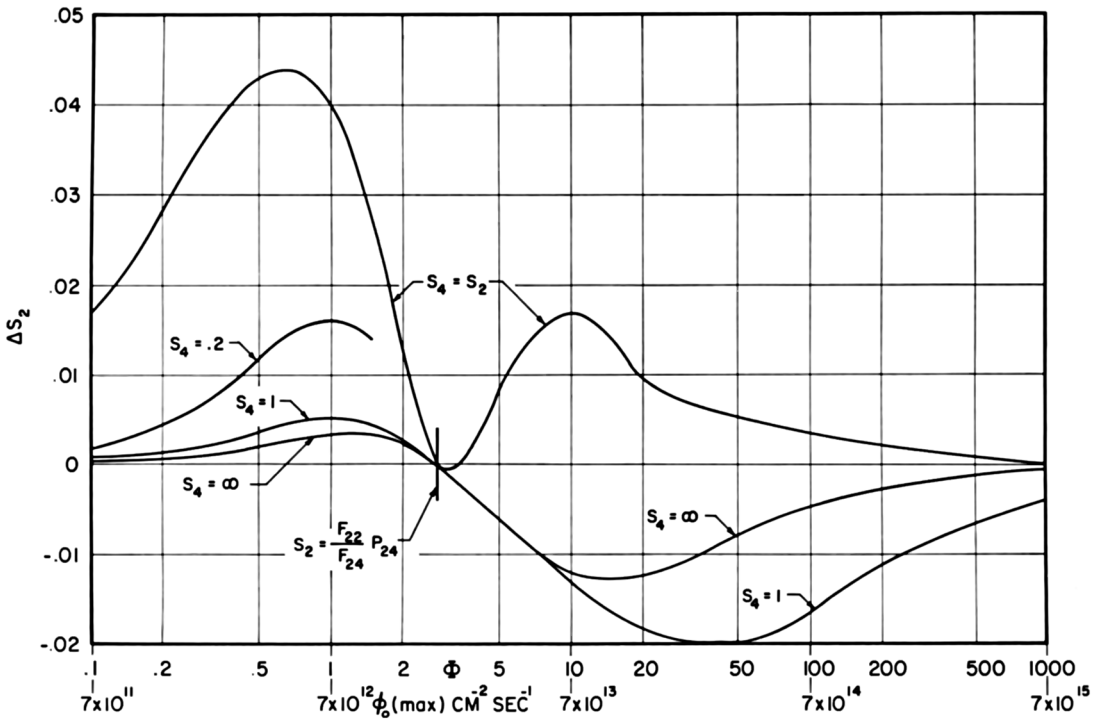

FIG. 4. The values of ΔS_2 as a function of S_4 and Φ

the difference between the values of S_4 found by this search and the critical values of S_4 as predicted by the approximate stability criterion. This difference is relatively small everywhere in this region. Table I shows that in this region the value of S_4 is considerably larger than the critical values found by the search described above. Therefore, in this region, if the second mode is predicted to be marginally stable by the approximate stability criterion, the combined system of the two modes considered here will be stable.

The remainder of the numerical calculations consisted of the search for values of S_2 for which the combined system is marginally stable. The flux level and the value of S_4 were varied over wide ranges. Figure 4 shows the computed values of ΔS_2 : the difference between the values of S_2 found by this search and the critical values of S_2 as predicted by the approximate stability criterion.

The results indicate that if the reactor dimensions are not very large, less than about 60 times the migration length for the numerical values used here, second mode instability will set in at a high flux level: above 10^{13} neutrons/cm^2/sec. Interaction of the second mode with the fourth in this case enhances stability. The actual critical value of S_2 is only slightly different from the critical value obtained when modal interaction is neglected.

If the reactor dimensions are large, 70 times the migration length or more, second mode instability sets in at flux levels below 10^{13} neutrons/cm^2/sec. Interaction with the fourth mode in this region detracts from stability. As the reactor dimensions are made larger, the difference between the actual critical value of S_2 and that predicted when modal interaction is neglected becomes quite large.

Thus the stability of a large reactor is seriously overestimated if modal interaction is neglected.

ACKNOWLEDGMENT

It is a pleasure to express the author's appreciation to Professor P. F. Zweifel, Nuclear Engineering Department, University of Michigan, for his interest and suggestions during the course of this study.

REFERENCES

1. S. KAPLAN, *Nuclear Sci. and Eng.* **9**, 357–361 (1961).
2. A. G. WARD, The problem of flux instability in large power reactors. CRRP-657 (1956).
3. D. RANDALL AND D. S. ST. JOHN, *Nucleonics* **16**, No. 3, 82–86 (1958).
4. K. MOCHIZUKI AND A. TAKEDA, *Nuclear Sci. and Eng.* **7**, 336–344 (1960).
5. A. M. WEINBERG AND E. P. WIGNER, "The Physical Theory of Neutron Chain Reactors." Univ. of Chicago Press, Chicago, 1958.
6. G. L. GYOREY, On the theory of xenon induced instabilities in neutron flux distribution. Ph.D. Thesis, The University of Michigan, Ann Arbor, 1960.
7. E. A. GUILLEMIN, "The Mathematics of Circuit Analysis." Wiley, New York, 1949.
8. R. M. PEARCE, *Nuclear Sci. and Eng.* **11**, 328–337 (1961).

NUCLEAR SCIENCE AND ENGINEERING: **13**, 345–354 (1962)

Comparison of Flux Ratio Calculations in Lattices by Integral Transport Theory

YUZO FUKAI

Nippon Atomic Industry Group Co., Ltd., 12, Yurakucho, 1-chome, Chiyoda-ku, Tokyo, Japan

Received January 3, 1962

In calculating a closely packed lattice, it is well known that one-velocity integral transport theory is the most useful method. Results are briefly presented for calculation of the ratio of moderator to fuel flux in a lattice, $\bar{\phi}_1/\bar{\phi}_0$, by first and second approximations which have been developed by Corngold. In order to compare these approximations with various other calculating methods, some approximate formulations of a penetrability factor are discussed.

After comparing the numerical results from the first and second approximations with the ones of Wachspress, Amouyal, Bengston, and the blackness method, the second approximation is considered to be the best. Consequently the values of the flux ratio in a lattice of fuel cylinders are calculated by using a unit cell method, and the second approximation in the case of a slab lattice which has a mean chord length equivalent to that of the actual lattice, and the results are compared with experiment.

NOMENCLATURE

a, b dimensions (thickness) of fuel and moderator in slab lattice, respectively, or radius of fuel and unit cell in lattice of fuel cylinders, respectively

f_0', f_1' self-shielding factor for fuel and moderator, respectively

G penetrability factor

G_∞ G in the case of $l_0 \to \infty$

G_0 G in the case of $l_1 \to \infty$

G_2 G derived from the second collision probability

G_d G derived from the diffusion approximation

l_0, l_1 chord length of fuel and moderator in units of the total mean free paths, respectively

$\mathbf{n}$ perpendicular to the fuel surface element, ds

P_{s0} $= \Sigma_{0s}/\Sigma_0$

P_0, P_1 first flight collision probability for fuel and moderator, respectively

P_0', P_1' probability that a neutron born in moderator and fuel will be absorbed before leaving the same region, respectively

S_{c0} total neutron source in moderator

S total fuel surface

$T, \tilde{T}, U, \tilde{U}, W$ factors used in the calculation of second approximation and shown in the Appendix

V_0, V_1 volume of fuel and moderator, respectively

β_0, β_1 probability that a neutron entering the fuel or moderator will be absorbed before leaving the same region, respectively. These correspond to the blackness

μ $\cos\theta$; θ is an angle between x-axis and neutron path in slab lattice

$\Sigma_0, \Sigma_{0s}, \Sigma_{0a}$ total, scattering, and absorption macroscopic cross sections of fuel, respectively

$\Sigma_1, \Sigma_{1s}, \Sigma_{1a}$ total, scattering, and absorption macroscopic cross sections of moderator, respectively

$\bar{\phi}_0, \bar{\phi}_1$ average neutron flux of fuel and moderator, respectively

$\psi_{00}, \psi_{02}, \phi_{00}, \phi_{02}$ total and second-order flux in fuel and moderator, respectively

Ω operator, but taken equal to Σ_{1s}/Σ_1 in this paper

$\boldsymbol{\Omega}$ vector of neutron path

I. INTRODUCTION

In calculating a ratio of moderator to fuel flux in lattices, we can use various methods: diffusion theory, P_N approximation, S_N method, discrete ordinates method, and integral transport theory.

Among these methods, integral transport theory is the most useful method in the case of a closely packed lattice, as Davison (*1*) has pointed out. And many calculating methods which could be classified as integral transport methods have already been suggested.

First, we calculate the ratio of moderator to fuel flux in a slab lattice, $\bar{\phi}_1/\bar{\phi}_0$, by the first and second approximations developed by Corngold, (*2*), because we consider it the best of the integral transport theory methods after a comparison of them in Section IV. In the case of a lattice of fuel cylinders, we can calculate the same by using the unit cell method of Takahashi (*3*). It is then necessary to reduce the error introduced by transformation of an actual cell boundary to cylindrical geometry, which is discussed in Section III. Finally, numerical results for the flux ratio in a lattice of fuel cylinders are presented.

II. AVERAGE FLUX RATIO FROM FIRST AND SECOND APPROXIMATIONS

Since the calculations for the ratio of moderator to fuel average flux in lattices by the first and second approximations are given in detail in BNL-669 (*4*), this work is only briefly described here.

The expression for the flux ratio in a slab lattice can be derived by assuming uniform and isotropic distributions of a neutron source only in the moderator region and using four-index coefficients which have been derived by Corngold (*2*). After the four-index coefficients are calculated, by using the notations shown in the Appendix, the first approximation results in simultaneous linear equations with respect to ψ_{00} and ϕ_{00},

$$\psi_{00} = P_{s0}\left(1 - \frac{G}{2\Sigma_0 a}\right)\psi_{c0} + \frac{G}{2\Sigma_0\,\Sigma_1 b}\,(\Sigma_1\Omega\phi_{00} + S_{0c})$$

$$\phi_{00} = P_{s0}\,\frac{G}{2\Sigma_1 a}\,\psi_{00} + \frac{1}{\Sigma_1}\left(1 - \frac{G}{2\Sigma_1 b}\right)(\Sigma_1\Omega\phi_{00} + S_{00}) \tag{1}$$

and the second approximation results in similar ones with respect to ψ_{00}, ϕ_{00}, ψ_{02}, and ϕ_{02}. Although Ω is an operator, $\Omega = \Sigma_{1s}/\Sigma_1$ can be used because of the assumption of isotropic scattering of neutrons by moderator atoms.

Since ψ_{00} and ϕ_{00} are the total integrated fluxes in the fuel and in moderator, respectively, the average neutron flux ratio is defined as

$$\frac{\bar{\phi}_1}{\bar{\phi}_0} = \frac{\phi_{00}/b}{\psi_{00}/a} \tag{2}$$

From Eq. (1) the flux ratio for the first approximation can be seen to be

$$\left(\frac{\bar{\phi}_1}{\bar{\phi}_0}\right)_1 = \frac{\Sigma_{0s}}{\Sigma_0} - \frac{\Sigma_{0a}\,a}{\Sigma_1 b} + \frac{2\Sigma_{0a}\,a}{G} \tag{3}$$

Similarly, the second approximation of the flux ratio is given as follows;

$$\left(\frac{\bar{\phi}_1}{\bar{\phi}_0}\right)_2 = \frac{\Sigma_{0s}}{\Sigma_0} - \frac{\Sigma_{0a}\,a}{\Sigma_1 b} + \frac{2\Sigma_{0a}\,a}{G - 10\Delta G} \tag{4}$$

where ΔG, is given by Eq. (5) below.

Consider the behavior of ΔG. Since absorption is generally much smaller than scattering in a moderator, $\Omega = 1$ is considered first. If $P_{s0} = 1$, then, from Eq. (5),

$$\Delta G = \tilde{T}^2/5\tilde{U} \tag{6}$$

On the other hand, if $P_{s0} = 0$,

$$\Delta G = \frac{\tilde{U}T^2 + U\tilde{T}^2 - 2T\tilde{T}W}{5(U\tilde{U} - W^2)} \tag{7}$$

For large $\Sigma_0 a$ and $\Sigma_1 b$, neglecting $(1/\Sigma_0 a)^2$, $(1/\Sigma_1 b)^2$ and E_n, in the case of $P_{s0} \to 0$,

$$\Delta G \to \frac{1}{10} - \frac{4}{5\Sigma_1 b}$$

in the case of $P_{s0} \to 1$,

$$\Delta G \to \frac{1}{10}$$

Since G approaches unity as both $\Sigma_0 a$ and $\Sigma_1 b$ become large, it is comparable to 10 ΔG. Therefore, in the case of a lattice with only weak moderator absorption, the value of the flux ratio for the first approximation is different from the one for the second approximation in the range of large $\Sigma_0 a$ and $\Sigma_1 b$.

For $\Omega = 0$, Eq. (5) gives

$$\Delta G = \frac{P_{s0}\,T^2/\Sigma_0\,a}{1 - P_{s0}(1 - 5U/\Sigma_0\,a)} \tag{8}$$

$$\Delta G = \frac{P_{s0}\,\dfrac{T^2}{\Sigma_0 a} + \Omega\,\dfrac{\tilde{T}^2}{\Sigma_1 b} - P_{s0}\,\Omega\left[\dfrac{T^2}{\Sigma_0 a}\left(1 - \dfrac{5\tilde{U}}{\Sigma_1 b}\right) + \dfrac{\tilde{T}^2}{\Sigma_1 b}\left(1 - \dfrac{5U}{\Sigma_0 a}\right) + 10\,\dfrac{T\tilde{T}W}{\Sigma_0 a\Sigma_1 b}\right]}{\left[1 - P_{s0}\left(1 - \dfrac{5U}{\Sigma_0 a}\right)\right]\left[1 - \Omega\left(1 - \dfrac{5\tilde{U}}{\Sigma_1 b}\right)\right] - P_{s0}\,\Omega\,\dfrac{25W^2}{\Sigma_0 a\Sigma_1 b}} \tag{5}$$

TABLE I

COMPARISON OF RESULTS FROM INTEGRAL TRANSPORT THEORY WITH RESULTS FROM P_N APPROXIMATION

Thick Slab

$\frac{\Sigma_{0a}}{\Sigma_0}$	$\Sigma_0 a$	$\Sigma_1 b$	Exact value[a]	Spherical harmonics[b]		Integral transport		Thin region	Amouyal–Theys
				P_3	P_5	1st	2nd		
0.1	2	2	1.2937	1.2784	1.2897	1.2497	1.2935	1.2513	1.2598
		5	1.4269	1.4200	1.4250	1.2863	1.4266	1.2864	1.4098
		10	1.6695	1.6645	1.6681	1.3057	1.6690	1.3057	1.6598
0.5	2	2	2.4161	2.3331	2.3905	2.2485	2.4149	2.2565	2.2470
		5	3.0894	3.0499	3.0757	2.4314	3.0873	2.4318	2.9970
		10	4.3051	4.2754	4.2946	2.2583	4.3019	2.5283	4.2470
0.9	2	2	3.4823	3.3206	3.4268	3.2473	3.4808	3.2617	3.1658
		5	4.7035	4.6226	4.6723	3.5766	4.6999	3.5772	4.5158
		10	6.8951	6.8326	6.8701	3.7509	6.8889	3.7509	6.7658
0.1	5	2	1.9986	1.9776	1.9926	1.7157	1.9959	1.7159	1.8493
		5	2.3117	2.3045	2.3094	1.8035	2.3098	1.8035	2.2243
		10	2.9103	2.9060	2.9091	1.8518	2.9087	1.8518	2.8493
0.25	5	2	3.3118	3.2470	3.2919	2.7893	3.3002	2.7897	3.0495
		5	4.1075	4.0816	4.0987	3.0088	4.0983	3.0088	3.9870
		10	5.6086	5.5913	5.6030	3.1294	5.6002	3.1294	5.5495
0.5	5	2	5.2544	5.0944	5.2015	4.5786	5.2304	4.5794	4.8622
		5	6.8737	6.8010	6.8471	5.0175	6.8526	5.0176	6.7372
		10	9.8857	9.8328	9.8668	5.2588	9.8656	5.2588	9.8622

[a] These values are calculated by J. Suich (*22*).
[b] Numerical results from BNL-655 (*5*).

If, in addition, $P_{s0} = 1$, then

$$\Delta G = \frac{T^2}{5U} \rightarrow \frac{1}{10} - \frac{4}{5\Sigma_0 a} \quad \text{(for large } \Sigma_0 a\text{)}$$

This case is equivalent to weak moderator absorption. But, if $P_{s0} \neq 1$,

$$\Delta G = \frac{P_{s0}}{4(1 - P_{s0})\Sigma_0 a} \quad \text{(for large } \Sigma_0 a\text{)}$$

Then, in the case of lower values of P_{s0} and Ω, the results of the first approximation approach those of the second approximation. This is true even for large $\Sigma_0 a$ and $\Sigma_1 b$, provided Ω is small enough.

The values of the flux ratio from both first and second approximations with $\Omega = 1$ are calculated by using the IBM 704 and shown in Tables I and II. It is clear that, for the thick slab case, the discrepancy between the results of the first and second approximations is large, and the values from the second approximation are in better agreement with the exact values than those from P_5 approximation, except for a few cases, but, for the thin slab case, both sets of results from the integral transport theory are in good agreement with the exact values at all points.

The first approximation is based on such a physical conception as keeping uniform flux distribution in both regions even after the neutron has collided with atoms of the moderator and fuel. Since such an assumption can be established for the case of small dimensions compared with the mean free path of the neutron, the first approximation for the thin slab case is in good agreement with the exact. However, for the thick slab which has large dimensions compared with the mean free path, the neutron suffers many collisions in both regions, and the consequent flux distributions do not become uniform. Then it is necessary, for the thick slab case, to use the second approximation which contains the P_2 term of the Legendre expansion with respect to the spatial variable of the flux distribution.

In the case of a lattice of fuel cylinders, equations similar to Corngold's equations with four-index coefficients can be derived by the unit cell method of Takahashi (*3*). For both cases of a lattice of fuel slabs and cylinders, the first approximation for the flux ratio is derived as follows,

$$\left(\frac{\bar{\phi}_1}{\bar{\phi}_0}\right)_1 = \frac{\Sigma_{0s}}{\Sigma_0} - \frac{\Sigma_{0a} V_0}{\Sigma_1 V_1} + \frac{4\Sigma_{0a} V_0}{SG} \qquad (9)$$

where, in the case of the slab lattice, the expression for G is given in the Appendix, and, in the case of

TABLE II

COMPARISON OF RESULTS FROM INTEGRAL TRANSPORT THEORY WITH RESULTS FROM P_N APPROXIMATION

Thin Slab

$\frac{\Sigma_{0a}}{\Sigma_0}$	$\Sigma_0 a$	$\Sigma_1 b$	Exact value[a]	Spherical harmonics[a]		Integral transport		Thin region	Amouyal–Theys
				P_3	P_5	1st	2nd		
0.1	0.25	0.5	1.0247	1.0093	1.0133	1.0240	1.0246	1.0324	1.0226
0.25			1.0616	1.0233	1.0332	1.0601	1.0615	1.0810	1.0564
0.5			1.1231	1.0465	1.0664	1.1201	1.1229	1.1620	1.1124
0.1	0.25	1.0	1.0292	1.0150	1.0201	1.0274	1.0291	1.0317	1.0257
0.25			1.0729	1.0374	1.0503	1.0685	1.0728	1.0791	1.0642
0.5			1.1456	1.0748	1.1005	1.1370	1.1456	1.1583	1.1280
0.1	0.5	0.5	1.0491	1.0243	1.0334	1.0377	1.0490	1.0592	1.0400
0.25			1.1225	1.0606	1.0833	1.1192	1.1223	1.1480	1.0995
0.5			1.2440	1.1209	1.1659	1.2383	1.2438	1.2960	1.1976
0.1	0.5	1.0	1.0546	1.0348	1.0445	1.0516	1.0546	1.0577	1.0463
0.25			1.1363	1.0869	1.1112	1.1290	1.1364	1.1443	1.1152
0.5			1.2719	1.1735	1.2217	1.2580	1.2721	1.2885	1.2289
0.1	1.0	0.5	1.1088	1.0692	1.0885	1.1032	1.1088	1.1154	1.0795
0.25			1.2698	1.1717	1.2191	1.2580	1.2698	1.2885	1.1965
0.5			1.5332	1.3386	1.4312	1.5159	1.5331	1.5770	1.3863
0.1	1.0	1.0	1.1129	1.0870	1.1032	1.1056	1.1130	1.1124	1.0920
0.25			1.2806	1.2162	1.2563	1.2640	1.2808	1.2810	1.2276
0.5			1.5563	1.4282	1.5070	1.5280	1.5566	1.5621	1.4488

[a] Numerical results from BNL-655 (*5*).

the cylindrical fuel lattice, G is given by

$$G = 1 - \frac{4}{\pi}\int_0^{\pi/2}\sum_{n=0}^{\infty}\{K_{i3}[2n(u+v)+2u] + K_{i3}[2n(u+v)+2v] - 2K_{i3}[2(n+1)(u+v)]\}\cos\phi\, d\phi \tag{10}$$

where,

$$u = \Sigma_0 a\cos\phi$$

$$v = \Sigma_1[b\,|\sqrt{1-(a^2/b^2)\sin\phi}\,| - a\cos\phi]$$

ϕ is the angle between a projective neutron path and the radius of the fuel at its surface.

III. APPROXIMATE FORMULA FOR G

The G-function (penetrability factor) can not be calculated analytically, but many approximate formulas for G have been suggested. In BNL-669, Wigner's and Roe's formula for G were discussed, and the former was adopted in numerical calculations. The equations for these approximations are

Wigner (*6*):
$$G_W = \frac{(4\Sigma_0 V_0/S)G_\infty}{(4\Sigma_0 V_0/S) + G_\infty} \tag{11}$$

Roe (*7*):
$$G_R = G_\infty\left[(1-G_\infty)\cdot\frac{\Sigma_0 V_0}{\Sigma_0 V_0 + \Sigma_1 V_1} + G_\infty G_0\right] \tag{12}$$

where

$$G_0 = \lim_{\Sigma_1 V_1\to\infty} G$$
$$G_\infty = \lim_{\Sigma_0 V_0\to\infty} G \tag{13}$$

G_∞ is the Dancoff correction. Roe has suggested Eq (12) as the approximate formula for G in the slab lattice, and extended his expression to the case of the cylindrical fuel lattice. But its extension can be concluded only in the case that neutron paths across all fuels and moderators are always equal. This condition can be established in the case of the slab lattice and the cylindrical fuel lattice converted to the equivalent unit cell.

Applying the following assumptions to a conceptional expression for a generalized lattice suggested by Rothenstein (*8*):

Condition I, the integral of the product of $e^{-\Sigma_0 R_{0n}}$ and/or $e^{-\Sigma_1 R_{1n}}$ equals the product of the integral of $e^{-\Sigma_0 R_{0n}}$ and/or $e^{-\Sigma_1 R_{1n}}$ with respect to unit fuel surface element, ds, and unit solid angle subtended by ds at dV_0, $d\Omega$,

Condition II, the averaged values of $e^{-\Sigma_0 R_{0n}}$ or $e^{-\Sigma_1 R_{1n}}$ are equal, where these averaged values are defined as

$$\langle e^{-\Sigma R}\rangle = \frac{\int\int(\mathbf{n}\cdot\boldsymbol{\Omega})\, ds\, d\Omega e^{-\Sigma R}}{\int\int(\mathbf{n}\cdot\boldsymbol{\Omega}) ds\, d\Omega}$$

and, R_{0n} and R_{1n} are the lengths of neutron path across any fuel and any moderator region between any two fuels, respectively, then, the other approximate expression for G has been obtained (*9*), namely,

$$G_{WN} = \frac{G_0 G_\infty}{G_0 + G_\infty - G_0 G_\infty} \qquad (14)$$

It should be noted that Condition II can be applied only to the G of the slab lattice and the cylindrical fuel lattice derived from the unit cell method, but not to the actual lattice of fuel cylinders.

In 1958, Wachspress (*10*) also suggested the same equation as Eq. (14), from a different point of view, for the case of a slab lattice. In his conception, the expression for the probability that a neutron which has escaped from a moderator region is scattered in any other moderator region is derived from the transmission probabilities of the fuel and the moderator, calculated under the assumption that the thickness of one region is infinite when the transmission probability for the other region is calculated. The above-cited Condition I is included in Wachspress' derivation of his collision probability. Accordingly, Eq. (14) is called Wachspress–Nordheim's formula (W. N. approximation) here.

Comparing the expressions for G_W, G_R, and G_{WN}, the following conclusions can be drawn,

1. G_W is the simplest expression, and, by using this expression, Eq. (9) can be changed to a simpler one; namely,

$$\left(\frac{{}_1\bar{\phi}}{\bar{\phi}_0}\right)_W = 1 - \frac{\Sigma_{0a} V_0}{\Sigma_1 V_1} + \frac{4\Sigma_{0a} V_0}{S G_\infty} \qquad (15)$$

2. If $\Sigma_0 a$ and $\Sigma_1 b$ are interchanged in the case of slab lattice, the value of the exact G is invariant. Only G_{WN} show this invariance.

3. If $\Sigma_0 a$ and $\Sigma_1 b$ become extremely small in the case of slab lattice, G_{WN} is not coincident with the exact G, as Nordheim (*9*) has pointed out.

4. It is clear from Table III that G_{WN} is the best, except for the case of extremely small $\Sigma_0 a$ and $\Sigma_1 b$. Though G_{WN} has two disadvantages (1 and 3), we adopt it as a better approximate formula of G from numerical results shown in Table III.

In the cylindrical fuel lattice, if the expression for G derived from the unit cell method was used, the results of the flux ratio would have some error due to cylindricalizing lattice cells, which would be important in the case of a H_2O lattice, as Chernick pointed out. We use the W. N. approximation which has the relatively exact equation of the Dancoff correction as G_∞ instead of the one by the unit cell method. By such treatment, its error may be partly diminished.

TABLE III

COMPARISON OF VARIOUS APPROXIMATIONS FOR G

Slab lattice

$\Sigma_0 a$	Exact	Wigner approximation		Roe approximation		W. N. approximation	
			$\Sigma_1 b = 0.1$				
0.1	0.09583	0.09112	(4.92)[a]	0.07439	(22.38)	0.09136	(4.67)
0.2	0.12564	0.11803	(6.06)	0.10123	(19.43)	0.11975	(4.69)
0.4	0.14771	0.13845	(6.27)	0.12512	(15.30)	0.14218	(3.75)
0.6	0.15615	0.14692	(5.92)	0.13677	(12.42)	0.15165	(2.89)
0.8	0.16033	0.15156	(5.47)	0.14384	(10.29)	0.15676	(2.23)
1.0	0.16270	0.15449	(5.05)	0.14860	(8.67)	0.15990	(1.73)
1.5	0.16545	0.15857	(4.16)	0.15553	(6.00)	0.16391	(0.94)
2	0.16650	0.16069	(3.49)	0.15909	(4.46)	0.16564	(0.52)
4	0.16735	0.16400	(2.01)	0.16386	(2.09)	0.16726	(0.06)
6	0.16741	0.16512	(1.37)	0.16512	(1.37)	0.16740	(0.00)
8	0.16742	0.16569	(1.04)	0.16570	(1.03)	0.16742	(0.00)
10	0.16742	0.16603	(0.84)	0.16604	(0.83)	0.16742	(0.00)
			$\Sigma_1 b = 10.0$				
0.1	0.16742	0.16667	(0.45)	0.16742	(0.00)	0.16742	(0.00)
0.2	0.29611	0.28571	(3.52)	0.29611	(0.00)	0.29611	(0.00)
0.4	0.48543	0.44444	(8.45)	0.48543	(0.00)	0.48543	(0.00)
0.6	0.61690	0.54545	(11.59)	0.61689	(0.00)	0.61691	(0.00)
0.8	0.71135	0.61538	(13.50)	0.71133	(0.00)	0.71134	(0.00)
1.0	0.78061	0.66667	(14.60)	0.78059	(0.00)	0.78060	(0.00)
1.5	0.88652	0.75000	(15.40)	0.88650	(0.00)	0.88652	(0.00)
2	0.93973	0.80000	(14.87)	0.93971	(0.00)	0.93972	(0.00)
4	0.99447	0.88889	(10.62)	0.99445	(0.00)	0.99446	(0.00)
6	0.99942	0.92308	(7.64)	0.99940	(0.00)	0.99941	(0.00)
8	0.99993	0.94118	(5.88)	0.99991	(0.00)	0.99992	(0.00)
10	0.99999	0.95238	(4.77)	0.99998	(0.00)	0.99998	(0.00)

[a] The values in the parenthesis show a relative error in %;

$$\epsilon = \frac{G_{approx} - G_{exact}}{G_{exact}} \times 100\ \%$$

These values are all negative.

IV. COMPARISON WITH VARIOUS OTHER METHODS

The various other methods using the integral transport theory are compared with the first and second approximations represented in this paper.

A. THIN REGION THEORY

According to this method developed by Wachspress (*10*), we can derive the expression for the flux ratio in the slab lattice for the case that a neutron source in unit volume exists in a moderator region uniformly and isotropically.

TABLE IV
COMPARISON OF GREEBLER'S AND PUECHL'S METHODS

Slab lattice							
$\frac{\Sigma_{0a}}{\Sigma_0}$	$\Sigma_0 a$	$\Sigma_1 b$	Greebler	Puechl	1st approximation	Exact	P_3 approximation
0.1	0.25	0.5	1.0252	1.0426	1.0240	1.0247	1.0093
0.25	0.25	1.0	1.0639	1.1065	1.0685	1.0729	1.0374
0.5	0.5	0.5	1.2704	1.3980	1.2383	1.2440	1.1209
0.1	0.5	1.0	1.0509	1.0796	1.0516	1.0546	1.0348
0.25	1.0	0.5	1.2706	1.3905	1.2580	1.2698	1.1717
0.5	1.0	1.0	1.5820	1.7810	1.5280	1.5563	1.4282

Comparing G_0 and G_∞ with self-shielding factors which are defined by him, f_0' and f_1', $G_0 = 2\Sigma_0 a f_0'$ and $G_\infty = 2\Sigma_1 b f_1'$ are obtained. Therefore, Wachspress' expression for the flux ratio can be derived as follows,

$$\frac{\bar{\phi}_1}{\bar{\phi}_0} = \frac{\Sigma_{0s}}{\Sigma_0} - \frac{\Sigma_{0a}\, a}{\Sigma_1 b} + 2\,\Sigma_{0a}\, a \left(\frac{1}{G_0} + \frac{1}{G_\infty} - 1\right) \quad (16)$$

Equation (16) is equivalent to the expression Eq. (3) where G in Eq. (3) is replaced by the W. N. approximation. It is clear from Tables I and II that results by this method are in good agreement with the ones given by the first approximation for the thick slab case, but, for the thin slab case, these results are not in agreement with those, as expected from Table III.

(B) HURWITZ–WACHSPRESS' METHOD

The treatment of Hurwitz was introduced at the 1958 Geneva Conference by Stewart and Zweifel (*11*). Since P_1 is a first flight collision probability for a moderator in the slab lattice, from the relation between $(1 - P_1)$ and G, the expression for the flux ratio is

$$\frac{\bar{\phi}_1}{\bar{\phi}_0} = -\frac{\Sigma_{0a}\, a}{\Sigma_1 b} + \frac{2\Sigma_{0a}\, a}{G} \quad (17)$$

Equation (17) is equivalent to Eq. (3) for the case of $\Sigma_{0s} = 0$. And Wachspress (*11*) has calculated Eq. (17) by using the W. N. approximation instead of the exact G, and compared it with Eq. (16).

(C) VARIATIONAL METHOD

From a variational expression of the integral transport theory for each region, the same equation as the first approximation is derived, by using a constant trial function for each region. Bohl *et al.* (*12*) have obtained the expression for the flux ratio in the slab lattice, and Bohl (*11*) for the cylindrical fuel lattice. Therefore, the variational method in the case of the slab lattice is equal to the first approximation, Eq. (3). But, in the cylindrical fuel lattice, whereas we use the equation calculated by the unit cell method for G, Bohl has suggested the one derived from the first flight collision probability, P_0, represented in the following equation,

$$P_0 = P_{0s}' + \sum_i P(r_i) \quad (18)$$

where P_{0s}' is P_0 for the case of a single fuel and $P(r_i)$ is the contribution from the other fuel which surrounds its single fuel.

(D) BLACKNESS THEORY

The derivation of the flux ratio by using blackness, β, has been suggested by many people (*13*, *14*, *17*). In this method, the flux ratio is given as a reciprocal of the self-shielding factor, (here the self-shielding factor is different from the one defined by Wachspress, f', without scattering), namely,

$$\frac{\bar{\phi}_1}{\bar{\phi}_0} = \frac{\phi_\infty}{\bar{\phi}_0} = \frac{4\Sigma_{0a}\, V_0}{S\beta} \quad (19)$$

According to the result of the multiple scattering method which Stuart (*15*) has derived from the variational expression by using a constant trial function, Puechl (*14*) has found

$$\beta = \frac{\Sigma_{0a}\, G_0}{\Sigma_{0a} + (\Sigma_{0s}/\Sigma_0)\,(SG_0/4V_0)} \quad (20)$$

and Greebler *et al.* (*16*) have used the following approximate equation for β instead of Eq. (20),

$$\beta \doteqdot 1 - e^{-4\Sigma_{0a} V_0/S} \quad (21)$$

Comparison of the numerical results of Greebler and Puechl is shown in Table IV. It is clear from this table that the results of Greebler are in fairly good agreement with the exact one in spite of a rough approximation for β such as Eq. (21). The reason that the results calculated using Eq. (20) are always larger than those using any other methods is due to recovering the depressed flux in the moderator by the neighboring fuel because the distance between neighboring fuels becomes infinite.

In the slab lattice, Maynard (*17*) has suggested a double blackness theory for calculation of the flux ratio. In the case of Maynard's zeroth moment, DB-0 approximation, we get the same equation for the flux ratio as the Wachspress' equation, Eq. (16). In the case of the next higher order approximation, DB-1 approximations, its derived results would be unequal to the second approximation, because the incident flux is proportional to μ^n and the transmis-

sion and reflecting probabilities are calculated independently for each region.

(E) Amouyal's Method

By using a collision probability calculated by the integral transport theory in the fuel region and the diffusion theory in the moderator region, the flux ratio in a cylindrical fuel lattice can be derived by Amouyal *et al.* (*18*). Theys (*19*) has extended this method to a slab lattice.

According to Amouyal, the relations between β and $(1 - P')$ are

$$\beta_1 = \frac{4\Sigma_{1a} V_1}{S}(1 - P_1') \quad \text{in the moderator}$$

$$\beta_0 = \frac{4\Sigma_{0a} V_0}{S}(1 - P_0') \quad \text{in the fuel}$$

If P_0' is put on a first collision probability for fuel, the expression for β_0 becomes the same equation as Eq. (20). Although Amouyal has derived P_1' directly from diffusion theory as follows,

$$P_1' = \Sigma_{1a} \int_{V_1} \frac{\phi(r)\, dV}{S_{00}}$$

with $\phi(r)$ calculated from solving the diffusion equation for the moderator region, the following equation for G_d which is simulated to Eq. (20) is used here,

$$1 - P_1' = \frac{SG_d}{4\Sigma_1 V_1}\left(\frac{\Sigma_{1a}}{\Sigma_1} + \frac{\Sigma_{1s}}{\Sigma_1}\frac{SG_d}{4\Sigma_1 V_1}\right)^{-1}$$

in order to compare his method with the others. Then Amouyal's expression for the flux ratio is

$$\frac{\bar{\phi}_1}{\bar{\phi}_0} = \frac{\Sigma_{0s}}{\Sigma_0} - \frac{\Sigma_{0a} V_0}{\Sigma_1 V_1} + \frac{4\Sigma_{0a} V_0}{S}\left(\frac{1}{G_0} + \frac{1}{G_\infty} - 1\right) \quad (22)$$

Further, Amouyal has replaced G_0 with G_2 which is derived from the second collision probability in order that the flux distribution within the fuel is more exactly derived.

Therefore, Amouyal's expression for the flux ratio is

$$\frac{\bar{\phi}_1}{\bar{\phi}_0} = \frac{\Sigma_{0s}}{\Sigma_0} - \frac{\Sigma_{0a} V_0}{\Sigma_1 V_1} + \frac{4\Sigma_{0a} V_0}{S}\left(\frac{1}{G_2} + \frac{1}{G_d} - 1\right) \quad (23)$$

This expression contains the error due to the effect of cylindricalizing, but it would be less as a result of using the diffusion equation for the moderator region of the unit cell, if V_1 was larger.

In conclusion, Amouyal's method is equivalent to Eq. (9), in which G takes the place of the W. N. approximation that consists of G_2 derived from second collision considerations and G_d derived from the diffusion theory. It is clear from Tables I and II that such treatment for using the more exact G_2 and the G_d based on the diffusion theory is more effective, in the case of a relatively larger dimension of lattice, but, in the case of a closely packed lattice, Amouyal's method is not so suitable as a result of using the diffusion theory for the moderator region and assuming isotropic current flow for the boundary condition.

TABLE V

Comparison of Bengston's and Amouyal–Theys Methods

($\Sigma_{0s} = 0$ and $\Sigma_{1a} = 0$)

$\Sigma_0\, a$	$\Sigma_1\, b$	Bengston	A–Theys	1st approximation	2nd approximation
0.25	0.5	1.2417	1.2235	1.2403	1.2455
	1.0	1.2805	1.2548	1.2740	1.2909
0.5	0.5	1.4790	1.3910	1.4767	1.4842
	1.0	1.5272	1.4535	1.5159	1.5414
1.0	0.5	2.0360	1.7521	2.0319	2.0439
	1.0	2.0762	1.8771	2.0560	2.0962
2	2	3.6734	3.3871	3.4970	3.7414
	5	4.9700	4.8871	3.8629	5.0980
	10	7.3800	7.3871	4.0565	7.5310
5	2	8.5877	7.8450	8.1572	8.7387
	5	11.764	11.595	9.0351	12.034
	10	17.770	17.845	9.5176	18.077

(F) Bengston's Method

In a slab lattice, Bengston (*20*) has obtained an expression for the flux ratio from solving the integral transport equation for the fuel and the diffusion equations without absorption of the moderator, by using the Serber–Wilson method as the boundary condition. Since the relation between J_0, K_1, and J_2 given in Bengston's paper and G or $\tilde{T}$ are given as follows,

$$4J_0 = \lim_{\Sigma_0 \to \Sigma_{0a}, \Sigma_1 \to \Sigma_{1s}} G \equiv G'$$

$$2J_0 - \frac{12K_1}{\Sigma_{1s} b} + \frac{24J_2}{(\Sigma_{1s} b)^2} = \lim_{\Sigma_0 \to \Sigma_{0a}, \Sigma_1 \to \Sigma_{1s}} \tilde{T} \equiv \tilde{T}'$$

the flux ratio, that is, a reciprocal of R mentioned in his paper, is

$$\frac{\bar{\phi}_1}{\bar{\phi}_0} \equiv \frac{1}{R} = -\frac{\Sigma_{0a}\, a}{\Sigma_{1s}\, b} + \frac{2\Sigma_{0a}\, a}{G' - A} \quad (24)$$

where

$$A = \frac{G'\,\tilde{T}'}{\tilde{T}' + (4/\Sigma_{1s}\, b)} \quad (25)$$

If we put $\Omega = 1$ and $P_{s0} = 0$, the expression for

TABLE VI

COMPARISON OF VARIOUS METHODS

Name	Proposer	Class	Appl.	Expression for $\bar{\phi}_1/\bar{\phi}_0$	Relation of this method			
					Σ_{0s}	Σ_{1a}	V_1	G
1st approx.		T	S.C.	$\frac{\Sigma_{0s}}{\Sigma_0} - \frac{\Sigma_{0a}V_0}{\Sigma_1 V_1} + \frac{4\Sigma_{0a}V_0}{GS}$				In case of C, use of W.N. approximation
2nd approx.		T	S	$\frac{\Sigma_{0s}}{\Sigma_0} - \frac{\Sigma_{0a}V_0}{\Sigma_1 V_1} + \frac{4\Sigma_{0a}V_0}{S(G - 10\Delta G)}$				ΔG is the function of $\Sigma_0 V_0$ etc.
Thin region	Wachspress (*10*)	T	S	$\frac{\Sigma_{0s}}{\Sigma_0} - \frac{\Sigma_{0a}V_0}{\Sigma_1 V_1} + \frac{4\Sigma_{0a}V_0}{S}\left(\frac{1}{G_0} + \frac{1}{G_\infty} - 1\right)$				W.N. approximation
H & W	Hurwitz (*13*) Wachspress (*10*)	T	S	$-\frac{\Sigma_{0a}V_0}{\Sigma_1 V_1} + \frac{4\Sigma_{0a}V_0}{SG'}$; $G' = G\|_{\Sigma_{0s}\to 0}$	0			H: Exact G W: W.N. approximation
Vari. −I	Bohl *et al.* (*14*)	T	S	Same as 1st approximation				
Vari. −II	Bohl (*13*)	T	C	Same as 1st approximation				G is derived from $(1 - P_0)_s$ plus $\Sigma P(r_i)$
Black. −I	Puechl (*16*), etc.	T	S.C.	$\frac{\Sigma_{0s}}{\Sigma_0} + \frac{4\Sigma_{0a}V_0}{SG_0}$			∞	
Black. −II	Greebler (*18*)	T	S.C.	$\frac{4\Sigma_{0a}V_0}{S\beta}$; $\beta = 1 - e^{-4\Sigma_{0a}V_0/S}$			∞	G is included in β
Dou. Black.	Maynard (*19*)	T	S	DB—0; Same as thin region method DB—1; Unequal to 2nd approximation				W.N. approximation
Amouyal	Amouyal (*20*) Theys (*21*)	T-D	S.C.	$\frac{\Sigma_{0s}}{\Sigma_0} - \frac{\Sigma_{0a}V_0}{\Sigma_1 V_1} + \frac{4\Sigma_{0a}V_0}{S}\left(\frac{1}{G_2} + \frac{1}{G_d} - 1\right)$				G_2 is based on second collison G_d from diffusion
Bengston	Bengston (*22*)	T-D	S	$-\frac{\Sigma_{0a}V_0}{\Sigma_{1s}V_1} + \frac{4\Sigma_{0a}V_0}{S(G' - A)}$; $A = \frac{G'\tilde{T}'}{\tilde{T}' + (4/\Sigma_{1s}V_1)}$	0	0		

T: Transport theory; D: Diffusion theory; S: Slab lattice; C: Cylinder lattice.

ΔG becomes Eq. (6). Then Eq. (25) corresponds to 10 ΔG, where ΔG is given by Eq. (6).

Therefore, Bengston's equation is similar to the limited case of Eq. (4), as scattering of fuel and absorption of the moderator are neglected. It is shown in Table V that this method is in good agreement with the second approximation.

(G) SUMMARY OF COMPARISON OF VARIOUS METHODS

A summary of the above-discussed comparison of various methods is shown in Table VI. In this table, the meaning of classification is whether a method is based on the transport or diffusion theory, and the column of application shows whether its method applies to the slab lattice or the cylindrical fuel lattice.

In conclusion, the following items can be pointed out from comparison of these calculating methods for the flux ratio;

(a) Regarding the methods based on the flux distribution due to the second collision of neutron only in fuel, the relation between these methods and

the second approximation in the case of $\Sigma_1 b \to \infty$ is not yet clear. For example, the limiting equation of $(G - 10\ \Delta G)$ in the case when $\Sigma_1 b \to \infty$ does not coincide with Theys' more exact equation for the fuel region, G_2 .

(b) Although the author has derived the exact expression for the first flight collision probability for the actual lattice, the effect of transformation to cylindrical geometry for a closely packed lattice is not yet perfectly considered since its derived result is complicated.

(c) The reason that the expression corresponding to G in Amouyal's, Wachspress,' and the DB-0 method becomes the same as the W. N. approximation is due to using the neutron current integrated with respect to μ for the equation of neutron balance, which is the same as the assumption that the current flow into or out of fuel or moderator region is always isotropic. Descrepancy between the exact and the W. N. approximate value in the case of smaller $\Sigma_0 a$ and $\Sigma_1 b$ is introduced by such assumption. It is then introduced by assuming for the isotropic current flow at the boundary that the results by Amouyal's method are slightly different from the ones by Bengston's, as shown in Table V.

(d) Since the second approximation represented in this paper is a method which is based on the second collision of a neutron in both regions of lattice, and solved by the exact boundary condition, it is considered to be the best of the other methods.

V. CALCULATION OF FLUX RATIO FOR CYLINDRICAL FUEL LATTICE

We try to compare experimental values of the flux ratio with calculated ones by using a corrected second approximation, i.e.,

$$(G - 10\ \Delta G)_{\text{cyl.}} = (G - 10\ \Delta G)_{\text{slab}} \times (G_{\text{cyl.}}/G_{\text{slab}})$$

where $(G - 10\ \Delta G)_{\text{slab}}$ and G_{slab} are calculated in the case of the slab lattice which has a mean chord length equivalent to the actual lattice of fuel cylinders, and $G_{\text{cyl.}}$ is calculated by using the W. N. approximation instead of the exact G and the equation for G_∞ suggested by the author (*21*).

It is important to discuss the input data for calculation of the cross section etc., when a calculated value is compared with an experimental one, because the experimental results are dependent on the neutron spectrum in lattice. Namely, in order to judge an accuracy for calculation, it must be clear whether the descrepancy is owing to the calculating method for the neutron spectrum or the flux ratio itself. Table VII shows a comparison of the calculated results with the experimental ones in BNL and WAPD H_2O moderated lattices which were compiled by Chernick (*5*). We calculated these values by assuming a mixture of Al fuel cladding in the moderator region, the use of the transport cross section of H_2O instead of the total one, and the input data averaged by the Wilkins neutron spectrum. Although the input cross section based on the Wilkins neutron spectrum is used, it is clear from Table VII that the agreement of calculation with experiment is not so bad in both cases. However, since we do not have other appropriate results for the flux ratio in monoenergy for judging the accuracy of the calculating method for the flux ratio, any exact conclusion can not be drawn from the table.

TABLE VII

FLUX RATIOS FOR H_2O–URANIUM ROD LATTICE

(Rod diameter = 0.6 in.)

$\%U^{235}$ enrich.	$\frac{V_1}{V_0}$	$\bar{\phi}_1/\bar{\phi}_0$			l_0	l_1
		Exp.[a]	1st approx.	2nd approx.		
1.0	1	1.278	1.288	1.363	1.13	3.00
	1.5	1.321	1.298	1.388	1.14	4.74
	2	1.356	1.312	1.434	1.15	6.49
	3	1.448	1.335	1.523	1.16	10.0
	4	1.519	1.349	1.625	1.16	13.6
1.15	1	1.270	1.312	1.385	1.17	3.00
	1.5	1.289	1.329	1.423	1.19	4.74
	2	1.383 (1.426)	1.344	1.473	1.20	6.49
	3	1.449 (1.436)	1.368	1.589	1.21	10.0
	4	1.515	1.385	1.695	1.22	13.6
1.3	1	1.285	1.342	1.427	1.22	3.00
	1.5	1.354 (1.386)	1.358	1.461	1.24	4.74
	2	1.427 (1.454)	1.375	1.534	1.25	6.49
	3	1.482 (1.491)	1.404	1.641	1.27	10.0
	4	1.582	1.422	1.774	1.28	13.6

[a] Experimental values are from BNL's experiment but the values in the parenthesis come from ohat of WAPD (*5*).

APPENDIX. FACTORS USED IN THE CALCULATIONS

The expressions for G, T, U, and W which are used in this paper are as follows;

$$G(x,y) = 2\int_0^1 d\mu\mu \frac{(1 - \Gamma_0)(1 - \Gamma_1)}{1 - \Gamma_0\Gamma_1} \qquad \text{(A.1)}$$

$$T(x,y) = \int_0^1 d\mu\mu \frac{1-\Gamma_1}{1-\Gamma_0\Gamma_1}\left\{\left[1+\frac{12\mu^2}{x^2}\right]\cdot(1-\Gamma_0) - \frac{6\mu}{x}(1+\Gamma_0)\right\} \tag{A.2}$$

$$U(x,y) = \int_0^1 \frac{d\mu\mu}{1-\Gamma_0\Gamma_1}\left\{\left[1+\frac{12\mu^2}{x^2}\right]^2\cdot(1-\Gamma_0)(1-\Gamma_1) - \left(\frac{12\mu}{x} + \frac{144\mu^3}{x^3}\right)(\Gamma_0-\Gamma_1) - \frac{24\mu^2}{x^2}[1+\Gamma_0\Gamma_1+2(\Gamma_0+\Gamma_1)]\right\} \tag{A.3}$$

$$W(x,y) = \int_0^1 \frac{d\mu\mu}{1-\Gamma_0\Gamma_1}\left[\left(1+\frac{12\mu^2}{x^2}\right)\cdot(1-\Gamma_0) - \frac{6\mu}{x}(1+\Gamma_0)\right]\cdot\left[\left(1+\frac{12\mu^2}{y^2}\right)(1-\Gamma_1) - \frac{6\mu}{y}(1+\Gamma_1)\right] \tag{A.4}$$

$$\tilde{T}(x,y) = T(y,x) \quad \text{and} \quad \tilde{U}(x,y) = U(y,x) \tag{A.5}$$

where

$$\Gamma_0 = e^{-x/\mu} \quad \text{and} \quad \Gamma_1 = e^{-y/\mu} \tag{A.6}$$

The second-order approximation of Corngold in BNL-445 does not contain the factor of $W(x, y)$.

ACKNOWLEDGMENTS

The author wishes to express his appreciation for useful suggestions by J. Chernick, N. Corngold, M. M. Levine, and research members of Nippon Atomic Industry Group Co., Ltd.

REFERENCES

1. B. DAVISON, *Can. J. Phys.* **36,** 784 (1958).
2. N. CORNGOLD, BNL-445 (T-93) (March 1956); *J. Nuclear Energy* **4,** 293 (1957).
3. H. TAKAHASHI, *J. Nuclear Energy* **12A,** 26 (1960).
4. Y. FUKAI, BNL-669 (T-222) (May 1961).
5. J. CHERNICK, BNL-622 (T-189) (August 1960).
6. J. CHERNICK AND R. VERNON, *Nuclear Sci. and Eng.* **4,** 649 (1958).
7. G. M. ROE, KAPL-1241 (October 15, 1954).
8. W. ROTHENSTEIN, BNL-563 (T-151) (June 1959).
9. L. W. NORDHEIM, "Proceedings of Symposia in Applied Mathematics," Vol. XI, p. 58. American Mathematical Society, Providence, R. I., 1961.
10. E. L. WACHSPRESS, *Nuclear Sci. and Eng.* **3,** 186 (1958).
11. J. C. STEWART AND P. F. ZWEIFEL, *Proc. Conf. Peaceful Uses Atomic Energy, Geneva,* p/631 (1958).
12. L. S. BOHL, J. C. STEWART, AND N. C. FRANCIS, *Nuclear Sci. and Eng.* **4,** 257 (1958).
13. S. A. KUSHNERIUK, CRT-712 (June 1957).
14. K. H. PUECHL, *Nuclear Sci. and Eng.* **9,** 241 (1961).
15. G. W. STUART, *Nuclear Sci. and Eng.* **6,** 617 (1957).
16. P. GREEBLER, W. HARKER, AND J. HARIMAN, *Nuclear Sci. and Eng.* **6,** 129 (1959).
17. G. W. MAYNARD, *Nuclear Sci. and Eng.* **6,** 174 (1959).
18. A. AMOUYAL, P. BENOIST, AND J. HOROWITZ, *J. Nuclear Energy* **6,** 79 (1957).
19. M. H. THEYS, *Nuclear Sci. and Eng.* **7,** 58 (1960).
20. J. BENGSTON, *Nuclear Sci. and Eng.* **3,** 71 (1958).
21. Y. FUKAI, *Nuclear Sci. and Eng.* **9,** 370 (1960).
22. J. SUICH, private communication (February 1962).

NUCLEAR SCIENCE AND ENGINEERING: **13**, 355-365 (1962)

Fast Reactor Rocket Engines—Criticality*

RALPH COOPER

Los Alamos Scientific Laboratory, University of California, Los Alamos, New Mexico

Critical sizes are determined for a variety of fast assemblies appropriate for nuclear rocket reactors. These are based on cores of UO_2-W cermets or UC-metal carbide solid solutions reflected by beryllium. Rocket reactors weighing as little as 200 lb are possible, and, in larger sizes, either high power density or high exit gas temperature can be achieved. The fast spectrum allows the use of the most refractory materials (such as HfC) in bulk to obtain high performance. Use of U^{233} in place of U^{235} can lead to substantial improvements in reactor weight, specific power, and/or temperature capability at the cost of the radiation associated with U^{233}. The core sizes are generally quite small, which is valuable where shielding may be significant. Nuclear aspects, including control, uranium investment, power distribution, and reflector materials, are briefly discussed.

INTRODUCTION

Although the fact that fast spectra could lead to the development of small reactors for nuclear rocket engines was observed as early as 1949 (*1*), no comprehensive and quantitative study of this possibility has appeared. In this paper we present some results of such a study, emphasizing the criticality aspects which are reported in greater detail in ref. *2*. Subsequent work will deal with heat transfer, materials, applications, etc.

The application of direct cycle nuclear heat exchangers to space propulsion puts a premium on low reactor weight, high power density, and very high temperature (>1500°C) capability. We shall show that fast reactors can meet these requirements over a wide range of interest, particularly for lightweight engines with thrusts of the order of 10,000 to 100,000 lb and for heavier engines with very high melting fuel elements. In addition, fast reactors with small dimensions would require much less shielding where it is necessary.

CRITICALITY

Of the various problems associated with fast reactors for rocket propulsion, the nuclear criticality results are the least questioned, as there are considerable experimental data and theoretical techniques in this area. Furthermore, those features that cause major uncertainties in criticality surveys (heterogeneity, resonance effects) have a minimum effect on this type of reactor (homogeneous and fully enriched). Void space and fuel element thicknesses will be of the order of 0.1 in., which is one-twentieth of the neutron mean free path. Since nuclear criticality results have been obtained with rather sophisticated methods and are checked against experimental data where possible, they should be useful as check points for other methods of calculation of small fast systems, particularly those with thermalizing reflectors, such as are considered for compact power sources. Note that while our basic criticality results for fully reflected spheres are computed as precisely as possible, the results for the rocket reactors will be more approximately and conservatively computed to allow for control, departure from the idealized geometry and composition, etc.

Because of the effective homogeneity of the core, critical masses will be relatively independent of core details such as fuel element thickness, and will depend primarily upon the composition and average void fraction. Thus, results will be presented as masses vs. total cross-sectional flow area. The achievable power level is contingent on core details, such as heat transfer area, fuel element thickness and conductivity, operating pressure, and exit gas Mach number. For orientation purposes, with the above items considered, up to 2000 Mw (or 100,000 lb thrust) per square foot of cross-sectional flow area seems feasible. This corresponds to an exit Mach number of 0.25 at an operating pressure of 1000 psi and is based on a detailed heat transfer study which will be reported when complete. While this is very high power density on an absolute basis (~30 kw/cc)

* Work performed under the auspices of the U. S. Atomic Energy Commission.

TABLE I

NEUTRON ENERGY GROUPS AND SPECTRA

Group	Upper energy limit	50–50 vol % UC–ZrC, Be-reflected reactor			Oy sphere + 2 in. Be
		Core spectrum (%)	Reflector spectrum (%)	Fissions/ group (%)	Fissions/ group (%)
1	10 Mev	3.3	1.7	2.2	5.4
2	3.7 Mev	15.3	8.2	10.5	23.0
3	1.3 Mev	28.1	16.6	17.9	27.6
4	0.5 Mev	26.2	17.3	18.2	18.8
5	0.183 Mev	19.2	16.6	20.0	11.9
6	24 kev	5.8	12.7	12.0	5.0
7	3 kev	1.5	8.9	6.4	2.4
8	0.45 kev	0.4	6.1	4.5	1.9
9	61 ev	0.08	4.0	2.6	1.0
10	8 ev	0.10	2.7	1.2	0.7
11	1 ev	0.025	1.8	1.5	0.7
12	0.1 ev	0.005	1.2	1.0	0.5
13	0.025 ev	0.006	2.2	1.8	1.0

the relatively short lifetime requirements (minutes to hours) allow greater leeway in this direction and theoretical values of this order and higher have been reported (*3*).

BASIS OF CALCULATIONS

Most of the criticality computations were made with a one-dimensional S_4 transport code (*4*) employing 20 to 40 space points and 13 energy groups. Uranium and zirconium cross sections were transscribed from a Hansen-Roach 16 group (*5*) and rechecked against experimental assemblies. Various theoretical and empirical correlations were used where data were insufficient. "Cloudy crystal ball model" results (*6*) were used to obtain high energy transport cross sections and the statistical model for inelastically scattered neutron distributions (*7*). Where appropriate (e.g., for U, W, Mo), resonance effects were accounted for by using the work of Bell (*8*). Energy-dependent cross sections were, in general, weighted by appropriate flux spectra within the group energy interval to obtain group values. The 13 groups covered energies from 10 Mev to thermal, and are listed in Table I along with the spectra and fission rates for a typical fast reactor. By comparison with an Oy sphere reflected with 2 in. of Be, we see that the propulsion reactor cores are truly fast, although coverage of the complete energy range is necessary due to the thermalizing effect of the reflector.

The microscopic cross sections were checked against a wide variety of critical assemblites (*9*) and replacement in fast spectra (*10*). The uranium cross sections gave k within 1% for spheres of various enrichments (also see ref. *5* for more comparisons). Some of the nonfissile materials (C, Be, W, Ni) were checked against experiments were Oy spheres were reflected by several inches of the other material. These gave k to within about 2% and in some cases (e.g. Be, Ni) the high energy cross sections were altered to match the experiments to within 1% in k. After the cross sections were developed they were compared with unreflected, diluted uranium fast critical experiments conducted by G. Jarvis at Los Alamos. Based on preliminary results the material cross sections which had been checked against reflected assemblies (W, C) gave critical radii differing by an average of 1% from experiment, whereas the relatively unchecked Ta cross sections gave critical radii about 3% larger than experiment. A further check of the calculations was made with an independent set of 18 group cross sections (*11*), and gave good agreement for the few cases examined.

The one-dimensional transport code was used for straightforward calculations, such as variation of core composition, reflector thickness and density, fission distribution, and reactivity worth of H_2. We ran a series of two-dimensional S_4 transport theory calculations (*4*) to check a few of the more difficult points: the control worth of a movable inlet end reflector, the extra core length required in the absence of an exit end reflector, and the conversion for spheres to cylinders. In order to conserve computing machine time, the 13 group cross sections were collapsed to four groups based on the neutron spectra obtained from the one-dimensional calculations. Group collapsing was done with the ZOT code (*12*) and was based on equations by G. Bell. The four group constants gave satisfactory results for the reactivity (k = 1.006 in contrast to 1.000 for 13 groups) for the one-dimensional case (Fig. 1a).

For the first two-dimensional calculation (Fig. 1b) the core was assumed to be a circular cylinder of the same radius as the spherical core, and the core height was determined by equating the bucklings of the cores assuming no reflector savings or extrapolation distance. This is deliberately conservative (the reflector saving is ~12 cm for this case) and results in an excess reactivity of 0.032, giving some leeway for control, elimination of power peaking, uncertainty in cross sections, etc. Burnup and fission product poisoning will be negligible over the short life of these reactors. Fig. 1c shows a two-dimensional check of the reflector savings for the exit reflector which was computed to be 12 cm from spherical calculations.

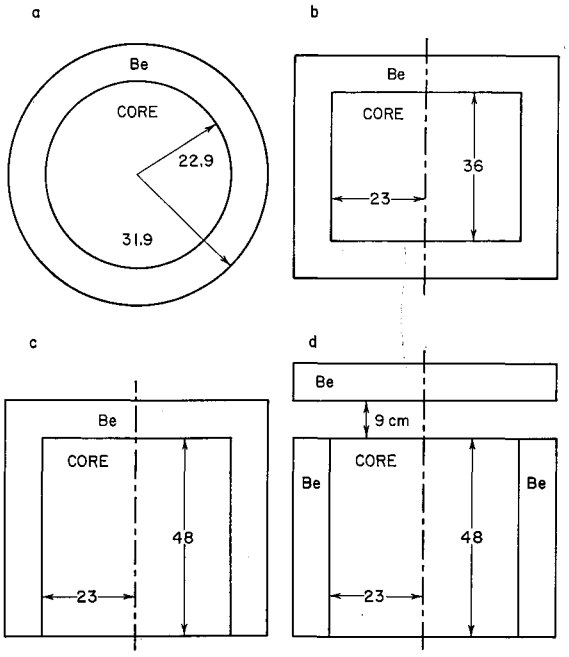

FIG. 1. The geometry used for several one- and two-dimensional criticality calculations. The core consists of 20 vol % UC, 20 vol % ZrC, 10% Mo, 50% void. The reflector is full density Be, 9 cm thick. a—One-dimensional (spherical) case. Computed with 13 group cross sections ($k = 1.000$) and with a collapsed set of 4 groups which gave good agreement ($k = 1.006$), and was used for two-dimensional computations. b—Two-dimensional (finite circular cylinder) case, completely reflected, $k = 1.038$. c—Similar to b with exit reflector replaced by 12 cm of core, $k = 1.033$. d—Similar to c with inlet reflector moved 9 cm from core for control purposes. $\Delta k = 0.062 \approx 1.0$ \$/cm.

This is the geometry assumed for the rocket reactors. One method of control is motion of the inlet reflector away from the core. The calculation (Fig. 1d) indicated adequate reactivity change (~\$1/cm) for control purposes.

RESULTS

URANIUM DIOXIDE–TUNGSTEN

One of the most obvious classes of fast reactor types for use as nuclear rocket engines is UO_2 dispersed in a refractory metal such as Mo or W. A comparison of their properties (Table II) shows that their nuclear properties are somewhat similar, but that W is about twice as dense and, most significantly has a much higher melting point. The larger W absorption, particularly in the resonance region, tends to offset its larger scattering cross section. This leads to larger critical radii with W than with Mo for a fixed UO_2 concentration (14% larger core radius for 30 vol % UO_2 and 30 vol. % refractory metal) and, because of tungsten's much higher density, to heavier reactors for the same UO_2 investment. Owing to tungsten's higher melting point, we will emphasize the W systems.

TABLE II

PROPERTIES OF MOLYBDENUM AND TUNGSTEN

Element	Mp (°C)	ρ_{theor} (gm/cc)	N (10^{24} atoms/cc)	σ_{tr} (1 Mev) (barns)	σ_{in} (1 Mev) (barns)	σ_a (barns)
Mo	2620	10.2	0.0640	4.2	1.1	0.02
W	3370	19.3	0.0632	5.2	2.0	0.05

Though results vary with UO_2 and metal concentration the reactivities of Mo and W are approximately zero in reactors of practical interest (Be reflected, 10 to 30 vol % UO_2 and 20 to 60% refractory metal in the core). Molybdenum has a positive worth; e.g. in a core with ~15 vol % UO_2, doubling the Mo from 30% to 60% reduced the core radius 4.6%, giving an 0.15% decrease in radius per vol % increase of Mo in the core. Tungsten has a much smaller worth, usually negative. The core radii for three cases with 30 vol % UO_2 and 0, 30, and 50 vol % W were 26.21, 26.08, and 26.30 cm, respectively, less than 1% variation over the range. In a case with 15 vol % $U^{233}O_2$ in the core, the radius increased 1.7% in doubling the W content from 22.5% to 45%. W. Kirk, who first surveyed the UO_2–W system, reported (*13*) the core radius constant within 2 or 3% for a fixed amount of UO_2 in the core (15 to 40 vol %) over a range of W concentrations (about 25 to 60 vol %). Thus the critical core radius (R_s) for a Be-reflected sphere is a function only of the volume fraction of UO_2 in the core, which we shall call u. This relation,

$$R = f(u) \qquad (1)$$

together with an assumption of the volume fraction (l) of UO_2 in the fuel (fuel loading) define the reactor critical weight and (with a specification of the core L/D ratio) the cross-sectional flow area.

Although a variety of compositions and thickness were examined, for this survey we fix the reflector to be 12 cm of Be at 75% of theoretical density (ρ = 1.38 gm/cc) to allow for coolant flow channels. This is a reasonable reflector for the cores of interest in terms of reducing reactor weight and flattening the power distribution, but is not optimized for any given reactor. These considerations are discussed later. The fuel materials are assumed to be ~95% of their theoretical densities, i.e., 10.4 gm/cc for UO_2 and 18.4 gm/cc for W. In converting from spheres to idealized reactors (cylinders with one end

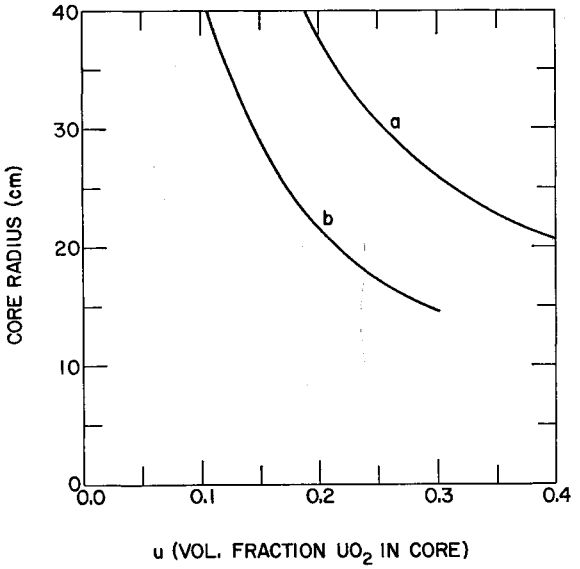

FIG. 2. Critical radii of UO_2–W cores reflected by 12 cm of Be at 75% of full density. Curve a—OyO_2 fuel (93% enriched U^{235}), 50 vol % W in fuel. Curve b—U^{233} O_2 fuel, 60 vol % W in fuel element. Other calculations indicate the radii to be relatively insensitive to the amount of W in the core.

bare), we have made the conservative assumption of equal core buckling (zero reflector savings) and replacement of one end reflector by an equivalent amount of core. Examination of these results and the two-dimensional calculations has led to a simple generalization that is adequate for preliminary criticality estimates. This is that a right circular cylinder of radius R and height $2R(L/D = 1)$ reflected on the sides and one end, is neutronically equivalent to a fully reflected sphere of equal radius. Defining the core void fraction V, we have

$$V = 1 - \frac{u}{l} \tag{2}$$

and the core cross-sectional flow area A_f becomes

$$A_f = \pi R^2 \left(1 - \frac{u}{l}\right) \tag{3}$$

The component masses are given by

$$M(UO_2) = 2\pi R^3 u \rho(UO_2) \tag{4a}$$

$$M(W) = 2\pi R^3 u \frac{(1-l)}{l} \rho(W) \tag{4b}$$

$$M(Be) = \pi t(5R^2 + 4Rt + t^2)\rho(Be) \tag{4c}$$

where t is the reflector thickness and ρ the assumed material densities. Thus, the reactor mass is given by

$$M_r = M(UO_2) + M(W) + M(Be) \tag{5a}$$

which specifically excludes pump, pressure shell, nozzle, piping, and valves, and ignores such items as structural supports in core and reflector, and controls and instrumentation in and about the reactor. For our assumptions

$$M_r = 65.3R^3u + 115.5u\frac{(1-l)}{l} + 260(R^2 + 9.6R + 28.8) \tag{5b}$$

with M in grams and R in centimeters.

The critical spherical core radii for UO_2–W reactors (for both U^{235} and U^{233}) are given in Fig. 2 as functions of the UO_2 volume fraction, u. The calculations were performed with $l = 0.5$, but apply within ~3% over a range of values for l from 0.3 to 0.6. Using these results for $R(u)$ and the above assumptions, one can compute M_r and A_f for various fuel loadings. Results (Fig. 3) are given as M_r vs A_f (in English units), which can also be interpreted as M_r vs. reactor power or engine thrust (1 ft² = 2000 Mw or 100,000 lb thrust). Masses are given for fixed fuel loadings (l) and for fixed u (or fixed core radius). The latter is strictly linear, which follows simply from our assumptions. The former (fixed l) are approxi-

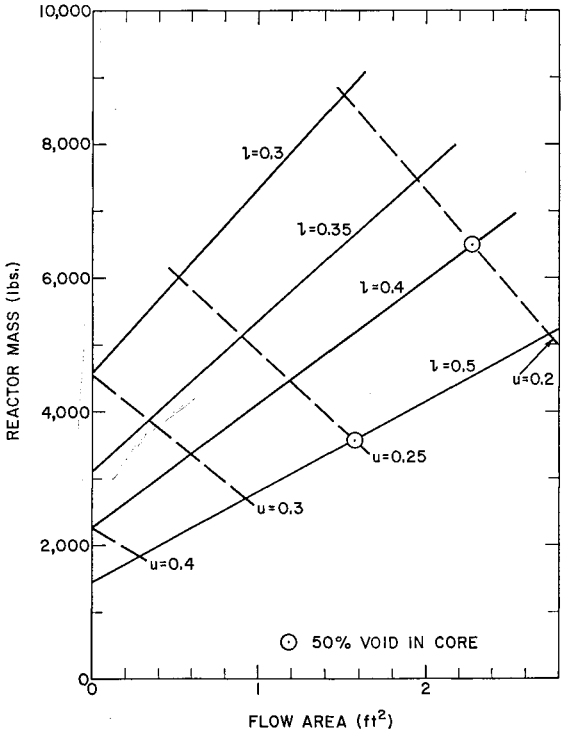

FIG. 3. Mass vs. cross sectional flow area in core for UO_2–W reactors. l (fuel loading) = vol % UO_2 in fuel, u = vol % UO_2 in core. Heat transfer and fluid flow analyses indicated up to 2000 Mw (100,000 lbs thrust) per 1 ft² of flow area appear feasible.

TABLE III

REPRESENTATIVE UO_2 REACTORS

Metal	l	Vol % UO_2 in core	Wt (lb)				Core diam. (in.)	Void frac.	Flow area (ft^2)	Thrust[a] (lb)
			UO_2	Metal	Be	Reactor				
W	0.4	0.3	730	2060	530	3320	20.4	0.25	0.577	57,700
W	0.4	0.25	1030	2720	720	4470	24.4	0.375	1.18	118,000
W	0.5	0.4	550	970	380	1800	16.2	0.2	0.29	29,000
W	0.5	0.25	1030	1700	720	3550	24.4	0.5	1.57	157,000
Mo	0.4	0.3	495	730	430	1655	17.7	0.25	0.428	42,800
Mo	0.5	0.25	885	870	560	2315	21.2	0.5	1.23	123,500

[a] Thrust based on 2000 Mw/ft^2 of flow area (50 lb thrust/Mw).

mately linear, although somewhat fortuitously so due to the dependence of R upon u. One can expect linearity for small void fractions ($A_f \ll \pi R^2$). Since criticality studies for Be-reflected graphite reactors (*14*) indicate weights of 4000 to 6000 lb in the range of 0 to 3 ft^2 of flow area, we see that fuel loadings of 40 to 50% are necessary for the UO_2–W reactors to surpass them on a power per weight basis. Other factors, such as physical size and recycling ability must also enter into comparison of the two systems.

Table III presents details of UO_2 reactors with void fractions in the range of 0.2 to 0.5. The enriched uranium requirement is relatively high, 500 to 1000 lb UO_2 (93% U^{235}) being necessary. The use of Mo in place of W generally reduces reactor weights by a factor of 2 for the same flow area at the cost of lower fuel element melting point.

URANIUM CARBIDE–METAL CARBIDE REACTORS

Uranium carbide–metal carbide reactors present a more complex picture for several reasons. First, UC forms solid solutions with many metal carbides, generally with a continuous range of properties (e.g. melting point) dependent upon the metal carbide and the composition. Thus, one must examine and select from a great many possible systems. Second, the metal carbide usually has a nonzero (positive or negative) reactivity worth, which prevents the simplifying approximation for critical core radius made for UO_2–W reactors and therefore requires a greater number of criticality calculations. Finally, the mechanical properties of the carbides are such that some unknown amount of metallic support structure might be required, which would lead to uncertainties in the reactor mass.

Selected properties of some carbides are listed in Table IV. One could conceive of a reactor core composed of unalloyed UC (which melts at 2450°C). Although the gas temperature would be limited, useful exhaust velocities ($\geq$18,000 ft/sec) could be achieved with very small reactors (200 to 300 lb). The desire for higher performance leads to consideration of solid solutions with the higher melting carbides. We choose ZrC for our examples, as many of its chemical and nuclear properties are known, and seem suitable for this application. Furthermore, UC–ZrC solid solutions have been studied (*15*) and used in connection with the plasma thermocouple program at Los Alamos, including in-pile tests in the Omega West reactor (*16*).

From the UC–ZrC phase diagram (Fig. 4), we see that a continuous series of solid solutions with varying melting points exists. We must compromise be-

TABLE IV

METAL CARBIDE PROPERTIES

Compound	Mp (°C)	ρ_{theor} (gm/cc)
UC	2450	13.5
ZrC	3500	6.9
NbC	3500	7.8
TaC	3800	14.5
HfC	3800	12.7
WC	2777	15.7
MoC	2570	8.48
B_4C	2450	2.54

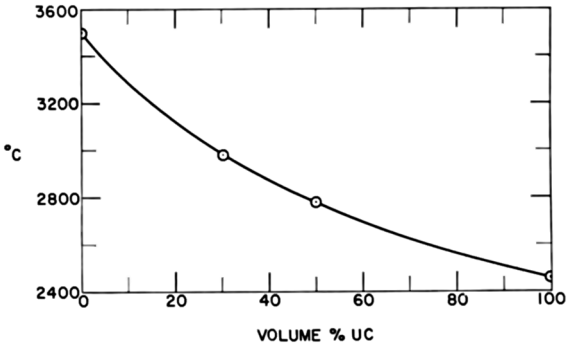

FIG. 4. Melting point of UC–ZrC solid solutions. Single phase solid solutions occur also for UC in TaC and in HfC.

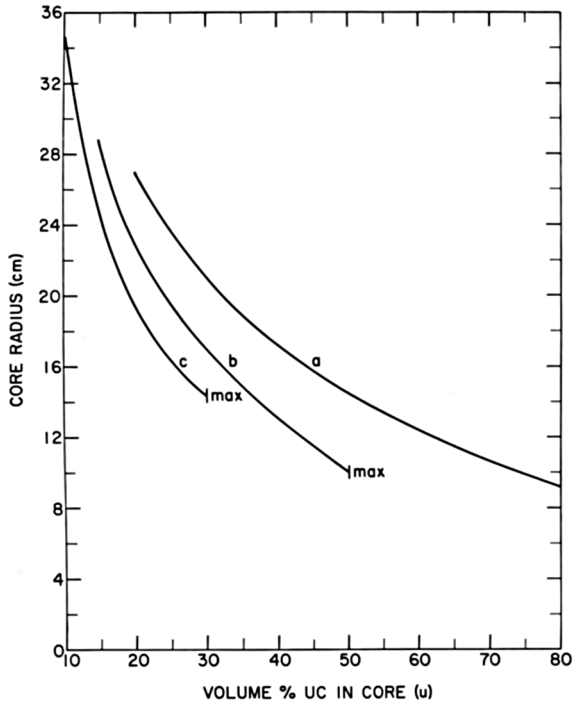

FIG. 5. Critical radii of UC–ZrC cores reflected with 12 cm of 75% dense Be. Curve a—Fuel consists of 100% UC. Curve b—50 vol % UC–50 vol % ZrC fuel. Curve c—30 vol % UC–70 vol % ZrC. "Max" indicates the point where core void is reduced to zero.

tween the desire for high melting point (low UC concentration) and low reactor weight (high UC concentration). Three compositions will be examined—100% UC, 50 vol % UC, and 30 vol % UC—with emphasis on the second value. The core radius vs. vol % UC in the core is shown in Fig. 5 for these three fuel compositions. Since the reactivity worth of Mo and W is small in these cores also, we can ignore the structure in estimating criticality and exchange structure for void when necessary. Actually, most of the calculations included 10% by volume of the core of Mo or W, which was assumed as a conservative value for the structure. The value in practice will depend upon detailed core design, but limiting conditions (no structure and 10% W) are examined for the 50 vol % UC solid solution core. If we assume zero reactivity worth, the effect of structure is to reduce the flow area and increase the core mass, leaving the core radius fixed.

Reactor weights vs. flow area are presented in Fig. 6 with an ordinate scale different from that for the UO_2–W reactors, since the UC–ZrC reactor weights are much smaller, generally by a factor of about 2 for the same flow area. This shows the variation in reactor weight which can occur for changes in the amount of structure required (curves b and c) or changes in fuel composition (curves c and d). 100% UC fueled reactors (curve a) are very low in weight (200 to 600 lb) but are restricted to low flow areas for moderate void fractions (<60%). Quantities of interest for typical reactors are shown in Table V. The 50 vol % UC–50 vol % ZrC reactors require 200 to 400 lb enriched uranium and weigh 600 to 2000 lb. Their diameters are similar to the UO_2–W reactors (12 to 24 in.), which are half those of graphite reactors. Pure UC core reactors can be made with only 100 lb of U^{235} and with total weights of less than 300 lb, again at the expense of lower melting point. To go in the direction of higher exit gas temperature requires lower concentrations of UC in the solid solution, higher melting diluents (HfC, TaC), and/or varying the UC concentration through the core. (The use of U^{233} in this connection will be discussed later.) For example, raising the fuel element melting point 200°C by changing the composition from 50% UC to 30% UC in ZrC adds about 400 lb for a uniformly

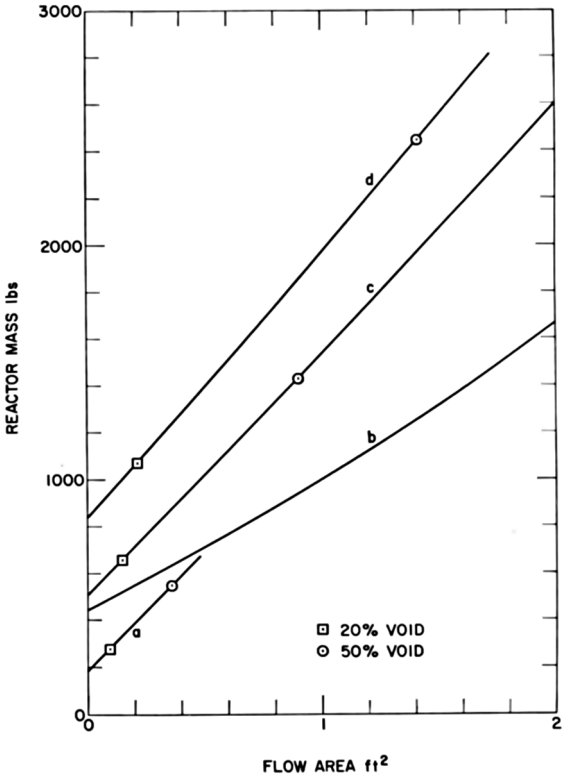

FIG. 6. Mass vs. cross sectional flow area in core for carbide reactors reflected by 12 cm of 75% dense Be. Curve a—100% UC fuel leads to very small reactors. Curve b—Fuel composed of 50% UC–50% ZrC, no structure in core. Curve c—The effect upon b of adding 10% by volume of the core of W structure. The flow area is reduced and the core mass increased. Curve d—A more dilute fuel, 30% UC–70% ZrC, 10% W structure included.

TABLE V
REPRESENTATIVE UC REACTORS

Fuel	Wt (lb)					Void frac.	Core diam. (in.)	Flow area (ft^2)	Thrust[a] (lb)
	UC	ZrC	W	Be	Reactor				
50% UC–50% ZrC	212	107	90	227	648	0.2	11.8	0.152	15,200
50% UC–50% ZrC	436	220	323	445	1424	0.5	18.1	0.893	89,300
30% UC–70% ZrC	257	303	182	327	1069	0.2	15.0	0.224	22,400
30% UC–70% ZrC	524	615	645	655	2439	0.5	23.2	1.42	142,000
100% UC	104	—	50[b]	114	268	0.2	7.1	0.055	5,500
100% UC	266	—	83[b]	213	562	0.5	11.3	0.35	35,000

[a] Thrust based on 2000 Mw/ft^2 of flow area (50 lb thrust/Mw).
[b] Support plate at exit end, otherwise 10 vol % of core.

loaded core with the same flow area. Zirconium has very good neutronic properties, and UC composition can be lowered to the point where the system is intermediate or thermal (<1% UC). For very high exit gas temperatures, one might use TaC or HfC (mp ~3800°C) with low concentrations of UC. Although Ta and Hf are strong poisons in intermediate and thermal spectra, their use in bulk is permissible in fast reactors even where the C/U ratio is ~5. Based on the best available cross-section data, Hf appears neutronically superior, as can be seen from Table VI and Fig. 7, which give critical radii for several such reactors. No metallic support structure has been included, since metal-carbide eutectics might form at lower temperatures, defeating the goal of high exit gas temperature. Thus, such reactors might have to use the carbides structurally as well as for fuel elements. Hafnium carbide has a negative coefficient of reactivity that tends to limit loadings to a minimum of about 25% OyC in the fuel if the reactor core is to be less than 3 ft in diameter. Further dilution of the OyC leads to greater neutron leakage, a degraded spectrum, and a greater capture in the Hf, which causes the critical radius and reactor mass to increase very rapidly.

URANIUM-233

The nuclear properties of U^{233} are much superior to those of oralloy (93% enriched U^{235}) for fast spectra, as can be seen from comparison of their bare sphere critical masses of 16 and 52 kg, respectively (*9*). One can take advantage of this superiority in a number of different ways, e.g., reduce the minimum reactor size by a factor of about 2, reduce the reactor weight for a given flow area (power level), increase the void space and therefore the flow area for a fixed core size, alter the power distribution with fixed uranium loadings, or reduce the loadings while maintaining the same core size and void fraction. The latter is probably the most promising, particularly with regard to achieving high gas temperatures (and consequently obtaining hydrogen dissociation). This nuclear superiority extends to the intermediate spectra of small graphite reactors (C/U ~150) of the type described in ref. *14* which could be reduced to 2000 to 3000 lb with U^{233}.

TABLE VI
CRITICAL RADII OF Be-REFLECTED UC-HfC ASSEMBLIES

Vol % in core	Loading[a]	% Void	Core radius (in.)
15% OyC, 35% HfC	0.3	50	33.5
15% OyC, 35% TaC	0.3	50	66
15% OyC, 60% HfC	0.2	25	42
10% OyC, 40% HfC	0.2	50	59

[a] Vol % OyC in fuel.

The major practical disadvantage of U^{233} is radioactivity, some of which is intrinsic, but most of which is due to a contaminant (U^{232}). As does Pu^{239}, U^{233} emits α's followed by soft γ's. A greater difficulty is due to the 2.6 Mev γ-ray from the decay products of the U^{232} impurity formed with the U^{233}. Briefly this decay chain ($4n$ series) is

$$U^{232} \xrightarrow[70\ yr]{\alpha} Th^{228} \xrightarrow[1.9\ yr]{\alpha} \xrightarrow[fast]{\alpha,\beta} \cdots\cdots \rightarrow$$

$$Bi^{212} \xrightarrow[fast]{\alpha(34\%)} Tl^{208} \xrightarrow[fast]{\beta} Pb^{208*}$$

The Pb^{208} is formed only in its 2.6 Mev excited state and is the source of the trouble. The 1.9 yr half-life of Th-228 controls the buildup of activity for short times (≤4 years), which increases linearly from zero activity just after separation of the U from the Th (*17*). One can try to minimize the U^{232} production or fabricate the reactor soon after the metal separation. In either case, complications are involved, and one would expect U^{233} to be used only after much experience is gained with U^{235} reactors. Much of the

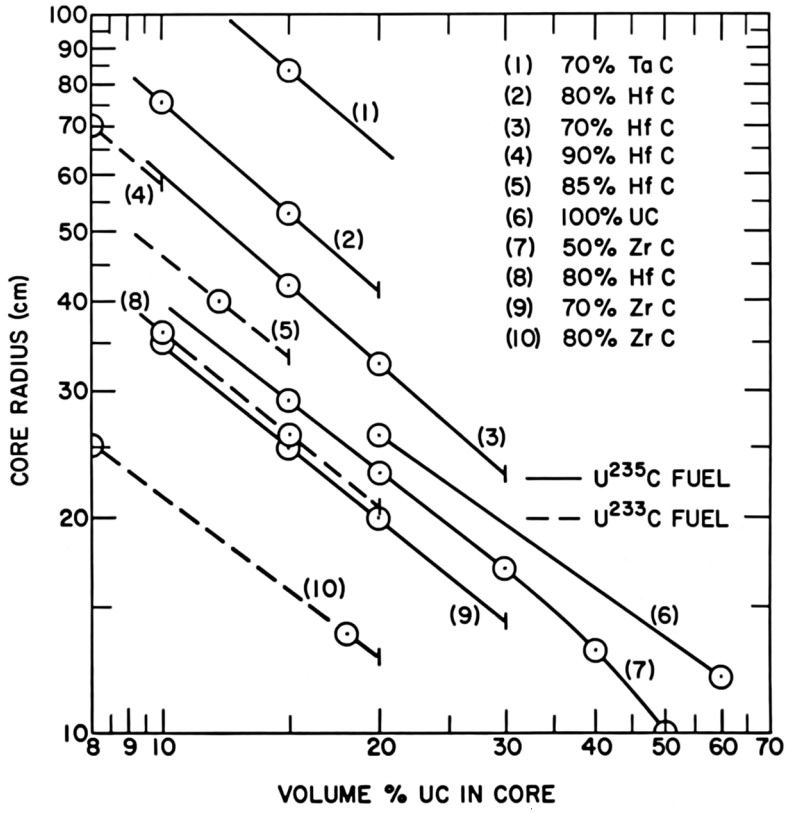

FIG. 7. Critical core radii of various carbide cores reflected by 12 cm of 75% dense Be. Curves labeled by vol % of non-fissile metal carbide in fuel.

TABLE VII

U^{233} REACTORS

Fuel	Void	Wt (lb)			Diam. (in.)	A_f (ft^2)	Thrust[a]	Wt of equivalent[b] U^{235} reactor
		U^{233}	Core	Reactor				
40% UO_2 in W	0.375	150	640	920	13.4	0.37	37,000	2900
40% UO_2 in W	0.625	420	1310	2395	22.1	1.65	165,000	5300
22% UC in ZrC	0.5	183	860	1305	18.1	0.893	89,300	1424
50% UC in ZrC	0.3	70	142	282	8.65	0.12	12,000	620
50% UC in ZrC	0.5	150	355	615	12.9	0.42	42,000	930
20% UC in HfC	0.5	840	4290	5300	29	2.28	228,000	20,000
20% UC in HfC	0.25	450	2270	2820	20.5	0.57	57,000	—
15% UC in HfC	0.2	1230	8230	9330	31	1.05	105,000	—

[a] Based on 2000 Mw/ft^2 flow area.

[b] Equivalent means same % composition and flow area.

U^{233} technology would follow directly (fuel element fabrication, etc.) because of the chemical and physical similarities, and even U^{238} would be adequate for the early nonnuclear research (thermal conductivity, melting points, etc.).

A U^{233} fueled reactor would be somewhat radioactive before startup, necessitating additional ground support effort; but after one operation, the fission product decay would probably dominate the activity, and reuse would not be further complicated. Uranium-233 (and Pu^{239}) have smaller delayed neutron fractions, which may make control more difficult but not unfeasible, as demonstrated by the existing Pu fast critical assemblies and reactors. Whereas Pu itself might also be considered as a fuel, in general, the physical properties (melting point, vapor pressure, etc.) of its compounds are not as desirable for this application.

The spherical core radius as a function of $U^{233}O_2$ fraction is given in Fig. 2, curve b. Only 50 to 60%

as much $U^{233}O_2$ as $U^{235}O_2$ (93% enriched) is required for a fixed core radius; another way of interpreting this is that a 25 to 30% loading of $U^{233}O_2$ in the fuel is equivalent to a 50% loading of $U^{235}O_2$. Alternatively, one could keep the loading high and reduce the reactor weight by a factor of 2 to 3 for equal flow area, as illustrated by the examples of Table VII. The value of reducing the loading for UO_2–W fuel elements is difficult to assess quantitatively, since the metal retains its melting point for all compositions, whereas the maximum operating temperature would be some unknown function of composition of the UO_2–W two-phase cermet. On the other hand, the UC–MC solid solutions are single phase and have definite relations between melting point and composition. Although other factors may limit temperature (structural members, uranium loss from the fuel, etc.), we shall assume the melting point as an index of the achievable exit gas temperature (which may be some fraction of the melting point or some number of degrees below it). Then the performance is simply related to the composition. A calculation has shown that 22 vol % U^{233} C–78 vol % ZrC fuel is neutronically equivalent to an equal volume of 50 vol % OyC–50 vol % ZrC fuel in a 15 in. diameter core. The former melts at ~3090°C, which is 315° higher than the OyC–ZrC fuel, and in addition weighs only 81% as much.

DISCUSSION

There are a number of topics including control, uranium investment, power distribution, reflector materials, and shielding that are associated with the nuclear aspects of these engines and warrant some consideration here.

Control of fast reactors was a problem that inhibited their consideration in the early period of nuclear development. Normal control of fast reactors depends upon the delayed neutrons, as is the case with thermal reactors, and thus the shorter prompt neutron lifetime does not strongly affect the normal control problem. Should the reactor become prompt critical, the shorter lifetime, smaller temperature coefficient, and smaller mass of nonfissile material to absorb the energy release would make fast reactors more likely to melt or vaporize. Nevertheless, fast critical assemblies (*18*) have been pulsed above prompt critical without damage. The high reactivity worth of hydrogen in fast cores necessitates care in preventing large amounts (such as in slugs of liquid H_2) from suddenly entering the core. This can be alleviated by vaporizing the H_2 in the reflector and/or keeping the pressure above the critical value (188 psi) to avoid two-phase flow. It might be possible to use the positive hydrogen reactivity as a control technique coupled directly to the power demand. Other techniques that have been shown to be neutronically feasible in providing control include movement of the inlet reflector, control drums in the side reflector, movement of fuel out of the core, and boron control rods in the core.

Fast reactors characteristically have high uranium investments compared to thermal assemblies of comparable size. However, for power levels of the order of 1000 Mw, the requirements (200 to 500 lb of highly enriched U^{235}) are similar to those of graphite reactors which are neutronically limited (small flow areas) and rather intermediate in their energy spectra for this size. The fast reactor fissile mass increases with power level, whereas that for graphite and other moderated systems decreases with size and power level. Thus, for large, high power reactors, thermal systems may be more economical, and due to the lower density of the moderator, can even have lower reactor weights per unit power where heat transfer considerations are limiting. For test purposes, one could make very small, low power UC reactors with 50 to 100 lb of enriched U^{235}, but the long term usefulness of such reactors is not clear.

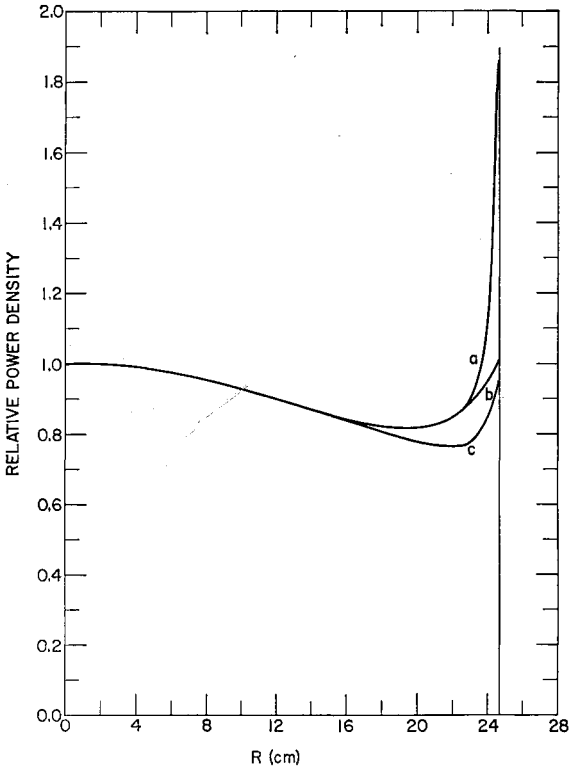

FIG. 8. Radial power distribution for typical fast reactors. Curve a—Be reflector, no poison. Curve b—Be reflector with B^{10}. Curve c—Ni reflector.

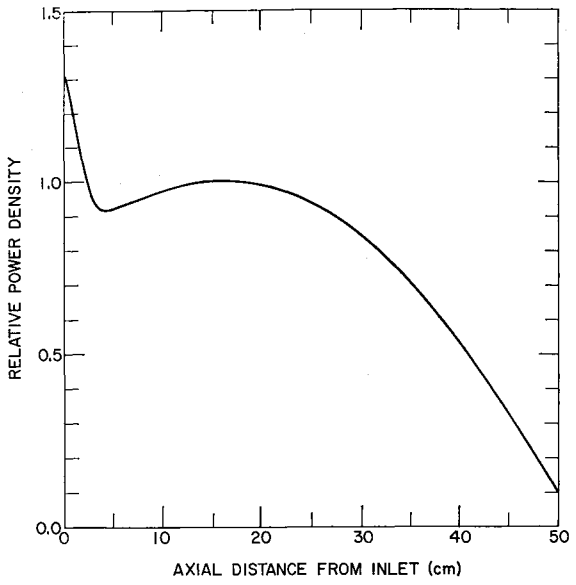

FIG. 9. Axial power distribution for 19 in. long reactor, reflected at inlet end.

TABLE VIII

RELATIVE SHIELDING REQUIREMENTS

Reactor	Diameter (in.)		Wt (lb)		
	Core	Reflector (Be)	Engine	Lead shields	
				10 in. shadow	5 in. circum.
200 Mw UC	10	18	500	1200	2,700
1000 Mw UC–ZrC	18	26	2000	2600	5,200
1000 Mw Graphite	36	48	5500	9000	16,000

Power distributions will vary considerably with reactor and reflector sizes and compositions. One desires to have the radial power as flat as possible, and this is typically so within ±10%. Thermalizing reflectors (Be, C) lead to a power spike at the core surface, (Fig. 8, curve a), but this can be eliminated or reduced by putting some absorbing (or fissile) material in the reflector (curve b). Generally the larger the core, the more it will approach a cosine-shaped distribution. The axial distribution will be close to a cosine for a 4 ft core, whereas it will be considerably truncated (as shown in Fig. 9) for a small (19 in. long) core. Such a shape is generally desirable, since it has high power density at the cold inlet and tails off where the gas is hot, although high power density at the cold end can lead to fuel stress and heat transfer problems.

On a weight basis, Be is the best reflector material. A direct replacement of a 12 cm Be reflector would require over twice the thickness of graphite. In a typical case, this could be reduced to 18 cm by increasing the core diameter 15%, which changes the weight, power level, power distribution, etc. For these fast spectra, heavy element reflectors are feasible, and Ni is almost as good as Be on a volume basis. An equivalent (14 cm) Ni reflector would weigh about six times as much as Be. If gamma shielding were a consideration, the Ni reflector would act as a shield as well and, being closer to the core, would be more efficient. Beryllium would be better for slowing neutrons, and some composite might be optimum. Loading part of the reflector with fissile material would improve the core power distribution and supply a portion of the temperature rise of the H_2, which would improve control and heat transfer at the core inlet.

The small physical size of the fast reactors leads to much smaller shield weights than for less dense (e.g., graphite) reactors. Table VIII illustrates relative values for three types of reactors with two types of shield. The shadow shield covers the inlet end of the reactor and lies between it and the propellant tankage and payload. It gives an attenuation of ~5000 for 1 Mev gamma rays. The 5 in. circumferential shield gives an attenuation of ~70, and such a shield might be required for rendezvous operations. Even with the reactor shut down, the fission product decay gammas represent an appreciable source. We do not imply that the specific shield weights given are either necessary or sufficient; only the relative values are significant. However, a 10 in. lead shadow shield has been estimated to be sufficient for a biological shield under certain conditions, and a circumferential shield with a factor of 70 attenuation would permit debarkation from a nuclear vehicle a short time after landing.

CONCLUSIONS

A number of conclusions can be drawn from these calculations, and only the more important will be mentioned. First, fast reactors offer possibilities both for lightweight nuclear rocket engines and for very high temperature engines. Second, there is a wide variety of reactor weights, sizes, and compositions from which to choose. Cermets of $U^{235}O_2$–W require about 40 vol % loading to be superior to intermediate, heavily loaded graphite reactors. Uranium carbide offers a spectrum of possibilities ranging from very small, lightweight (~300 lb) pure UC reactors with low exit gas temperature (≤2000°), through moderate size and power UC–ZrC reactors, to heavier UC–HfC reactors of high (≥3000°C) temperature potential. Uranium-233 may be used to lower weights

or increase gas temperatures. The small physical size of fast reactors (small mass, high density) is attractive where considerable shielding is required (such as for manned orbital ferries). The increase in fissile mass with size of fast reactors makes them less competitive with moderated systems for very high power applications.

REFERENCES

1. H. S. Tsien, Rockets and other thermal jets using nuclear energy. *In* "The Science and Engineering of Nuclear Power," Clark Goodman (ed.), Vol. II, Chapter 11. Addison Wesley, Reading, Mass., 1949.
2. R. S. Cooper, Fast reactor rocket engines—Criticality. LA-2707 Los Alamos Scientific Laboratory Report in preparation.
3. E. W. Sams, Performance of nuclear rocket for large-payload, earth-satellite booster. *J. Aero/Space Sci.* **27,** 481 (1960).
4. B. G. Carlson, C. E. Lee, and W. J. Worlton, The DSN and TDC transport codes. LAMS-2346 (October 16, 1959).
5. G. E. Hansen and W. H. Roach, Six and sixteen group cross sections for fast and intermediate critical assemblies, LAMS-2543. Also, W.H. Roach, Computational survey of idealized fast breeder reactors. *Nuclear Sci. and Eng.* **8,** 621 (1960).
6. J. R. Beyster, Predictions of fast neutron scattering data with a diffuse surface potential wall. LA-2099 (December 1956).
7. A. M. Weinberg and E. P. Wigner, "The Physical Theory of Neutron Chain Reactors." Univ. of Chicago Press, Chicago, 1958.
8. G. I. Bell, Theory of effective cross sections. LA-2322 (June 1959).
9. H. C. Paxton, Critical masses of fissionable metals as basic nuclear safety data, LA-1958 (June 1955). Also, Fast neutron critical assemblies and related topics. *Nuclear Sci. and Eng.* **8,** 523 (1960).
10. L. B. Engle, G. E. Hansen, and H. C. Paxton, Material replacement measurementt in Topsy and Godiva assemblies. LA-1708 (July 1954). Also, Reactivity contributions of various materials in Topsy, Godiva, and Jezebel. *Nuclear Sci. and Eng.* **8,** 543 (1960).
11. C. B. Mills, Physics of intermediate reactors. LAMS-2288 (January 1959).
12. R. S. Cooper, A code for reducing many group cross sections to few groups. Los Alamos Scientific Laboratory Report, in preparation.
13. W. Kirk, Los Alamos Scientific Laboratory, private communication.
14. P. G. Johnson and R. Smith, An optimization of power-plant parameters for orbital launch nuclear rockets. NASA-TN-D-675 (February, 1961).
15. W. G. Witteman, J. M. Leitnaker, and M. G. Bowman. The solid solubility of uranium monocarbide and zirconium carbide. LA-2159 (October 15, 1957).
16. S. Glasstone, Plasma thermocouple quarterly report. LAMS-2447 (July, 1960).
17. J. J. Devaney, Radiation intensity from spheres of U^{233} contaminated with U^{232}. LAMS-1892 (February (1955).
18. T. F. Wimett, R. H. White, W. R. Stratton, and D. P. Wood, Godiva II—An unmoderated pulse irradiation reactor. *Nuclear Sci. and Eng.* **8,** 691 (1960).

NUCLEAR SCIENCE AND ENGINEERING: **13**, 366–373 (1962)

A Review of the Methods Used for the Determination of Hydrogen in Uranium*†

HAROLD F. WALDRON

Mallinckrodt Chemical Works, Uranium Division, Saint Charles, Missouri

Received January 8, 1962; Revised April 25, 1962

Of the many published methods for determining hydrogen in uranium, those based on complete separation of the gas by vacuum or inert-gas extraction are the most satisfactory. When 5- to 10-gm samples are used, the average operator time can be reduced to about ten minutes per sample for either of these techniques. Routine operation of one inert-gas and six vacuum extraction units has produced an overall laboratory precision of ±0.3 ppm for production material containing up to 7 ppm hydrogen. Improved precision, at a considerable expense of time, can be obtained with larger samples.

INTRODUCTION

The need to know and control the amount of hydrogen in uranium was prompted by the observation that hydrogen can cause objectionable discontinuities in the bond between a uranium core and its protective metal encasement (*1*). Sensitive and quantitative analytical procedures were needed for exploratory study of the role of hydrogen during the cladding operation and, subsequently, for quality control of the metal. Such methods have been developed and refined to the point where precise measurements can be made in a rapid and routine manner. Since the determination has become one of major importance in the uranium industry, this review and evaluation of available procedures has been made. As in many analytical procedures, the reliability of the answer may be closely dependent on the method of securing and preparing the sample.

Although two methods which permit the hydrogen to be measured *in situ* have been proposed, the more practical and useful measurements follow a separation of the gas from the metal by fusion or extraction techniques. In the latter case, the separation is dependent on the same property which makes the presence of hydrogen undesirable, namely, mobility of hydrogen in the metal at elevated temperatures (*2–7*).

Unfortunately, standard samples of hydrogen in uranium are not available to aid in comparing analytical methods and techniques used for this measurement. Superficial standards may be prepared by measuring the gas absorbed when uranium–hydrogen systems are equilibrated at various temperatures and pressures, but these are of no value in appraising the accuracy of the more common tests which merely reverse the diffusion process. Metal prepared by the equilibrium technique, however, has uniform hydrogen distribution and provides an excellent source of samples for precision studies when it is desired to minimize the contribution of sampling errors. In the absence of absolute standards, the accuracy of the procedures can only be evaluated by comparing the results of different methods with due consideration of varied operating conditions and sample sizes.

SAMPLING AND SAMPLE PREPARATION

The nature of the source material with respect to hydrogen distribution and the degree of accuracy with which the concentration must be known determine the size and shape required for a representative sample. These criteria need to be evaluated for each situation. Generally, one or more selectively located small samples (5 to 10 gm) are adequate replace-

* Presented at the Fifth Conference on Analytical Chemistry in Nuclear Reactor Technology, Gatlinburg, Tennessee, October 10–12, 1961.

† Work performed under U. S. Atomic Energy Commission Contract W-14-108-Eng-8.

ments for the massive samples (400 to 500 gm) frequently used and can produce considerable savings in analytical time.

The sample size, method of cutting, and perhaps other parameters dependent on chemical and metallurgical properties of the metal determine the cleaning required for adequate sample preparation. A degreasing agent (*8–10*) and/or nitric acid (*6*, *7*, *11–13*) have been used for large samples and may be adequate for the ideal specimen with a smooth surface and a low surface-to-volume ratio. Although some reports have indicated that a degreasing (*2*, *14*) and/or nitric acid treatment (*1*, *15*, *16*) is satisfactory for small samples, it is not recommended because of its tendency to produce high answers (*17*, *18*). This conflict in data has been attributed to the source and history of the samples (*18*) and, doubtlessly, the method of cutting the samples is of prime importance. Sheared or punched samples, which are likely to contain many fissures to trap hydrogen-containing materials, are much more difficult to prepare adequately than sawed or machined samples. File-abrasion to a bright smooth surface has been accepted as a reliable cleaning method (*3*, *17–24*). Our experience, however, indicates that the abrasion should be both preceded and followed by vapor degreasing, with carbon tetrachloride, to be adequate for all sources of samples (*3*).

Fergason *et al.* (*25*) have recently described an ultrasonic chemical cleaning method which was shown to be a reliable substitute for the more laborious and expensive file-abrasion technique. In this method, the samples are vapor degreased with carbon tetrachloride and then, with the aid of ultrasonic vibration, cleaned in a solution of nitric and sulfuric acids in water (3:1:1 volume ratio, respectively) and rinsed in water and acetone.

Ideally, samples should be analyzed immediately after cleaning, but reports indicate that a storage period of one to several days at low humidity, preferably over a desiccant, does no harm (*8*, *13*, *21*). If the humidity is high, however, the hydrogen pickup may be appreciable (*8*, *21*). An electropolish to give a less reactive surface should decrease the sensitivity to exposure, but this has not been verified experimentally.

METHODS OF ANALYSIS

Without Separation

Two methods have been reported for measuring the hydrogen without separation from the metal. Both are based on the fact that at or below room temperature the hydrogen is present in the hydride form. Kloepper *et al.* (*15*) attempted a semiquantitative application of micrographic inspection. The polished specimen was heat-tinted to provide sharper contrast of the hydride and metal and photographed at a magnification of 50 diameters. Although the hydride is discernible under these conditions, it was found that, at best, the observation could tell only whether a relatively large or small amount of hydrogen was present. Robillard and Calais (*26*) used a much higher magnification of 150 to 400 diameters as a sensitive means of observing the desorption of hydrogen on heat treating. The small amount of surface that can be observed at the higher magnifications, however, would render any estimate of the hydrogen content valueless for most samples.

The ferromagnetic property of uranium hydride below 173°K (*27–29*) has been used by Wahl and Liboff (*30*) as a measure of the hydrogen content in uranium cores. The effect of other ferromagnetic materials was minimized by obtaining the difference in the force exerted by a nonuniform field at about 90°K and at room temperature. The test is nondestructive and rapid, but the accuracy was reported to be no better than 20% and may be considerably poorer (*23*). With poor accuracy and inability to handle samples of random size and shape, the method has limited application.

Vacuum Fusion

The reliability of vacuum fusion for the determination of gases in metals was an established technique when the need to measure hydrogen in uranium occurred. Reports describing design details of the equipment used for hydrogen-in-uranium are relatively few (*16*, *19*, *22*, *31*, *32*) and frequently describe another application of the unit (*33*, *34*). The universally accepted fusion chamber is a graphite crucible that is usually insulated with graphite powder and suspended in an envelope as described by Guldner and Beach and shown in Fig. 1 (*35*). The crucible is heated inductively and the fusion of a sample, or dissolution in a bath, normally produces a mixture of gases which must be analyzed. Direct analysis of the gases after collection may be made with a mass spectrometer (*16*, *32*), but a separation based on chemical and/or physical properties is usually performed. A typical separation scheme as described by Yeaton (*36*) is shown schematically in Fig. 2. The use of copper oxide to convert the hydrogen and carbon monoxide to water and carbon

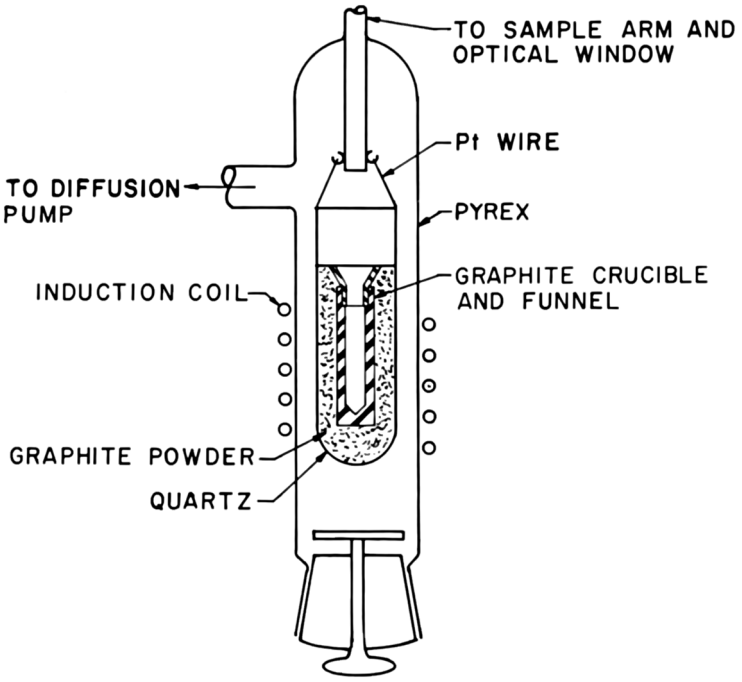

FIG. 1. Guldner–Beach furnace assembly for vacuum fusion (*35*). (Courtesy of *Analytical Chemistry*.)

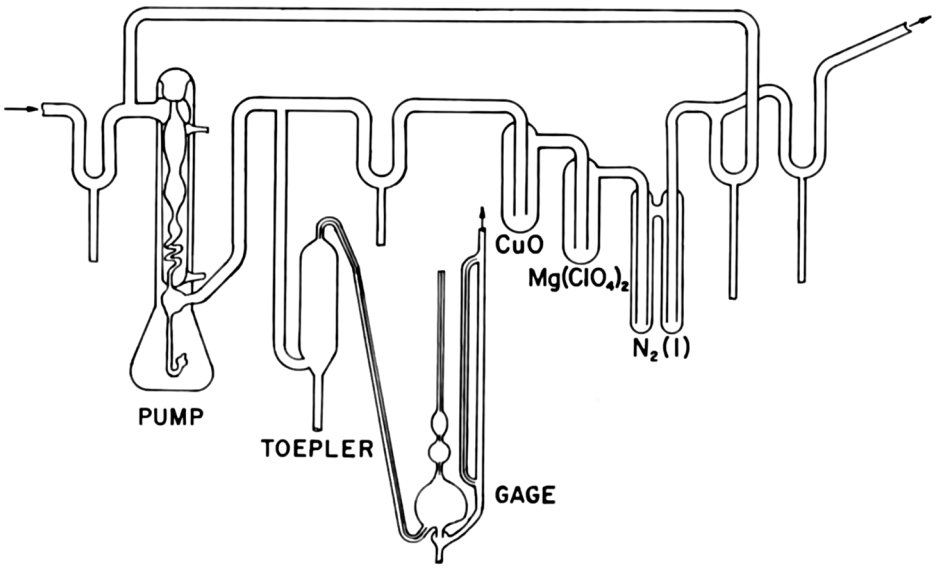

FIG. 2. Diagram of a system for the separation and measurement of gases in vacuum fusion analyses (*36*)

dioxide, respectively, is quite common, but the separation methods range from complete use of absorbants (*37*, *38*) to fractional freezing (*39–41*). Without conversion to water, hydrogen has been separated from the fusion gases by diffusion through a palladium membrane (*19*, *22*) and by chromatographic techniques (*42*).

Applicability of the vacuum fusion equipment and techniques to the determination of hydrogen in uranium was verified by Thompson and associates (*43*). Descriptions of work performed by other investigators indicate that conditions have varied from direct fusion of the sample at 1200–1900°C (*1*, *17*, *31*, *42*, *44*) to dissolution of the sample in: an iron–tin mixture at 1235°C (*17*); iron at 1600–1900°C (*16*, *17*, *23*, *32*, *44*, *45*); or platinum at 1800–1900°C (*19*, *22*, *32*, *46*). Although all of these conditions are reportedly capable of producing correct results, they are not equally desirable. Sloman and Harvey (*47*) concluded that the best

temperature for fusion without a bath would be just above the melting point because of the anomalous solubility behavior of hydrogen in the molten metal. If a bath is used, such as platinum or iron, a temperature of 1800°C, or over, is desirable to minimize the time needed to completely remove the hydrogen. In this case, the fact that oxygen may be determined (*47–51*) simultaneously offers the only advantage of vacuum fusion over the much simpler extraction method for hydrogen.

Vacuum Extraction

Vacuum extraction is the term applied to the process of removing gases from metals heated to a temperature below their fusion point in an evacuated chamber. The fact that hydrogen could be quantitatively removed from uranium by this technique was reported by Thompson and associates (*52*) and later verified by a number of investigators (*2*, *13*, *15–17*, *20*, *24*, *43*). Much of the early work was performed in equipment designed for fusion work (*11*, *15–17*, *53*), but usually the complicated crucible assembly was replaced by a quartz tube, which was heated with a resistance furnace. The exact temperature of the sample is not critical if the extraction is carried to completion, but about 800°C is usually used.

Tews and Miller (*10*) developed equipment specifically for this problem with a palladium membrane for the separation of hydrogen from other gases. Based on the equipment of Tews and Miller, I designed a similar apparatus, shown photographically in Fig. 3 (*3*). Mercury manometers are used to measure the relatively large amounts of gas evolved from samples weighing between a hundred and a few thousand grams, and stopcocks are used to control the gas flow. Automatic Toepler pumps transfer the gas from the quartz extraction tube to the palladium section and exhaust the hydrogen from the opposite side of the membrane to a known volume. The analysis time for this type of equipment is three to six hours, and the established precisions, at the 95% confidence level, are ±0.06 (*3*) and ±0.08 (*10*) ppm (the ±0.08 figure was calculated from data presented by Tews and Miller (*10*)).

The use of the separation methods described above, together with mass spectrometric analysis (*13*, *14*, *24*, *54*), established that the gas extracted from a uranium sample is essentially all hydrogen and that a separation is unnecessary. Thus, indication of the hydrogen content may be obtained by heating a sample in an evacuated chamber to a temperature where the solubility is small and measuring the equilibrium pressure (*2*, *12*, *55*). Alternatively, this may be done in a deuterium atmosphere, and the hydrogen concentration may be calculated from the isotopic ratios when equilibrium is obtained (*56*, *57*). Generally, however, it is desirable to remove the gas from the sample chamber before measurement.

Elimination of the separation step permits increased capacity with simplified equipment. With improved pumping efficiency and multiple sample loading, Miller (*58*) found that six 400- to 500-gm

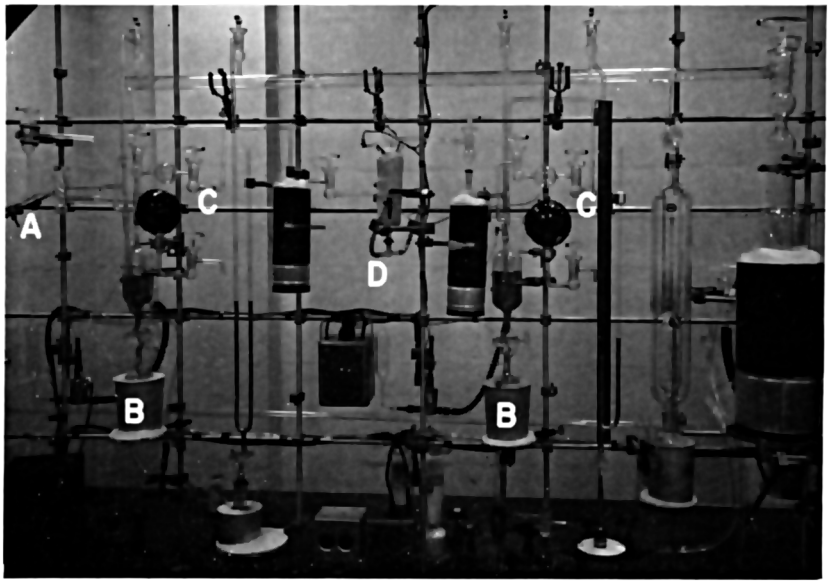

Fig. 3. Vacuum extraction unit with a palladium membrane for separation of the hydrogen (*3*). A—to furnace; B—Toepler pump; C—measuring section; D—palladium membrane.

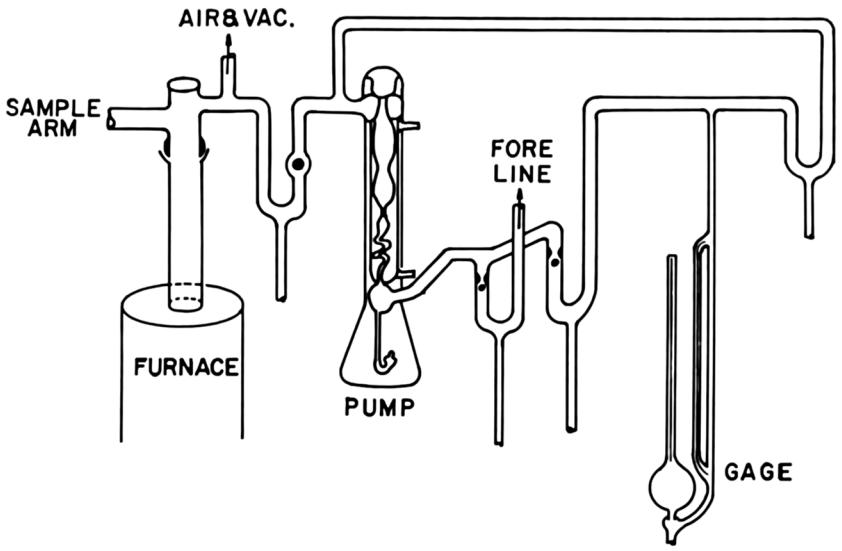

FIG. 4. Diagram of a vacuum extraction apparatus for routine determination of hydrogen in uranium (*3*).

samples could be analyzed per day instead of one sample in five hours by the separation method (*10*). A decrease in sample size allows an even greater increase in sample output. Development work at Mallinckrodt Chemical Works has resulted in the equipment shown schematically in Fig. 4 (*3*). The 5- to 10-g samples are loaded in a storage arm and an iron push-bar is used to drop them, individually, into a graphite crucible. Extraction is completed in twenty minutes, and the evolved gas is transferred by a diffusion pump to a calibrated volume where the pressure is measured on a McLeod gage. Mercury cutoffs are used to control the flow of gas. Compactness of the equipment is an aid in clustering several units for simultaneous operation. In this manner, one operator routinely handles six units with an output of sixty samples in one eight-hour shift. Under these conditions with samples prepared to minimize heterogeneity, the precision, including the variation between the six pieces of equipment, is ± 0.1 ppm, at the 95% confidence level, for a single determination on metal containing 3.3 ppm hydrogen.

Other attempts to reduce the time required for a determination have included partial extraction with or without an attempt to correlate the result to the total hydrogen content. In the latter case, the goal was to obtain a practical test that was sensitive to the hydrogen in the surface layers of the metal. Generally, induction heating to about 600°C and gas collection for about five minutes were used (*9, 11, 53, 59, 60*). Although somewhat indicative of canning behavior, this test has been abandoned in favor of a physical separation of the outer layers (*3*) because of difficulty in reproducing the operating conditions from time to time and at different installations. Partial extraction as a measure of the total hydrogen content has been described by Oblinger and Dube (*6, 7*). The total hydrogen is calculated from the amount extracted in a short period of time by using an empirically predetermined relationship involving the diffusion coefficient, sample geometry, and experimental conditions. This method is best applied to samples with uniform hydrogen distribution, but reasonable reproducibility for samples with similar hydrogen gradients was reported. It appears likely, however, that the empirical relationship may change with shifts in the hydrogen gradient as indicated by the difference between the diffusion coefficient reported by Oblinger and Dube (*6, 7*) and those reported for homogeneous samples (*2, 3*). This possibility of error, together with the time and sample geometry that are required, limits the appeal of this method.

Inert-Gas Extraction

Inert-gas extraction is similar to vacuum extraction except that the hydrogen is removed from the sample chamber by a flow of inert gas rather than by evacuation. Fergason *et al.* (*61, 62*) have recently described the use of mass spectrometry and inert-gas extraction as a rapid method for the determination of hydrogen in uranium. The Bendix Time-of-Flight and Consolidated Electrodynamics Model 21-611-1 mass spectrometers were both successfully used to monitor the hydrogen in a stream of helium or argon after it had passed over the hot uranium sample. The simplicity of the extraction section and

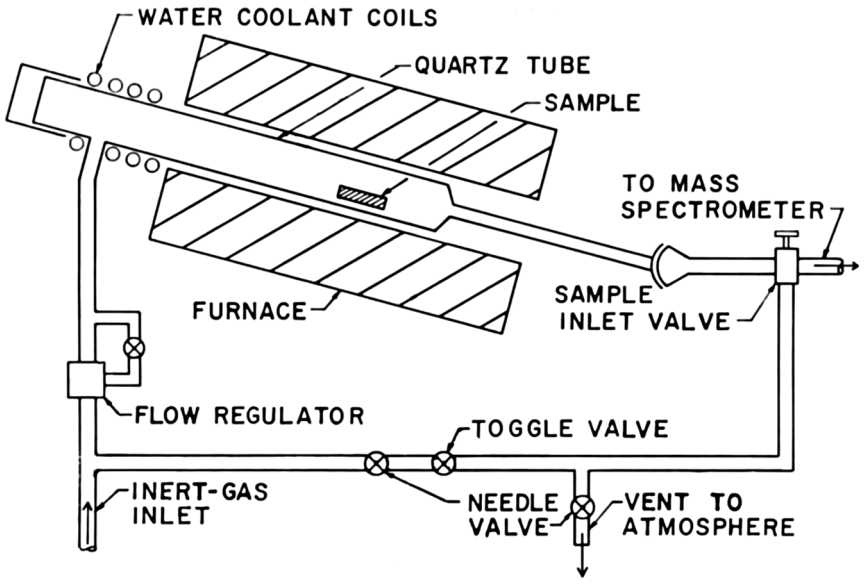

FIG. 5. Inert-gas extraction system with mass spectrometer inlet (*61*). (Courtesy of The American Nuclear Society, Inc.)

sample introduction system, as shown in Fig. 5, is one of the distinct advantages of this method. The furnace section is back-flushed with the inert gas during sample loading which permits each sample to be introduced immediately prior to analysis. During the extraction, the mass spectrometer response is directly proportional to the hydrogen content of the gas stream. In practice, the response voltage is converted to a voltage-dependent frequency, and the number of pulses during a complete extraction is registered on a decade scaler. This count is directly related to the total hydrogen content of the sample.

The Consolidated instrument, with some modifications (*62*), has been successfully adapted to routine use for 5- to 10-gm samples and can produce twenty to seventy determinations per man-day depending on the hydrogen content and the sample geometry. Under these conditions with samples prepared to minimize heterogeneity, the precision is ±0.1 ppm, at the 95% confidence level, for a single determination on metal containing 3.3 ppm hydrogen.

Current work at Mallinckrodt Chemical Works indicates that measurement of the thermal conductivity of the inert-gas stream may be a satisfactory substitute for the mass spectrometric measurement. The thermal conductivity unit offers a cheaper, simpler, and more rugged instrument for the determination. This method is still in the development stage and will be described in a later report.

SUMMARY

Methods involving measurement of the hydrogen after it is separated from the uranium metal by fusion or extraction techniques are the most desirable. Because of the operational complexities, vacuum fusion is advantageous only when oxygen is to be determined simultaneously. Both vacuum extraction and inert-gas extraction offer fast convenient methods. Vacuum extraction is a primary method with measurements based on the fundamental gas laws. Inert-gas extraction with mass spectrometric monitoring is a secondary method requiring precalibration with a standard. The latter, however, has the distinct advantage of permitting a sample to be introduced, in a very convenient manner, and immediately analyzed. When either of these is applied to samples of about ten grams in size, which is adequately representative in most cases, the average operator time can be reduced to the order of ten minutes per sample. When necessary, large samples, in the order of hundreds of grams, can be analyzed by vacuum extraction with excellent precision but require several hours for a determination. This wide range of sample sizes and the highly diverse operating conditions that have been used to produce identical results, within the precision of the tests, offer firm evidence of the accuracy of fusion and extraction techniques, even in the absence of absolute standards.

Both vacuum extraction and inert-gas extraction are used routinely at Mallinckrodt Chemical Works for the determination of hydrogen in 5- to 10-gm samples of uranium. With sampling error minimized, the precision of each technique for a single determination on metal containing 3.3 ppm hydrogen is ±0.1 ppm, at the 95% confidence level. The corre-

sponding over-all laboratory precision, for production material containing up to 7 ppm hydrogen, is ±0.3 ppm. The latter figure includes sampling error and instrument variation among six vacuum units and the inert-gas extraction equipment.

ACKNOWLEDGMENT

The author is indebted to S. H. Huston and R. T. Springgate for the statistical interpretations used in this report.

REFERENCES

1. A. E. GUAY, Summary Technical Report for the Period January 1, 1955 to March 31, 1955, National Lead Co. of Ohio. TID-10112, 137–145 (April 15, 1955).
2. W. D. DAVIS, Solubility, determination, diffusion and mechanical effects of hydrogen in uranium. General Electric Co., Knolls Atomic Power Lab., KAPL-1548 (August 1, 1956).
3. J. A. FELLOWS, Alpha phase vacuum outgassing of dingot uranium. Mallinckrodt Chemical Works, MCW-1467 (August 10, 1961).
4. M. W. MALLETT AND M. J. TRZECIAK, *Trans. Am. Soc. Metals* **50**, 981–993 (1958).
5. H. W. MYERS, J. W. VARWIG, J. L. MARSHALL, L. G. WEBER, AND J. A. KENNELLEY, The application of diffusivity data in reducing the hydrogen content of gamma-extruded uranium bars. Mallinckrodt Chemical Works, MCW-1439 (December 10, 1959).
6. C. J. OBLINGER, Summary Technical Report for the Period April 1, 1960 to June 30, 1960, National Lead Co. of Ohio. NLCO-810, 117–119 (August 11, 1960).
7. C. J. OBLINGER AND H. A. DUBE, *Nuclear Sci. and Eng.* **11**, 263–266 (1961); *Proc. First Conf. Nuclear Reactor Chemistry, Gatlinburg, Tenn., October 12–14, 1960*, Paper No. 34, A.E.C. Technical Information Service Extension, Oak Ridge, Tenn.
8. H. R. GARDNER, An investigation of specific processes which influence the hydrogen content of uranium. General Electric Co., Hanford Atomic Products Operation, HW-33725 (January 7, 1955).
9. H. R. GARDNER AND R. I. MILLER, Preliminary report on a surface hydrogen analytical technique. General Electric Co., Hanford Atomic Products Operation, HW-36011 (May 16, 1955).
10. W. G. TEWS AND R. I. MILLER, A high vacuum apparatus for the determination of hydrogen and other gases in reactor fuel metals. General Electric Co., Hanford Atomic Products Operation, HW-33724 (January 31, 1955).
11. C. F. HALL, Summary Technical Report for the Period July 1, 1958 to September 30, 1958, National Lead Co. of Ohio. NLCO-760, 95–98 (October 24, 1958).
12. P. R. MORRIS, Summary Technical Report for the Period July 1, 1954 to September 30, 1954, National Lead Co. of Ohio. FMPC-475, 117–119 (October 15, 1954).
13. W. E. RAY AND H. C. BOWEN, The hydrogen content of fabricated uranium. General Electric Co., Hanford Atomic Products Operation, HW-30116 (November 30, 1953).
14. F. K. HEUMANN AND L. A. ALTAMARI, Determination of hydrogen in irradiated reactor materials. *Proc. Second Conf. Anal. Chem. in Nuclear Reactor Technol. Gatlinburg, Tenn., September 29–October 1, 1958*, TID-7568, Pt. 2, pp. 85–90, A.E.C. Technical Information Service Extension, Oak Ridge, Tenn.
15. H. C. KLOEPPER, JR., H. W. MYERS, AND N. MCCALPIN, Process Development Quarterly Report, Part I, Mallinckrodt Chemical Works. MCW-1371, 53–63 (January 1, 1955).
16. R. E. TAYLOR, Determination of gases in metals by gasometric methods. General Electric Co., Hanford Atomic Products Operation, HW-42663 (May 1, 1956).
17. M. W. MALLETT AND C. B. GRIFFITH, Minutes of the Meeting on the Analysis and Metallography of Hydrogen in Uranium, Held June 22, 1955. Battelle Memorial Institute, BMI-X-128 (September 15, 1955).
18. H. W. MYERS, Process Development Quarterly Report, Part I, Mallinckrodt Chemical Works. MCW-1377, 59–62 (July 1, 1955).
19. E. BOOTH, F. J. BRYANT, AND A. PARKER, *Analyst* **82**, 50–61 (1957).
20. L. CHAMPEIX, G. COBLENCE, AND R. DARRAS, *Comm. energie atomique (France), Rappt. No. 1385* (1959); *Mém. sci. rev. met.* **57**, 502–512 (July, 1960) (English translation by L. Appleby, General Electric Co., Hanford Atomic Products Operation, HW-tr-19 (October 14, 1960)).
21. H. W. MYERS, Process Development Quarterly Report, Part I, Mallinckrodt Chemical Works. MCW-1382, 105–107 (January 3, 1956).
22. A. PARKER, The determination of gases in metals using the semi-micro vacuum fusion technique. United Kingdom Atomic Energy Authority, AERE-AM-61 (August, 1960).
23. C. R. TIPTON, JR., Minutes of Conference on Hydrogen in Uranium, Held at Battelle Memorial Institute, June 11, 1954. Battelle Memorial Institute, BMI-X-126 (July 2, 1954).
24. J. T. WABER AND E. S. WRIGHT, A method for the analysis of hydrogen in uranium. Univ. of California, Los Alamos Scientific Lab., AECD-4280 (1955).
25. L. A. FERGASON, C. H. MCBRIDE, AND D. E. SEIZINGER, Process Development Quarterly Progress Report, Mallinckrodt Chemical Works. MCW-1464, 57–60 (May 1, 1961).
26. A. ROBILLARD AND D. CALAIS, *Compt. rend.* **245**, 59–62 (1957).
27. W. E. HENRY, *Phys. Rev.* **109**, 1976–1980 (1958).
28. W. TRZEBIATOWSKI, A. SLIWA, AND B. STALINSKI, *Roczniki Chem.* **26**, 110–112 (1952).
29. W. TRZEBIATOWSKI, A. SLIWA, AND B. STALINSKI, *Roczniki Chem.* **28**, 12–20 (1954).
30. D. WAHL AND A. LIBOFF, Magnetic determination of impurities in uranium fuel slugs. Sylvania Electric Products, Inc., Atomic Energy Div., SEP-167 (June 18, 1956).
31. J. N. GREGORY, D. MAPPER, AND J. A. WOODWARD, *Analyst* **78**, 414–427 (1953).
32. R. E. TAYLOR, *Anal. Chim. Acta* **21**, 549–555 (1959).
33. W. S. HORTON AND J. BRADY, *Anal. Chem.* **25**, 1891–1898 (1953).
34. M. W. MALLETT AND C. B. GRIFFITH, *Trans. Am. Soc. Metals* **46**, 375–388 (1954).
35. W. G. GULDNER AND A. L. BEACH, *Anal. Chem.* **22**, 366–367 (1950).

36. R. A. YEATON, *Vacuum* **2**, 115–124 (1952).
37. C. H. PRESCOTT, JR., *J. Am. Chem. Soc.* **50**, 3237–3240 (1928).
38. H. C. VACHER AND L. JORDAN, *J. Research Natl. Bur. Standards* **7**, 375–399 (1931).
39. R. H. DALTON, *J. Am. Chem. Soc.* **57**, 2150–2153 (1935).
40. I. LANGMUIR, *J. Am. Chem. Soc.* **34**, 1310–1325 (1912).
41. H. M. RYDER, *J. Am. Chem. Soc.* **40**, 1656–1662 (1918).
42. C. BAQUE AND L. CHAMPEIX, *Comm. energie atomique, Rappt. No. 1386* (1959).
43. C. J. RODDEN, "Analytical Chemistry of the Manhattan Project," pp. 644–661. McGraw-Hill, New York, 1950.
44. F. E. JENKINS AND C. F. HALL, Summary Technical Report for the Period January 1, 1955 to March 31, 1955, National Lead Co. of Ohio. FMPC-540, 195–196 (April 15, 1955).
45. YU. A. KLYACHKO, L. L. LUNIN, and E. M. CHISTYAKOVA, *Trudy Komissii Anal. Khim., Akad. Nauk SSSR, Inst. Geokhim i Anal. Khim.* **10**, 10–16 (1960).
46. Z. M. TUROVTSEVA, N. F. LITVINOVA, N. M. VASIL'EVA, AND K. G. SEMENYUK, *Trudy Komissii Anal. Khim., Akad. Nauk SSSR, Inst. Geokhim. i Anal. Khim.* **10**, 109–116 (1960).
47. H. A. SLOMAN AND C. A. HARVEY, *J. Inst. Metals* **80**, 391–407 (1951).
48. C. B. GRIFFITH, W. M. ALBRECHT, AND M. W. MALLETT, Analysis for oxygen and nitrogen in uranium. Battelle Memorial Institute, BMI-1033 (April 23, 1955).
49. P. R. MORRIS, Summary Technical Report for the Period January 1, 1954 to March 31, 1954, National Lead Co. of Ohio. FMPC-405, 94–100 (April 15, 1954).
50. C. N. RICE, Determination of oxygen by the vacuum fusion method. U. S. Atomic Energy Commission, MDDC-356 (LADC-143) (October 5, 1944).
51. H. F. WALDRON, Process Development Quarterly Progress Report, Mallinckrodt Chemical Works. MCW-1465, 45–51 (August 1, 1961).
52. J. G. THOMPSON, V. C. F. HOLM, AND M. M. CRON, Report from Cooperating Laboratories for Month Ending June 1, 1944, U. S. Engineer Office, Manhattan District. CT-1819 (A-2645), 34 (July 6, 1944).
53. F. E. JENKINS AND C. F. HALL, Summary Technical Report for the Period April 1, 1955 to June 30, 1955, National Lead Co. of Ohio. NLCO-565, 172–174 (July 15, 1955).
54. J. T. WABER, Effect of annealing practice on the hydrogen content of uranium. Univ. of California, Los Alamos Scientific Lab., LA-1605 (November 1953).
55. H. W. RUSSELL AND H. R. NELSON, An analytical method for determining hydrogen in tuballoy. Battelle Memorial Institute, CC-1366 (A-2010) (February 9, 1944).
56. J. BIGELEISEN AND A. KANT, *J. Am. Chem. Soc.* **76**, 5957–5960 (1954).
57. A. N. ZAIDEL AND K. I. PETROV, *Zavodskaya Lab.* **24**, 1000–1001 (1958).
58. R. I. MILLER, An apparatus for the determination of total gas in fuel element samples. General Electric Co., Hanford Atomic Products Operation. HW-51452 (July 30, 1957).
59. T. C. EVANS, C. E. POLSON, J. A. FELLOWS, AND J. W. RICHES, Quarterly report of the Working Committee on Uranium Quality and Fabrication. E. I. du Pont de Nemours and Co., Savannah River Lab., DPST-55-488 (December, 1955).
60. H. R. GARDNER AND G. B. RITTER, Quarterly Technical Activities Report, Fuel Technology Sub-Section, April, May, June, 1955, General Electric Co., Hanford Atomic Products Operation. HW-37622, 3.14 (July 8, 1955). AEC Technical Information Service Extension, Oak Ridge, Tenn.
61. L. A. FERGASON, D. E. SEIZINGER, AND C. H. MCBRIDE, *Nuclear Sci. and Eng.* **10**, 53–56 (1961); *Proc. First Conf. Nuclear Reactor Chem. Gatlinburg, Tenn., October 12–14, 1960*, Paper No. 35.
62. D. E. SEIZINGER, L. A. FERGASON, AND C. H. MCBRIDE, Process Development Quarterly Progress Report, Mallinckrodt Chemical Works. MCW-1465, 53–54 (August 1, 1961).

NUCLEAR SCIENCE AND ENGINEERING: 13, 374–377 (1962)

An Improved Procedure for U^{235} Isotopic Ratio Analysis in Impure Materials

W. D. KELLEY* AND B. L. TWITTY

National Lead Company of Ohio, Cincinnati, Ohio

Received January 26, 1962; Revised May 1, 1962

An improved neutron activation procedure for determining the U^{235} content in impure uranium samples is presented. With 95% confidence, a relative precision of ±1% is obtained at the level of 0.7 wt % U^{235}.

An ethyl acetate extraction is used to purify the uranium chemically. Most of the uranium decay products are removed by extraction with 2-thenoyltrifluoroacetone (TTA) in xylene. The purified uranium, which is subsequently activated as U_3O_8, has a consistent gamma background level.

Utilization of a $1\frac{7}{8}$-in. i.d. well scintillation crystal has permitted the use of large diameter aluminum planchettes holding 2 gm aliquots of U_3O_8. This system has minimized the problem of varying irradiation geometries caused by differences in U_3O_8 bulk density.

Data from a sample recycle program are presented to illustrate the relative precision of ±1%. Comparisons between neutron activation and mass spectrometric results agree within ±1%.

INTRODUCTION

A method was needed to determine the isotopic abundance of U^{235}, precise to ±1% relative, in a variety of sample matrices, such as process residues, incinerator ashes, and magnesium fluoride bomb liners. The concentration of the uranium in the samples ranges from 1% to 100%. Most of the uranium processed has a U^{235} abundance in the 0.7% to 1% range.

The basic neutron activation procedure was reported by Beyer *et al.* (*1*) in 1958. This procedure was developed using relatively pure uranium materials.

When samples of widely divergent matrices were encountered, the accuracy and precision of the assay were affected by the different bulk densities encountered in the samples prepared for activation.

This paper presents modifications of the original procedure which permit the desired precision and accuracy with all of the types of uranium samples encountered at this laboratory.

* Present address: Westinghouse Atomic Fuels Department, Westinghouse Electric Company, Cheswick, Pennsylvania.

INSTRUMENTATION

A 2.5 gm radium–7.5 gm beryllium neutron source, in a 6 × 6 × 8 in. block of beryllium, is used for the thermal neutron activation. The sample irradiation port, $1\frac{3}{4}$ in. in diameter, extends upward from the beryllium moderator. The source shield consists of a 20-in. cube of paraffin surrounded by 8000 lb of lead bricks. A wire cage above the shield prevents accidental personnel exposure near the port.

A motor driven sample transport system is used to move the sample into and out of the irradiation port (*1*). It is controlled by an electronic sequential programmer.

A $1\frac{7}{8}$-in. i.d. NaI(Tl) well scintillation crystal is used to gross count the gamma activity. This crystal has replaced the previously used $\frac{5}{8}$-in. i.d. well crystal.

An electronic sequential programmer, designed and fabricated by J. Kramer of our Electronic Maintenance Section, replaced the electromechanical cam programmer formerly used (*1*). The programmer automatically controls the activation and counting cycle. The timing accuracy of the electronic system, which uses a 60-cycle time base, is inherently

superior to the accuracy of an electromechanical system. The sequential programmer incorporates a patch board so that all portions of the activation and counting cycle may be varied. This versatility is needed for the analysis of uranium samples highly enriched or depleted in U^{235}.

URANIUM PURIFICATION

In the original method (*1*), the uranium was dissolved in nitric acid and separated from the soluble impurities by a diethyl ether extraction. The uranium was stripped from the organic phase with water, precipitated with H_2O_2 at a pH of 1.0, and converted to U_3O_8 for activation analysis.

Because of the dangers involved in the routine use of diethyl ether, R. L. Pannemann of this laboratory substituted ethyl acetate as the organic extractant (*2*). The ethyl acetate is reclaimed for reuse by distillation, thus obtaining considerable economy in solvent costs. However, the ethyl acetate extraction did not adequately purify the uranium in samples containing large amounts of fluorides and phosphates. To overcome this problem, aluminum ion, added as an aluminum nitrate salting agent, was utilized to complex and render nonextractable any phosphate and/or fluoride ions present.

In many samples, the very large counting backgrounds, produced by uranium decay products, contributed to high coincidence losses and poor counting statistics. To reduce the decay products, principally thorium and protactinium, to a uniformly low level, an extraction with 0.5 *M* 2-thenoyltrifluoroacetone (TTA) in xylene was incorporated in the procedure (*3*). The extraction is made on a nitrate solution at a pH of 1.0.

The original peroxide precipitation and the conversion to U_3O_8 steps were retained.

Examples showing the degree of purification obtained on samples of high and low uranium content may be seen in Table I.

TABLE I

ANALYSES SHOWING DEGREE OF URANIUM PURIFICATION

Element	MgF_2 bomb liner		Dust collector	
	Original sample	Purified U_3O_8	Original sample	Purified U_3O_8
U	4.30%	84.64%	74.97%	84.69%
Th	954 ppm[a]	60 ppm[a]	296 ppm[a]	54 ppm[a]
Al	2300	<6	>8000	100
B	1900	0.25	8	0.25
Cr	2300	<5	130	<5
Fe	35,000	8	>1300	11
Mg	>300,000	43	>8000	41
Mn	1400	<4	135	<4
P	14,000	<20	540	<20
Si	>23,000	259	3300	17

[a] Impurities are expressed in parts per million on a uranium basis.

ACTIVATION SAMPLE PREPARATION

The original activation sample adopted by Beyer *et al.* (*1*) consisted of $\frac{1}{2}$ gm of purified U_3O_8 in a $\frac{1}{2}$-in. i.d. polystyrene vial. Four vials of each sample were prepared and analyzed.

R. L. Pannemann increased the sample size to two grams to provide better counting statistics. However, the increased sample size magnified the effect of differences in the bulk density of the purified U_3O_8 samples. The total vertical, as well as horizontal, area of the sample must be relatively constant since an appreciable portion of the neutrons is scattered from the moderator surrounding the well into the sample. A bulk density correction factor was devised, but it proved to be inadequate because of the variations in the packing of individual sample vials. Later work involved the measurement of the actual sample height in the plastic vial with a machinist's height gage. This technique resulted in improved, but still unsatisfactory, accuracy. The use of a controlled, low-temperature peroxide precipitation did not sufficiently reduce the variations in bulk density.

Two alternatives were available to minimize the density variation effect: (1) an increase in sample size to a constant volume by dissolution of the purified U_3O_8 in HNO_3, or (2) a decrease in the sample height to that of a thin disc. In the first case, the irradiation geometry is constant; and in the second case, small differences in sample height would cause only negligible changes in the observed activation. The dissolution method suffers the disadvantage that the low solubility of uranium in HNO_3 limits the amount of uranium that can be dissolved in the 5-ml volume of the vial to approximately 1.5 gm; and the larger sample volume causes the bulk of the uranium to be in a low neutron flux area of the well, yielding reduced counting levels and precision.

Since common uranium compounds have a low compressibility, compaction into a thin disc is not practical, but increasing the diameter of the vial permits a thin disc while utilizing the 2 gm sample necessary for good counting statistics. Since a solid scintillation crystal does not provide the necessary

TABLE II

TYPICAL COUNTING RESULTS

	Aliquots			
	1	2	3	4
Gross count (count/min)	335768	333568	334624	332453
Background (count/min)	50145	49175	50075	49202
Net count (count/min)	285623	284393	284549	283251
% U^{235} (by comparison)	0.942	0.937	0.938	0.932

Average % U^{235}: 0.937
Precision at 2σ: ± 0.004
Relative precision: $\pm 0.43\%$

TABLE III

TYPICAL RESULTS OF RECYCLE CONTROL
(wt % U^{235})

Type of material	Activation analysis			Mass spectrometric analysis	
	1st run	Recycle	Difference	Recycle	Difference[a]
Sump cake	0.946	0.951	−0.005	0.947	+0.004
Phosphate ash	0.711	0.712	−0.001	0.715	−0.003
Sump cake	0.947	0.941	+0.006	0.946	−0.005
Dust collector	0.946	0.943	+0.003	0.946	−0.003
Black oxide	0.952	0.948	+0.004	0.945	+0.003
Kiln ash	0.948	0.944	+0.004	0.940	+0.004
Black oxide	0.711	0.711	0.000	0.712	−0.001
Black oxide	0.709	0.713	−0.004	0.712	+0.001
Sump cake	0.943	0.942	+0.001	0.944	−0.002

[a] Mass spectrometric results subtracted from the activation recycle results.

TABLE IV

COMPARISON OF ACTIVATION AND MASS SPECTROMETRIC ANALYSES

Sample type	Activation % U^{235}	Mass spectometer % U^{235}	Difference
Dust collector	0.834	0.827	+0.007
Rolling sludge	1.27	1.26	+0.010
Dust collector	0.907	0.910	−0.003
Incinerator residue	0.734	0.733	+0.001
Furnace salt	0.738	0.738	0.000
Dust collector	0.920	0.925	−0.005
Sump cake	0.872	0.873	−0.001
Furnace sludge	0.756	0.754	+0.002
Dust collector	0.865	0.870	−0.005

detection efficiency, a 3-in. by 3-in. NaI(Tl) well scintillation crystal with a $1\frac{7}{8}$-in. i.d. was acquired. When the sample's horizontal surface area was increased by a factor of nine in going from a $\frac{1}{2}$-in. to a $1\frac{1}{2}$-in. diameter sample, density variation effects were no longer observed in the activation results.

Aluminum planchettes ($1\frac{1}{2}$-in. diameter) are used, since commercial plastic planchettes are not rigid enough. A tamper is used to distribute uniformly the 2 gm of U_3O_8. Several light coats of a quick-drying clear acrylic plastic from a pressurized can are sprayed on the U_3O_8 to cement it to the planchette. The plastic film maintains the uniform sample distribution during subsequent handling but does not affect the analysis.

NEUTRON ACTIVATION

Four sample aliquots are activated. The following cycle is used:

1. Background count (3 min).
2. Travel to activation (10 sec).
3. Activation with 4×10^5 thermal neutrons per second source (5 min).
4. Travel from activation (10 sec).
5. Delay (6 sec).
6. Gross count (1 min).

The sequential programmer controls the activation and counting steps. The counting results obtained on a bomb liner sample are shown in Table II. The impurities of this sample are given in Table I.

The net count is compared with those of standard samples, to obtain the wt % U^{235}. There is a linear relationship between wt % U^{235} and the net count over the working range of 0.7 to 1.0%.

The relative counting precision of the aliquot values is calculated. Any analysis with a counting precision numerically greater than $\pm 1\%$ relative at the 2σ level is not reported.

PRECISION AND ACCURACY

A quality control recycle program has been established. Previously reported samples are resubmitted under disguised numbers for neutron activation analysis and also for mass spectrometric analysis. Table III shows some of the results of this program. The mass spectrometric values have been rounded off to three significant figures.

Table IV shows a comparison of neutron activation and mass spectrometric analyses at other low enrichments.

CONCLUSION

The basic procedure for the neutron activation analysis of impure uranium materials for U^{235} content has been improved. The procedure has been applied

to samples ranging from 1 to 100% uranium, and potentially may be adapted to analyze samples bearing less than 1%. A relative precision at the 95% confidence level of ±1% at the 0.7 wt % U^{235} level is obtained. One experienced technician can routinely analyze from 3 to 8 samples in an eight hour day.

ACKNOWLEDGMENT

The authors wish to acknowledge the contributions of R. L. Pannemann to the procedure.

REFERENCES

1. W. W. BEYER, J. N. LEWIS, AND G. L. STUKENBROEKER, The determination of U^{235} by neutron activation. *Proc. Conf. on Modern Approaches to Isotopic Analysis of Uranium, Chicago, February 5–7, 1957*, USAEC report TID-7531 (Pt. 1), pp. 97–120. (October, 1957).
2. R. J. GUEST AND J. B. ZIMMERMAN, Determination of uranium in uranium concentrates, use of ethyl acetate. *Anal. Chem.* **27**, 931 (1955).
3. P. G. LAUX AND E. A. BROWN, Determination of thorium in uranium ores and feeds by solvent extraction employing thenoyltrifluoroacetone. USAEC report NLCO-742 (May 23, 1958).

NUCLEAR SCIENCE AND ENGINEERING: **13**, 378–384 (1962)

Capsule Irradiations of a Paste of Uranium–10 wt % Molybdenum Powder in NaK

E. C. KOVACIC AND PAUL R. HUEBOTTER
Atomic Power Development Associates, Inc., Detroit, Michigan

AND

JOHN E. GATES
Battelle Memorial Institute, Columbus, Ohio

Received March 2, 1962

Two in-pile capsule experiments have been performed to study the behavior during irradiation of a "paste" of fissionable particles settled at maximum density in a liquid-metal medium. The paste consisted of 150-μ nominal diameter, spherical particles of U–10 wt % Mo alloy in NaK and was irradiated to burnups of 0.0055 and 0.061 total at % in the Battelle Research Reactor. The irradiation capsule consisted essentially of a tube divided into two compartments by an orifice plate. The inside diameter of twin orifice tubes, projecting in either direction from the orifice plate, was such that the paste could flow by gravity from one compartment to the other. An underwater device to measure the gamma-ray emission from the irradiated fuel was used to check the mobility of the paste between increments of irradiation. The paste in the first experiment failed to flow after the first increment of irradiation, and examination of the capsule and particles failed to provide an explanation. The second experiment, performed after some refinements in procedure, was more successful. The mobility of the paste was demonstrated up to a burnup of 0.031 total at %, after which the flow became very sluggish even when assisted by vibration. Examination of the paste indicated that a buildup of oxide contamination in the capsule probably caused the sluggishness of the paste. There was no evidence in either experiment of particle agglomeration by a sintering or fission welding mechanism.

I. INTRODUCTION

A settled bed of particles or paste containing about 60 vol % fissionable particles in a liquid-metal carrier offers promise as a mobile fuel for a high-temperature fast breeder reactor. For the past five years, Atomic Power Development Associates, Inc. (APDA) has been conducting and sponsoring research to explore some of the problem areas in this fuel concept. To provide a focal point for the research activities, a conceptual fast breeder reactor employing a paste fuel and a paste blanket has been designed. In essence, the fuel and blanket subassemblies are vertical shell-and-tube heat exchangers, in which the paste flows downward on the shell side. Orifices at the bottom of the subassemblies restrict the velocity of the paste to a value in the range of 1 to 10 ft/hr. Upon leaving the subassemblies, the paste is diluted to a lean (approximately 5 vol %) slurry and pumped to cyclone separators located in the upper plenum, where the paste is reconstituted and gravity-fed to the top of the core and blanket subassemblies.

Among several feasibility problems, the one concerning the effect of irradiation on the mobility of the paste required experimental evaluation. Specifically, it was feared that a fission event occurring near the point of contact between two particles would supply sufficient energy to cause interparticle diffusion and the "stitching" of particles one to another throughout the paste bed. Obviously this would curtail the mobility of the fuel and could prevent its flowing through orifices sized to accommodate the original paste. Although paste in the conceptual reactor would be flowing, and the movement of particles with respect to one another could break these bonds, a more convenient and conservative test would be one in which the paste was static during irradiation.

The swelling of particles and the formation of fission gas bubbles within the paste bed could also affect the rheology of the fuel, but because such effects can be simulated out-of-pile, the irradiation program described here was designed primarily to prove or disprove the stitching mechanism described above.

An attempt was made to estimate the burnup at which particle-stitching would render the paste immobile. Dienes and Vineyard (*1*) give the volume of the cylindrical thermal spike created by a 100-Mev fission fragment as about 1.2×10^{-15} cm³. If the energy were dissipated uniformly, all the atoms within this volume would be spiked to a temperature of about 4000°C. The other fragment from the same fission event would bring the total affected volume to about 2×10^{-15} cm³. Since the volume of a 150-μ sphere is 1.76×10^{-6} cm³, a given point on the sphere (the point of contact with an adjacent sphere) has the following probability of escaping a fission event:

$$\frac{1.76 \times 10^{-6} - 2 \times 10^{-15}}{1.76 \times 10^{-6}} = 1 - 1.135 \times 10^{-9}$$

The number of fission events, n, which produce a 50% probability of affecting the contact point, can be evaluated as follows:

$$(1 - 1.135 \times 10^{-9})^n = 0.5$$

$$n = 6.12 \times 10^8$$

In the 150-μ sphere of U–10 wt % Mo, there are a total of 8.67×10^{16} atoms. Therefore the burnup which corresponds to a 50% probability of spiking the contact point is:

$$\frac{6.12 \times 10^8(100)}{8.67 \times 10^{16}} = 0.7 \times 10^{-6} \text{ total at \%}.$$

The burnup for a 90% probability is 2.3×10^{-6} at %. Even if the spiked volume were two or three orders of magnitude smaller than that estimated by Dienes and Vineyard, it is clear that the effects of stitching, if a real phenomenon, would be apparent at very low burnup. The burnup per pass through the core of the conceptual reactor is about 1×10^{-3} at %. Thus the danger exists that the paste would become immobilized during a single core residence time.

The experimental research was performed at Battelle Memorial Institute, under contract from APDA. Two experiments were performed, both involving the irradiation of a paste of U–10 wt % Mo particles in NaK. The paste was contained in a capsule divided into two compartments by an orifice plate. Twin orifice tubes, projecting in either direction from the orifice plate, permitted the paste to flow from one compartment to the other when the capsule was inverted. The mobility of the paste was studied periodically by a device which measured the intensity of gamma radiation emitted from the fuel. The flow of paste into the empty compartment of the capsule was indicated by an increase in the measured intensity of gamma radiation being emitted from that compartment. Two capsules containing the paste were irradiated in the Battelle Research Reactor (BRR), a swimming-pool-type research reactor. After irradiation, the capsules were opened and the fuel particles were examined. The results of these experiments are described in this paper.

II. PREPARATION OF ALLOY POWDER

Spherical particles of U–10 wt % Mo alloy were prepared for the irradiation tests by the spinning-disk method in which molten metal was poured onto a ceramic disk rotating at high speed. Droplets of the material were thrown from the spinning disk, solidifying in predominantly spherical particles in a range of sizes.

The basic spinning-disk equipment (Fig. 1) consisted of a small vacuum induction-melting furnace, 3 ft in diameter, adapted to contain a vertically mounted high-speed motor. A steel wheel, 2.5 in. in outside diameter, with a contoured, conical ceramic insert was mounted on the motor shaft. The insert was 1 in. high and had a diameter of 2 in. along the base. This wheel was centered in the furnace directly below the pouring lip of a stabilized-zirconia crucible.

The alloy charge, which consisted of 10% enriched uranium and high-grade molybdenum melting stock, was placed in the crucible and heated to 3000°F under a dynamic vacuum of less than 2×10^{-3} mm Hg. After the alloying was complete, the furnace chamber was back filled with Bureau of Mines Grade A helium to an absolute pressure of ⅓ atm. The motor was energized and, after the terminal disk speed of 10,000 rpm was attained, the molten alloy was top-poured from the crucible onto the spinning disk.

A number of experimental runs were made to optimize the process variables. For example, the pouring temperature was the mean between two temperature extremes that produced the following effects: (1) too low a pouring temperature (2500 to 2700°F) caused the molten alloy to collect on the disk and overload the motor; (2) too high a pouring temperature (> 3000°F) resulted in the failure of

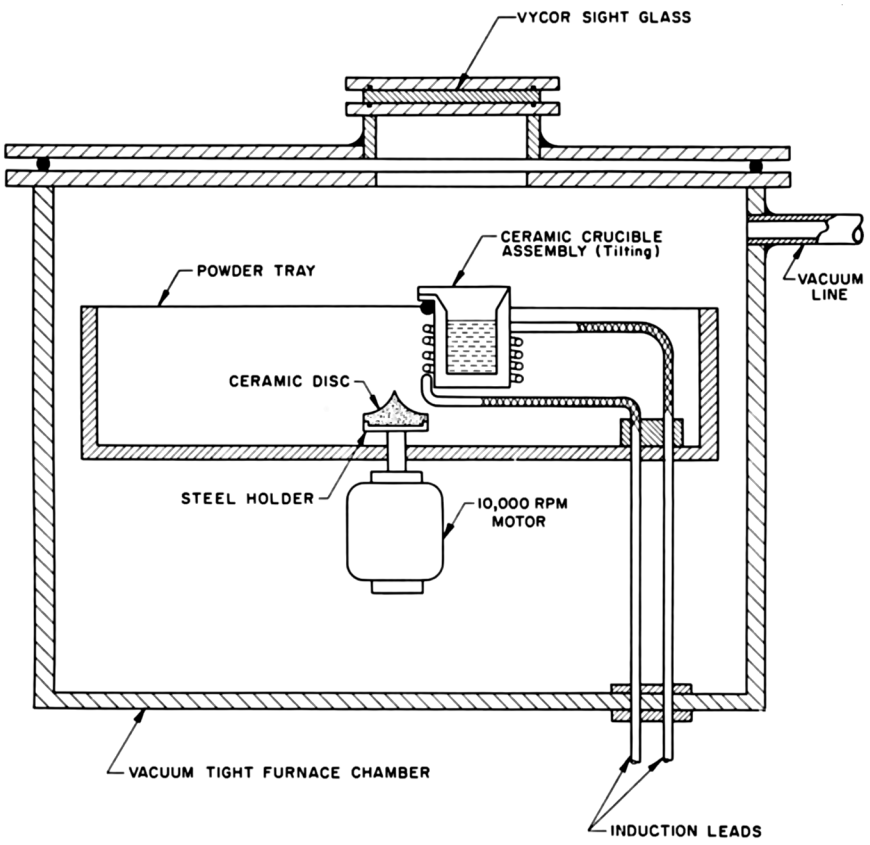

FIG. 1. Schematic of spinning disc apparatus as adapted for preparation of powder.

droplets to solidify before splattering against the side of the powder tray.

In a typical run, about 60% of the alloy charged to the spinning-disk equipment was converted to powder. Much of the loss was independent of batch size, so the yield could have been increased by increasing the amount of alloy charge. The sieve analysis of a typical run is given in Table I. Most of the powder was spherical or near-spherical in shape. Irregularly-shaped particles fell predominantly in the larger-particle-size fractions.

The size fraction of particular interest in this program was the 150-μ fraction ($-70 + 140$ mesh). Nonspherical particles were separated from this fraction by a tabling operation. Thirty-six percent of the 150-μ fraction was retained for the in-pile tests. Figure 2 shows a group of particles representative of those used in the irradiation experiments.

III. EXPERIMENTAL APPARATUS

The capsule developed for the paste-flow experiments is shown in Fig. 3. Basically, it consisted of an inner capsule compartmented by an orifice plate, housed within an outer containment capsule. The annulus between the two capsules was fitted with a Lavite sleeve, which provided the desired resistance to heat flow. The nominal values of centerline paste temperature and power generation were 900°F and 700 Btu/hr. This power generation was based on the following nuclear parameters: (1) 30-gm charge of alloy powder, containing 2.7 gm of U^{235}, and, (2) an unperturbed thermal neutron flux of 6×10^{12} nv which, based on a nuclear mock-up study, yielded an effective flux of 1.8×10^{12} nv.

Noteworthy features of the capsule design were: (1) the thermocouples, (2) the twin orifices, and (3) a flexible lead tube which allowed the capsule to be inverted for paste mobility demonstrations in a special scanning rig erected in the BRR pool.

Of the nine chromel–alumel thermocouples, eight monitored temperatures on the outside surface of the inner capsule. The remaining thermocouple was a stainless-steel-sheathed unit inserted into a $\frac{3}{8}$-in. long well. This well protruded into the paste chamber to allow the thermocouple to measure the temperature of the bulk paste. The design of the orifice plate and tubes and the sizing of the orifices followed studies at APDA that employed glass capsules and simulant pastes. It was found that bridging of an orifice could occur if the ratio of orifice diameter to particle di-

ameter was less than seven. Accordingly, an orifice diameter of 0.067 in. was selected. This was 11 times the nominal particle diameter and 8 times the maximum diameter in the −70 + 140 mesh fraction.

Apparatus to study the mobility of the paste was located in the BRR pool. This apparatus was made up of the following components:

1. A stationary ionization chamber the output signal of which was fed into a rate meter for visual indication.

2. A holding jig that permitted the capsule to be positioned adjacent to the detector but separated from the detector by a lead shield with a collimating slit.

3. Mechanisms which allowed the holding jig (with capsule inserted) to be rotated 180 deg and adjusted vertically with respect to the slit.

With this apparatus, the location of the paste within the capsule could be determined when the capsule was in either the normal or inverted position. The location, of course, depended on the ability of the paste to flow back and forth through the orifices.

TABLE I

TYPICAL SIZE DISTRIBUTION OF PARTICLES MADE BY THE SPINNING-DISK METHOD

Mesh size	Average particle diameter (μ)	Percent by weight
−12 + 18	1350	21.5
−18 + 30	800	22.4
−30 + 50	410	22.2
−50 + 70	250	8.0
−70 + 140	150	17.0
−140 + 325	75	8.0
−325	<44	0.9
		100.0

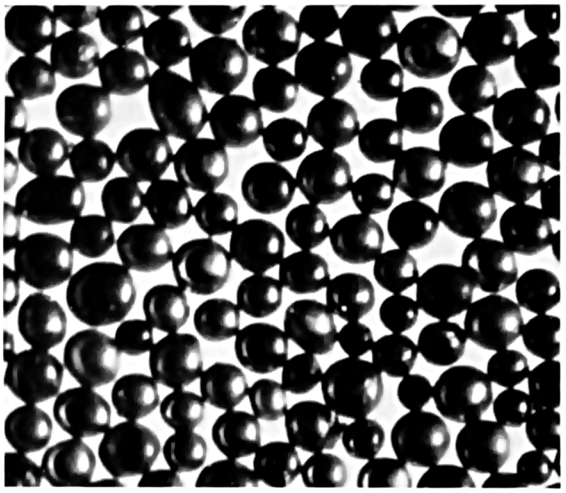

FIG. 2. Typical U–10 w % Mo powder used in irradiation capsules.

IV. PREIRRADIATION PROCEDURES

The capsule charge consisted of about 30 gm of the alloy powder of proper size and shape, and about 12 cm³ of NaK of the eutectic composition (~23% Na, 77% K). Routine procedures to minimize oxygen contamination were followed. The capsules were thoroughly cleaned and loaded in a dry box, from which oxygen and moisture could be all but eliminated by evacuation and purging with Grade A helium.

After the capsules were loaded and sealed, they were subjected to a routine helium leak check. A heat-treatment at 900°F was performed to insure wetting of the powder and the stainless-steel capsule components by the NaK. The first capsule was heat-treated for one day; the second, fourteen days. A number of room temperature flow determinations were made to establish the flow characteristics of the paste in the unirradiated condition. For example, individual measurements were made with the capsule rotated in 90 deg increments to determine whether the position of the orifices with respect to the axis of rotation had any influence on flow behavior. It did not. Temperature was found to affect flow rate; for example, higher temperatures pro-

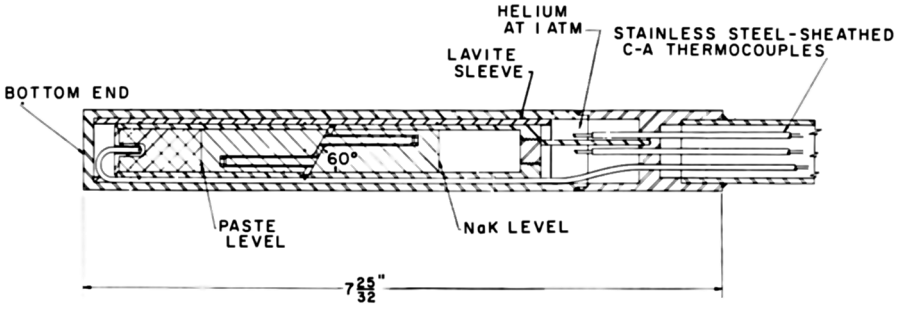

FIG. 3. Paste capsule

duced higher flow rates. However, flow was regular at all temperatures tested.

The preirradiation tests of the two capsules were somewhat different, but the indications were the same. Paste flow was consistent, and it seemed at this point as though all possible nonnuclear causes of paste immobility could be discounted.

V. IRRADIATION OF PASTE CAPSULE NO. I

The first capsule was manually positioned in an aluminum holder located adjacent to the face of the BRR core. About 100 sec after the start of this irradiation, the temperature of the paste reached a maximum of 1100°F. The capsule was immediately moved into a lower flux, and the temperature dropped to 750°F. Later the capsule was moved into a higher flux, and the desired temperature of 900°F was established.

After 247 hr of irradiation, the alloy powder had accumulated a calculated burnup of 0.0055 total at %, and the first paste mobility check was attempted with the apparatus described above. The paste did not flow through the orifice. The sample activity scans in Fig. 4 illustrate the situation. Although the activity scan was expected to follow the solid line when the capsule was in the inverted position, it actually followed the dotted line, indicating that the paste had moved to the orifice plate but not through the orifice. Attempts to initiate paste flow by striking the capsule against the side of the pool were unsuccessful. The ensuing decision was to terminate the experiment and ship the capsule to the Argonne National Laboratory for examination.

Postirradiation examination of the capsule and its contents did not provide an explanation for the immobility of the paste after the relatively short period of irradiation. The orifices were not plugged, and a microscopic examination of the particles revealed that their size, shape, and surface characteristics were essentially unchanged. There was no evidence of particle agglomeration; however, it was feared that if the particles had become agglomerated by the stitching mechanism described above, the weak bonds between the particles could have been broken during the removal of the NaK from the capsule by reaction with butyl·alcohol. Care had been taken to avoid breaking of the bonds, but it was considered that the examination did not provide decisive evidence upon which the stitching theory could be disproved.

VI. IRRADIATION OF PASTE CAPSULE NO. II

To avoid any temperature excursion such as was experienced at the beginning of the first experiment, the lead tube of the second paste capsule was attached rigidly to a machine rack which could be moved vertically by a hand-operated crank. At the bottom end, the capsule was supported and located by the aluminum holder used in the irradiation of the first capsule.

After 33 min in a neutron flux such that the paste temperature was only 350°F, the capsule was given a mobility check which showed that, as in the first experiment, the paste did not flow through the orifice. As permitted by its low radioactivity, the capsule was removed from the pool, vibrated for one minute, and given a heat treatment which consisted of a 500°F to 900°F to 500°F cycle in 30 min. One or both of these operations reestablished paste mobility, and the capsule was returned to its position in the reactor, where the irradiation was continued for 30 min at a temperature of 425°F. This time, the capsule was withdrawn from the flux position so slowly that the rate of cooling was about 30°F/min from 425°F down to pool temperature. Measurements showed that the paste flowed through the orifice.

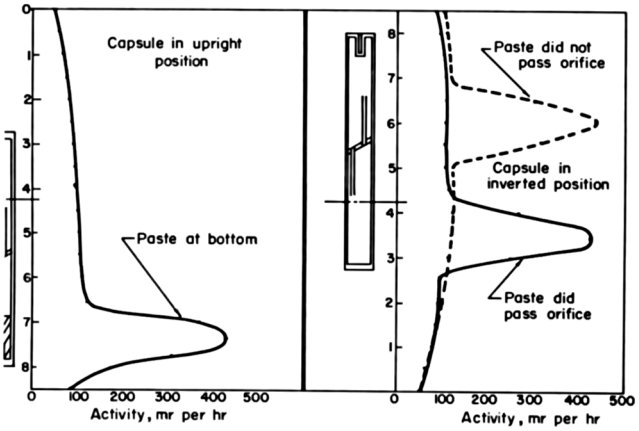

FIG. 4. Indicated paste location by activity scanning

The capsule was then irradiated for one hour at 850°F, and was cooled at a somewhat faster rate than that following the second run. The paste did not flow, and the capsule had to be vibrated once again.

At this point in the experimentation, a failure mechanism based on the rate of cooling was postulated. The solubilities of the oxides of NaK increase with temperature. Although precautions were taken to minimize oxygen contamination, it is quite likely that the NaK either initially contained, or picked up from the capsule and particles, a sufficient amount of oxide insoluble at pool temperature to either (1) agglomerate and plug the orifices, or (2) flocculate the particles and prevent their passage through the orifices. If the cooling rate was slow, as it had been in all of the out-of-pile tests, the oxides may have had an opportunity to migrate to the cooler capsule wall, leaving the NaK in the paste and around the orifices free from insoluble oxides. Paste mobility would thus not have been impaired during the measurements.

Subsequent to the third run, the withdrawal rate was carefully controlled and this seemed to help. (Table II gives the pertinent data for 18 runs.) After the fourteenth run, the flow of paste became noticeably sluggish and had to be assisted by vibration of the lead tube. Finally, after the eighteenth run, vibration became ineffective in maintaining flow, and the irradiation was terminated.

The procedure for examining the second capsule and its contents at the Battelle Hot Cell Facility was somewhat different from that used for examining the first capsule in that it was considered essential to avoid a NaK reaction before determining whether the particles were agglomerated. To accomplish this, the capsule was opened in a lucite tank filled with reagent-grade xylene, a liquid that does not react

TABLE II

SUMMARY OF PERTINENT IRRADIATION CONDITIONS AND RESULTS OF PASTE-FLOW DETERMINATIONS FOR PASTE CAPSULE II

Run	Duration (hr)	Accumulated time (hr)	Maximum paste temperature[a] (°F)	Cooling rate (°F/min)	Summary of paste-flow behavior
1	0.55	0.55	350	—	Good after out-of-pool vibration and heating
2	0.58	1.13	430	30	Good
3	1.0	2.1	860	40	Good after out-of-pool vibration
4	1.5	3.6	720	24	Good
5	2.6	6.2	895	10	Good
6	17.0	23.2	860	10	Good
7	27.5	50.7	875	[b]	No determination made
8	85.3	136	955	10	Long vibration period required to achieve full paste flow
9	7.0	143	900	[b]	No determination made
10	255	398	710	6	Good
11	280	678	960	[b]	No determination made
12	286	964	860	24	Erratic, finally full flow achieved (without vibration)
13	215	1179	760	[b]	No determination made
14	253	1432	855	[b]	Erratic, did not achieve full flow with vibration
15	86	1518	910	[b]	No determination made
16	165	1683	820	15	Very poor flow even with vibration
17	51	1734	1160	10	Partial flow observed vibration
18	155	1889	1070	10	Very little flow, vibration ineffective

[a] Temperature data are from readings of Thermocouple 9, which was inserted into the well located in the paste zone.

[b] Except for Run 14, which was terminated by a reactor scram, the runs thus designated ended by a normal reactor shutdown. Since mobility determinations were not planned, no attempt was made to exercise the slow-cooldown procedure.

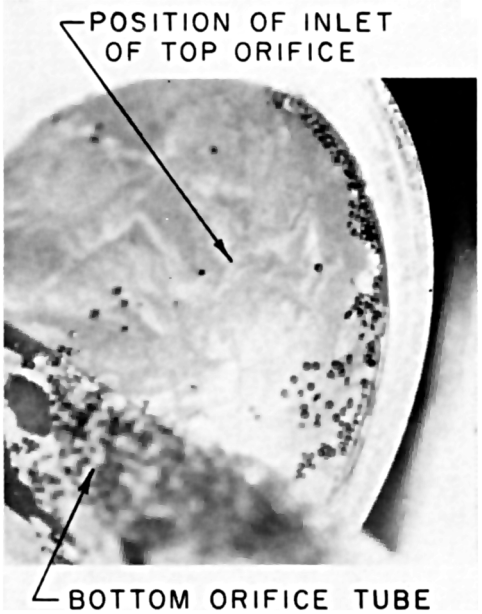

FIG. 5. Orifice tube and plate showing oxidelike accumulation on outside of bottom orifice tube and apparent blockage at inlet of top orifice tube.

with NaK nor absorb moisture from the air at a rapid rate. The contents of the capsule were emptied onto a screen with 300-μ openings. The NaK was silvery in appearance as it flowed from the capsule and it coalesced into globules on the screen at the bottom of the tank. Most of the particles passed through the screen and were collected in a sheet metal box. This observation provided the best evidence that the stoppage of flow was caused by something other than "stitching" of the particles.

The particles appeared to be unaffected by irradiation. Examination of the capsule provided evidence that the stoppage of paste flow was probably caused by a buildup of oxide contamination. A prime example of this is shown in Fig. 5, a photograph which shows an oxide-like skin completely bridging the entrance to the top orifice tube. The presence of oxides and the gradual buildup of this skin across the orifice tubes would explain the reduction in paste mobility observed during the final increments of irradiation. Extraction by the NaK of adsorbed gas from the surfaces of the capsule components and fuel particles could account for the gradual buildup of NaK oxides.

VII. CONCLUSIONS

The theory that small particles in intimate contact would be stitched together into an immobile mass after a very low burnup, seems to have been discredited by these experiments. Thus, a major feasibility problem concerning the potential use of a settled particle bed or paste in a mobile-fueled-reactor has been removed.

The loss of mobility in both experiments was attributed to oxide contamination in the capsules. The effect of the initial contamination can be minimized by promoting the mass transport of low temperature insolubles to the capsule wall. This, at least, seems to be the only logical explanation for the observation that paste mobility depended upon the rate of cooling. It is believed that the first capsule would have been more successful had it been possible to control the cooling rate.

It is considered that the loss of paste mobility in the second capsule resulted from a gradual buildup of oxide contamination, probably formed by oxygen leached from the particle and capsule surfaces. These oxide problems plague the static type of experiment described herein but, fortunately, through the use of cold traps and oxygen "getters," can be eliminated in loop experiments, and in the conceptual reactor discussed previously.

Acknowledgments

The authors would like to express appreciation for the contributions of S. D. Bowers and R. J. Hennig of Atomic Power Development Associates, Inc., and J. H. Stang and E. C. Foster of Battelle Memorial Institute. The authors would like also to express their gratitude to the Argonne National Laboratory, where the postirradiation examination of the first paste capsule took place.

REFERENCES

1. G. J. Diens and G. H. Vineyard, "Radiation Effects in Solids." Interscience, New York, 1957.

NUCLEAR SCIENCE AND ENGINEERING: 13, 385–390 (1962)

Resonance and Thermal Neutron Self-Shielding in Cobalt Foils and Wires*

T. A. EASTWOOD AND R. D. WERNER

Atomic Energy of Canada Limited, Chalk River, Ontario, Canada

Received March 5, 1962

An experimental study of neutron self-shielding in cobalt foils and wires has been made by an activation technique. Cobalt foils ranging in thickness from 0.0004 to 0.004 in. and 0.005 in. thick Co–Al alloy reference foils containing 1% Co were irradiated under cadmium in the NRX reactor. The Co^{60} specific activity in the pure foils was compared with that in the reference foils to give the gross self-shielding factors. Experimental resonance self-shielding factors were obtained by separating the $1/v$ part from the gross self-shielding factors, and agreement with calculated resonance self-shielding factors for foils was observed. Self-shielding factors for wire ranging in diameter from 0.001 to 0.025 in. and for 0.050 in. diam 1% Co–Al alloy wire were also measured since they are of practical importance and have not been calculated. Measurements of self-shielding factors for thermal neutrons were made for cobalt wires and these agree with theory.

INTRODUCTION

Cobalt is frequently used in reactor experiments to measure the neutron flux. For this purpose a knowledge of the thermal neutron capture cross-section and the resonance capture integral is required. The latter quantity was recently remeasured by Johnston *et al.* (*1*) and their result, 75 ± 5 barns, is about 50% higher than the previously accepted value (*2*). They point out that the early result was obtained with thick samples (6.1×10^{19} Co atoms/cm^2), whereas their experiments were made with a dilute Co–Al alloy (1.2×10^{18} Co atoms/cm^2) and give the resonance capture integral at infinite dilution. This suggests large self-shielding effects with cobalt and indicates a need for correction factors in those experiments in which thick cobalt detectors are used.

It is not surprising that there should be considerable self-shielding in cobalt because there is a prominent resonance in the neutron cross section at 132 ev which rises to a maximum of about 10,000 barns. This resonance is known to be primarily due to scattering but this can, of course, result in self-shielding in thick samples. Cobalt also has a number of smaller resonances at much higher energies. Neutron self-shielding theories have been reviewed by Zweifel (*3*) and there does not appear to be a satisfactory general treatment for resonances in which scattering predominates. However, Selander has used a semianalytical method to evaluate self-shielding factors for activation measurements with cobalt and manganese foils (*4*). His calculations are based on the published resonance parameters for these elements (*5*). We have measured the self-shielding factors for cobalt foils and compare the results of the experiments and calculations in the Results and Discussion section.

Cobalt wires are used more frequently than foils in reactor experiments and self-shielding factors for wires have not been calculated. Therefore, self-shielding factors for cobalt wires up to 0.025 in. diam were determined experimentally and are presented later. In addition, thermal neutron self-shielding factors for cobalt wires of the same diameter were obtained from the experiments and have been compared with the results of calculations reviewed by Zweifel (*3*) following the work of Case *et al.* (*6*).

EXPERIMENTAL

A. MATERIALS

Since cobalt foils of the required thicknesses could not be obtained quickly from commercial sources, the foils used in these experiments were prepared by electroplating cobalt onto copper. After a layer of sufficient thickness had been deposited electrolysis

* A preliminary account of this work was given at the ANS Meeting, June 1961 in Pittsburg.

was stopped and the copper was dissolved in trichloroacetic acid-ammonium hydroxide mixture. The thickness of the foils was explored with a micrometer that had small ball bearings attached to its jaws and so measured the thickness over a small area. Disks, 0.15 in. diam, were punched out of a uniform portion of each foil for irradiation.

For reference, Co–Al alloy foils of the same diameter and 0.005 in. thick containing 1 % cobalt were irradiated simultaneously. The alloy foils were made by rolling alloy wire to the required thickness.

Spectroscopically pure cobalt wires ranging in diameter from 0.001 to 0.025 in. were obtained from Johnson Matthey and Mallory, Ltd., Montreal, Canada. The wires taken for irradiation were 0.5 to 0.75 in. long.

Cobalt–aluminum alloy wires, 0.05 in. diam, with nominal cobalt contents of 0.1 and 1 % were obtained from The Sigmund Cohn Corp., Mount Vernon, N. J., and 0.5 to 0.75 in. lengths were taken for irradiation. The Co–Al alloy foil just referred to was prepared from this wire. The cobalt contents of the alloys were determined by an ASTM colorimetric method (*7*), and were found to be 0.104 ± 0.001 and 0.976 ± 0.006 wt %.

B. Irradiations

The irradiations were all made in an air-filled tube at a lattice position in the NRX reactor (*8*). Cylindrical cadmium boxes $\frac{5}{16}$ in. diam, 1 in. long, and 0.030 in. wall thickness were used for under-cadmium irradiations. Two or three foils were irradiated at a time and they were supported by aluminum so that the maximum separation within the confines of the cadmium box was ensured. The wires were also irradiated a few at a time. Aluminum supports were used to keep them parallel to the axis of the cadmium box at maximum separation (about $\frac{3}{16}$ in.).

C. Measurements

The Co^{60} activity produced in the foils was measured with a well-type NaI (Tl) crystal counter, 1.75 in. diam and 2 in. long. The discriminator in the amplifier was adjusted so that only pulses from gamma rays of energy greater than about 1 Mev were passed to the scaler. A Co^{60} standard source was counted at frequent intervals during the measurements and so allowance could be made for small changes in the efficiency of the counter.

In order to allow for the decay of short-lived radioactive impurities, such as Na^{24} from the Al^{27} (n, α) reaction, a cooling period of at least two weeks preceded the Co^{60} measurements. The most likely long-lived radioactive contaminants are Co^{58} and Fe^{59} formed by the Co^{59} (n, 2n) and Co^{59} (n, p) reactions respectively. It has been estimated from the systematics of fast neutron reaction cross sections observed in NRX (*9*) that the contribution to the total radioactivity from these contaminants is less than 0.5 %. This expectation has been confirmed by observations of the decay of the radioactivity in representative foils and wires extending over a period of 1 to 1.5 years, in which it was found that the rate of decay did not depart from that of a five year old Co^{60} source.

RESULTS AND DISCUSSION

As mentioned in the Introduction, our object is to determine the extent of self-shielding in cobalt foils and wires. To this end we now present the experimental data, our method of analyzing the data, and the self-shielding factors thus obtained. In addition, we make a comparison of the experimental self-shielding factors with the results of calculations by Selander (*4*) for resonance neutrons in cobalt foils and with those summarized by Zweifel (*3*) for thermal neutrons in cobalt wires.

Selander calculated self-shielding factors for the "resonance" part of the epithermal neutron absorption, while the experimental results include contributions both from the "resonance" and the "$1/v$" components of the cross section. We use the convention for neutron flux and cross sections proposed by Westcott *et al.* (*10*) to discuss the resolution of our experimental results into "resonance" and "$1/v$" components for comparison with calculation.

The reactor neutron flux, according to the convention, is composed of Maxwellian and epithermal components. The Maxwellian part is characterized by a temperature T and the epithermal component is proportional to dE/E with a low energy cutoff at $5kT$ (0.13 ev) in reactors such as NRX. We are concerned with experiments made with cadmium covers and the convention gives the following relationship for the cadmium ratio of an infinitely thin detector:

$$R_{Cd} = \frac{(r\sqrt{T/T_0})^{-1} + s_0/g}{s_0/g + 1/K} \qquad (1)$$

This relation applies to detectors such as cobalt which follow the $1/v$ law reasonably closely below 0.5 ev although resonances exist at higher energies. The full significance of the symbols is discussed by Westcott *et al.* (*10*) but briefly:

r is a measure of the epithermal component of the reactor spectrum.

T is the temperature characterizing the Maxwellian component.

$T_0 = 293.60°K$ (20.44°C).

$s_0 = s\sqrt{T/T_0}$.

s and g depend on the departure of the cross section from a $1/v$ dependence in the epithermal and thermal regions respectively. For cobalt $g = 1$ (*11*).

K is a function of the cadmium cover thickness and calculated values for beam and isotropic neutron incidence are given by Westcott *et al.* (*10*).

For our present purpose Eq. (1) requires further development. In irradiations under cadmium the resonance capture contribution, s_0, is reduced by the attenuation of the resonance neutrons by cadmium. We represent this by a factor F. Thermal neutrons leak through the cadmium and contribute to the activity produced in the detector. The term $(r\sqrt{T/T_0})^{-1}$ mainly represents the contribution from thermal neutrons in an uncovered irradiation and the contribution under cadmium will therefore be $h(r\sqrt{T/T_0})^{-1}$ where h is the transmitted fraction of the thermal neutron density for the initially Maxwellian component.

Bigham and Pearce (*12*) have shown that the slowing-down spectrum at a vacant lattice site in a rod-type reactor such as NRX departs from the $1/E$-form assumed by Westcott in developing the convention. Consequently, both the resonance- and $1/v$-capture contributions to the activity induced in cobalt irradiated under cadmium in a vacant NRX lattice site will differ from contributions observed in irradiations made in a $1/E$ spectrum. It follows that the effective s_0 value observed in irradiations in a vacant NRX lattice position should differ from that observed in experiments made with a $1/E$ spectrum and, in fact, unpublished results of preliminary experiments by the authors show this behavior. Therefore, s_0 should be corrected by a factor D_1 in experiments made in a non-$1/E$ slowing-down spectrum. Similarly, in order to correct for the effect of the departure of the slowing-down spectrum from $1/E$ dependence on $1/v$-capture we multiply the $1/K$ term, which represents $1/v$-capture in Eq. (1), by a factor D_2.

In a thick detector self-shielding reduces the response (a) to resonance neutron capture by a factor G_1, and (b) to $1/v$-capture by G_2. It is these factors that have been calculated by Selander (*4*), and it is with the former that we are particularly concerned. The under-cadmium response of a cobalt detector of thickness t, A_t, relative to that of an infinitely thin cobalt detector, A_0, is therefore as follows:

$$\frac{A_t}{A_0} = \frac{FD_1 G_1 s_0 + D_2 G_2/K + h(r\sqrt{T/T_0})^{-1}}{FD_1 s_0 + D_2/K + h(r\sqrt{T/T_0})^{-1}} \quad (2)$$

and hence

$$G_1 = \frac{1}{FD_1 s_0}\left\{\frac{A_t}{A_0}\left[FD_1 s_0 + \frac{D_2}{K} + h\left(r\sqrt{\frac{T}{T_0}}\right)^{-1}\right] - \left[\frac{DG_2}{K} + h\left(r\sqrt{\frac{T}{T_0}}\right)^{-1}\right]\right\} \quad (3)$$

Results of Foil Experiments

Equation (3) was used to obtain resonance self-shielding factors for foils from the experimental values of A_t/A_0, the ratio of the rate of the $Co^{59}(n, \gamma)Co^{60}$ reaction in cobalt foils to the rate in the Co–Al alloy foil in irradiations under cadmium. Thus we have assumed that the alloy foil (3.6×10^{18} Co atoms/cm^2) is an infinitely thin detector, but this seems reasonable because Selander has shown that G_1 is unity for foils up to about 2×10^{19} Co atoms/cm^2 thickness, i.e., six times the thickness of the alloy foil. The results are given in Table I and a comparison of these experimental values with the results of Selander's calculations is given in Fig. 1. The values used for the various factors which appear in Eq. (3) are also given in Table I. A discussion of the choice of these factors follows.

We assume that G_2 is unity for all our foils; this is supported by Selander's calculation which shows that $G_2 = 1$ for foils five times the thickness of our thickest foil. The value of $D_1 s_0$ used is the effective value of s_0 obtained from several measurements made in the irradiation position used for the present experiments. It happens that it agrees with the value based on the work of Johnston *et al.* (*1*, *11*). The value of $(r\sqrt{T/T_0})^{-1}$ was also taken from several measurements made in the vacant lattice site used in the present experiments.

There is some uncertainty in the choice of $1/K$. Westcott *et al.* (*10*) give values for both beam geometry and isotropic neutron incidence but the conditions of the present irradiations are somewhere

TABLE I

Resonance Self-Shielding Factors for Cobalt Foils
$F = 0.977$, $D_1 s_0 = 1.74$, $D_2 = 0.968$, $K = 2.06$, $h = 1.36 \times 10^{-4}$, $r\sqrt{(T/T_0)} = 2.4 \times 10^{-2}$

Foil thickness (in. $\times 10^3$)	0.4	0.9	1.0	2.0	3.6	4.0
Cobalt atoms/cm^2 ($\times 10^{-19}$)	9.24	20.8	23.1	46.2	83.1	92.4
A_t/A_0	0.873	0.765	0.715	0.679	0.576	0.573
G_1	0.84	0.70	0.63	0.59	0.46	0.45

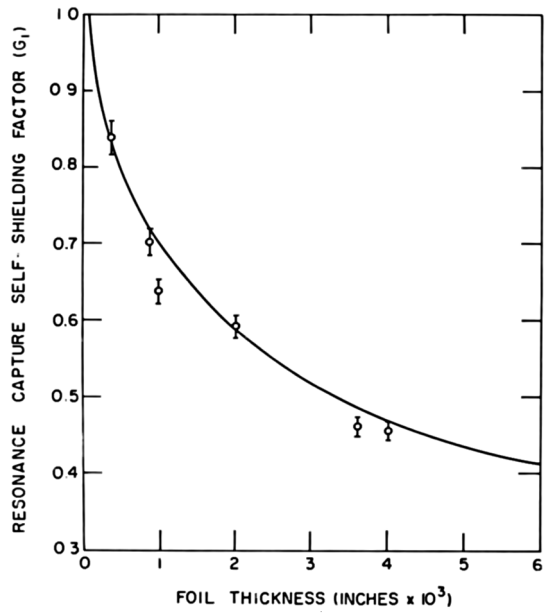

FIG. 1. Resonance capture self-shielding factors for cobalt foils. The points are experimental results; the line is from Selander's calculations (*4*) made using the parameters for the first resonance in the cobalt cross section.

between these extremes. We have used the mean of the two and increased the error assigned to G_1 so that it includes the effect of variations of $1/K$ within the two limits.

The values of F and h were taken from a preliminary investigation of neutron attenuation by cadmium covers made by Matayas and Eastwood. They used cobalt–cadmium assemblies similar to those used in the present experiments, but the irradiations were made in a different spectrum and so their results only yield 1.00 and 0.95 for the limits of F. However, G_1 is not sensitive to F when F is close to unity and the use of a value midway between the limits introduces an error of less than 0.5% in G_1 for the thickest foil and less than that for the others. The factor G_1 is even less sensitive to the choice of h within the limits set by the experiments of Matayas and Eastwood.

The factor D_2 is a correction to $1/K$ for the non-$1/E$ form of the slowing-down spectrum. Bigham and Pearce (*12*) have studied the slowing-down spectrum in a rod-type reactor similar to NRX and have shown that the departure from $1/E$ dependence increases with increasing distance between rods. The results they obtained with a lattice spacing of 24.1 cm are consistent with a $1/E^{1.052}$ dependence. We have calculated the response of a $1/v$-detector in $1/E$ and $1/E^{1.052}$ spectra and obtained a correction factor of 0.935 for irradiations under 0.030 in. cadmium covers. This is probably an overestimate of the correction for NRX irradiations where the rod spacing is 17.3 cm and we have used a value midway between the limits $D_2 = 1.00$ and $D_2 = 0.935$. Here again, it turns out that G_1 is relatively insensitive to the choice of D_2. Pushing D_2 to the limit in either direction results in a variation of 0.6% in G_1 for the thickest foil and the effect with thinner foils is less.

The experimental error in G_1 is estimated to be about 3%. It includes contributions from the following sources: (a) experimental error in the measurement of A_t/A_0 (2.5%), (b) experimental error in $D_1 s_0$ (0.7%), and (c) uncertainty in the choice of $1/K$ (1.0%), F (0.5%), and D_2 (0.6%).

Figure 1 shows that the experimental self-shielding factors agree with the calculated values within the errors and indicates that the first cobalt resonance is responsible for most of the self-shielding effects observed.

Results of Wire Experiments

Most cobalt monitors used in reactor experiments are in wire form and therefore self-shielding factors for wires are of more practical importance than factors for foils. Furthermore, the theoretical calculations for cobalt foils have not been extended to wires, so that there is no alternative but to use experimental values. Therefore self-shielding in cobalt wires ranging in diameter from 0.001 to 0.025 in. and in 0.050 in. diam Co–Al alloy wire containing 0.1 and 1% Co was studied.

The ratio A_t/A_0, the rate of the $Co^{59}(n, \gamma)Co^{60}$ reaction in wire of diameter t relative to the rate in the 0.1% Co–Al alloy wire, was determined experimentally. Average values obtained from ten or more determinations at each wire diameter are

TABLE II

SELF-SHIELDING FACTORS FOR COBALT WIRES

$F = 0.977$, $D_1 s_0 = 1.74$, $D_2 = 0.968$, $K = 2.06$, $h = 1.36 \times 10^{-4}$, $r\sqrt{(T/T_0)} = 2.4 \times 10^{-2}$

Wire diam (in. × 10^3)	Cobalt content (wt %)	Cobalt thickness[a] (Co atoms per cm² × 10^{-18})	Uncorrected A_t/A_0	Correction to A_t/A_0 for γ-ray self-absorption	Resonance neutron self-shielding factor (G_1)
50	0.104	1.83		1.000	1.00
50	0.976	17.4	0.961 ± 0.014	1.001	0.95 ± 0.04
1	100	115	0.860 ± 0.013	0.988	0.81 ± 0.03
5	100	577	0.633 ± 0.009	0.991	0.52 ± 0.02
10	100	1150	0.551 ± 0.008	0.995	0.42 ± 0.02
15	100	1730	0.514 ± 0.008	1.000	0.38 ± 0.01
20	100	2310	0.479 ± 0.007	1.004	0.34 ± 0.01
25	100	2890	0.463 ± 0.007	1.008	0.32 ± 0.01

[a] Cobalt thickness = cobalt atoms per cm³ × wire radius.

given in Table II. The observed rate of the $Co^{59}(n, \gamma)$ reaction in the thicker pure cobalt wires and the Co–Al alloy wires is less than the true rate owing to self-absorption of the Co^{60} gamma rays. This is a negligible correction for the foils discussed in the previous section but, for example, amounts to about 2% with 0.025 in. diam wire. Corrections to be applied to the observed A_t/A_0 ratio have therefore been deduced and are given in Table II. To obtain these corrections we take the fraction of the emitted gamma rays that suffer self-absorption to be $(2\mu t)/3$ where μ is the gamma-ray absorption coefficient and t is the wire diameter. Thus we assume that the gamma rays escape through the sides of the wire, that the detector geometry is 4π, and that gamma-ray absorption depends directly on the thickness of the absorber; these are all satisfactory approximations for the present purpose. Errors in A_t/A_0 after correction for gamma-ray self-absorption amount to 1.4%. They are based on the standard deviations from the average value of A_t/A_0 at each wire diameter (1%) and the cobalt content of the 0.104% Co–Al alloy wire (1%).

The resonance self-shielding factors have been calculated for wires using Eq. (3). With the wires, just as with foils, we take G_2 to be unity for the range of wire diameter used. This is probably satisfactory because Selander has shown that $G_2 = 1.00$ for foils up to a thickness of 4.6×10^{21} Co atoms/cm² (1.6 times the "thickness" of 0.025 in. diam cobalt wire), and in general self-shielding in wires is less than in foils. The values for the factors used in solving Eq. (3) are the same as those used in the foil experiments and are given in Table II together with our values for the resonance self-shielding factors for cobalt wires.

The errors in the G_1 values given in Table II are estimated to be about 3%. They include 2.8% uncertainty in A_t/A_0 (twice the observed standard deviations), 0.7% experimental error in $D_1 s_0$, and 1.0%, 0.5%, and 0.6% variations arising from uncertainties in the choice of the factors $1/K$, F, and D_2, respectively.

Thermal Neutron Self-Shielding in Cobalt Wires

A few measurements of thermal neutron self-shielding in cobalt wires were made for comparison with the calculations reviewed by Zweifel (*3*). The experimental method was similar to that used for resonance self-shielding measurements except that the irradiations were made in pairs. Cadmium covers were used in one member of the pair and yielded the data already included with the results given in Table II. The other member of the pair was an irradiation without cadmium. The reactor conditions were the same for both members of the pair. The thermal neutron rate of the $Co^{59}(n, \gamma)Co^{60}$ reaction was obtained by subtracting the covered reaction rate from the uncovered rate for a particular wire diameter. The thermal neutron self-shielding factors, G_{th}, were deduced by comparing the thermal rate in the wires of the different diameters studied with that in the 0.1% Co–Al alloy wire after making the corrections for gamma-ray self-absorption. The results are given in Table III and a comparison with calculated values, using the thermal neutron cross section of cobalt, is shown in Fig. 2. The errors shown are the standard deviations from the averages and are larger than those in the cadmium covered

TABLE III

Thermal Neutron Self-Shielding Factors for Cobalt Wires

Wire diam (in. × 10^3)	Cobalt content wt %)	Cobalt thickness (Co atoms per cm² (× 10^{-18})	Relative uncorrected reaction rate	Correction to relative rate for γ-ray self-absorption	Thermal neutron self-shielding factor (G_{th})
50	0.104	1.83	1.000	1.000	1.00
50	0.976	17.4	0.993 ± 0.010	1.001	0.99 ± 0.01
1	100	115	1.002 ± 0.016	0.988	0.99 ± 0.02
5	100	577	0.974 ± 0.010	0.991	0.97 ± 0.01
10	100	1150	0.942 ± 0.011	0.995	0.94 ± 0.01
15	100	1730	0.919 ± 0.015	1.000	0.92 ± 0.02
20	100	2310	0.893 ± 0.018	1.004	0.90 ± 0.02
25	100	2890	0.877 ± 0.027	1.008	0.88 ± 0.03

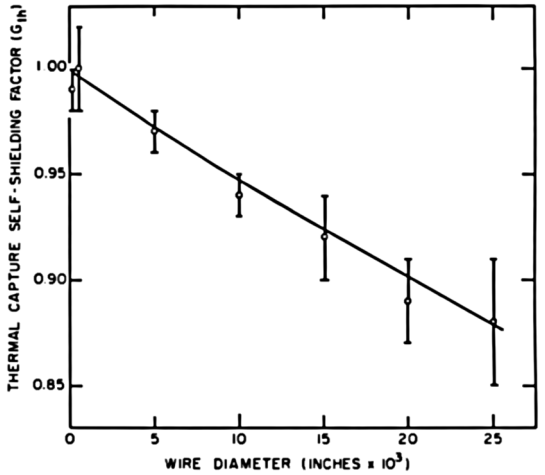

Fig. 2. Thermal neutron self-shielding factors for cobalt wires. The points are experimental, the line is calculated from Case *et al.* (*6*) using the thermal cross section of cobalt.

experiments because the errors in four measurements are compounded into the ratio for a particular wire diameter. Nevertheless, the agreement with the calculation is satisfactory.

ACKNOWLEDGMENTS

We acknowledge with pleasure several useful discussions with Dr. C. B. Bigham and the help of Dr. W. G. Cross, who deduced the correction for gamma-ray self-absorption used in this paper.

REFERENCES

1. F. J. JOHNSTON, J. HALPERIN, AND R. W. STOUGHTON, *J. Nuclear Energy, Pt. A, Reactor Sci.* **11,** 95 (1960).
2. R. L. MACKLIN AND H. S. POMERANCE, *Proc. 1st Intern. Conf. Peaceful Uses Atomic Energy, Geneva, 1955,* **5,** 96 (1955).
3. P. F. ZWEIFEL, *Nucleonics* **18,** 174 (1960).
4. W. N. SELANDER, AECL No. 1077 (June, 1960).
5. D. J. HUGHES AND R. B. SCHWARTZ, Neutron cross sections. BNL-325, 2nd ed. (1958).
6. K. M. CASE, F. DE HOFFMAN, AND G. PLACZEK, Introduction to the theory of neutron diffusion. U. S. Government Printing Office (1953).
7. "ASTM Methods for Chemical Analysis of Metals," pp. 218-9. American Society for Testing Materials, Philadelphia, 1950.
8. D. G. HURST, *Proc. 1st Intern. Conf. Peaceful Uses Atomic Energy, Geneva, 1955,* **5,** 111 (1955).
9. J. C. ROY AND J. J. HAWTON, AECL-1181 (December 1960).
10. C. H. WESTCOTT, W. H. WALKER, AND T. K. ALEXANDER, *Proc. 2nd Intern. Conf. Peaceful Uses Atomic Energy, Geneva, 1958,* **16,** 70 (1958).
11. C. H. WESTCOTT, AECL No. 1101 (November 1960).
12. C. B. BIGHAM AND R. M. PEARCE, *Nuclear Sci. and Eng.* **6,** 459 (1959).

NUCLEAR SCIENCE AND ENGINEERING: **13**, 391–397 (1962)

Laboratory-Scale Demonstration of the Fused Salt Volatility Process

G. I. CATHERS, R. L. JOLLEY, AND E. C. MONCRIEF

Oak Ridge National Laboratory, Oak Ridge, Tennessee

Received January 5, 1962

The feasibility of processing enriched irradiated zirconium–uranium alloy fuel by the fused salt-fluoride volatility procedure has been demonstrated in laboratory tests with fuel having a burnup of over 10%. Uranium recoveries were greater than 99% and decontamination factors for radioactive fission products were 10^6 to 10^9. The UF_6 product contained significant quantities of nonradioactive impurities; additional work in this area is needed.

INTRODUCTION

The fused salt-fluoride volatility process for zirconium–uranium reactor fuel consists of (1) hydrofluorination and dissolution of the fuel in molten salt, (2) fluorination to volatilize UF_6 from the melt, and (3) complete decontamination of the UF_6 in an absorption–desorption cycle (*1*, *2*). Development of this nonaqueous process has proceeded through small-scale laboratory work to limited operation of a small pilot plant. Its advantages include low waste volumes (<1 liter/kg Zr–U alloy), high decontamination from fission product activities, a greatly decreased criticality problem with enriched fuel due to the absence of neutron moderators, and the elimination, because the product is UF_6, of some of the chemical conversion steps needed in the aqueous uranyl nitrate–uranium metal process cycle. Some possible disadvantages are corrosion at high temperatures in a fluoride system, the necessity of a gas-tight system, and the difficulty of manipulating molten salt.

Small-scale process tests, carried out in a hot cell, included study of the hydrofluorination and fluorination reactions, the behavior of various fission product activities, and the degree of uranium recovery and decontamination. The tests were conducted primarily to demonstrate the chemical feasibility of the process with highly irradiated fuel for operation of the ORNL Volatility Pilot Plant, which has been adapted to process Zr–U reactor fuel (*3*). If this operation is successful, the pilot plant may be modified to test variations of the process with other types of fuel.

PROCESS DESCRIPTION AND EXPERIMENTAL PROCEDURE

The major process steps of fuel dissolution, UF_6 volatilization, absorption, and desorption were used (see Fig. 1). In each of 12 tests, 650 gm of 2- to 3-year-decayed zirconium-uranium alloy fuel, with gross β and γ activity levels of 1.8×10^9 and 1.0×10^9 counts/min/mg U (counted at an efficiency of ~10%), respectively, was dissolved at 500–700°C by hydrofluorination in molten 57–43 mole% LiF–NaF with a liquidus temperature of 670°C. As hydrofluorination and dissolution proceeded, the composition of the molten salt changed as represented by the line shown in the phase equilibrium diagram (Fig. 2). Dissolution was completed at a salt composition of 31–24–45 mole % Lif–NaF–ZrF_4, i.e., close to a eutectic composition melting at 449°C. The resulting final UF_4 concentration in the melt was <1%. The system LiF–NaF–ZrF_4 is one of the few fluoride systems known in which liquidus temperatures are so low for large concentrations of ZrF_4 (*4*). The composition of the initial dissolution salt was chosen so as to minimize the liquidus temperature encountered in the 0–20 mole % ZrF_4 region of the phase diagram.

The dissolution product salt containing UF_4 was fluorinated at 500°C with elemental fluorine, and the volatilized UF_6 was absorbed on sodium fluoride at

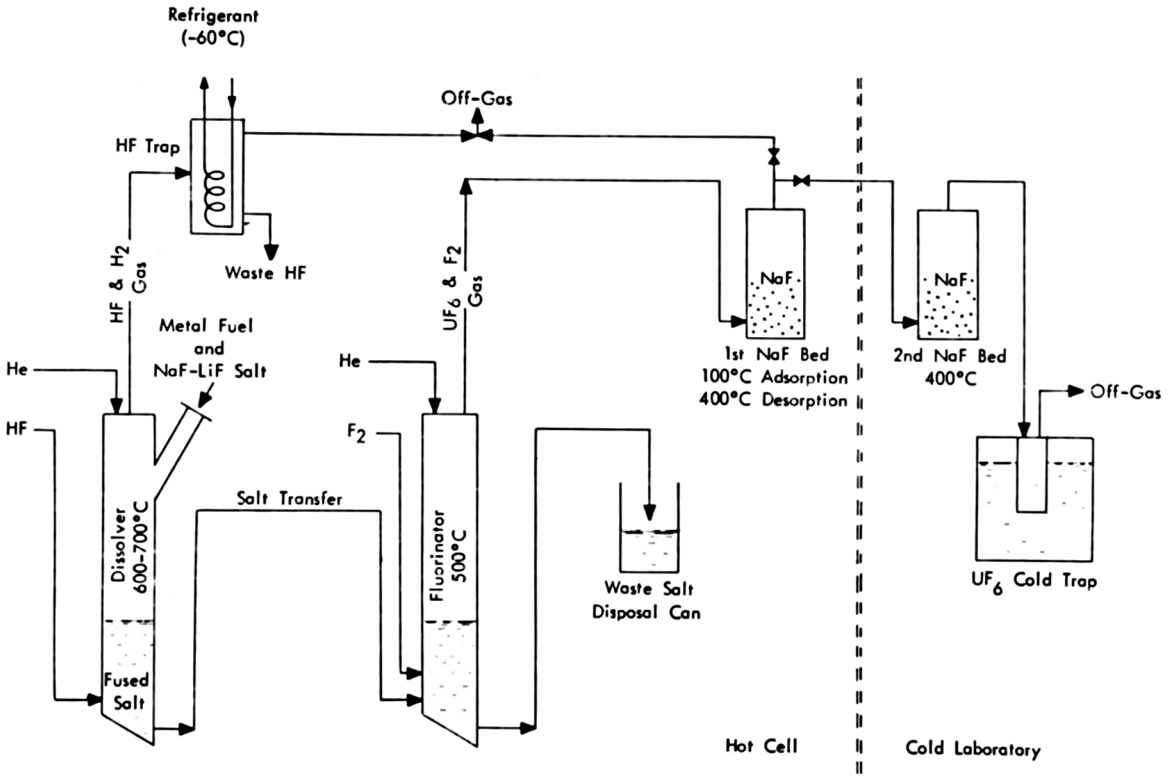

FIG. 1. Schematic of laboratory process test equipment

100°C. The UF_6 vapor pressure over the $UF_6 \cdot 3NaF$ complex at this temperature is $\sim 2 \times 10^{-3}$ mm, and essentially all the UF_6 is removed from the F_2–UF_6 gas stream (*5*). Desorption consisted in heating the UF_6–NaF complex bed from 100 to 400°C while passing F_2 through to a second NaF bed held at 400°C. The dissociation pressure of the $UF_6 \cdot 3NaF$ complex exceeds 760 mm at 400°C. The final UF_6 product was cold-trapped at −60°C, then hydrolyzed with a 1 *M* $Al(NO_3)_3$ solution for analysis.

Equipment for the laboratory tests was installed in a hot cell equipped with Argonne Model 8 slave manipulators (see Fig. 1). It consisted of a dissolution reactor, fluorination vessel, NaF absorption beds, cold traps, and the necessary pneumatically operated valves for coupling the system together.

The Hastelloy N dissolver was 18 in. deep and 3 in. i.d., with a 250-mil thick wall, and had a loading chute. The L-nickel fluorinator was also 18 in. deep, 3 in. i.d., with a 250-mil wall. Both vessels were heated by a 5-in. diam 12-in. long tube furnace, supported vertically. The salt transfer lines ⅜ of-in. diam Inconel tubing (30 mils wall thickness) were heated auto-resistively with high-amperage current. The salt transfer line between the two salt reactors was also used as a common gas inlet line for the two vessels.

In runs 1 through 7, U-tube nickel absorption reactors containing 200 gm of NaF, 12–20 mesh, were used. Since less than 10 gm of uranium was involved, smaller nickel vessels containing 50 gm of NaF on grade H sintered nickel filter were used in runs 8 through 12. In these last runs the UF_6 was desorbed in a "cold" laboratory, the absorption bed having a maximum activity of about 200 mr/hr at contact, a large part of this being due to external surface contamination picked up in the hot cell.

The stainless steel cold traps for waste HF and product were cooled by a mixture of trichloroethylene and dry ice. The waste HF was jetted into ice water, warmed to ambient temperature, sampled, and poured into a waste drain. The molten salt was sampled by a dip rod-frozen salt technique before being transferred into heavy iron cans, sealed over with a high-melting wax while still warm, for subsequent disposal.

RESULTS

DISSOLUTION

The total dissolution time varied from 16 to 62 hr, the HF efficiency varied from 19 to 48%, and the

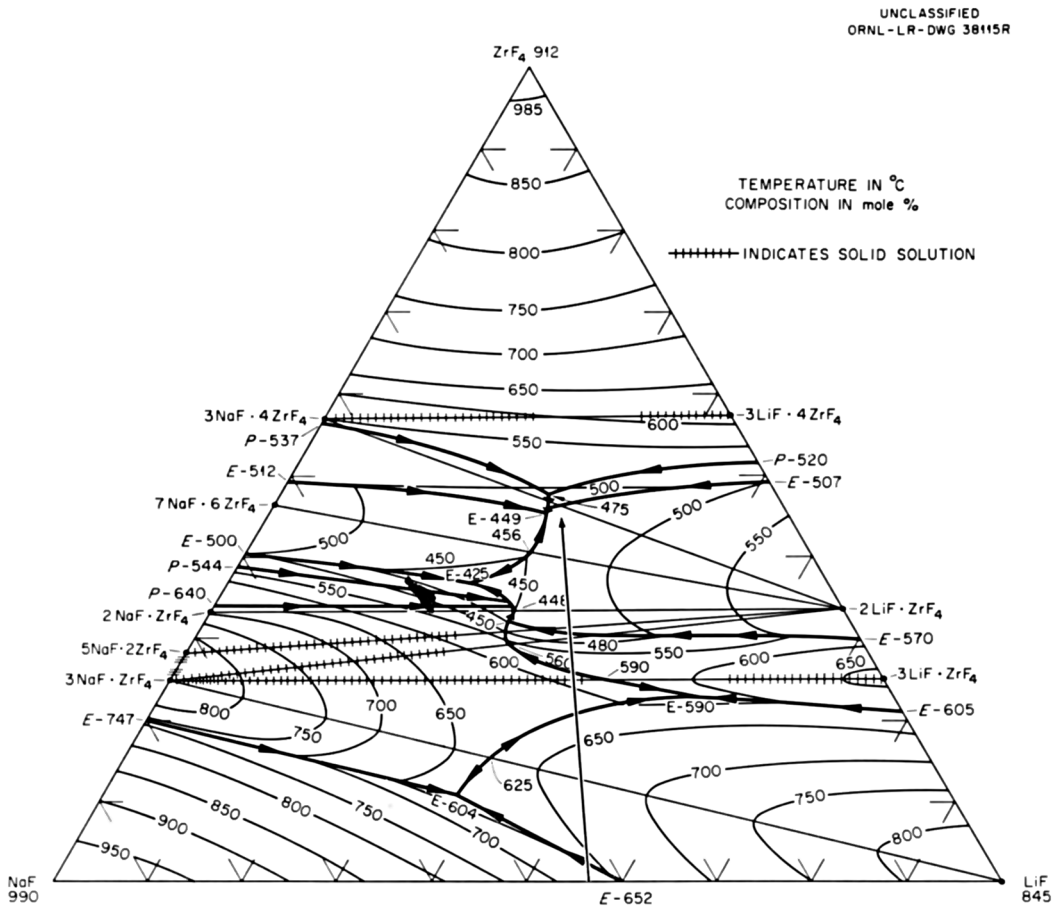

FIG. 2. LiF–NaF–ZrF_4 phase diagram with process composition line

TABLE I

TYPICAL DISSOLUTION RESULTS

Run No.	Average HF flow rate, (ml/min)	HF concentration (%)	HF utilization efficiency (%)	Dissolution time (hr)	Average dissolution rate (mg cm^{-2} min^{-1})
1	820	100	20.1	62	0.17
3[a]	1130	100	30.3	34	0.30
10[b]	1200	70	27.3	29	0.35
12[c]	1400	100	47.7	16	0.64

[a] Direct gas phase reaction occurred in first 6 hr.
[b] Salt prehydrogenated; fuel hydrided to $ZrH_{0.33}$.
[c] Salt prehydrogenated; fuel hydrided to $ZrH_{1.2}$.

average dissolution rate varied from 0.17 to 0.64 mg cm^{-2} min^{-1} (Table I). These rates, although lower than in early laboratory work, are comparable to those obtained in engineering studies. The variables in the dissolution tests were flow rate, temperature, amount of alloy exposed to direct gas phase reaction, salt purification, zirconium hydriding, and HF concentration. Dissolution was most rapid in run 12, in which the salt had received some prepurification, the zirconium was prehydrided, and a high HF flow rate was used. Entrained or volatilized material carried over in the HF stream, with the exception of Nb γ activity, was usually $<0.1\%$ (Table II), and the maximum uranium loss, probably as UF_4, was 0.03%. Entrainment of Na, Cs, Sr, and rare earth fluorides was similar in magnitude to that of uranium. The transfer of Nb, and possibly also of Ru and Zr, may have been due to volatilization, followed by desublimation and entrainment in the H_2–HF gas stream. The fluorides NbF_5, RuF_5, and ZrF_4 are relatively volatile, with boiling or sublimation temperatures of 229, 313, and 903°C, respectively.

Some of the variables present in the test dissolutions have not been evaluated adequately in nonradioactive laboratory work, but they were used in an effort to reduce the dissolution time. The probable effect of some of the variations are summarized in Table III, but the nature of the tests precluded drawing firm conclusions about optimum dissolution

TABLE II

ENTRAINMENT IN WASTE HF OF DISSOLUTION STEP

Run No.	Amount, % of total in feed										
	U	Zr	Na	Gross β	Gross γ	Ruγ	Zrγ	Nbγ	Csγ	Srβ	TRE β
1	0.007	—	—	0.02	0.1	0.005	0.02	—	0.1	—	—
3	0.007	—	—	0.02	0.2	0.04	0.1	7	0.07	—	—
10	0.01	0.3	0.04	0.03	0.2	0.3	0.04	0.9	0.05	0.02	0.004
12	0.007	0.1	0.05	0.08	0.2	2.0	0.4	1.2	0.04	0.02	0.006

TABLE III

SUMMARY OF FACTORS AFFECTING DISSOLUTION OF Zr–U ALLOY

Factor and its effect on dissolution rate	Comments
Increasing HF flow rate increases rate logarithmically	Probably due to increased agitation and more chance of direct gas-solid reaction as well as maintaining HF saturation of the salt
Increasing temperature increases rate	Generally true, but effect is not much over a factor of 2 in available temperature range
Nonsubmergence of fuel in salt promotes direct HF-alloy fuel reaction	Contact of 100% HF with unconditioned massive metal at 700°C results in a run-away reaction; however, formation of a ZrF_4 surface coating inhibits the reaction
HF dilution with H_2 decreases rate	H_2 arises from reaction of HF with metal or metal hydride, or is added as diluent
Prehydriding of fuel before salt addition possibly increases rate	Indefinite at low H/Zr ratio, since much surface cracking and swelling generally occur only above a H/Zr ratio of 1.5/1
Salt purification by H_2 reduction of Fe^{2+}, Ni^{2+}, and Cr^{2+} possibly removes inhibition of reaction	Effect not proved although plating-out of Ni, Fe, and other electronegative elements on Zr surfaces has been noted

conditions. The effect of impurities in the salt on dissolution has not been definitely established although the plating-out of nickel on the zirconium metal surface has been observed, and this presumably hinders dissolution of the zirconium. Other elements such as iron, molybdenum, tin, and chromium are also electronegative relative to zirconium and would presumably act similarly. All these elements are fission products, or arise from corrosion of the Inor-8 (71% Ni, 16% Mo, 5% Fe, and 7% Cr), or are present in the fuel alloy, or are impurities in the initial salt. Two reactions involved in the nickel cycle are

$$2NiF_2 + Zr \rightarrow ZrF_4 + 2Ni, \quad \Delta F^\circ = -130 \text{ kcal}$$

$$Ni + 2HF \rightarrow H_2 + NiF_2, \quad \Delta F^\circ = +6 \text{ kcal}$$

Reduction of NiF_2 to nickel metal at the zirconium fuel surface probably proceeds mainly by the first reaction although the second reaction in reversal leads also to reduction if the H_2/HF mole ratio is sufficiently high. At the end of zirconium fuel dissolution the production of hydrogen becomes small and the second reaction leads to total redissolution of the amorphous nickel metal formed in the earlier stage.

URANIUM RECOVERY

Greater than 99% UF_6 volatilization was obtained only in the last four tests because of inexperience with the equipment and the use of low fluorine flow rates (Table IV). Volatilization was repeatedly 99.8% or more in earlier work with simulated process tests.

The NaF absorption–desorption cycle also operated effectively, resulting in little uranium loss and duplicating the behavior observed in earlier laboratory and pilot plant work. The total uranium

TABLE IV

TYPICAL URANIUM VOLATIZATION IN FLUORINATION STEP

Run No.	Temperature (°C)	Fluorination time (hr)	F_2 flow rate (ml/min)	U volatilized[a] (%)
8	500	4	300	97.9
9	520	4	300	99.4
10	500	3	340	99.2
11	520	3	340	99.9
12	500	3	430	99.8

[a] Based on analysis of fluorinated salt. Initial salt contained ~0.5% uranium.

TABLE V

OVER-ALL DECONTAMINATION FACTORS IN COMPLETE PROCESS TESTS

Run No.	Decontamination factors							
	Gross β	Gross γ	Ru γ	Zr γ	Nb γ	Cs γ	Sr β	TRE β
8	2×10^6	$>1 \times 10^9$	2×10^8	8×10^5	4×10^7	3×10^9	3×10^8	5×10^8
9	3×10^6	2×10^8	4×10^7	2×10^6	$>2 \times 10^8$	1×10^9	$>3 \times 10^9$	$>1 \times 10^{10}$
10	9×10^6	5×10^7	2×10^6	3×10^6	8×10^7	1×10^9	$>1 \times 10^{10}$	$>7 \times 10^9$
11	1×10^6	2×10^6	5×10^4	1×10^5	$>6 \times 10^7$	2×10^{10}	$>9 \times 10^9$	$>3 \times 10^9$
12	2×10^9	6×10^7	1×10^7	9×10^4	8×10^5	2×10^9	$>5 \times 10^9$	$>1 \times 10^{11}$

retention on NaF beds was less than 0.1%, and this probably represents an upper limit with reuse of the beds and the tendency for refluorination of any retained residue.

DECONTAMINATION EFFECTIVENESS

Over-all gross β and γ decontamination factors ranged from 10^6 to 11^9 (Table V). In all but a few cases the amount of activity in the product UF_6 was less than 10-fold the "natural" activity of U^{235} (Table VI). In run 11 the ruthenium γ activity was high because an accidental pressure buildup and release carried some dust from the NaF bed into the UF_6 cold trap. In runs 1 and 6 the product UF_6 was trapped on NaF instead of in a cold trap, with the result that subsequent hydrolysis prior to analysis gave an excessively dilute solution and a high and uncertain background correction led to more apparent activity than in later runs. Runs 2 through 5 are not included since they were not complete flowsheet tests. In runs 7 through 12 the services of a special low-activity-level analytical laboratory were used, which, in conjunction with an improved product hydrolysis method, gave a more accurate picture of the activity in the product.

The principal chemical impurities in the UF_6 product were molybdenum, technetium, neptunium, and chromium, in order of decreasing concentration (Table VII). Molybdenum, the end product of several fission product decay chains and a hydrofluorinator vessel corrosion product, varied in concentration from 1200 to 10,100 ppm. Volatile MoF_6 formed in the fluorination step complexes with NaF, similarly to the behavior of UF_6. Investigation of the dissociation pressure of MoF_6–NaF complex showed that it is approximately 1 atm. at 225°C, compared to 360°C for the UF_6–NaF complex (*6*). Some separation of MoF_6 and UF_6 is thus achieved in the absorption step, dependent on the conditions of temperature, time, and gas flow.

The low activity levels of the UF_6 products in runs 8 through 12 and the fact that the usual individual fission product β activity contributors did not total up to the gross β activity indicated an unknown β contributor. This was found to be technetium, by both chemical and radiochemical analyses. It was calculated that the feed contained >3900 ppm based on the uranium, assuming >10% burnup. The volatile compound TcF_6 is presumably formed in fluorination and possibly behaves in the same way as MoF_6 and UF_6 in absorption.

There was no explanation for the consistent decrease of Mo and Tc impurities in the UF_6 product except possibly some improvement in operational techniques arising through experience.

TABLE VI

RATIO OF PRODUCT URANIUM ACTIVITY TO ACTIVITY OF UNIRRADIATED U^{235}[a]

Run No.	Activity ratio, product/unirradiated U^{235}					
	Ru γ	Zr γ	Nb γ	Cs γ	Sr β	TRE β
1	<10	<10	<10	<10	<0.1	<1
6	<10	<10	<10	<10	<0.1	<1
7	<1	<1	<1	<1	<0.1	<0.1
8	<0.1	<1	<0.1	<0.1	<0.1	<0.1
9	<1	<1	<0.1	<0.1	<0.1	<0.1
10	<10	<1	<0.1	<0.1	<0.1	<0.1
11	<100	<10	<0.1	<0.1	<0.1	<0.1
12	<1	<10	<1	<0.1	<0.1	<0.1

[a] Basis: 232β counts/min/mg U, 11γ counts/min/mg U for 90% U^{235} in equilibrium with daughters.

TABLE VII

IMPURITIES IN UF_6 PRODUCTS

Run No.	Amount (ppm of U)			
	Mo	Np	Tc	Cr[a]
8	10,100	260	1020	200
9	5200	240	490	290
10	2200	58	260	150
11	2500	310	240	80
12	1200	290	60	<100

[a] Probably from corrosion of the cold trap during the hydrolysis of the product to obtain a representative aqueous sample.

TABLE VIII

STEP DECONTAMINATION FACTORS IN RUN 12

Step	Decontamination factors							
	Gr β	Gr γ	Ru γ	Zr γ	Nb γ	Cs γ	Sr β	TRE β
Dissolution	2	1	40	2	30	1	1	1
Fluorination	4×10^5	3×10^5	4×10^3	5×10^4	4×10^3	4×10^5	1×10^7	2×10^7
Absorption–desorption	2×10^3	2×10^2	1×10^2	1	6	3×10^3	$>5 \times 10^2$	$>5 \times 10^3$
Over-all	2×10^9	6×10^7	1×10^7	9×10^4	8×10^5	2×10^9	$>5 \times 10^9$	$>1 \times 10^{11}$

TABLE IX

MEASURED DECONTAMINATION FACTORS OBTAINED IN FLUORINATION

Run No.	Gr β	Gr γ	Ru γ	Zr γ	Nb γ	Cs β	Sr β	TRE β
1	3×10^5	1×10^5	4×10^2	7×10^4	5×10^3	2×10^5	4×10^6	1×10^7
2	2×10^5	8×10^4	2×10^3	1×10^5	2×10^3	—	—	6×10^6
3	1×10^5	3×10^4	6×10^2	5×10^4	1×10^3	—	8×10^6	—
4	1×10^5	4×10^4	1×10^2	2×10^2	2×10^2	—	2×10^6	—
5	8×10^4	3×10^4	2×10^2	3×10^4	1×10^3	—	—	—
6	3×10^4	2×10^4	2×10^2	1×10^4	2×10^3	4×10^4	3×10^5	5×10^5

Neptunium hexafluoride also appeared to follow UF_6 through the absorption step. Chromium may have been introduced by hydrolysis of the UF_6 product in a stainless steel vessel.

Decontamination factors for the separate process steps are given for run 12 in Table VIII.

Dissolution Step. There was considerable but highly erratic disappearance of ruthenium and niobium activity during dissolution. The ruthenium γ d.f.'s were 5 to 120, and the removal of Ru is believed due primarily to adsorption on the dissolver wall. Some ruthenium was volatilized with the excess HF. The niobium d.f.'s were 3 to 620. The removal of niobium is believed primarily to be due to volatilization rather than adsorption on metal surfaces. Material balances for both ruthenium and niobium were low, possibly as the result of condensation of some NbF_5 (bp 229°C) in the top zone of the dissolver, and of adsorption of the ruthenium. The retention of cesium, strontium, and rare earth activities in the fused salt was expected since these elements form fluorides that are nonvolatile and difficult to reduce.

Fluorination Step. Decontamination of UF_6 from the most important volatile fission product activities, Ru γ and Nb γ (probably in the form of RuF_5 or RuF_6 and NbF_5), in the fluorination process was much higher at a fluorination temperature of ~500°C than in previous work at 600–650°C (*1*). In the first six tests conducted in the hot cell work, the absorption off-gas was trapped in caustic. From analyses of these solutions and of the first NaF beds, the gross β, gross γ, Ru γ, and Nb γ activity decontamination factors were calculated for the fluorination step (Table IX). At 600–650°C the gross β and γ d.f.'s were usually $\sim 10^3$ and the Ru γ and Nb γ d.f.'s ~5–10. Uranium is thus largely decontaminated from fission product activities in the fluorination step if the temperature is kept as low as possible.

Absorption–Desorption. Decontamination factors in the absorption–desorption step were in the range 10–100 for the more volatile NbF_5 and RuF_5 or RuF_6. The amount of Ru γ activity in the off-gas stream passing through the first NaF absorption bed was highly variable, due principally to the small amount volatilized in the 500°C fluorination step: 82, 11, 8, 13, 11, and 6% of the total volatilized Ru γ activity in runs 1 through 6, respectively. In previously reported work relatively more Ru γ activity passed through the first NaF bed and resulted in much higher d.f.'s over the absorption–desorption step, since a larger amount of Ru γ activity was volatilized in the fluorination step at 600–650°C and the effects of physical adsorption and poor counting statistics were less noticeable.

Actual absorption–desorption decontamination factors could be calculated only in runs 1 through 6 where the absorption off-gas activity was trapped and measured. The absorption–desorption d.f.'s presented in Table VIII for run 12 are minimum values since the absorption off-gas was not measured. Actually, inclusion of the off-gas activity in the calculation

would affect only the Ru γ and Nb γ d.f.'s and those only slightly. The d.f.'s given for the separate process steps in run 12 (Table VIII) were calculated from prorated activities measured in the first absorption bed since the same material was used in runs 8 through 12.

CONCLUSIONS

The fused salt-fluoride volatility process gave satisfactory decontamination of uranium from fission product activities with the processed fuel having a burnup of $>10\%$ and a decay period of 2–3 years. The main impurities in the product UF_6 were molybdenum, technetium, and neptunium. Some separation from molybdenum and technetium evidently occurs in the absorption–desorption step, and further work to optimize this effect appears warranted. The results also indicate that use of a fluorination temperature of 500°C rather than 600–650°C minimizes to a large extent the carryover of Ru γ and Nb γ activities along with the UF_6 gas stream in the fused salt fluorination step. Evaluation of the absorption–desorption step was only tentative due to the small carryover of all activities from the fluorination step.

The over-all results appear to confirm the chemical feasibility of recovering U^{235}, relatively free of fission product activity, by the fused salt-fluoride volatility process from irradiated Zircaloy-2-U alloy fuel. Further work is probably needed on the question of chemical impurities in the UF_6 product prior to reuse as fissile material. Other areas of chemical uncertainty exist, particularly in the dissolution step, but these are apparently not serious. The dissolution step involves gas–liquid–solid contact and is necessarily quite dependent on geometry. It appears desirable, however, to study further the zirconium metal reduction of NiF_2 and analogous impurities in the fused salt to determine how this affects the dissolution rate and the concurrent volatilization or deposition of relatively noble materials such as ruthenium and molybdenum.

ACKNOWLEDGMENTS

The assistance of T. E. Crabtree and C. J. Shipman in performing the laboratory work is gratefully acknowledged. The authors also express their appreciation for the work of personnel in the Analytical Chemistry Division of ORNL under the supervision of C. L. Burros, J. H. Cooper, W. R. Laing, C. E. Lamb, H. A. Parker, and G. R. Wilson.

REFERENCES

1. G. I. Cathers, *Nuclear Sci. and Eng.* **2,** 768–777 (1957).
2. W. H. Carr, Jr., *Chem. Eng. Symposium Ser.* **56,** 57–61 (1960).
3. R. P. Milford, S. Mann, J. B. Ruch, and W. H. Carr, Jr., *Ind. and Eng. Chem.* **53,** 357–362 (1961).
4. R. E. Thoma, (Ed.), ORNL-2548, p. 60. Oak Ridge National Laboratory (1959).
5. G. I. Cathers, M. R. Bennett, and R. L. Jolley, *Ind. and Eng. Chem.* **50,** 1709–10 (1958).
6. G. I. Cathers, Dissociation pressure of MoF_6–NaF complex and the interaction of other hexafluorides with NaF. Paper presented at American Chemical Society Meeting, Sept. 3–8, 1961.

NUCLEAR SCIENCE AND ENGINEERING: **13**, 398–402 (1962)

Book Reviews

Theory of Elastic Thin Shells. By A. L. GOLDENVEIZER. Translation from the Russian edited by G. Hermann. International Series of Monographs on Aeronautics and Astronautics. Pergamon Press, New York, 1961. 658 pp. $15.00.

The book appears to have been produced by the photo-offset process from a typewritten manuscript. Although the monograph is legible, except for a few blurred areas, it is not generally conducive to pleasant reading.

The author has subdivided the content of the book into five major parts. The first part contains an introduction into the theory of surfaces, and the derivation of the geometric and load relationships present in a general shell element. These relationships are presented in arbitrary curvilinear coordinates and in orthogonal curvilinear coordinates. Part I concludes with the equations of compatibility, the equations of equilibrium, and the mathematical specification of boundary conditions.

Part II is devoted to the membrane theory of shells. In contrast to the direct approach in the development of shell membrane theory the author has chosen to treat this facet of shell analysis as a limiting condition that can be obtained from the general theory of shell flexure. In this section the author has restricted himself to shells of cylindrical, spherical, and conical configuration. He has, intentionally, not included typical surfaces of revolution such as roof domes and liquid containers which are analyzed by membrane theory.

The third part of the monograph deals exclusively with circular cylindrical shells. The relationships and equations developed in Parts I and II are applied to cylindrical shells, generally the simplest type to analyze. Trigonometric series are used principally in the analysis of these shells, and approximate methods are developed for the solution of the problems. These methods, which are used extensively in the text that follows, are first introduced here, since the methods are best demonstrated when applied to a simple geometrical configuration. The development of the approximate methods of treatment of shell problems is one of the primary objectives of the book.

In Part IV of the monograph a detailed mathematical study is made of the approximate methods used in shell analysis. The author examines the methods of asymptotic integration as the shell thickness approaches zero. Part of the text is devoted to a discussion of the circular cylinder equations which have received considerable attention in America, and are known here as the Donnell equations.

The methods developed in the preceding parts of the book are applied in Part V to the solution of problems by membrane theory and by bending theory. The approximate methods are applied to edge effect problems and to the bending of cylindrical and conical shells.

The author has confined himself to a very general but mathematically comprehensive treatment of the theory of shells. Since a rigorous solution of these problems is normally not possible, the mathematical analysis is largely concerned with asymptotic and approximate methods. In his effort not to duplicate material that has already been adequately covered in other Russian books dealing with this subject he has produced a rather specialized monograph on the generalized mathematical approach to the solution of shell problems. For this reason the book is not useful as a general reference text.

The average engineer with a limited mathematical background will find this book too difficult to cope with. Other books on the subject, such as Timoshenko's "Theory of Plates and Shells," or Fluegge's "Statik und Dynamik der Schalen" will generally be of greater practical value to the average shell designer. For those that need to dig deeper into the subject, the mathematical techniques presented in this book will be of great value.

DAVID BURGREEN
United Nuclear Corporation
Development Division
White Plains, New York

(About the Reviewer: David Burgreen is a Consulting Engineer at the Development Division of the United Nuclear Corporation. For the past 12 years he has been concerned with the applied mechanics aspects of nuclear engineering, including the statics and dynamics of structures.)

Introduction to Nuclear Science. By ALVIN GLASSNER. Van Nostrand, Princeton, N. J. 213 pp. $3.75.

The preface to this book indicates the level and organization of the text with the observation that the book resulted from a series of courses or lectures presented to high school science teachers at Argonne National Laboratory. "Lectures were usually given by experts in the field, who took pains to keep them at an appropriate non-technical level. Mathematics was employed only to the extent that the diversified backgrounds of the teachers would permit." Thus the text is an elementary survey of nuclear science and engineering topics with little analysis. A tremendous amount of material is covered but only in a descriptive manner. It is a book, therefore, which would be of interest to a beginner who would like to get a speaking knowledge of a large portion of the nuclear field.

Topics covered in the book include nuclear particles, reactions of nuclei, radioactive decay, detection of radiation, accelerators, reactors, reactor fuels, and biological effects of radiation. There are no problems in the book and few example problems. The language of the text is rather complete in nuclear terms and should be a good reference book

for high school science teachers. It should also be of interest to those in nontechnical work who would like to become acquainted with the nuclear field. It is not recommended as a text for college use.

The last section of the book is devoted to a series of diverse experiments or demonstrations which can be performed with a "minimum of special equipment." Several of the experiments involve the construction or assembly of equipment which can be used as part of other experiments. The outlines of experiments are very concise showing the materials to be gathered, the procedures or methods to follow, and the results or conclusions that should be reached. The experiments range from the response of yeast cells to irradiation (ultraviolet) to the fabrication of fuel elements. The latter experiment obviously requires some special equipment.

The book is well written and serves as an excellent introduction to the field of nuclear science and engineering.

P. F. Pasqua
University of Tennessee
Knoxville, Tennessee

(About the Reviewer: P. F. Pasqua is Professor and Department Head in the Nuclear Engineering Department of the University of Tennessee. He has been on the staff of that university for the past nine years. He obtained his Ph.D. at Northwestern University in 1952.)

Rare Earth Alloys, A Critical Review of the Alloy Systems of the Rare Earth, Scandium and Yttrium Metals. By Karl A. Gschneider, Jr. Van Nostrand, Princeton, N. J., 1961. 449 + xiii pp. $12.75.

Scientists whose field includes the rare earth metals should be interested when a man who works at the Los Alamos Scientific Laboratory writes a book on alloys of the lanthanons. When this man has previously worked with Spedding and Daane at the Ames Laboratory and has received the PhD at Iowa State University, the probability is strong that the book will be good and that the author will know whereof he speaks.

Dr. Karl A. Gschneider, Jr. has made a very scholarly effort to collect and to evaluate data critically on the physical metallurgy of alloys containing one or more of the lanthanons, scandium, or yttrium. Data not readily accessible in the United States, particularly information published in some rather obscure Russian journals and books, are included. One hundred phase equilibrium diagrams have been redrawn after being carefully checked against all available sources of information.

The book is well-written. Organized into four sections, its first part deals with the physical properties of the metals themselves. The second section is given over to presentation of the phase equilibrium diagrams, together with an excellent discussion of some applicable portions of the theory of physical metallurgy. A particularly well-written discussion of the Hume-Rothery Rules and the related Darken and Gurry Plots furnishes some meat for the first section of Part II. Darken and Gurry ellipses for eight of the lanthanons are presented in the book. Part III is a carefully and critically evaluated collation of the crystallographic data on the lanthanons, yttrium, and scandium. Part IV, consisting of a list of all references cited in the previous parts of the book, actually forms a bibliography on rare earth alloys with 653 entries.

One of the most useful aspects of this book is the excellent job of indexing. All binary systems are indexed separately, followed by an index to multicomponent systems. A one-page index to structure types is useful, as is the complete author index.

Many people feel that a book reviewer has not done a good job unless he finds something about which to complain. In order not to disappoint these good people, your present reviewer would make a point that Dr. Gschneider, in his urgent efforts to pick the brains of the eminent Russian experts, may have overlooked a few items of good American work. For instance, the work of Robertson and Kato, at the Albany Station of the U. S. Bureau of Mines, was rather inadequately covered. Kato's work on the dysprosium–zirconium system, complemented by that of Ray and Wasielewski at KAPL on additions of dysprosium to Zircaloy-2, was missed. However, in defense of the author, it was impossible to find, even with reasonably diligent searching, any place in the book "Rare Earth Alloys" where Dr. Gschneider laid claim to complete coverage of all the bits of published information in this broad field.

This is a good book. The style of writing is excellent. Dr. Gschneider says briefly and lucidly what he means. The text is easily understood. No efforts at pedantry were found, and most of the book could be read with understanding and profit by even senior undergraduate level college students of metallurgy or physical chemistry. The format for the book is slightly unconventional, but not in any sense offensive. On the contrary, the format serves its purpose quite well, improving the facility with which the book may be used for reference. This reviewer can only join Dr. Gschneider in recommending the book to those physicists, chemists, and metallurgists engaged in research "in the field of metals" as well as solid state physicists, physical chemists, and engineers who have even a passing idea that some alloy containing yttrium, scandium, or one or more of the lanthanon metals might help them to arrive more quickly at some desirable end.

W. Kermit Anderson
Knolls Atomic Power Laboratory
Schenectady, N. Y.

(About the Reviewer: Dr. W. Kermit Anderson is Consultant—Materials Engineering to the staff of the Materials Development Operation at the Knolls Atomic Power Laboratory. Trained in chemical engineering and physical chemistry at the Agricultural and Mechanical College of Texas, he received the first PhD granted by that institution in the physical sciences. His interest in the rare earths was first aroused at Oak Ridge during a search for high efficiency shielding materials while employed by the NEPA project. This interest was maintained during employment at the Argonne National Laboratory and, more recently, at the Knolls Atomic Power Laboratory, where his desire to apply the lanthanons as absorbers for control of reactors has led to several publications in the field.)

Protective Construction in a Nuclear Age. Proceedings of the Second Protective Construction Symposium: The Rand Corporation. J. J. O'Sullivan, editor. Macmillan, New York, 1961. 2 vols., 884 pp. $25.00.

Collected in these two volumes are 45 papers presented at the Second Rand Corporation Protective Construction

Symposium, held in March 1959. These proceedings, originally circulated to the Symposium attendees in loose-leaf notebook form, remain almost unchanged in the hard-cover version. The papers are grouped into the following sections:

General Problems
Problems of the Underground Area
Site Selection for Deep Underground Installations
Design of Exposed Items
Utilities for Deep Underground Installations
New Construction Methods and Equipment
Underground Construction Experience
Nuclear Burst-Underground Phenomena

Most attendees were connected in some way with the military, and the emphasis is heavily placed on underground construction for military offsensive forces, with only a few papers contributing to the problems of nonmilitary protective construction. Even the military problem is somewhat unevenly handled. For example, in the section on General Problems, Herman Kahn discusses the philosophy of thermonuclear war and the need for protected offensive forces without so much as mentioning the relative merits of hardened versus mobile forces.

Where uncertainties are as great as in the construction of hardened military installations, the avoidance of problems is often a sign of prudence not cowardice. One such case occurs in a discussion on the vulnerability of communications. Proposed solutions include duplicate facilities, hardened facilities, routing of communications around target areas, and diversification; the latter two are chosen, apparently only because of the higher costs and many uncertainties of the former. Occasionally, the existence of problems is overlooked. Two papers concerned with communication systems consider only mechanical effects (blast), avoiding completely the possibility of electromagnetic effects on hardwire systems or the nuclear blackout of radio communications.

Another point concerns an inherent weakness in a collection of this kind, namely, that the reports are separate and are not integrated to focus directly on the pertinent problems. For example, there are two excellent papers in the section on Problems of the Underground Area, one on the dynamics and mechanics of spalling by John S. Rinehart and another concerned primarily with static stresses around openings in rock by Wilbur I. Duvall. Had these papers been prepared together, spalling around openings in rock could have been considered and a much more significant contribution made to the design of shock-resistant tunnels.

Sherwood B. Smith ably summarizes the damage produced on tunnels in tuff by deep underground nuclear bursts of relatively small yield. While such bursts cannot be compared directly with the large-yield surface bursts to be expected in a nuclear attack on hardened bases, this is still probably the most useful information now available for the design of underground facilities.

Edward Cohen suggests a number of clever arrangements for blast-resistant openings, including several that are fail safe, and H. L. Brode proposes novel means for reducing air blast in tunnels. Typical of the lack of integration is the fact that while Brode deals with a surface burst of several megatons—a logical choice against the hardened targets being considered—the authors of a following paper on antenna hardening inconsistently deal with air bursts of a few tens of kilotons.

In the section devoted to the design of utilities for underground facilities, major emphasis is placed on the provision of heat sinks for the period during which access to the outside is denied. (Here another inconsistency is noted when one compares the long periods of "button-up" considered with the use of fast-acting blast valves mentioned earlier.) While conventional engineering procedures are used to determine the heat-sink requirement, no attention is paid to the vulnerability of the utilities, except that isolation from exterior blast is presumed.

Some of the papers are tutorial; instances are "Adaptation of Oil Well Drilling Techniques" by Gene Graham and "Recent Developments for Drilling Large Diameter Hlles" by John C. Haspert and Jack McKinney. They described methods in current use, but the relation of these techniques to the problems of protective construction is left for the reader. Furthermore, the articles on tunneling and mining techniques seem far more pertinent to protective construction problems than those on vertical drilling techniques. Especially noteworthy is the article on high-speed, low-cost excavation methods by J. J. Walsh and Robert Budd, whose contribution stems not so much from improvements in technology as from a careful re-evaluation of the mining operation.

In the section on Underground Construction Experience are several excellent descriptions of the design and construction of underground power stations, again without specific relation to military problems. The best is a description of the Australian Snowy Mountain Hydroelectric Authority program written by Thomas A. Lang; of special interest are the applications of small-scale laboratory models to the investigation of critical stress problems in rock.

The last section, Nuclear Burst-Underground Phenomena, consists of the reports of three working groups which met separately but as a part of the Symposium. These groups considered both present knowledge of basic phenomena and ways in which understanding could be improved in the areas of cratering, wave propagation, and underground structures. Since the recommendations of these committees are of great interest to research workers in these and related fields, it seems that a more extensive treatment than that given was warranted.

Briefly, these volumes constitute a state-of-the-art presentation, as of March 1959, to the extent permitted by classification. In reading the proceedings, one is conscious throughout that the new ideas and concepts presented are based almost entirely upon intuition, conventional techniques, and practical experience; extrapolation of theoretical consideration or engineering principles into areas of uncertainty is notably lacking. Only in the last section is the needed bid for a better understanding of basic phenomena made.

Illustrations at the end of each paper rather than inserted in the text are always an irritant.

The major accomplishments of the Symposium were to bring related (although sometimes only remotely related) experience and techniques to bear on military problems and to introduce new faces into an already somewhat inbred discipline. However, an omnibus of this kind can be expected to receive little attention from those not concerned with problems directly related to hardened underground facilities for the military.

L. J. VORTMAN
Sandia Corporation
Albuquerque, New Mexico

(About the Reviewer. L. J. Vortman has been associated with the Nuclear Burst Physics Department at Sandia Corporation, Albuquerque, New Mexico, since 1949. There, he has accumulated experience in weapon effects with emphasis on air blast loading and underground phenomena, especially explosive cratering. Since 1955, he has directed Program 34 of the AEC's Civil Effects Test Group at the Nevada Test Site. He is currently a member of the Subcommittee on Protective Structures of the National Academy of Sciences.)

Treatment and Disposal of Radioactive Wastes. By C. B. AMPHLETT. Pergamon Press, New York, 1961. 289 + viii pp. $12.00.

As the preface of this book points out, the field of radioactive waste treatment has recently been undergoing considerable development. In the early stages of nuclear energy, the emphasis was entirely on rapid production and the waste which could not be dispersed to the environment was simply stored; concentration by evaporation was almost the only treatment used.

Recently many new processes have been investigated, most in the laboratory but some on a field scale. Dr. Amphlett, of the Chemistry Division at Harwell, has written this book with the intention of describing these developments, from both the fundamental and applied viewpoints. He has succeeded admirably and his book will be of great importance, not only to those directly concerned with treating radioactive wastes, but also to a great many in the nuclear industry and in fields connected with public health.

The book begins with a discussion of the origin and nature of radioactive wastes, considering quantities, radiochemical properties, behavior in the environment, legal and economic factors, and the relative hazards of various types. This is followed by three chapters on the treatment of high level wastes, including chemical separation, evaporation, and fixation as a solid. In each of these chapters the approach is to describe first the theoretical basis, then the existing practice, and finally new methods which are still experimental. There follows a chapter on disposal of solid wastes including incineration and burial or storage.

A long chapter on the chemical and biological treatment of wastes containing low and medium activity levels follows. The treatment here is historical and very complete, possibly too complete. Some of the early work in this field might well have been passed over.

The next chapter covers disposal to the environment, including discharge into the ground, into rivers, and into the sea. Here again for each of these methods of discharge, the author has considered the principles involved, and then the actual operating procedures. Both American and British practices are given, the differences in attitude often being very interesting. Treatment and disposal of gaseous wastes, both particulate and vapor, is next presented, followed by chapters on minor waste problems such as isotope users, and on the future in waste treatment and disposal.

Dr. Amphlett has done a remarkable job of covering the many diverse aspects of radioactive wastes. He appears equally conversant with all these aspects, and his coverage is both thorough and clear. Bibliographies at the end of each chapter are extensive, covering the literature generally into 1959 and including the large volume of information presented at the Second Geneva Conference on the Peaceful Uses of Atomic Energy in 1958.

Taken all in all, this book is a must for anybody seriously interested in the problems associated with radioactive wastes. The only serious fault I can find with it is that the price of $12.00 will make it inaccessible to many individuals who will unfortunately have to rely on library copies.

ABRAHAM S. GOLDIN
Northeastern Radiological Health Laboratory
Winchester, Massachusetts

(About the Reviewer: Abraham S. Goldin has specialized in environmental radionuclide analysis, radioactive pollution, and radioactive wastes. He received his Ph.D. degree from the University of Tennessee. From 1943 to 1950 he worked for the Manhattan District, first at Columbia University and later at the Gaseous Diffusion Plant at Oak Ridge. Following this he spent nine years at the U. S. Public Health Service in Cincinnati as Chief Radiochemist. After serving for a time as Chemical Director of the Atomic Energy Commission's Winchester Laboratory and as an Associate Professor of Industrial Medicine at New York University he has just become Deputy Officer-in-Charge of the Northeastern Radiological Health Laboratory, U. S. Public Health Service.)

Criticality Control in Chemical and Metallurgical Plant. (Proceedings of the Karlsruhe Symposium, 1961, sponsored by the Organization for Economic Co-Operation and Development of the European Nuclear Energy Agency.) (About 90% of the book is in English, and the remainder in French.) 1961. 622 pp. $10.00.

This compilation of the papers and discussions given by many of the leaders in the field of criticality control (nuclear safety), succeeds very well in covering the entire subject from its theoretical and experimental aspects to its practical applications and even some administrative methods currently in use. The summarized discussions following the various papers are of particular note, and rather complete bibliographies are given for each subject. The printing and binding are excellent.

For obvious reasons, the book does not have the continuity and conciseness of a single-author document, and there is some repetitiveness and apparent minor contradictions in the different sections. Indications of personal preference of the various authors are usually handled with restraint, although there are some instances in which what is identified as an over-all summary or review of a given subject is treated somewhat as would be a research-type paper given at a professional meeting to present an apparently recently developed theory or interpretation.

The book does not have a preface indicating clearly its purpose, nor a simple summary of the basic principles upon which practical criticality is based, but these factors are covered by indirection in the various sections as well as in the bibliographical references and discussions.

The excellent and up-to-date summaries given of experimental data now available from various laboratories are especially noteworthy, and these sections provide what are probably the most valuable single contribution of the volume.

The presentations of theoretical methods are individually well handled and summarized. However, correlations between theory and experiment and their application to practical problems are not as well treated as might be desirable. Thus, the theoretical methods are presented in some

papers more in the way of mathematical exercises than as useful methods for criticality control, the types of systems for which the various theories have proven most successful are not always identified, and it is sometimes difficult to determine if a "critical" curve is experimental, theoretical, or an empirical extrapolation of data. In addition, the rather considerable difficulties frequently encountered in making theory applicable to practice are not usually discussed, theoretical predictions are not always compared with experiment, even where this is possible, and estimates are not always made of the extent of possible errors in the predictions, although such information is sometimes given.

The practical sections are well presented and generally cover their subjects rather well. However, a reader should recognize that these sections will unavoidably reflect the experience of the authors. For example, this reviewer believes that the descriptions of organizations assume more responsibility for the staff criticality control group than his own experience has indicated may be necessary, and the analyses given for some of the specific problems apparently lean more heavily on detailed theoretical treatments than may be necessary. In general, there also appears little recognition in the formal papers that rather detailed calculations frequently can give no more useful results for actual plant problems than do much simpler determinations, although this is implied in some of the discussions. It is particularly unfortunate that the section on interaction gives an inadequate and partially incorrect review of the solid angle method of spacing determination; such information is available in K-1335 and K-1478, in addition to the documents quoted.

It is the reviewer's opinion that this book, in reflecting the conference reports, summarizes very well the present state of the art, is the currently most complete summary of this field, and is highly recommended for all having an interest in the subject, especially those given the responsibility for establishing nuclear safety in production operations. It should be considered as a guide, however, and not necessarily a handbook or detailed reference.

HUGH F. HENRY
DePauw University
Greencastle, Indiana

(About the Reviewer: Hugh F. Henry is currently Chairman of the Department of Physics at DePauw University. From 1949 to 1961 he was responsible for criticality control (nuclear safety) at the Oak Ridge Gaseous Diffusion Plant. Among the many authoritative documents he has written on the subject are included "Criticality Data and Nuclear Safety Guide Applicable to the Oak Ridge Gaseous Diffusion Plant," K-1019, and "Studies in Nuclear Safety," K-1380. He continues active in many phases of health physics and criticality control.)

NUCLEAR SCIENCE AND ENGINEERING: **13,** 403 (1962)

Computer Code Abstracts

AIMFIRE

1. Code Name: AIMFIRE
2. Computer for which code is designed: IBM 704, 709, 7090
   Programming system: FORTRAN II
3. Nature of problem solved: Calculation of costs in fixed length multicycle fuel reprocessing. The code solves the zero-dimensional reactor criticality and isotope equations. At the end of a preassigned fuel exposure, fission products are removed according to specified removal fractions, the fuel is re-enriched according to one of several options, and the cycle is repeated.
4. Restrictions on the complexity of the problem:
   Maximum number of isotopes = 100
   Uranium fuels
   Machine requirements: 8K 704, 709 or 7090 and 8 tape units
5. Unusual features of the code: The code will search for the enrichment of the reprocessed fuel which will give the same initial (final) reactivity as calculated for the beginning (end) of the first cycle.
   In the cases investigated to date it was found that for fixed initial reactivity the final reactivity was in excess of that needed for control; thus the search for fixed final reactivity assures optimum fuel utilization. Heterogeneous effects (thermal spectrum, disadvantage factors, etc.) are varied through fitting constants supplied as input data obtained by calculating the effects for several values of the fuel absorption and fitting to a quadratic. A later version will incorporate FORM, TEMPEST, and an S_n cell code. A library of isotopic cross sections, fission yields, and decay constants for 50 isotopes is available.
6. *Reference:* R. A. Blaine, AIMFIRE—A fuel economics code. NAA-SR-6706 (September 1961).

R. A. Blaine
Atomics International
Canoga Park, California

KERNMAT

1. Code name: KERNMAT
2. Computer for which code is designed: IBM-7090, adaptable to IBM-704
   Programming system: FORTRAN II
3. Nature of problem solved: Effective multiplication factor and relative power distribution at fuel assemblies by the heterogeneous method or small source theory of reactor calculations. Fuel assemblies that are fully equivalent to each other within the heterogeneous lattice form a "rod type." Coordinate specification of every pair of rods for all the rod types must be entered. For rectangular lattices, a separate routine, DECART, is available for coordinate grid generation.
4. Restrictions on the complexity of the problem: A maximum of 36 rod types is available. Thermal age-diffusion kernels or their linear combination up to three terms corresponding to infinite line source-sinks in an infinite moderator are assumed, with all resonance absorptions-fissions in fuel lumped at one energy. Machine requirements: 32 K memory, 3 intermediate tapes, input-output tapes under Fortran Monitor.
5. Typical running times: 1 to 5 min, depending upon problem size/options.
6. Unusual features of the code: Coordinate, kernel and/or matrix intermediate data can be written on and read from auxiliary tapes for use in subsequent problems.
7. Present status: Production; source deck/listing of the main program and all the functions and matrix operations subroutines or object deck available.
8. *Reference:* S. A. Raje; KERNMAT, A FORTRAN code for the heterogeneous method of reactor calculations. CVNA-107 (September 1961).

S. A. Raje
Atomic Power Department
Westinghouse Electric Corporation
Forest Hills, Pennsylvania

NUCLEAR SCIENCE AND ENGINEERING: **13,** 404–405 (1962)

Author Index

NUCLEAR SCIENCE AND ENGINEERING: **13,** 406–408 (1962)

General Subject Index

NUCLEAR SCIENCE and ENGINEERING

THE JOURNAL OF THE AMERICAN NUCLEAR SOCIETY

Volume 13, 1962

ACADEMIC PRESS New York and London

NUCLEAR SCIENCE AND ENGINEERING: **13**, iii–iv (1962)

CONTENTS OF VOLUME 13

NUMBER 1, MAY 1962

NUMBER 2, JUNE 1962

NUMBER 3, JULY 1962

NUMBER 4, AUGUST, 1962